Ab initio molecular dynamics calculations on reactions of molecules with metal surfaces

Nattino, F.

Citation

Nattino, F. (2015, October 28). *Ab initio molecular dynamics calculations on reactions of molecules with metal surfaces*. Retrieved from https://hdl.handle.net/1887/35980

Version: Corrected Publisher’s Version

License: Licence agreement concerning inclusion of doctoral thesis in the Institutional Repository of the University of Leiden

Downloaded from: https://hdl.handle.net/1887/35980

Note: To cite this publication please use the final published version (if applicable).

Cover Page

The handle http://hdl.handle.net/1887/35980 holds various files of this Leiden University dissertation

Author: Nattino, Francesco
Title: Ab initio molecular dynamics calculations on reactions of molecules
with metal surfaces
Issue Date: 2015-10-28

Ab Initio Molecular Dynamics Calculations on Reactions of Molecules with Metal Surfaces

PROEFSCHRIFT

ter verkrijging van
de graad van Doctor aan de Universiteit Leiden,
op gezag van Rector Magnificus prof.mr. C.J.J.M. Stolker,
volgens besluit van het College voor Promoties
te verdedigen op woensdag 28 oktober 2015
klokke 13:45 uur

door

Francesco Nattino
geboren te Lecco, Italy, 1987

Promotiecommissie

Promoter:	Prof. dr. G. J. Kroes	
Overige leden:	Prof. dr. J. Brouwer	
	Prof. dr. M. T. M. Koper	
	Prof. dr. D. J. Auerbach	(MPI für Biophysikalische Chemie, Göttingen, D)
	Prof. dr. R. D. Beck	(École Polytechnique Fédérale de Lausanne, Lausanne, CH)
	Dr. M. Alducin	(Centro de Física de Materiales, Donostia-San Sebastian, ES)
	Dr. L. B. F. Juurlink	
	Dr. J. Meyer	

The research described in this thesis was performed in the Theoretical Chemistry Group at the Leiden Institute of Chemistry (Einsteinweg 55, 2300 RA, Leiden NL). This work was made possible by financial support from the Nederlandse Organisatie voor Wetenschappelijk Onderzoek (Netherlands Organisation for Scientific Research, NWO). NWO Exacte Wetenschappen, EW (NWO Physical Sciences Division) is acknowledged for granting access on supercomputer facilities. PRACE is also acknowledged for awarding access to the MareNostrum supercomputer based in Spain at the Barcelona Supercomputing Center (BSC).

Ai miei genitori

Contents

1 General Introduction **1**

1.1 Molecule-Surface Reactions 1

1.2 Reactive Scattering of Molecules from Metal Surfaces 3

1.2.1 Diatomic Molecules 4

1.2.1.1 Scattering 6

1.2.1.2 Adsorption 7

1.2.2 Polyatomic Molecules: Methane 8

1.3 Aim of This Thesis 10

1.4 Main Results 11

1.5 Outlook 14

2 *Ab Initio* Molecular Dynamics for Modeling Gas-Surface Reaction Dynamics **23**

2.1 The *Ab Initio* Molecular Dynamics Technique 23

2.1.1 Deriving Born-Oppenheimer Molecular Dynamics 24

2.1.2 The Hellmann-Feynman Forces 26

2.1.3 Alternative Dynamical Methods 27

2.2 Density Functional Theory 28

2.2.1 The Exchange-Correlation Functional 30

2.2.2 Plane wave DFT 34

2.3 The AIMD Implementation 35

2.3.1 The Choice of the Initial Conditions 36

2.3.1.1 The Surface 36

2.3.1.2 The Molecule 37

2.3.2 The Time Propagation 38

2.3.3 The Analysis of the Trajectories 39

2.4 The Computation of Observables 39

2.4.1 The Initial State-Selected Reaction Probability 39

2.4.2 Simulation of Molecular Beam Adsorption Experiments 40

3 Effect of Surface Motion on the Rotational Quadrupole Alignment Parameter of D_2 Reacting on Cu(111) **49**

3.1 Introduction 50

3.2 Methods 52

3.3 Results and Discussion 55
3.4 Summary and Conclusions 62
3.A Appendix 64
  3.A.1 Statistical Analysis 64
  3.A.2 Relative Importance of the Two Mechanisms for Reducing the Alignment Parameter 68

4 Dissociation and Recombination of D_2 on Cu(111): *Ab initio* Molecular Dynamics Calculations and Improved Analysis of Desorption Experiments 73
4.1 Introduction 74
4.2 Methods 80
  4.2.1 BOSS Model 80
  4.2.2 AIMD Method 81
  4.2.3 The Hole Model 82
  4.2.4 Reaction Probability Curve Fitting 84
  4.2.5 Time of Flight (TOF) Spectra Analysis 88
  4.2.6 Determination of the Relative Saturation Values 91
  4.2.7 Determination of absolute saturation values 92
  4.2.8 Average Desorption Energy 93
4.3 Results and Discussion 93
  4.3.1 Hole Model Results 93
  4.3.2 Fits to BOSS and AIMD Reaction Probabilities 94
  4.3.3 Fits of measured TOF spectra 95
  4.3.4 Experimental Reaction Probability Curves 97
  4.3.5 Simulated TOF Spectra 106
  4.3.6 Experimental and Theoretical Effective Barrier Heights (E_0) . . . 108
  4.3.7 Average Desorption Energies 108
4.4 Summary and Conclusions 110
4.A Appendix 113

5 *Ab Initio* Molecular Dynamics Calculations versus Quantum-State Resolved Experiments on CHD_3 + Pt(111): New Insights into a Prototypical Gas-Surface Reaction 127
5.1 Introduction 128
5.2 Methods 131
5.3 Results and Discussion 133
5.4 Summary and Conclusions 139
5.A Appendix 141
  5.A.1 Experimental Methods 141
  5.A.2 Convergence Tests 141
  5.A.3 Avoiding the Pitfalls of the Quasi-Classical Trajectory (QCT) Method 143
    5.A.3.1 Zero Point Energy (ZPE) Conservation Problems 143
    5.A.3.2 Artificial Intramolecular Vibrational Energy Redistribution (IVR) 143

5.A.3.3 Role of Tunneling 144

6 Methane Dissociation on Pt(111): Searching for a Specific Reaction Parameter Density Functional 151

6.1 Introduction 152

6.2 Methods 154

6.3 Results and Discussion 158

6.3.1 The Van der Waals Well 158

6.3.2 The Dissociation Barrier 162

6.3.3 The Sticking Probability 166

6.4 Summary and Conclusions 172

7 N_2 Dissociation on W(110): an *Ab Initio* Molecular Dynamics Study on the Effect of Phonons 177

7.1 Introduction 178

7.2 Methods 182

7.3 Results and Discussion 187

7.3.1 Molecular Adsorption States 187

7.3.2 Sticking Probability 194

7.3.3 Energy Transfer to the Lattice 199

7.3.4 The Role of Molecular Adsorption in the Dynamics 206

7.4 Summary and Conclusions 208

7.A Appendix 210

7.A.1 NEB Calculations 210

Samenvatting 217

Riassunto 225

Curriculum Vitae 233

List of Publications 235

Chapter 1

General Introduction

1.1 Molecule-Surface Reactions

Molecule-surface reactions are everywhere: They are extensively used in industry [1], where solid catalysts are employed to lower the reaction barriers of chemical processes by detouring the reactants from the direct gas-phase reaction [2]; They are believed to play a major role in the formation of organic molecules and other complex species in star-forming regions in the outer space [3]; They are present in everyday life, in phenomena such as the oxidation of an iron chain, in the catalytic conversion of exhaust gases in automobiles [4], and in the discharge of a battery to obtain electricity [5].

One class of molecule-surface reactions that are of particular interest are reactions on metal surfaces. In heterogeneous catalysis, transition metals are often the active part of the catalyst: they can bind the reactants from the gas-phase, cleave their bonds, provide a good environment for atomic diffusion and formation of new molecules and let the products desorb. Unfortunately, studying the elementary steps that form a catalytic cycle is not a trivial task. The difficulty derives from the fact that the active phase in a real catalyst is usually poorly characterized and inhomogeneously distributed over an inert support with high surface area. Furthermore, catalytic conditions often involve high temperature and pressure.

The complexity of studying gas-surface reactions of catalytic interest can be considerably reduced if a single crystal accurately cut along a particular crystallographic direction and kept under controlled physical conditions is employed as a model for the real catalyst. This approach allows to get some fundamental insight into the elementary steps of the reaction, which is necessary to better understand how a real catalyst works. This knowledge represents the first step towards the ability of improving the catalyst. This approach was used, for instance, by Gerhard Ertl, who was able to propose a reaction mechanism [6] for the ammonia synthesis process, also known as Haber-Bosch process after the industrial chemist who designed it, Fritz Haber, and the chemical engineer who scaled it to industrial level, Carl Bosch. Ertl also suggested that the rate limiting step of this process, which produces ammonia from molecular nitrogen and hydrogen using an iron catalyst, is the N_2 dissociation on the catalyst surface.

Modern surface science instruments allow for preparing, orienting and cleaning crystal samples with very high accuracy. The samples are generally kept at very low pressures (ultrahigh vacuum conditions) to avoid that polluting atoms and molecules would deposit on the surface. A large number of techniques which generally involve the scattering, absorption or emission of electrons, photons and neutrons allows one to characterize surface properties with great detail (see Ref. [7] for an extensive method overview).

In the surface science field, computer simulations have a high potential to help with interpreting experiments: they can provide an atomic-scale movie of a chemical process and they are generally cheaper, safer and faster than regular laboratory experiments. Nowadays, theoretical methods are able to very accurately reproduce experimental observables for gas-phase reactions. The same level of accuracy, however, is far from being achieved for reactions on metal surfaces. This has to do with the large number of electrons present in transition metals, and with the peculiar electronic and mechanical properties arising from the periodic nature of surfaces. In the field of surface science, the accuracy of theory is such that it can generally provide a semi-quantitative description of equilibrium structures, adsorption energies, reaction coordinates and activation energies but further improvement has to be achieved to be able to quantitatively reproduce or predict experimental observables. Note that the accuracy of theoretical methods can only be tested against experimental data measured under accurately determined conditions, so that they can be modeled as carefully as possible in the simulations.

The adsorption of a molecule on a metal surface often represents the first step in a catalytic cycle. A large number of studies have focused on the reactive and the non-reactive scattering of molecules from surfaces with the aim of improving the fundamental understanding about the adsorption phenomenon. Note that also the study of the molecules that bounce back after the impact with the surface is relevant, since they may carry detailed information about the molecule-surface interaction that they experienced during the collision. In the next section we discuss the adsorption phenomenon together with the other possible outcomes of the collision of a molecule with a metal surface.

1.2 Reactive Scattering of Molecules from Metal Surfaces

In general, the outcome of a molecule-surface collision is determined by the details of the interaction potential between the molecule and the surface. It is important to mention, however, that the molecule does not simply interact with an infinite ideal lattice through a single potential energy surface, but other elements might play a role. First of all, surface atoms might be displaced from their equilibrium positions due to their thermal motion, and this might modify the interaction potential. Furthermore, the impacting molecule can exchange energy with the lattice, due to the coupling with lattice vibrations (phonons). In addition, the continuum of electronic states that characterizes a metal surface enables a second energy exchange channel between the molecule and the surface. Arbitrary small amounts of energy, in fact, can be transferred from the molecular degrees of freedom to the electrons lying just below the Fermi level, generating an electron-hole pair. In order to model the effect of electron-hole pair excitations, multiple electronic states and the couplings between them have to be taken into account. These effects are often called non-adiabatic because they cannot be captured if the system is assumed to move on the instantaneous ground state, as in the adiabatic approximation (see also

Section 2.1 in Chapter 2). The role that surface temperature, surface motion, and non-adiabatic effects play in molecule-surface reactions might differ from system to system.

In discussing the reactive scattering of molecules from metal surfaces we will focus on diatomic molecules for simplicity (Section 1.2.1), but we will also discuss how the same concepts can be generalized to the case of polyatomic molecules, using methane as a working example (Section 1.2.2).

1.2.1 Diatomic Molecules

Let us consider the simplest type of molecule, a diatomic molecule, like H_2, N_2 or CO. Let's assume the Born-Oppenheimer approximation [8] to be valid, so that the nuclei move on the instantaneous electronic ground state. For a molecule in the gas-phase, the solutions of the Schrödinger equation for the nuclei are labelled by three quantum numbers: v, J and m_J.

The first quantum number, v, defines the vibrational state of the molecule. According to quantum mechanics, only certain vibrational energies are allowed. In Figure 1.1A the interaction energy between two atoms in a diatomic molecule is plotted as a function of the vibrational coordinate, i.e. the bond length of the molecule r. The energy curve has a minimum for $r = r_e$, the equilibrium bond length of the molecule, then it increases for both smaller and larger values of r. For larger values of r, the interaction energy approaches the dissociation energy of the molecule D_e. The horizontal lines in Figure 1.1A represent the allowed energy levels, labeled with the quantum number v.

In addition to the vibrational energy, the magnitude of the angular momentum vector $\mathbf{J}$ and its projection on a space-fixed reference axis (usually labelled as z) $\mathbf{J}_z$ are quantized, such that: $|\mathbf{J}| = \hbar\sqrt{J(J+1)}$ and $|\mathbf{J}_z| = \hbar m_J$, where both J and m_J are integer numbers and $-J \leq m_J \leq J$. Under the rigid rotor approximation, the rotational energy of the molecule $E(J) = \frac{\hbar^2}{2\mu r^2}J(J+1)$, where μ is the reduced mass of the molecule, is a function of only the quantum number J. Therefore, for a fixed value of J, the $(2J+1)$ possible m_J states are degenerate. Note that, for homonuclear diatomic molecules, the symmetry requirements of the molecular wave function allow only certain pairings of

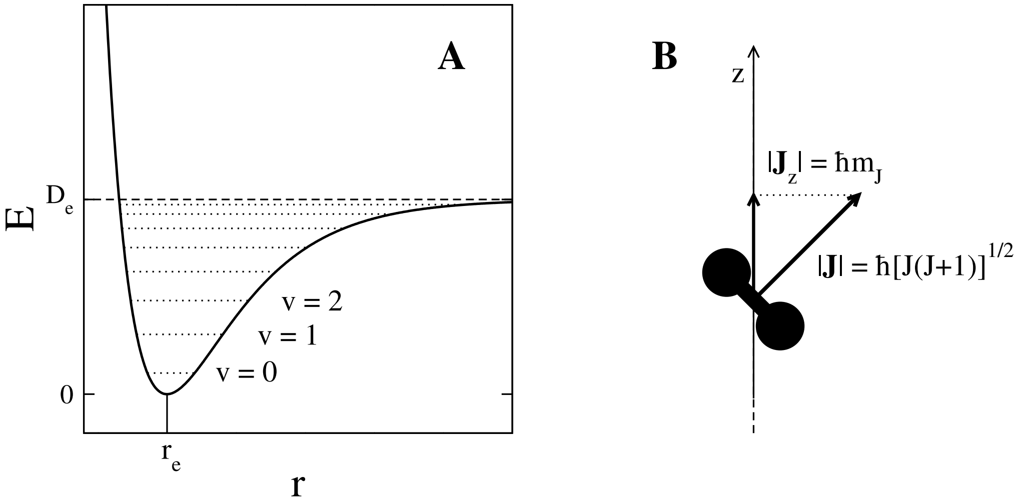
A
B
E
r
D_e
r_e
0
v = 0
v = 1
v = 2
z
$|\mathbf{J}_z| = \hbar m_J$
$|\mathbf{J}| = \hbar[J(J+1)]^{1/2}$

Figure 1.1: (A): Interaction energy as a function of the bond length for a diatomic molecule. The equilibrium bond length and the dissociation energy are labeled as r_e and D_e, respectively. (B): Classical representation of a molecule in the rotational state (J, m_J).

rotational states and nuclear spins. In particular, the molecular wave function has to be either symmetric or antisymmetric with respect to the interchange of the nuclei for nuclei with integer spin (bosons) or half-integer spin (fermions), respectively. The nuclear spin state can be either symmetric (ortho) or antisymmetric (para) with respect to this symmetry operation. The same is true for the rotational part of the molecular wave function, which is symmetric and antisymmetric for even and odd values of J, respectively. The vibrational part of the molecular wave function for a diatomic, on the other hand, is always symmetric. Therefore, the only combinations allowed for nuclear spin states and rotational states are the ones for which these two parts of the molecular wave function have the same symmetry with respect to the nuclei interchange for bosons (e.g. in D_2), while the opposite is true for fermions (e.g. in H_2).

The classical representation of a molecule in a specific (J, m_J) rotational state is depicted in Figure 1.1B. Note that $\mathbf{J}$ is always perpendicular to the bond of the molecule, and that m_J defines the orientation of $\mathbf{J}$ in space. This suggests that there is a correlation between the rotational state of the molecule (J, m_J) and its spatial orientation. More precisely, $|m_J|$ defines the rotational alignment of the molecule with respect to the z-

axis: high $|m_J|$ states correspond to 'helicopter'-like rotation, with the molecular bond close to be perpendicular to the z-axis, while low $|m_J|$ states correspond to 'cartwheel' rotations, with the molecular bond also sampling configurations parallel to the z-axis.

For what concerns the translation of the center of mass of the molecule, the solutions of the nuclear Schrödinger equation represent a continuum of states. Therefore, the translational energy can assume all possible values.

When a molecule in the initial state (v, J, m_J) and linear momentum $\mathbf{k}$ approaches a clean metal surface, a large variety of phenomena can occur. We can divide these phenomena in two broad classes of events: the molecule can bounce back towards the vacuum, in what we call a scattering event, or the molecule can adsorb on the surface.

1.2.1.1 Scattering

Scattering events can be classified according to the final state and momentum vector associated with the molecule when leaving the surface, (v', J', m'_J) and $\mathbf{k}'$, respectively. If $v' = v$, $J' = J$, and $|\mathbf{k}'| = |\mathbf{k}|$ we talk about *elastic scattering*, which means that energy is neither exchanged with the surface nor is it shuffled between the various molecular degrees of freedom. On the other hand, *vibrationally inelastic scattering* and *rotationally inelastic scattering* occur when the interaction with the surface leads to a change of vibrational state $(v' \neq v)$ or rotational state $(J' \neq J)$ of the molecule, respectively. Inelastic scattering can be both a consequence of the strong coupling that the surface interaction potential induces between the internal molecular degrees of freedom or a signature of energy exchange with the surface. Finally, when interacting with the periodic potential of the surface, the molecule can undergo *diffraction*, revealing its dual wave-particle nature. This is a consequence of Bloch's theorem [9,10], according to which the wave function of a particle in a periodic potential can always be written as a function with the same periodicity of the potential times a phase factor. It can be shown that in such a periodic potential the linear momentum components parallel to the surface can only change by discrete amounts, so that $k'_x = k_x + n\Delta k_x$ and $k'_y = k_y + m\Delta k_y$, with n and m integer numbers. Note that these quantization rules are exactly followed in the

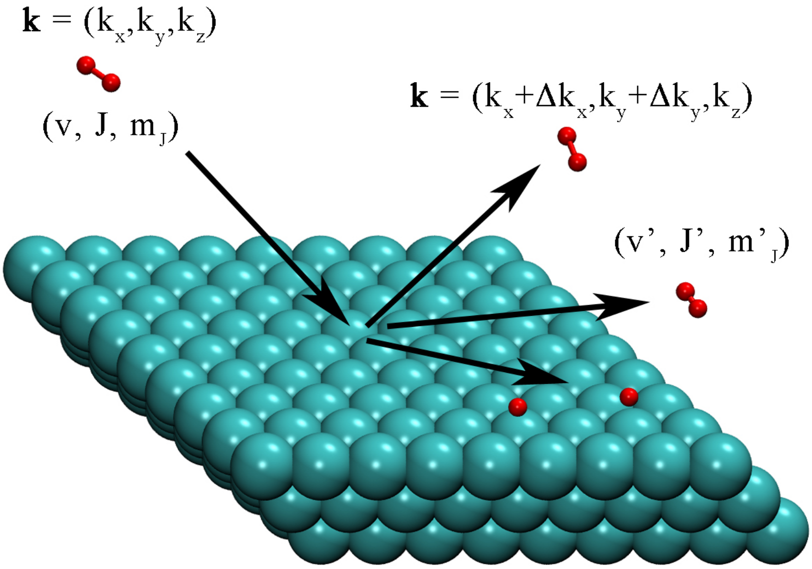
$\mathbf{k} = (k_x,k_y,k_z)$
(v, J, m_J)
$\mathbf{k} = (k_x+\Delta k_x,k_y+\Delta k_y,k_z)$
(v', J', m'_J)

Figure 1.2: Graphical representation of some of the possible outcomes that can follow the approach of a molecule to a metal surface: molecular diffraction, inelastic scattering and dissociative chemisorption, in clockwise order.

limit that no energy transfer to or from the surface occurs, in which case experiments can determine the probabilities for diffractive scattering (possibly accompanied by rotational transitions as well) by measuring the intensity of the molecules scattered to specific solid angles and taking into account the effect of energy conservation. The diffraction quantum $\mathbf{\Delta k}$ is then a surface reciprocal lattice vector, and is therefore determined by the periodicity of the (direct) lattice. The $n = m = 0$ special case of diffraction is often called *specular reflection* or *specular scattering.*

1.2.1.2 Adsorption

We have already mentioned that a gas-phase molecule can adsorb on a metal surface. Different kinds of adsorption exist. According to a first classification, we can divide adsorption into *physisorption* and *chemisorption.* A molecule is physisorbed on a surface when it weakly interacts with the substrate, generally through van der Waals forces. Chemisorption, on the other hand, occurs when the electron density rearranges itself to form new chemical bonds between (parts of) the molecule and the surface. The chemisorption process can be classified as activated or non-activated: in the first case an energy barrier has to be overcome by the impinging molecules in order to adsorb on the surface, while at least one barrierless adsorption path exists in the second case.

Chemisorption can be either dissociative or molecular, depending on whether one or more bonds in the molecule are broken during the adsorption process. The dissociative chemisorption is a consequence of the interaction between the bonding and anti-bonding electronic states of the gas-phase molecule with the surface valence electrons. In particular, the molecular states are broadened due to the interaction with the surface s and p electrons, while they are split in surface bonding and surface anti-bonding states due to the interaction with the d-states [11, 12]. If both surface bonding and molecular anti-bonding states are populated (i.e. they are below the Fermi level), the molecule can dissociatively chemisorb on the surface.

1.2.2 Polyatomic Molecules: Methane

What we described so far applies to diatomic molecules, but can be generalized to polyatomic molecules, like methane. Within the harmonic oscillator approximation, the normal mode description can be employed for representing the molecular vibrations. A molecule constituted by N atoms, has $3N - 6$ vibrational degrees of freedom ($3N - 5$ if linear), which can be grouped into vibrational modes. Each mode belongs to an irreducible representation of the point group of the molecule. The degeneracy of a vibrational level is given by the number of isoenergetic vibrational states corresponding to this level. Vibrational modes are composed of the collective motion of many atoms in the molecule. As an example, the vibrational modes of methane are illustrated in Figure 1.3. Normal modes generally involve a strong coupling between identical oscillators in the molecule. For instance, both the symmetric (ν_1) and the antisymmetric (ν_3) stretch modes in methane involve the simultaneous stretch of the four (identical) CH bonds of the molecule. For the same reason, in the CHD_3 isotopologue of methane, the CH stretch is decoupled from the stretch of the CD bonds.

With respect to rotation, the magnitude of the angular momentum vector and its

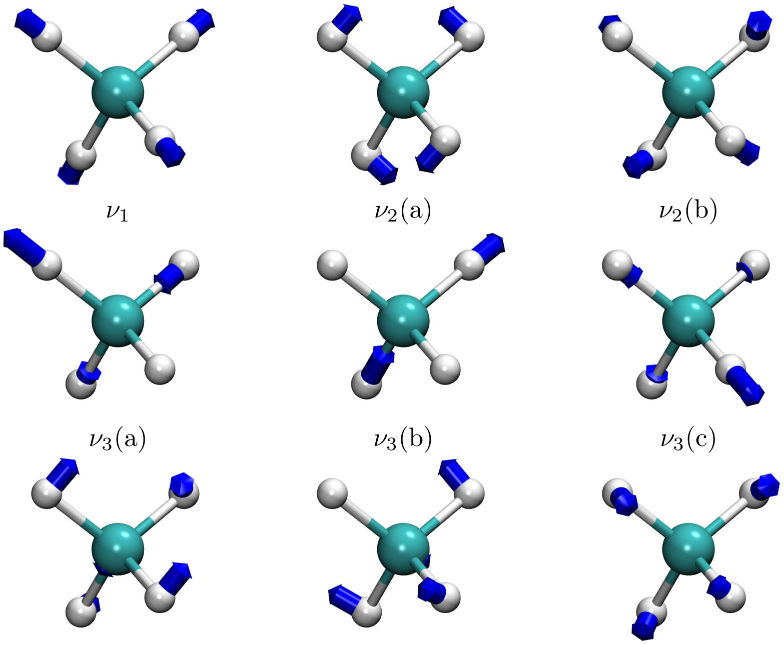

ν_1 ν_2(a) ν_2(b)

ν_3(a) ν_3(b) ν_3(c)

ν_4(a) ν_4(b) ν_4(c)

Figure 1.3: Representation of the four vibrational modes of methane (CH_4).

projection on a space-fixed reference axis are quantized for polyatomic molecules as for diatomic molecules, the corresponding quantum numbers being J and M, respectively. In addition, for molecules in which at least two of the three principal inertia moments are equal to each other (symmetric and spherical top rotors), a third quantum number K reflects the quantization of the projection of the angular momentum vector on the principal axis of rotation of the molecule. The quantum number K (as M) can assume integer values in the range $[-J; J]$. In methane, the three principal inertia moments are all equal to each other so that the molecule can be classified as a spherical top rotor. Under the rigid rotor approximation, the rotational energy is $E(J) = \frac{\hbar^2}{2I}J(J+1)$, where I is the inertia moment, as for diatomic molecules. Note that $E(J)$ does not depend on M and K, so that the degeneracy of the J rotational level is $(2J+1)^2$. CHD_3, on the other hand, is classified as a oblate symmetric top rotor, because the moment of inertia of the rotation about the symmetry axis of the molecule (the so-called 'umbrella' axis), $I_{\parallel}$, is bigger than the moment of inertia along any of the perpendicular directions

$(I_\perp)$. For a oblate symmetric top, the K degeneracy is lifted and the rotational energy is given by $E(J,K) = \frac{\hbar^2}{2I_\perp}J(J+1) + \left(\frac{\hbar^2}{2I_\parallel} - \frac{\hbar^2}{2I_\perp}\right)K^2$. The degeneracy of the rotational level (J,K) is therefore $(2J+1)$, since it is only due to the quantum number M. Note that the energy expression for a symmetric top rotor does not depend on the sign of K, therefore the rotational levels (J,K) and $(J,-K)$ are degenerate (for $K = 0$ only one level exists). Note also that for methane, as for diatomics, the symmetry constraints on the total molecular wave function allow only certain pairings of rovibrational states with nuclear spin states.

The same outcomes as for diatomic molecules can be expected for a methane molecule approaching a metal surface: elastic and inelastic scattering, adsorption. Note, however, that for methane the vibrationally inelastic scattering can involve vibrational (de-)excitation (as for diatomic molecules) of a specific mode but also energy transfer from one vibrational mode to another.

1.3 Aim of This Thesis

Many state-of-the-art methods for modeling gas-surface reaction dynamics consist of three steps: first, the molecule-surface ground-state interaction energy is calculated for various molecular configurations through a suitable electronic structure method (usually density functional theory [13,14] at the generalized gradient approximation level [15–18]); next, the computed energy points are fitted or interpolated to obtain a continuous expression of the energy as a function of the molecular configuration (the so-called potential energy surface, PES [8, 19]); finally, dynamics is performed on the pre-calculated PES [20, 21]. The second step sets some limitations to the general applicability of the method just described to the field of molecule-surface reactions. In fact, performing an accurate fitting or interpolation of pre-calculated energy points is a very complex task for a large number of nuclear degrees of freedom (> 6). Therefore, the calculations that employ this approach often involve the static surface approximation (or model surface temperature with approximate methods) [22–30]. For the same reason, untested dynamical approximations or model potentials are necessary for describing the reaction of polyatomic molecules on surfaces [31–37].

The aim of this thesis has been to apply the *ab initio* molecular dynamics (AIMD) technique to the study of reactions on metal surfaces. This technique is not new [38–40], nor is its application to the field of surface science [41–43], but only recently it became possible to calculate experimental observables (like dissociation probabilities) with reasonable statistical accuracy [44]. The use of AIMD bypasses the need of pre-computing and fitting the PES, since the forces acting on the nuclei are calculated at each time step of the dynamics. By using AIMD we achieved two main goals: first, we were able to model the effects of surface temperature and lattice recoil through the inclusion of surface-atom motion, and to study how these affect two prototypical gas-surface reactions; second, we could model the reaction of a polyatomic molecule on metal surfaces, without the need of introducing *a priori* dynamical approximations for the nuclear motion. The AIMD method is described further in Chapter 2.

1.4 Main Results

Overall, three systems have been the object of study. Chapter 3 and Chapter 4 are about the dissociation of hydrogen on a copper surface. This system is not important because of particular industrial applications but its relevance comes from the large number of experimental and theoretical studies which focused on this molecule-surface reaction, such that it is considered a benchmark for activated dissociative chemisorption. This system is ideal for testing the accuracy of theoretical models and electronic structure methods, since evidence exists that this reaction is, essentially, electronically adiabatic [45]. Previous calculations that used the static surface approximation were able to reproduce with high accuracy several observables that were either measured at low surface temperature or weakly dependent on surface temperature [27,28]. These calculations, however, failed at reproducing some observables computed at high surface temperature such as the rotational quadrupole alignment parameter [46], which is a parameter that expresses the dependence of the reactivity on the rotational alignment of the molecule. In Chapter 3 we show that surface temperature effects modeled with AIMD on average lower the alignment parameter for D_2 reacting on Cu(111), considerably improving the agreement between theory and experiments. We also show that the initial state-selected reaction probability is slightly improved against static surface calculations, for the two initial states for which the rotational alignment parameter has been computed.

The initial state-selected reaction probability of D_2 on Cu(111) is the main topic of Chapter 4. Pre-existing discrepancies between static-surface calculations and experimental data have been tackled by running new AIMD calculations modeling surface temperature effects and by performing an improved analysis of the raw experimental data [47]. We have also simulated time-of-flight spectra from theoretical reaction probabilities in order to compare theory to experiments without performing any manipulation of the raw measured data. Results show that the new analysis of the experimental data improves the agreement between theory and experiments: by using more flexible functions to fit the experimental data, we obtain reaction probability curves of which the saturation value does not depend on the initial vibrational state, as found in the simulations, whereas the opposite was suggested by the original analysis of the data. Furthermore, the mean absolute error of the energy at which the initial state-resolved reaction probability equals half the experimental saturation value (the so-called effective barrier height) is now lower than 1 kcal/mol (limit that defines the chemical accuracy) for both static-surface and AIMD calculations. As also found in Chapter 3, only a slight improvement in the initial state-selected reaction probability curves is obtained over the static surface calculations when modeling surface temperature effects with AIMD.

Chapter 5 focuses on methane dissociation on a platinum surface. The dissociation of methane on metals is both of practical and fundamental interest. The cleavage of the CH bond of the molecule and the consecutive adsorption of the methyl fragment and the hydrogen atom on a nickel catalyst is the first and a rate limiting step of the steam reforming process [48], which is the main commercial source of molecular hydrogen. Molecular beam experiments showed that the reactivity depends non-statistically on the way in which energy is disposed in the different degrees of freedom of the molecule [49–51]. In Chapter 5 we present AIMD calculations based on the PBE density functional on the reactivity of the trideuterated isotopologue of methane CHD_3 on Pt(111). Experiments that used a laser to vibrationally excite the CH stretch mode of the reacting molecules showed that the excitation of this mode significantly enhances the reactivity [52]. Furthermore, CHD_3 molecules which normally dissociate to give $H_{(a)}$ + $CD_{3(a)}$ and $D_{(a)}$ + $CHD_{2(a)}$ with the statistical relative ratio 1:3, only produce $H_{(a)}$ + $CD_{3,(a)}$ upon excitation of the CH stretch mode [52, 53]. Our calculations reproduce the experimental branching ratios and semi-quantitatively describe the experimental sticking probability as a function of the average collision energy of the molecules. We have also tested the validity of the dynamical approximations which have been previously used for modeling the methane dissociation reaction [31–35]. We have found that a sudden approximation, which assumes that a degree of freedom can be ‘frozen’ when it does not change considerably in the dynamics, could be used in the calculation of the reaction probability to describe the lateral motion of the molecule and its rotation. Finally, we have investigated the role played by the surface atom motion in the dynamics, and we have found that the surface atom below the dissociating molecule is on average outside the surface plane for reactive trajectories at low collision energies. This finding is consistent with previous studies according to which the motion of the surface atom towards the impinging molecule lowers the barrier for dissociation [32, 54–56]. These observations can explain the strong surface temperature dependence observed for methane dissociation on metal surfaces [57].

In Chapter 6 we study the effect of the density functional on calculations of methane dissociation on Pt(111). Our goal is to find a semi-empirical density functional able to accurately describe the reactivity of molecular beams in which only a fraction of the molecules is vibrationally excited (‘laser-off’ molecular beams), and of molecular beams in which the CH-stretch mode has been excited with a laser. Various density functionals are considered, including functionals that account for the van der Waals interaction. This type of functional has recently been shown to work reasonably well for describing the reaction of H_2 [58] and N_2 [59] on metal surfaces. The density functional that returns the overall best agreement with experimental data is a functional consisting of the correlation functional from Dion et al. [60], developed to mimic van der Waals interactions, and a linear combination of the RPBE and PBE exchange functionals. In particular, this functional produces good agreement with the experimental laser-off data at the lowest collision energies simulated, and with the CH-stretch excited data, thereby improving over the PBE description.

Finally, the dissociation of nitrogen on a tungsten surface (W(110)) is the topic of Chapter 7. This system is relevant as a model system for heterogeneous catalysis, as the N_2 dissociative adsorption on iron is believed to be the rate limiting step of the ammonia synthesis process already mentioned in Section 1.1. In fact, tungsten and iron exhibit some similarities with respect to nitrogen adsorption. For instance, both metals are characterized by a large crystallographic anisotropy, which means that the N_2 adsorption properties highly depend on the crystallographic face of the metal exposed to the molecules [61]. Accurately modeling the reactive and non-reactive scattering of N_2 from tungsten surfaces is a challenge that has not yet been met [25, 59, 62–65]. In Chapter 7 we have investigated the effect of surface atom motion on the reactivity of N_2 on W(110) using AIMD, testing two density functionals for the electronic structure calculations. In particular, we have found that modeling lattice motion in the dynamics strongly increases the reactivity, and we suggest that this has to do with the availability of very deep molecular adsorption wells in the PES and the large energy exchange with the surface, such that molecules remain trapped in the proximity of the surface with a higher chance to react than in the frozen-surface simulations [25, 62, 63].

1.5 Outlook

In the last section of this chapter we discuss the possible research directions that could follow the work described in this thesis and the open questions that require further investigation.

Given the benchmark status of the H_2+Cu system and given the high accuracy that could be achieved in modeling many observables for this system [27, 28], it would be desirable to understand the reason of the disagreement still present between theory and experiment in the description of the rotational quadrupole alignment parameter $A_0^{(2)}$. Further work should be directed to reduce systematic errors in the AIMD method (e.g. by increasing the surface unit cell size in the model) and to improve the statistical analysis of the experimental data, since the reported measured values of $A_0^{(2)}$ are based on very few measurements (only one data set for one initial rovibrational state). A persisting disagreement between theory and experiment would suggest that the assumption of the validity of detailed balance has to be reconsidered. Other possible sources of errors are inaccuracies in the electronic structure method employed and the neglect of electron-hole pair excitation.

Further work is also desirable to identify the cause of the discrepancy between the theoretical initial state-selected reaction probability curves and the reaction probability curves extracted from desorption experiments [47]. In particular, the dynamical model employed underestimates the surface temperature effect, with theory predicting a smaller broadening of the reaction probability curves with surface temperature than the experiment. Furthermore, discrepancies still exist in the saturation values of the dissociation probability curves. Also for this observable, possible causes of discrepancy include systematic errors in AIMD, the validity of the assumption of detailed balance, and the neglect of electron-hole pair excitation.

An experimental observable that was not accurately described within the static surface approximation [27, 28], and on which the effect of surface temperature has not yet been tested is the probability of vibrational excitation for H_2 scattering from Cu(111) [66]. Modeling this experiment with AIMD might represent a validation test for the ability of this method to describe the effect of phonons on dynamical observables.

Concerning the dissociation of methane on metal surfaces, many points deserve further investigation. We have modeled the dissociation of methane on Pt(111), but the metal that is more relevant to the catalytic steam reforming process is nickel [48]. Preliminary AIMD calculations performed using the PBE exchange-correlation functional (also employed for modeling the dissociation of CHD_3 on Pt(111)) have revealed similar trends for the reactivity on Ni(111) as for Pt(111), and the sticking probability obtained simulating laser-off molecular beams is too high compared to the experiment [67]. However, the accuracy in modeling molecular beams in which the CH-stretch mode has been excited with a laser for CHD_3 on Ni(111) remains to be investigated. Furthermore, for methane reaction on Ni surfaces, it would be interesting to investigate the use of functionals that account for the van der Waals interaction, as already done for the reaction on a Pt surface.

In the long run, high dimensional quantum dynamics calculations could be used to investigate the role of tunneling in the methane dissociation reaction, but this is best done after identifying a density functional able to produce accurate potential energy surfaces. For what concerns the dissociation of methane on Pt(111), our work suggests that a density functional returning a larger energetic corrugation with respect to the lateral motion of the molecule would improve the overall agreement with the experimental laser-off sticking probability curve. Apart from the sticking probability of CH-stretch excited and laser-off CHD_3 molecular beams, other experimental observables that could be used in tests for the accuracy of a density functional in describing the interaction between methane and metal surfaces are the dependence of the reactivity on the surface temperature [57, 68], the alignment dependence of the reaction [69, 70] and the vibrational mode specificity of the CH_2D_2 [49] and CH_4 [50] isotopologues of methane. Note, however, that the study of the mode specificity for molecules which present vibrational modes the frequencies of which are not sufficiently isolated, might be hampered by the use of classical mechanics, as no constraint avoids that the energy initially disposed into one vibrational mode would flow into other modes within the classical picture.

About the dissociation of N_2 on W(110), the large effect that surface atom motion has on the reactivity at normal incidence, together with the still missing agreement between theory and experiment, raises a number of questions. First of all, the role that surface atom motion might play at high incidence angles is not known. Previous static-surface calculations suggested that the reaction mechanism at high incidence angles can differ from the reaction mechanism at normal incidence [71]. Furthermore, Bocan et al. [63] showed how challenging it is for a density functional to accurately describe this reaction both at normal incidence and at high incidence angles. Our work suggests that a good functional for this system should predict lower molecular adsorption energies compared to the PBE and RPBE functionals, in order to lower the trapping-mediated reactivity that dominates in AIMD calculations including surface atom motion. It would be interesting to see whether any of the promising van der Waals-corrected density functionals that have been tested by Martin-Gondre et al. [59] for this system within the static surface approximation performs well when modeling surface recoil and surface temperature effects.

In addition to the dissociation probability, another observable for which the effect of surface motion could be investigated is the rotationally inelastic scattering of N_2 from W(110), for which experimental data are available [72]. Moreover, the reactive and non-reactive scattering of N_2 from another tungsten surface, W(100) [73, 74], has not yet been studied with AIMD, simulating the experimental surface temperature. If AIMD calculations, which rely on the Born-Oppenheimer approximation [8], would be able to accurately model both reactive and non-reactive scattering of nitrogen from tungsten surfaces, the importance of modeling electron-hole pair excitation for this system, which is a topic of a recent debate [64, 75, 76], could be ruled out.

Finally, for both the H_2 + Cu system and N_2 + W system the AIMD calculations that we have performed might work as a benchmark for (approximated) methods that aim at modeling surface temperature effects (like the surface corrugation model [77]) and surface recoil effects (like the generalized Langevin oscillator model [78]). These models are attractive since they allow one to compute a large number of trajectories and to propagate them for relatively long times, in such a way that low dissociation probabilities and state-to-state scattering probabilities can be determined with good statistical accuracy.

Bibliography

[1] G. A. Somorjai and Y. Li, Proc. Natl. Acad. Sci. U. S. A. **108**, 917 (2011).

[2] A. Nilsson, L. G. M. Pettersson, and J. K. Nørskov (Eds.), *Chemical Bonding at Surfaces and Interfaces*, Elsevier, Amsterdam, 2008.

[3] R. T. Garrod, S. L. Widicus Weaver, and E. Herbst, Astrophys. J. **682**, 283 (2008).

[4] P. A. J. Bagot, Mater. Sci. Technol. **20**, 679 (2004).

[5] R. Marom, S. F. Amalraj, N. Leifer, D. Jacob, and D. Aurbach, J. Mater. Chem. **21**, 9938 (2011).

[6] G. Ertl, Catal. Rev. Sci. Eng. **21**, 201 (1980).

[7] G. A. Somorjai, *Introduction to Surface Chemistry and Catalysis*, Wiley, New York, 1994.

[8] M. Born and J. R. Oppenheimer, Ann. Physik. **84**, 457 (1927).

[9] F. Bloch, Z. Phys. **52**, 555 (1928).

[10] N. W. Ashcroft and N. D. Mermin, *Solid State Physics*, Saunders College, Philadelphia, 1976.

[11] B. Hammer and J. K. Nørskov, Nature **376**, 238 (1995).

[12] B. Hammer and J. K. Nørskov, Surf. Sci. **343**, 211 (1995).

[13] P. Hohenberg and W. Kohn, Phys. Rev. B **136**, 864 (1964).

[14] W. Kohn and L. J. Sham, Phys. Rev. **140**, A1133 (1965).

[15] J. P. Perdew, J. A. Chevary, S. H. Vosko, K. A. Jackson, M. R. Pederson, D. J. Singh, and C. Fiolhais, Phys. Rev. B **46**, 6671 (1992).

[16] J. P. Perdew, K. Burke, and M. Ernzerhof, Phys. Rev. Lett. **77**, 3865 (1996).

[17] B. Hammer, L. B. Hansen, and J. K. Nørskov, Phys. Rev. B **59**, 7413 (1999).

[18] A. D. Becke, Phys. Rev. A **38**, 3098 (1988).

[19] H. Eyring and M. Polanyi, Z. Phys. Chem. Abt. B **12**, 279 (1931).

[20] M. Karplus, R. N. Porter, and R. D. Sharma, J. Chem. Phys. **43**, 3259 (1965).

[21] R. Kosloff, J. Phys. Chem. **92**, 2087 (1988).

[22] H. F. Busnengo, A. Salin, and W. Dong, J. Chem. Phys. **112**, 7641 (2000).

[23] S. Lorenz, A. Groß, and M. Scheffler, Chem. Phys. Lett. **395**, 210 (2004).

[24] S. Lorenz, M. Scheffler, and A. Groß, Phys. Rev. B **73**, 115431 (2006).

[25] M. Alducin, R. Díez Muiño, H. F. Busnengo, and A. Salin, Phys. Rev. Lett. **97**, 056102 (2006).

[26] J. Behler, S. Lorenz, and K. Reuter, J. Chem. Phys. **127**, 014705 (2007).

[27] C. Díaz, E. Pijper, R. A. Olsen, H. F. Busnengo, D. J. Auerbach, and G. J. Kroes, Science **326**, 832 (2009).

[28] C. Díaz, R. A. Olsen, D. J. Auerbach, and G. J. Kroes, Phys. Chem. Chem. Phys. **12**, 6499 (2010).

[29] I. M. N. Groot, J. C. Juanes-Marcos, C. Díaz, M. F. Somers, R. A. Olsen, and G. J. Kroes, Phys. Chem. Chem. Phys. **12**, 1331 (2010).

[30] I. Goikoetxea, J. Meyer, J. I. Juaristi, M. Alducin, and K. Reuter, Phys. Rev. Lett. **112**, 156101 (2014).

[31] B. Jackson and S. Nave, J. Chem. Phys. **135**, 114701 (2011).

[32] B. Jackson and S. Nave, J. Chem. Phys. **138**, 174705 (2013).

[33] M. Mastromatteo and B. Jackson, J. Chem. Phys. **139**, 194701 (2013).

[34] B. Jiang and H. Guo, J. Phys. Chem. C **117**, 16127 (2013).

[35] B. Jiang, R. Liu, J. Li, D. Xie, M. Yang, and H. Guo, Chem. Sci. **4**, 3249 (2013).

[36] X. J. Shen, A. Lozano, W. Dong, H. F. Busnengo, and X. H. Yan, Phys. Rev. Lett. **112**, 046101 (2014).

[37] P. M. Hundt, B. Jiang, M. E. van Reijzen, H. Guo, and R. D. Beck, Science **344**, 504 (2014).

[38] R. Car and M. Parrinello, Phys. Rev. Lett. **55**, 2471 (1985).

[39] G. Kresse and J. Hafner, Phys. Rev. B **47**, 558 (1993).

[40] G. Kresse and J. Hafner, Phys. Rev. B **49**, 14251 (1994).

[41] A. De Vita, I. Štich, M. J. Gillan, M. C. Payne, and L. J. Clarke, Phys. Rev. Lett. **71**, 1276 (1993).

[42] I. Štich, M. C. Payne, A. De Vita, M. J. Gillan, and L. J. Clarke, Chem. Phys. Lett. **212**, 617 (1993).

[43] I. Štich, A. De Vita, M. C. Payne, M. J. Gillan, and L. J. Clarke, Phys. Rev. B **49**, 8076 (1994).

[44] A. Groß and A. Dianat, Phys. Rev. Lett. **98**, 206107 (2007).

[45] P. Nieto, E. Pijper, D. Barredo, G. Laurent, R. A. Olsen, E. J. Baerends, G. J. Kroes, and D. Farías, Science **312**, 86 (2006).

[46] H. Hou, S. J. Gulding, C. T. Rettner, A. M. Wodtke, and D. J. Auerbach, Science **277**, 80 (1997).

[47] H. A. Michelsen, C. T. Rettner, D. J. Auerbach, and R. N. Zare, J. Chem. Phys. **98**, 8294 (1993).

[48] G. Jones, J. G. Jakobsen, S. S. Shim, J. Kleis, M. P. Andersson, J. Rossmeisl, F. Abild-Pedersen, T. Bligaard, S. Helveg, B. Hinnemann, J. R. Rostrup-Nielsen, I. Chorkendorff, J. Sehested, and J. K. Nørskov, J. Catal. **259**, 147 (2008).

[49] R. D. Beck, P. Maroni, D. C. Papageorgopoulos, T. T. Dang, M. P. Schmid, and T. R. Rizzo, Science **302**, 98 (2003).

[50] R. R. Smith, D. R. Killelea, D. F. DelSesto, and A. L. Utz, Science **304**, 992 (2004).

[51] P. Maroni, D. C. Papageorgopoulos, M. Sacchi, T. T. Dang, R. D. Beck, and T. R. Rizzo, Phys. Rev. Lett. **94**, 246104 (2005).

[52] D. R. Killelea, V. L. Campbell, N. S. Shuman, and A. L. Utz, Science **319**, 790 (2008).

[53] L. Chen, H. Ueta, R. Bisson, and R. D. Beck, Faraday Discuss. **157**, 285 (2012).

[54] S. Nave and B. Jackson, J. Chem. Phys. **127**, 224702 (2007).

[55] S. Nave and B. Jackson, Phys. Rev. Lett. **98**, 173003 (2007).

[56] A. K. Tiwari, S. Nave, and B. Jackson, J. Chem. Phys. **132**, 134702 (2010).

[57] A. C. Luntz and D. S. Bethune, J. Chem. Phys. **90**, 1274 (1989).

[58] M. Wijzenbroek and G. J. Kroes, J. Chem. Phys. **140**, 084702 (2014).

[59] L. Martin-Gondre, J. I. Juaristi, M. Blanco-Rey, R. Díez Muiño, and M. Alducin, J. Chem. Phys. **142**, 074704 (2015).

[60] M. Dion, H. Rydberg, E. Schröder, D. C. Langreth, and B. I. Lundqvist, Phys. Rev. Lett. **92**, 246401 (2004).

[61] S. P. Singh-Boparai, M. Bowker, and D. A. King, Surf. Sci. **53**, 55 (1975).

[62] M. Alducin, R. Díez Muiño, H. F. Busnengo, and A. Salin, J. Chem. Phys. **125**, 144705 (2006).

[63] G. A. Bocan, R. Díez Muiño, M. Alducin, H. F. Busnengo, and A. Salin, J. Chem. Phys. **128**, 154704 (2008).

[64] J. I. Juaristi, M. Alducin, R. Díez Muiño, H. F. Busnengo, and A. Salin, Phys. Rev. Lett. **100**, 116102 (2008).

[65] I. Goikoetxea, J. I. Juaristi, M. Alducin, and R. Díez Muiño, J. Phys.: Condens. Matter **21**, 264007 (2009).

[66] C. T. Rettner, H. A. Michelsen, and D. J. Auerbach, Chem. Phys. **175**, 157 (1993).

[67] E. Dombrowski, E. High, and A. Utz, Unpublished data, 2015.

[68] P. M. Holmblad, J. Wambach, and I. Chorkendorff, J. Chem. Phys. **102**, 8255 (1995).

[69] B. L. Yoder, R. Bisson, and R. D. Beck, Science **329**, 553 (2010).

[70] B. L. Yoder, R. Bisson, P. M. Hundt, and R. D. Beck, J. Chem. Phys. **135**, 224703 (2011).

[71] M. Alducin, R. Díez Muiño, H. F. Busnengo, and A. Salin, Surf. Sci. **601**, 3726 (2007).

[72] T. F. Hanisco and A. C. Kummel, J. Vac. Sci. Technol. A **11**, 1907 (1993).

[73] C. T. Rettner, E. K. Schweizer, H. Stein, and D. J. Auerbach, Phys. Rev. Lett. **61**, 986 (1988).

[74] C. T. Rettner, E. K. Schweizer, and H. Stein, J. Chem. Phys. **93**, 1442 (1990).

[75] A. C. Luntz, I. Makkonen, M. Persson, S. Holloway, D. M. Bird, and M. S. Mizielinski, Phys. Rev. Lett. **102**, 109601 (2009).

[76] J. I. Juaristi, M. Alducin, R. Díez Muiño, H. F. Busnengo, and A. Salin, Phys. Rev. Lett. **102**, 109602 (2009).

[77] M. Wijzenbroek and M. F. Somers, J. Chem. Phys. **137**, 054703 (2012).

[78] H. F. Busnengo, M. A. Di Césare, W. Dong, and A. Salin, Phys. Rev. B **72**, 125411 (2005).

Chapter 2

Ab Initio Molecular Dynamics for Modeling Gas-Surface Reaction Dynamics

The aim of this chapter is to introduce the theoretical framework of *ab initio* molecular dynamics (AIMD) and to show how this technique can be employed to study gas-surface reactions. In Section 2.1 the AIMD method is presented, followed by a brief description of the electronic structure method employed, namely density functional theory (DFT, Section 2.2). The AIMD implementation to study gas-surface reaction dynamics is then described in Section 2.3, and the description of the most important observables computed concludes this chapter (Section 2.4).

2.1 The *Ab Initio* Molecular Dynamics Technique

The term *ab initio* molecular dynamics has been used in literature to refer to a large variety of techniques [1]: molecular dynamics simulations involving a pre-calculated *ab initio* based potential energy surface (PES), but also methods that calculate the relevant features of the PES (energy, forces) on the fly, i.e. during the dynamical evolution of the nuclei; wave function based methods, but also techniques that exploit density functional theory (DFT); techniques in which the Kohn-Sham (KS) DFT equations are diagonalized at each time-step while evolving the nuclear positions (Born-Oppenheimer molecular dynamics), but also methods in which the KS orbitals are classically propagated together with the nuclear positions (Car-Parrinello molecular dynamics [2]). Despite the variety of techniques which have been named AIMD in the past, this term is nowadays generally used as a synonym of Born-Oppenheimer molecular dynamics (BOMD) and we will use it with this meaning in the rest of the thesis.

2.1.1 Deriving Born-Oppenheimer Molecular Dynamics

The equations that govern the AIMD technique can be derived from the time-dependent Schrödinger equation, which describes the time evolution of a molecular system whose state is defined by the wave function $\Psi(\{\mathbf{r}_i\}, \{\mathbf{R}_I\}, t)$:

$$i\frac{\partial}{\partial t}\Psi(\{\mathbf{r}_i\}, \{\mathbf{R}_I\}, t) = \hat{H}\Psi(\{\mathbf{r}_i\}, \{\mathbf{R}_I\}, t). \tag{2.1}$$

Here $\{\mathbf{r}_i\}$ and $\{\mathbf{R}_I\}$ represent the sets of electronic and nuclear degrees of freedom, respectively. Note that atomic units have been used in Equation 2.1, and will be used in the rest of this chapter. $\hat{H}$ is the full Hamiltonian of the system and can be written in the following way:

$$\begin{aligned}\hat{H} = &-\sum_I \frac{1}{2M_I}\nabla_I^2 - \sum_i \frac{1}{2}\nabla_i^2 + \\ &-\sum_{i,I}\frac{Z_I}{|\mathbf{r}_i - \mathbf{R}_I|} + \sum_{j>i}\frac{1}{|\mathbf{r}_i - \mathbf{r}_j|} + \sum_{J>I}\frac{Z_I Z_J}{|\mathbf{R}_I - \mathbf{R}_J|}.\end{aligned} \tag{2.2}$$

The first two terms represent the kinetic energy of the nuclei and the electrons, respectively. The third term represents the (attractive) interaction between electrons and nuclei. The last two terms represent the (repulsive) interaction between electrons and between nuclei, respectively. M_I and Z_I are the mass and the nuclear charge of the I-th nucleus, respectively. The Hamiltonian in equation 2.2 can also be written as:

$$\hat{H} = -\sum_I \frac{1}{2M_I} \nabla_I^2 + \hat{H}_e, \tag{2.3}$$

where $\hat{H}_e$ is the so-called clamped-nuclei Hamiltonian, the eigenstates of which depend parametrically on $\{\mathbf{R}_I\}$:

$$\hat{H}_e \psi_k(\{\mathbf{r}_i\};\{\mathbf{R}_I\}) = E_k(\{\mathbf{R}_I\}) \psi_k(\{\mathbf{r}_i\};\{\mathbf{R}_I\}). \tag{2.4}$$

Here, the $\psi_k(\{\mathbf{r}_i\};\{\mathbf{R}_I\})$'s are known as adiabatic electronic states. Using these states, we can formulate an *ansatz* for $\Psi(\{\mathbf{r}_i\},\{\mathbf{R}_I\},t)$:

$$\Psi(\{\mathbf{r}_i\},\{\mathbf{R}_I\},t) = \sum_k \psi_k(\{\mathbf{r}_i\};\{\mathbf{R}_I\}) \chi_k(\{\mathbf{R}_I\},t). \tag{2.5}$$

Inserting this *ansatz* into Equation 2.1, multiplying it from the left by $\psi_k^*(\{\mathbf{r}_i\};\{\mathbf{R}_I\})$ and integrating it over the electronic coordinates lead to a set of differential equations describing the nuclear motion. These equations are coupled through terms which arise from the action of the nuclear kinetic energy operator on $\psi_k(\{\mathbf{r}_i\};\{\mathbf{R}_I\})$. Neglecting these coupling terms is the basis of the adiabatic (or Born-Huang) approximation [3]. Such neglect is equivalent to considering only one term into the expansion of Equation 2.5, typically the electronic ground state:

$$\Psi(\{\mathbf{r}_i\},\{\mathbf{R}_I\},t) \approx \psi_0(\{\mathbf{r}_i\};\{\mathbf{R}_I\}) \chi_0(\{\mathbf{R}_I\},t). \tag{2.6}$$

We can then introduce a further approximation and neglect all the terms arising from the action of the nuclear kinetic energy operator on $\psi_0(\{\mathbf{r}_i\};\{\mathbf{R}_I\})$. This approximation is known as the Born-Oppenheimer (BO) approximation [4]. Both the adiabatic and the BO approximations are based on the consideration that the motion of the electrons and the nuclei occurs on different time-scales due to the large mass mismatch between the two particles. After applying the BO approximation, Equations 2.1 and 2.4 can be rewritten in the following way:

$$\left[-\sum_I \frac{1}{2M_I}\nabla_I^2 + E_0(\{\mathbf{R}_I\})\right]\chi_0(\{\mathbf{R}_I\},t) = i\frac{\partial}{\partial t}\chi_0(\{\mathbf{R}_I\},t), \tag{2.7a}$$

$$\hat{H}_e\psi_0(\{\mathbf{r}_i\};\{\mathbf{R}_I\}) = E_0(\{\mathbf{R}_I\})\psi_0(\{\mathbf{r}_i\};\{\mathbf{R}_I\}). \tag{2.7b}$$

The first equation describes the time evolution of the nuclei and contains the BO potential energy surface $E_0(\{\mathbf{R}_I\})$, obtained by solving the electronic time-independent Schrödinger equation for the ground state (Equation 2.7b).

At this stage we can introduce a further approximation for the nuclei and assume that they behave like classical point particles. It can be shown that taking the classical limit of Equation 2.7a leads to Newton's equation of motion:

$$M_I\ddot{\mathbf{R}}_I = -\nabla_I E_0(\{\mathbf{R}_I\}). \tag{2.8}$$

Therefore, the time-dependent problem of Equation 2.1 can be reduced to a time-independent electronic structure problem, with the time dependence remaining implicit in the time evolution of the nuclear positions: $\{\mathbf{R}_I\} = \{\mathbf{R}_I(t)\}$. Equation 2.8 can be integrated over time while solving concurrently the time-independent electronic Schrödinger equation, from which the forces $F_I = -\nabla_I E_0(\{\mathbf{R}_I\})$ are calculated for a specific fixed nuclear configuration $\{\mathbf{R}_I\}$. Since $E_0(\{\mathbf{R}_I\})$ is the Born-Oppenheimer potential energy surface, this approach is known as Born-Oppenheimer molecular dynamics.

2.1.2 The Hellmann-Feynman Forces

An efficient scheme for evaluating the forces acting on the nuclei is crucial for performing AIMD. We can write the following expression for the forces:

$$\begin{aligned} F_I &= -\nabla_I E_0(\{\mathbf{R}_I\}) = -\nabla_I \left\langle \psi_0 \middle| \hat{H}_e \middle| \psi_0 \right\rangle = \\ &= -\left\langle \nabla_I\psi_0 \middle| \hat{H}_e \middle| \psi_0 \right\rangle - \left\langle \psi_0 \middle| \hat{H}_e \middle| \nabla_I\psi_0 \right\rangle - \left\langle \psi_0 \middle| \nabla_I\hat{H}_e \middle| \psi_0 \right\rangle. \end{aligned} \tag{2.9}$$

According to the Hellmann-Feynman theorem [5,6], the first two terms in Equation 2.9 vanish, provided that ψ_0 is an eigenfunction of $\hat{H}_e$:

$$F_I^{HF} = -\left\langle \psi_0 \middle| \nabla_I \hat{H}_e \middle| \psi_0 \right\rangle . \tag{2.10}$$

This theorem is also valid if ψ_0 is not an eigenfunction of $\hat{H}_e$ but only in the limit of a complete basis set expansion for ψ_0. For incomplete basis sets, in addition to the Hellmann-Feynman force F_I^{HF} (Equation 2.10), two other terms have to be considered when computing the force F_I [7,8]. One term arises from the action of the nuclear derivative on the basis functions, and it is generally known as Pulay force. This contribution, however, is exactly zero if a basis set of non-atom-centered functions is employed (e.g. plane waves, see also Section 2.2.2), provided that the number of basis functions is kept fixed during the calculation. The second contribution is related to the way in which the electronic structure problem is solved to find the electronic ground state of the system. In Kohn-Sham DFT, the Kohn-Sham equations are solved iteratively until a certain convergence threshold is reached (see also Section 2.2). This means that the ground state electron density is not exactly self-consistent, and the same is true for the KS potential, which leads to a 'non-self-consistency' (NSC) contribution to the forces. This contribution, however, can be made arbitrarily small by setting tighter convergence criteria. Furthermore, schemes exist to estimate and approximately correct for the NSC contribution [7–9].

2.1.3 Alternative Dynamical Methods

In Section 2.1 we have seen that the time-dependent problem of Equation 2.1 can be reduced to the time-independent problem of finding the electronic ground state solution for a fixed nuclear configuration and the time evolution of the nuclear positions (Equation 2.8). The electronic and nuclear problems can in principle be solved in two separate steps: first one calculates the BO potential energy surface (PES) for various nuclear configurations, and then one employs the pre-calculated PES for running the nuclear dynamics. Note that only the first of these two steps is computationally expensive, while the integration of the nuclear equations of motion is relatively cheap. Therefore, the implementation of this approach allows for the computation of a large number of nuclear dynamics calculations, and a long time propagation in these. The drawback of this strategy is that the PES has to be represented by a continuous function, which means that a suitable functional form has to be employed to fit or interpolate the pre-calculated points of the PES. For molecules interacting with a metal surface, state-of-the-art PESs typically describe up to six degrees of freedom (DOFs), i.e. all the molecular DOFs for a diatomic [10–18]. The PES of systems like CH_4 + metal surfaces, where in principle a large number of molecular degrees of freedom (15) has to be modeled together with the relevant surface phonons, has been described so far only by using dynamical approximations or model potentials (e.g. reactive force-fields) [19–21].

The methods discussed so far exploit the classical approximation for the nuclei. Quantum effects could also play a role in gas-surface reactions. For instance, classical mechanics is not able to describe tunneling and does not guarantee zero point energy (ZPE) conservation. Such effects are especially relevant for reactions involving light atoms, like hydrogen, and at conditions such as low collision energies. Quantum dynamical methods have been used to solve directly Equation 2.7a [15, 22–24]. These methods are computationally expensive because they have to deal with the nuclear wave function. Therefore, the number of DOFs that can be explicitly modeled is limited. Moreover, a continuous representation of the PES is still needed by these methods.

2.2 Density Functional Theory

The electronic structure method which is mostly used in conjunction with AIMD is density functional theory (DFT), due to its relatively low computational cost and its favorable scaling ($\propto n^3$, where n is the number of electrons in the system, which compares to $\propto n^4$ or worse for wave function-based methods). The groundwork of DFT has been laid by Hohenberg and Kohn (HK) [25], who demonstrated that for a system constituted by n electrons in an external potential generated by the nuclei the ground state wave function is uniquely determined by the electron density. Therefore, the electron density defines all the properties of the system. Furthermore, HK demonstrated that the energy corresponding to any electron density other than the ground state density is larger than the ground state energy, giving a criterion for guiding the search of the ground state density. Note that in the original paper by HK, the demonstration was restricted only to non-degenerate ground states, while this restriction was lifted in later formulations of DFT [26].

Kohn and Sham (KS) [27] suggested a strategy for putting DFT into practice. Their approach involves a fictitious system constituted by non-interacting electrons. The exact ground-state wave function of such a system can be represented by a Slater determinant. The one-electron wave functions $\phi_i(\mathbf{r})$ (the KS orbitals) that compose such a determinant can be determined through the following set of equations:

$$\left[-\frac{1}{2}\nabla^2 + V_S(\mathbf{r})\right]\phi_i(\mathbf{r}) = \epsilon_i \phi_i(\mathbf{r}). \tag{2.11}$$

Here $V_S(\mathbf{r})$ is an effective potential, the KS potential, and ϵ_i is the orbital energy. In the first term in the brackets we recognize the one-electron kinetic energy operator. The KS orbitals can be used to construct the electron density of the non-interacting system according to:

$$\rho_S(\mathbf{r}) = \sum_i |\phi_i(\mathbf{r})|^2 . \tag{2.12}$$

The KS potential is crucial to connect the real system, i.e. the system with interacting electrons, to the fictitious system (with non-interacting electrons). In fact, it can be shown that $\rho_S(\mathbf{r})$ equals the ground state density of the real system $\rho_0(\mathbf{r})$ if the KS potential is set in the following way:

$$V_S(\mathbf{r}) = -\sum_I \frac{Z_I}{|\mathbf{r}-\mathbf{R}_I|} + \int d\mathbf{r}' \frac{\rho(\mathbf{r})}{|\mathbf{r}-\mathbf{r}'|} + V_{XC}(\mathbf{r}). \tag{2.13}$$

In the first term we recognize the electron-nuclei interaction potential. The second term is the Hartree potential, which gives rise to the classical part of the electron-

electron interaction energy (the electrostatic repulsion). The last term is the exchange-correlation potential, defined as the functional derivative of the exchange-correlation energy $E_{XC}[\rho(\mathbf{r})]$ with respect to the electron density:

$$V_{XC}(\mathbf{r}) = \frac{\delta E_{XC}[\rho(\mathbf{r})]}{\delta \rho(\mathbf{r})}. \tag{2.14}$$

The exchange-correlation energy represents the collection of all the energy terms of which the exact expression is unknown, i.e. the non-classical part of the electron-electron interaction and the difference between the kinetic energy of the real system and the kinetic energy of the non-interacting system. By substituting the expression of $V_S(\mathbf{r})$ into Equation 2.11 we obtain the so-called KS equations. Note that $V_S(\mathbf{r})$ depends on the density (and therefore on the orbitals ϕ_i) through the Hartree potential, therefore the KS equations have to be solved iteratively. The expression of the energy as a function of the electron density has the following form:

$$\begin{aligned} E[\rho] = & -\frac{1}{2}\sum_i \langle\phi_i|\, \nabla^2 \,|\phi_i\rangle - \sum_I \int \frac{Z_I}{|\mathbf{r}-\mathbf{R}_I|}\rho(\mathbf{r})d\mathbf{r} + \\ & + \int d\mathbf{r} \int d\mathbf{r}' \frac{\rho(\mathbf{r})\rho(\mathbf{r}')}{|\mathbf{r}-\mathbf{r}'|} + E_{XC}(\mathbf{r}) + \sum_{J>I} \frac{Z_I Z_J}{|\mathbf{R}_I - \mathbf{R}_J|}. \end{aligned} \tag{2.15}$$

Note that we have added the nuclei-nuclei interaction (last term), that contributes to the energy of the system as a mere constant for a given nuclear configuration. The fictitious non-interacting system is therefore used to represent at least the part of the kinetic energy for which we have an analytical expression, which involves the KS orbitals.

2.2.1 The Exchange-Correlation Functional

If the exact expression of $E_{XC}[\rho(\mathbf{r})]$ was known, the KS equations would lead to the exact ground state energy of the system. However, only approximations are available for this energy term. Using the local density approximation (LDA) the electrons of the system are assumed to behave as a uniform electron gas on a positive background. For such a system, $E_{XC}[\rho(\mathbf{r})]$ can be written in the following way:

$$E_{XC}^{LDA}[\rho(\mathbf{r})] = \int \rho(\mathbf{r})(\varepsilon_X(\rho(\mathbf{r})) + \varepsilon_C(\rho(\mathbf{r})))d\mathbf{r}, \tag{2.16}$$

where $\varepsilon_X(\rho(\mathbf{r}))$ and $\varepsilon_C(\rho(\mathbf{r}))$ are the exchange and the correlation energies per electron for a given electron density $\rho(\mathbf{r})$, respectively. An analytical expression exists for $\varepsilon_X(\rho(\mathbf{r}))$ [28, 29]:

$$\varepsilon_X(\rho(\mathbf{r})) = -\frac{3}{4}\left(\frac{3}{\pi}\rho(\mathbf{r})\right)^{\frac{1}{3}}, \tag{2.17}$$

while $\varepsilon_C(\rho(\mathbf{r}))$ can be calculated very accurately using analytical expressions [30, 31] which have been fitted to quantum Monte Carlo calculations [32].

Unfortunately, the LDA fails quite dramatically in reproducing properties like barrier heights for molecule-surface reactions (see for instance Refs. [33, 34]). If the gradient of the density is included in the expression of $E_{XC}[\rho(\mathbf{r})]$ in addition to the density itself we obtain the so-called generalized gradient approximation (GGA):

$$E_{XC}^{GGA}[\rho(\mathbf{r})] = \int f[\nabla\rho(\mathbf{r}), \rho(\mathbf{r})]d\mathbf{r}. \tag{2.18}$$

All the traditional GGA functionals employ an expression for the exchange-correlation energy E_{XC}^{GGA} in which this term is split into an exchange and a correlation contribution, E_X^{GGA} and E_C^{GGA}, respectively, as for the LDA. Furthermore, the exchange part of E_{XC}^{GGA} is always expressed in the following way [35–38]:

$$E_X^{GGA} = \int \rho(\mathbf{r})\varepsilon_X(\rho(\mathbf{r}))F(s)d\mathbf{r}, \tag{2.19}$$

where $F(s)$ is generally called exchange enhancement factor, and s is the so-called reduced density gradient:

$$s = \frac{|\nabla\rho|}{2(3\pi^2)^{1/3}\rho^{4/3}(\mathbf{r})}. \tag{2.20}$$

The exponent of the density at the denominator is such that s is dimensionless. We note in passing that Peverati and Truhlar use Equation 2.19 to define the GGA [39], since all the traditional GGA functionals exploit such an expression for the exchange part of E_{XC}^{GGA}. In addition, Peverati and Truhlar define the non-separable gradient approximation (NGA) according to which a functional of the electron density and its gradient is employed to represent both exchange and correlation in a non-separable term [39, 40].

One example of $F(s)$ is the following function, which constitutes the exchange enhancement factor for the PBE exchange-correlation functional [36]:

$$F^{PBE}(s) = 1 + \kappa - \frac{\kappa}{1 + \mu s^2/\kappa}, \tag{2.21}$$

where κ and μ are derived from physical constants (not semiempirical parameters). The RPBE exchange-correlation functional [37] differs from the PBE functional only in the expression of $F(s)$:

$$F^{RPBE}(s) = 1 + \kappa \cdot \left(1 - e^{-\mu s^2/\kappa}\right). \tag{2.22}$$

Various expressions have been proposed for E_C^{GGA}. Functionals like PW91 [35] and (R)PBE [36, 37] employ an expression for E_C^{GGA} based on the free-electron gas correlation:

$$E_C^{GGA} = \int \rho(\mathbf{r}) \left(\varepsilon_C(\rho(\mathbf{r})) + H[\nabla\rho(\mathbf{r}), \rho(\mathbf{r})]\right), \tag{2.23}$$

where H represents the gradient contribution to E_C^{GGA}. H differs from functional to functional, and is parameter-free for both PW91 and (R)PBE. The LYP correlation functional [41], on the other hand, is derived from the expression of the correlation energy for an helium atom based on wave function methods [42].

GGA functionals generally present a mean absolute error (MAE) in describing gas-phase reaction barrier heights of about 5 kcal/mol [43], the lowest value so far being obtained by the MOHLYP2 functional (MAE = 3.8 kcal/mol) [39, 43]. The MAE has not yet been determined for gas surface reactions but many examples are known in which a chemically accurate description (to within 1 kcal/mol) of the barrier heights was not achieved with regular GGA functionals (see for instance Refs. [15, 44, 45]).

The research of more accurate exchange-correlation functionals led to the formulation of functionals which take the Laplacian of the electron density $\nabla^2\rho(\mathbf{r})$ and the (non-interacting) kinetic energy density $\tau = \sum_i |\nabla\phi_i|^2$ into account (meta-GGA and meta-NGA functionals) and functionals that include a part of exact Hartree-Fock exchange (hybrid functionals). Meta-GGA, meta-NGA and in particular hybrid functionals are computationally more expensive than GGA functionals. For this reason their use in molecule-surface reactions has been scarce so far.

A limitation of regular GGA functionals is that they are not able to accurately describe long-ranged interactions such as van der Waals (vdW) forces. Different approaches have been developed to mimic these interactions using conventional KS-DFT. According to the methods of Grimme [46,47] and Tkatchenko and Sheffler [48] a dispersion potential in the form of a pairwise force field is added to the KS energy. Langreth, Lundqvist and coworkers, on the other hand, proposed a non-local correlation functional able to approximately account for dispersion interactions [49,50]. An efficient implementation of this correlation functional has recently appeared [51]. Functionals including this correlation have been recently tested in the field of gas surface reaction dynamics showing a moderate improvement over regular GGA functionals [44,52].

A semi-empirical approach to the unknown exchange-correlation functional is the so-called specific reaction parameter (SRP) approach. In its original version developed by Truhlar and coworkers [53,54] for gas-phase reactions, one or a few parameters in the exchange-correlation functional are fitted to a set of experimental data in order to make the functional optimal for describing a specific reaction; the fitted functional is then tested against other sets of experimental data for the same system. Díaz et al. [15,16] applied a novel implementation of this approach to a gas-surface reaction by fitting a weighted average of two GGA density functionals to a single set of experimental data sensitive to the minimum barrier height for H_2 + Cu(111). It has been shown that this new semi-empirical functional is able to reproduce various experimental data for the H_2 + Cu(111) system with chemical accuracy, and that this functional is transferable to another crystal face of the same metal, i.e. Cu(100) [55,56].

2.2.2 Plane wave DFT

As mentioned above, DFT is very often employed in conjunction with AIMD due to the favorable scaling of this electronic structure method with system size. Furthermore, in combination with a periodic slab approach, DFT is very suitable for representing an infinite surface. For periodic systems, the natural basis for the expansion of the KS orbitals consists of plane waves:

$$\phi_j(\mathbf{r},\mathbf{k}) = N\sum_{\mathbf{G}} c_{j\mathbf{G}\mathbf{k}} e^{i(\mathbf{k}+\mathbf{G})\cdot\mathbf{r}}. \tag{2.24}$$

Here j labels the KS orbitals, $\mathbf{G}$ is a reciprocal lattice vector, $\mathbf{k}$ is a vector in the first Brillouin zone, $c_{j\mathbf{G}\mathbf{k}}$ is an expansion coefficient and N a normalization factor. When performing actual calculations the first Brillouin zone has to be sampled by a discrete grid of points (the k-points) and the plane wave expansion of Equation 2.24 has to be truncated. The size of the basis set is generally specified further by a single parameter, i.e. the maximum kinetic energy E_{cut} that can be represented by a basis function. In formulas, the plane wave $e^{i(\mathbf{k}+\mathbf{G})\cdot\mathbf{r}}$ is included in the basis set if :

$$\frac{1}{2}\left|\mathbf{k}+\mathbf{G}\right|^2 < E_{cut}. \tag{2.25}$$

The use of a plane wave basis set brings a number of advantages. First, Pulay forces, which arise in the evaluation of the forces when using an (incomplete) localized basis set, automatically vanish, significantly simplifying the evaluation of $-\nabla_I E_0(\{\mathbf{R}_I\})$ (see also Section 2.1). Also, a basis set superposition error does not arise in the context of plane waves, since plane waves are non-atom-centered functions homogeneously distributed in the space. Furthermore, computational advantages arise from the fact that plane wave derivatives in real space correspond to simple multiplications in reciprocal space, and efficient algorithms exist to connect the real and the reciprocal space (Fast Fourier Transforms, FFTs).

One of the drawbacks of the use of plane waves is that the energy converges slowly with basis set size when trying to represent core electron atomic orbitals, which are rapidly varying functions due to their localization near the nucleus, and valence electron orbitals in the proximity of the nuclei, which can assume an highly-oscillating behaviour. Core electrons, however, do not significantly affect the chemistry of atoms and molecules, since the rearrangement of the valence electrons is mainly responsible for bonding. Therefore, they can be replaced by effective potentials named pseudopotentials [57, 58]. Furthermore, pseudopotentials can also be used to account for relativistic effects. Moreover, the pseudopotentials can be chosen such that the pseudized wave functions are smoother than the corresponding all-electron wave functions at short distances from the nuclei, while they reproduce the all-electron wave functions beyond a certain cut-off radius.

Another drawback of plane waves is that the basis-set size automatically increases with the unit cell size, regardless of the number of atoms in the unit cell. This means that the need to include a large vacuum space in the unit cell to minimize the ‘artificial’ interactions between periodic images, automatically translates in a large basis set size.

2.3 The AIMD Implementation

AIMD has been employed to investigate gas-surface reactions since the early 90’s [59–61]. However, the computational cost of AIMD limited these first studies to a few explorative trajectories. With the growth of computational power and the development of efficient algorithms, the use of AIMD to perform statistically relevant calculations for gas-surface reactions has recently become possible [62].

Ultimately, an AIMD study of a molecule-surface reaction can be divided into three steps:

- the choice of the trajectories’ initial conditions;
- the time propagation of the trajectories;
- the analysis of the computed trajectories.

These steps are now discussed below.

2.3.1 The Choice of the Initial Conditions

The way in which the initial positions and the velocities are assigned to the nuclei at the starting point of the trajectories is discussed separately for the surface atoms and for the molecule.

2.3.1.1 The Surface

As we already mentioned, the surface is modeled with a periodic slab. The atomic positions are chosen in such a way that the periodic repetition of a suitably chosen unit cell reproduces the desired surface structure. In the implementation used, the unit cell has to include a large vacuum space in order to minimize the interaction between periodic images of the slab, and of the molecule with the periodic replica of the slab it interacts with. The length of the vacuum space in the cell, the surface unit cell size and the number of atomic layers are all parameters for which convergence needs to be tested with respect to the properties of interest.

The initial conditions of the surface atoms are chosen with the aim of studying the effect that surface temperature and surface atom motion have on the dissociation probability of molecules on metal surfaces. Surface temperature can influence the dissociation probability in various ways. First, local lattice deformations caused by the thermal motion of surface atoms can affect the reaction barrier heights as known, for instance, for the dissociation of CH_4 on metals, where the outward displacement of the surface atom below the dissociating molecule significantly lowers the energy of the transition state [63, 64]. The dissociation barrier heights can also be affected by the thermal expansion of the whole lattice [65, 66], as observed for H_2 on Cu(111), where the *d*-band of the metal is up-shifted with increased surface strain [67]. Finally, the surface can act as a heat bath, and help to stabilize an adsorbate by subtracting an excess of kinetic energy from the impinging molecule through recoil. This last effect is expected to be the more significant the larger the ratio between the mass of the molecule and the mass of the surface atoms is, due to the larger efficacy of the energy transfer as predicted by the Baule model [68, 69].

In order to investigate the role that surface atom motion plays in each system investigated, we have performed three types of calculation. In the first type of calculations we simulate an ideal surface keeping the atoms fixed in their equilibrium positions, neglecting all the surface temperature effects (lattice distortion, thermal expansion) and surface atom motion effects (recoil). In the second type of calculations surface temperature effects are included, but the surface atoms are kept fixed in their (distorted) initial position, blocking the energy transfer to the surface. Surface deformation, surface atom motion and the expansion of the lattice constant to mimic the thermal expansion of the lattice are all effects included in the third and last kind of calculations performed. Displacements and velocities are assigned to surface atoms by sampling the initial configuration from long differently-initialized equilibration runs.

2.3.1.2 The Molecule

The molecules' initial conditions are chosen on the basis of the experiments that we want to simulate. The positions and the velocities of each atom define the initial position of the center of mass of the molecule, its orientation, the collision energy, and the (initial) quantum state. Concerning the molecule's initial position, the lateral displacement is chosen randomly in order to uniformly sample the surface unit cell plane with the impacting molecule's center of mass. The initial distance from the surface is chosen in an area where the molecule-surface interaction is negligible. The initial translational and rotational energies are set by assigning the corresponding velocities to the atoms. The rotational phase of the molecule is randomly sampled. The molecules are chosen to be isotropically oriented if the experimental conditions that we want to simulate do not require a specific rotational alignment. The vibrational coordinates are chosen such that normal vibrational coordinates and momenta sample classical microcanonical distributions. Note, however, that we exploit the quasi-classical trajectory (QCT) method, which means that vibrational zero-point energy is imparted to the molecules. If rotational alignment effects are investigated, the initial orientation of the molecule and of its angular momentum are sampled in accordance with the experimental distributions.

2.3.2 The Time Propagation

The time propagation of the trajectories has been carried out using the DFT and molecular dynamics code VASP [9, 70–73]. Once the forces are calculated from the optimized electron density, the nuclear positions are updated according to a propagator of the leapfrog form:

$$\mathbf{v}_I(t + {}^{\Delta t}\!/_2) = \mathbf{v}_I(t - {}^{\Delta t}\!/_2) + \mathbf{a}_I(t)\Delta t, \tag{2.26a}$$

$$\mathbf{R}_I(t + \Delta t) = \mathbf{R}_I(t) + \mathbf{v}_I(t + {}^{\Delta t}\!/_2)\Delta t. \tag{2.26b}$$

Here $\mathbf{v}_I$ and $\mathbf{a}_I$ are the velocity and the acceleration of the I-th nucleus, respectively, and Δt is the time-step chosen for the integration. Note that in contrast to the standard implementation of the leapfrog algorithm, the algorithm presented here propagates first the velocities and then the positions. Note also that the algorithm presented in Equations 2.26(a-b) is not self-starting, and that the velocities at time $t = -{}^{\Delta t}\!/_2$ have to be supplied together with the positions at time $t = 0$ to VASP when starting an AIMD calculation. The leapfrog propagator is equivalent to the Velocity Verlet algorithm [74], with the only difference being an half time-step stagger between positions and velocities in the former. However, the velocities at the times at which positions are available can be easily computed as:

$$\mathbf{v}_I(t) = \frac{\mathbf{R}_I(t - \Delta t) + \mathbf{R}_I(t + \Delta t)}{2\Delta t}. \tag{2.27}$$

Both the leapfrog and the Velocity Verlet algorithms are time-reversible and symplectic. These properties allow for a good conservation of total energy and other constants of motion such as linear and angular momentum. The truncation error in the leapfrog propagator is of the order of Δt^3 for a single time-step, while the global error, i.e. the error associated with the propagation for a finite time $T = n\Delta \mathrm{t}$, with n integer, is of the order of Δt^2, as for the Velocity Verlet algorithm.

2.3.3 The Analysis of the Trajectories

After the propagation over a certain number of time-steps, the trajectories are analyzed to determine whether a specific outcome has been reached. This outcome can be, for instance, the dissociation of the molecule, and its verification can be monitored through a suitable operational definition. For instance, we can monitor whether the distance between two fragments of the molecule becomes larger than a certain value, in which case we may consider the outcome of the trajectory as reaction. Given the slab approach employed, the periodic boundary conditions have to be taken into account when analyzing the computed trajectories. In case that no outcome has been reached yet, the trajectories can be further propagated in time.

Note that a single trajectory usually does not give information that can be directly compared to experimental observables, but that it is only from the statistical analysis of a set of trajectories that we can extract physically relevant data.

2.4 The Computation of Observables

In this subsection we describe two observables that we have computed with AIMD. Further details will be given for each specific system in the following chapters.

2.4.1 The Initial State-Selected Reaction Probability

The initial state-selected reaction probability $R_{v,J}(E,\Theta,\Phi)$ is the dissociation probability for molecules initially prepared in a specific quantum state (v,J) and with a specific collision energy E, averaged over impact site on the surface and molecular orientation. The dissociation probability can also depend on the polar and the azimuthal angles defining the direction with which the molecules approach the surface, Θ and Φ, respectively.

As a consequence of the multidimensionality of the PES that describes the molecule-surface interaction, each molecule approaching the surface experiences a different interaction depending on the path that it follows. A first rough estimate of the reaction probability for molecule-surface systems can be based on a (static) analysis of a pre-calculated PES, assuming that the molecules maintain their initial orientation and impact site on the surface, and that they follow the minimum energy path in the remaining degrees of freedom. Such a static model, for instance the hole model [75, 76], does not include any dynamical effects, such as steering, and cannot be used to describe experiments in which the dependence of the reactivity on the energy disposed in various molecular degrees of freedom is far from statistical. A dynamical model is therefore required to investigate such properties.

The initial state-selected reaction probability $R_{v,J}$ can be estimated by running a set of AIMD trajectories. The initial conditions of all the trajectories are chosen to model a specific initial quantum (rovibrational) state and a specific initial collision energy. $R_{v,J}$ can then be estimated as the ratio between the number of reactive events observed and the total number of simulated trajectories. Experimentally, $R_{v,J}$ has been determined for H_2 [77] and D_2 [78] reacting on Cu(111) from desorption experiments through application of the principle of detailed balance. $R_{v,J}$ can also be measured in adsorption experiments by using a laser to prepare the reacting molecules in a specific initial quantum state (see for instance Refs. [24,79]). Special care, however, has to be taken to discard the reactivity contribution coming from molecules not excited by the laser, and to deconvolute the dissociation probability from the velocity distribution of the molecular beam (see also Section 2.4.2).

2.4.2 Simulation of Molecular Beam Adsorption Experiments

The molecular beam technique is a powerful experimental method to study the dynamics of gas-surface reactions. A basic molecular beam apparatus consists of a gas chamber connected to a ultra high vacuum (UHV) chamber through a small orifice. The expansion of the gas through the orifice produces a beam of molecules, in which the number of collisions between particles is very low. The molecular beam can be directed towards a well-cut single crystal, and the sticking probability determined through various experimental techniques. Molecular beam experiments are very popular in surface science because they allow for a relatively high control of the physical properties of the molecules in the beam, such as their velocity or their vibrational and rotational state.

The sticking probability measured in a molecular beam experiment can be related to the initial state-selected reaction probabilities $R_{v,J}(E,\Theta,\Phi)$ through the following expression:

$$S_0(v_s,\alpha,T_n,\Theta,\Phi) = \sum_{v,J} F_{v,J}(T_n) \int_{E=0}^{\infty} R_{v,J}(E,\Theta,\Phi) f(v_s,\alpha,E) dE. \tag{2.28}$$

Note that we left the dependence of S_0 on Θ and Φ explicit. Experimental conditions are such that the polar angle Θ is usually accurately determined, while the azimuthal angle Φ, the determination of which requires the knowledge of the orientation of the beam with respect to the surface crystal directions, is often not known. The simulation of experiments in which Φ has not been determined is frequently performed by averaging over all the possible azimuthal orientations, i.e. by integrating the rhs of Equation 2.28 over Φ between 0 and 2π. The energy integral in Equation 2.28 includes the translational energy distribution of the molecules in the beam $f(v_s,\alpha,E)$. This distribution can be expressed as a function of two parameters, i.e. the stream velocity v_s and the width parameter α. These parameters can be obtained by determining the translational energy distribution from fits to recorded time-of-flight (TOF) measurements of the beam. In the velocity domain, this distribution has the following form [80]:

$$f'(v_s,\alpha,v)dv = N_v \exp\left[-\left(\frac{v-v_s}{\alpha}\right)^2\right] v^3 dv. \tag{2.29}$$

Here N_v is a normalization factor. The same distribution can also be expressed in the energy domain [80]:

$$f(v_s,\alpha,E)dE = N_E \exp\left[-4E_s\left(\frac{\sqrt{E}-\sqrt{E_s}}{\Delta E_s^2}\right)^2\right] EdE, \tag{2.30}$$

where N_E is a normalization factor, $E_s = \frac{1}{2}mv_s^2$ and $\Delta E_s = 2E_s\alpha/v_s$. The presence of various rovibrational states in the beam is taken into account by the sum in Equation

2.28. The contribution of each quantum state to the overall reactivity is weighted by the corresponding Boltzmann factor $F_{v,J}(T_n)$:

$$F_{v,J}(T_n) = N \cdot g_v \cdot g_J \cdot \exp\left(-\frac{E(v,J)}{k_b T_n}\right). \tag{2.31}$$

Here N is a normalization factor, g_v and g_J are the vibrational and the rotational degeneracy factors, respectively, $E(v,J)$ is the internal energy of the rovibrational state (v,J) and k_b is the Boltzmann constant. For molecular hydrogen, the rotational degeneracy factor is equal to $g_J = d_{op} \cdot (2J+1)$, where d_{op} is a factor that accounts for the ortho-para population ratio (3:1 for H_2 and 2:1 for D_2, at room temperature). In Equation 2.31 we are assuming the same rotational and vibrational temperatures for the molecules in the beam, both being equal to the nozzle temperature T_n. However, the rotational degrees of freedom might cool down during the expansion from the nozzle. To model this effect, a lower rotational temperature can be employed for calculating the Boltzmann population of the rotational states.

In order to simulate a molecular beam experiment and to calculate the corresponding sticking probability with AIMD a Monte Carlo integration is performed over the collision energies and the rovibrational states. The initial conditions are randomly selected by sampling the experimental translational energy distribution and the Boltzmann distribution of states and the sticking probability is estimated as the ratio between the number of reactive events observed N_r and the total number of trajectories simulated N_{tot}:

$$p = \frac{N_r}{N_{tot}}. \tag{2.32}$$

It is also important to adequately estimate a confidence interval for p. The set of possible outcomes (reaction or scattering) for N_{tot} simulated trajectories obeys a binomial distribution. According to the central limit theorem, this distribution approaches a Gaussian for large N_{tot}. Thus, under this condition, the confidence interval for the binomial proportion p can be estimated as for data normally distributed around the sample mean p with standard deviation of the mean $\sigma = \sqrt{p(1-p)/N_{tot}}$ [81]. The lower limit l and the upper limit u of the c confidence interval can therefore be written as:

$$l = p - z_{1-\frac{1}{2}(1-c)} \cdot \sqrt{\frac{p(1-p)}{N_{tot}}}, \tag{2.33a}$$

$$u = p + z_{1-\frac{1}{2}(1-c)} \cdot \sqrt{\frac{p(1-p)}{N_{tot}}}, \tag{2.33b}$$

where z_k is the k percentile of a standard normal distribution (e.g. for 95% confidence interval, $c = 0.95$, $z_{1-\frac{1}{2}(1-c)} = z_{0.975} = 2$). This interval, known as normal approximation interval or Wald interval, can be used whenever N_{tot} is large and p is far from both 0 and 1.

Bibliography

[1] M. R. Radeke and E. A. Carter, Annu. Rev. Phys. Chem. **48**, 243 (1997).

[2] R. Car and M. Parrinello, Phys. Rev. Lett. **55**, 2471 (1985).

[3] M. Born and K. Huang, *Dynamical Theory of Crystal Lattices*, Claredon Press, Oxford, 1954.

[4] M. Born and J. R. Oppenheimer, Ann. Physik. **84**, 457 (1927).

[5] H. Hellmann, Z. Phys. **85**, 180 (1933).

[6] R. P. Feynman, Phys. Rev. **56**, 340 (1939).

[7] P. Bendt and A. Zunger, Phys. Rev. Lett. **50**, 1684 (1983).

[8] D. Marx and J. Hutter, *Ab Initio Molecular Dynamics: Basic Theory and Advanced Methods*, Cambridge University Press, Cambridge, 2009.

[9] G. Kresse and J. Furthmüller, Phys. Rev. B **54**, 11169 (1996).

[10] H. F. Busnengo, A. Salin, and W. Dong, J. Chem. Phys. **112**, 7641 (2000).

[11] S. Lorenz, A. Groß, and M. Scheffler, Chem. Phys. Lett. **395**, 210 (2004).

[12] S. Lorenz, M. Scheffler, and A. Groß, Phys. Rev. B **73**, 115431 (2006).

[13] M. Alducin, R. Díez Muiño, H. F. Busnengo, and A. Salin, Phys. Rev. Lett. **97**, 056102 (2006).

[14] J. Behler, S. Lorenz, and K. Reuter, J. Chem. Phys. **127**, 014705 (2007).

[15] C. Díaz, E. Pijper, R. A. Olsen, H. F. Busnengo, D. J. Auerbach, and G. J. Kroes, Science **326**, 832 (2009).

[16] C. Díaz, R. A. Olsen, D. J. Auerbach, and G. J. Kroes, Phys. Chem. Chem. Phys. **12**, 6499 (2010).

[17] I. M. N. Groot, J. C. Juanes-Marcos, C. Díaz, M. F. Somers, R. A. Olsen, and G. J. Kroes, Phys. Chem. Chem. Phys. **12**, 1331 (2010).

[18] I. Goikoetxea, J. Meyer, J. I. Juaristi, M. Alducin, and K. Reuter, Phys. Rev. Lett. **112**, 156101 (2014).

[19] M. Mastromatteo and B. Jackson, J. Chem. Phys. **139**, 194701 (2013).

[20] B. Jiang and H. Guo, J. Phys. Chem. C **117**, 16127 (2013).

[21] X. J. Shen, A. Lozano, W. Dong, H. F. Busnengo, and X. H. Yan, Phys. Rev. Lett. **112**, 046101 (2014).

[22] B. Jackson and S. Nave, J. Chem. Phys. **135**, 114701 (2011).

[23] B. Jiang, R. Liu, J. Li, D. Xie, M. Yang, and H. Guo, Chem. Sci. **4**, 3249 (2013).

[24] P. M. Hundt, B. Jiang, M. E. van Reijzen, H. Guo, and R. D. Beck, Science **344**, 504 (2014).

[25] P. Hohenberg and W. Kohn, Phys. Rev. B **136**, 864 (1964).

[26] M. Levy, Proc. Natl. Acad. Sci. U. S. A. **76**, 6062 (1979).

[27] W. Kohn and L. J. Sham, Phys. Rev. **140**, A1133 (1965).

[28] F. Bloch, Z. Phys. **57**, 545 (1929).

[29] P. A. M. Dirac, Proc. Camb. Phil. Soc. **26**, 376 (1930).

[30] S. J. Vosko, L. Wilk, , and M. Nusair, Can. J. Phys. **58**, 1200 (1980).

[31] J. P. Perdew and Y. Wang, Phys. Rev. B. **45**, 13244 (1992).

[32] D. M. Ceperley and B. J. Alder, Phys. Rev. Lett. **45**, 566 (1980).

[33] J. A. White, D. M. Bird, M. C. Payne, and I. Stich, Phys. Rev. Lett. **73**, 1404 (1994).

[34] B. Hammer, K. W. Jacobsen, and J. K. Nørskov, Phys. Rev. Lett. **70**, 3971 (1993).

[35] J. P. Perdew, J. A. Chevary, S. H. Vosko, K. A. Jackson, M. R. Pederson, D. J. Singh, and C. Fiolhais, Phys. Rev. B **46**, 6671 (1992).

[36] J. P. Perdew, K. Burke, and M. Ernzerhof, Phys. Rev. Lett. **77**, 3865 (1996).

[37] B. Hammer, L. B. Hansen, and J. K. Nørskov, Phys. Rev. B **59**, 7413 (1999).

[38] A. D. Becke, Phys. Rev. A **38**, 3098 (1988).

[39] R. Peverati and D. G. Truhlar, Phil. Trans. R. Soc. A **372**, 20120476 (2014).

[40] R. Peverati and D. G. Truhlar, J. Chem. Theory Comput. **8**, 2310 (2012).

[41] C. Lee, W. Yang, and R. G. Parr, Phys. Rev. B **37**, 785 (1988).

[42] R. Colle and O. Salvetti, Theor. Chim. Acta **37**, 329 (1975).

[43] J. Zheng, Y. Zhao, and D. G. Truhlar, J. Chem. Theory Comput. **5**, 808 (2009).

[44] M. Wijzenbroek and G. J. Kroes, J. Chem. Phys. **140**, 084702 (2014).

[45] G. A. Bocan, R. Díez Muiño, M. Alducin, H. F. Busnengo, and A. Salin, J. Chem. Phys. **128**, 154704 (2008).

[46] S. Grimme, J. Comput. Chem. **27**, 1787 (2006).

[47] S. Grimme, J. Antony, S. Ehrlich, and H. Krieg, J. Chem. Phys. **132**, 154104 (2010).

[48] A. Tkatchenko and M. Scheffler, Phys. Rev. Lett. **102**, 073005 (2009).

[49] M. Dion, H. Rydberg, E. Schröder, D. C. Langreth, and B. I. Lundqvist, Phys. Rev. Lett. **92**, 246401 (2004).

[50] K. Lee, E. D. Murray, L. Kong, B. I. Lundqvist, and D. C. Langreth, Phys. Rev. B **82**, 081101 (2010).

[51] G. Román-Pérez and J. M. Soler, Phys. Rev. Lett. **103**, 096102 (2009).

[52] L. Martin-Gondre, J. I. Juaristi, M. Blanco-Rey, R. Díez Muiño, and M. Alducin, J. Chem. Phys. **142**, 074704 (2015).

[53] A. Chakraborty, Y. Zhao, H. Lin, and D. G. Truhlar, J. Chem. Phys. **124**, 044315 (2006).

[54] Y. Y. Chuang, M. L. Radhakrishnan, P. L. Fast, C. J. Cramer, and D. G. Truhlar, J. Phys. Chem. A **103**, 4893 (1999).

[55] L. Sementa, M. Wijzenbroek, B. J. van Kolck, M. F. Somers, A. Al-Halabi, H. F. Busnengo, R. A. Olsen, G. J. Kroes, M. Rutkowski, C. Thewes, N. F. Kleimeier, and H. Zacharias, J. Chem. Phys. **138**, 044708 (2013).

[56] G. J. Kroes, Phys. Chem. Chem. Phys. **14**, 14966 (2012).

[57] D. Vanderbilt, Phys. Rev. B **41**, 7892 (1990).

[58] P. E. Blöchl, Phys. Rev. B **50**, 17953 (1994).

[59] A. De Vita, I. Štich, M. J. Gillan, M. C. Payne, and L. J. Clarke, Phys. Rev. Lett. **71**, 1276 (1993).

[60] I. Štich, M. C. Payne, A. De Vita, M. J. Gillan, and L. J. Clarke, Chem. Phys. Lett. **212**, 617 (1993).

[61] I. Štich, A. De Vita, M. C. Payne, M. J. Gillan, and L. J. Clarke, Phys. Rev. B **49**, 8076 (1994).

[62] A. Groß and A. Dianat, Phys. Rev. Lett. **98**, 206107 (2007).

[63] G. Henkelman and H. Jónsson, Phys. Rev. Lett. **86**, 664 (2001).

[64] S. Nave, A. K. Tiwari, and B. Jackson, J. Chem. Phys. **132**, 054705 (2010).

[65] A. Mondal, M. Wijzenbroek, M. Bonfanti, C. Díaz, and G. J. Kroes, J. Phys. Chem. A **117**, 8770 (2013).

[66] A. Marashdeh, S. Casolo, L. Sementa, H. Zacharias, and G. J. Kroes, J. Phys. Chem. C **117**, 8851 (2013).

[67] S. Sakong and A. Groß, Surf. Sci. **525**, 107 (2003).

[68] B. Baule, Ann. Physik. **44**, 145 (1914).

[69] A. Gross, *Theoretical Surface Science*, Springer, Berlin, 2003.

[70] G. Kresse and J. Hafner, Phys. Rev. B **47**, 558 (1993).

[71] G. Kresse and J. Hafner, Phys. Rev. B **49**, 14251 (1994).

[72] G. Kresse and J. Furthmüller, Comput. Mat. Sci. **6**, 15 (1996).

[73] G. Kresse and D. Joubert, Phys. Rev. B **59**, 1758 (1999).

[74] W. C. Swope, H. C. Andersen, P. H. Berens, and K. R. Wilson, J. Chem. Phys. **76**, 637 (1982).

[75] M. Karikorpi, S. Holloway, N. Henriksen, and J. K. Nørskov, Surf. Sci. **179**, L41 (1987).

[76] K. Gundersen, K. W. Jacobsen, J. K. Nørskov, and B. Hammer, Surf. Sci. **304**, 131 (1994).

[77] C. T. Rettner, H. A. Michelsen, and D. J. Auerbach, J. Chem. Phys. **102**, 4625 (1995).

[78] H. A. Michelsen, C. T. Rettner, D. J. Auerbach, and R. N. Zare, J. Chem. Phys. **98**, 8294 (1993).

[79] R. D. Beck, P. Maroni, D. C. Papageorgopoulos, T. T. Dang, M. P. Schmid, and T. R. Rizzo, Science **302**, 98 (2003).

[80] H. A. Michelsen and D. J. Auerbach, J. Chem. Phys. **94**, 7502 (1991).

[81] W. L. Hayes, *Statistics*, Holt, Rinehart and Winston, NY, 3rd edition, 1981.

Chapter 3

Effect of Surface Motion on the Rotational Quadrupole Alignment Parameter of D_2 Reacting on Cu(111)

This chapter is based on:

F. Nattino, C. Díaz, B. Jackson, and G. J. Kroes, Phys. Rev. Lett. **108**, 236104 (2012).

Abstract

Ab initio molecular dynamics (AIMD) calculations using the specific reaction parameter approach to density functional theory are presented for the reaction of D_2 on Cu(111) at high surface temperature (T_s = 925 K). The focus is on the dependence of reaction on the alignment of the molecule's angular momentum relative to the surface. For the two rovibrational states for which measured energy resolved rotational quadrupole alignment parameters are available, and for the energies for which statistically accurate rotational quadrupole alignment parameters could be computed, statistically significant results of our AIMD calculations are that, on average: (i) including the effect of the experimental surface temperature (925 K) in the AIMD simulations leads to decreased rotational quadrupole alignment parameters, and (ii) including this effect leads to increased agree-

ment with experiment.

3.1 Introduction

Experiments on the alignment dependence of molecule-surface reactions yield detailed information on the interaction of molecules with surfaces [1–3]. Because the rotational alignment parameter of reacting molecules is connected with the local anisotropy of the potential energy surface (PES), measurements of this parameter in conjunction with theory can lead to the identification of the reaction site [4, 5]. Measurement of this parameter as a function of translational energy may also reveal important mechanistic information on, for instance, the importance of orientational steering for reaction [3].

The sensitivity of the alignment of reacting molecules to the details of the molecule-surface interaction makes experiments addressing this topic ideal for testing electronic structure theories that attempt to model this interaction. Such tests are highly relevant, and pose huge challenges. About 90% of the chemical manufacturing processes used worldwide employ heterogeneous catalysts [6]. However, the best *ab initio* theory that can now be used to map out PESs for elementary molecule-surface reactions, density functional theory (DFT) at the generalized gradient approximation (GGA), non-separable gradient approximation (NGA), meta-GGA or meta-NGA level, can provide reaction barriers with an accuracy of no better than 1.8 kcal/mol for gas phase reactions [7, 8]. Even this accuracy has only recently become available [7, 8], and it is therefore not surprising that quantum dynamics calculations using DFT PESs on the rotational quadrupole alignment parameter of H_2 desorbing from metal surfaces such as Pd(100) [9] and Cu(111) [10, 11] have not yet been able to quantitatively reproduce the experiments.

Dihydrogen-metal surface systems are ideal for testing electronic structure methods as accurate reaction probabilities can be computed within the Born-Oppenheimer (BO) approximation [12]. Making the static surface approximation (neglecting energy transfer involving phonons) should likewise lead to accurate results for low surface temperature (T_s) [13]. Taking advantage of this, it was recently shown that specific reaction parameter DFT (SRP-DFT) [14] allows a chemically accurate description (to within 1 kcal/mol $\approx$ 43 meV) of experiments on reaction of H_2 and D_2 in molecular beams, on the influence of the initial rovibrational state of H_2 on reaction, and on rotational excitation of H_2, in scattering from Cu(111) [10, 11]. However, a quantitative description of experiments on the rotational alignment parameter of D_2 desorbing from Cu(111) was not yet realized [11].

The failure was attributed to errors in the dynamical model (the Born-Oppenheimer static surface (BOSS) model), noting that the alignment experiments [3] were performed at high T_s. In the experiments D_2 was permeated through a copper crystal, and alignment parameters were measured for D_2 recombinatively desorbed from Cu(111) using linearly polarized laser light and time-of-flight techniques to achieve rovibrational state selectivity and translational energy (E) resolution. The use of the permeation technique dictated the use of a high T_s (925 K). Associative desorption experiments at this T_s have also been used to derive initial state-selected, degeneracy averaged dissociative chemisorption probabilities $R_{v,J}(E)$ [15], which are closely related to alignment parameters (v and J are the vibrational and rotational quantum numbers of D_2, see Section 3.2). Deriving parameters describing $R_{v,J}(E)$ required the assumption that dissociative chemisorption and associative desorption are related by detailed balance. The experimentalists confirmed the validity of this assumption by showing that sticking probabilities measured in molecular beam experiments at low T_s (120 K) could be well fitted using the $R_{v,J}(E)$ derived from associative desorption experiments, if the widths of the $R_{v,J}(E)$ curves were adjusted on the basis of existing knowledge regarding their dependence on T_s [15]. The detailed balance assumption is probably also valid for the fully initial state-selected resolved reaction probabilities R_{v,J,m_J} required for the computation of alignment parameters (m_J is the magnetic rotational quantum number of D_2, see Section 3.2), and theorists have relied on this assumption in previous calculations [9, 11]. However, for D_2 + Cu(111) and H_2-metal systems in general, no information is available on how T_s affects R_{v,J,m_J}, and thereby the alignment parameter. Here our aim is to resolve this issue for D_2 + Cu(111).

Using approximate molecule-phonon models, the effect of phonons on reactive scattering has been studied with reduced dimensionality models for H_2 + Cu [13, 16, 17], and treating all six molecular degrees of freedom for H_2 + Pd surfaces [18, 19]. DFT calculations on H_2 + Cu(111) have shown that the molecule-phonon coupling intricately depends on the motion of both first and second layer Cu atoms [20]. This complicated dependence is best handled by a method allowing surface atom motion and computing forces on the fly, such as the *ab initio* molecular dynamics (AIMD) method, which was first used to compute probabilities for molecule-surface reactions by Groß and coworkers [21]. They investigated H_2 dissociation on surfaces with initial $T_s = 0$ K. By extending the application of AIMD to non-zero initial T_s, here we show that quantitatively accurate modeling of the alignment parameter of D_2 desorbing from metal surfaces requires incorporation of surface motion in the theory. We show this by demonstrating that including the effect of the high experimental T_s in the theory yields rotational alignment parameters for D_2 + Cu(111) that, on average, differ significantly from static surface model results for the two rovibrational D_2 states for which experimental results have been obtained. Including the effect of the high experimental T_s also significantly improves the overall agreement with experiment. The AIMD results also yield an improved description of the initial state-selected reaction probability for D_2 + Cu(111).

3.2 Methods

The AIMD calculations were done using the *ab initio* total-energy and molecular dynamics program VASP [22–26]. Individual collisions are modeled through NVU simulations keeping the number of atoms N, the cell size V, and the total energy U constant, the approximation of omitting a thermostat being appropriate for the direct scattering problem addressed here. The quasi-classical trajectory (QCT) method was used (meaning that in all cases we impart zero-point energy to D_2), with appropriate averaging of the initial molecular coordinates and momenta [10, 11].

To mimic the effect of the high T_s used in the experiments (925 K), the initial coordinates and velocities of the Cu atoms in the upper 3 layers of the surface were sampled from 1 ps runs of eight differently initialized (111) surfaces, in which these atoms were allowed to move. The sampling procedure used consisted of initially sampling the displacements and velocities of moving Cu atoms from a classical Boltzmann distribution of atomic harmonic oscillators at $T_s = 925$ K, performing an equilibration AIMD run, an AIMD run with velocity rescaling to the target temperature, another equilibration run and a run for sampling, for each surface. In the AIMD simulations, the lowest layer of Cu atoms of the four layer (2x2) surface unit cell used was kept fixed, whereas the atoms in the upper 3 layers were allowed to move. In the slab and subsequent D_2 + Cu(111) simulations, the dimensions of the unit cell parallel to the surface were increased by 1.54% relative to their theoretical 0 K values to describe the experimentally determined expansion of bulk Cu [27, 28], based on a theoretical 0 K bulk lattice constant a_{3D} of 3.68 Å. The procedure used imposed an average T_s of 912 K on the surfaces, with a standard deviation of 167 K that mimics local variations that can be expected in the kinetic energy of an ensemble of $N = 12$ moving atoms ($\sigma_T = T/\sqrt{3N} = 154$ K). This allows us to model the effect of local variations of temperature without having to perform prohibitively expensive simulations involving too large surface unit cells.

The AIMD calculations on D_2 + Cu(111) used a timestep of 0.5 fs. Reaction is defined to take place if the D-D distance r becomes larger than 1.6 Å, and additionally it becomes larger than the distance between one D-atom and the closest periodic image of the other D-atom. This definition allows for scattering involving recrossings of the transition state (a minority event). The D_2 is started moving to the surface at a molecule-surface distance $Z = 6.0$ Å, and is considered as scattered once Z becomes larger than 6.1 Å.

The details of the DFT calculations (number of layers of the Cu slab, number of k-points, etc.) within the AIMD are mostly identical to those of earlier static surface calculations [10, 11]. However, the SRP functional used here (called SRP48) employs an RPBE coefficient of 0.48 instead of the previous value (0.43), to account for technical differences in the k-space integration between VASP (Γ-point included) and the previously used electronic structure code (Γ-point not included when using even numbers of

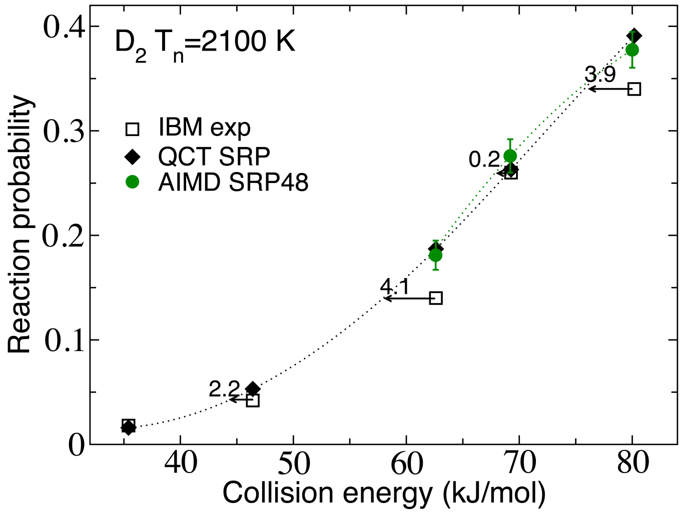

Figure 3.1: Reaction probabilities computed with AIMD are compared with experimental values for D_2 + Cu(111) [15], and to QCT results employing the BOSS model [10,11]. The experiments used a nozzle temperature of 2100 K. The arrows and the accompanying numbers (in kJ/mol) show the collision energy spacing between the experimental data and the cubic spline interpolated SRP48-DFT reaction probability curve.

k-points) [10, 11]. Also, in the SRP48 functional the PW91 functional was replaced by the PBE functional designed to mimic it [29]. SRP48 calculations on H_2 + Cu(111) for an ideal, 0 K slab reproduce the SRP energies at SRP reaction barrier geometries to within 15 meV. AIMD calculations on D_2 + Cu(111) using the SRP48 functional and Cu slabs equilibrated at T_s =120 K reproduced the sticking probability measured at that T_s for the three translational energies considered to within chemical accuracy (Figure 3.1, 1 kcal/mol ≈ 4.2 kJ/mol). This establishes the validity of the SRP48 functional when used with VASP and the present computational parameters.

We have also performed AIMD calculations with VASP in which the surface was kept fixed in an ideal lattice configuration that is appropriate for a 0 K surface, based on the computed 0 K lattice constant and interlayer relaxations of the four-layer slab (AIMDf, where the f stands for fixed lattice). Relative to our earlier QCT-BOSS model [10, 11], our AIMDf static surface model shows a number of improvements. The imposition of artificial symmetry that was used in constructing the SRP PES in the BOSS model (the approximation often made that dihydrogen interacts identically with the fcc and hcp hollow sites) was avoided. The SRP PES used in the QCT-BOSS calculation is affected by small errors incurred in the interpolation procedure used [10, 11]; these admittedly small errors are avoided in the AIMDf calculations. Furthermore the SRP48 0 K lattice constant value (3.68 Å) used in AIMDf agrees better with experiment (3.61 Å) than the RPBE value of 3.71 Å [10,11] used to construct the SRP PES. We believe that the above improvements made in the AIMDf model explain that the AIMDf results presented in Section 3.3 already agree better with experiment than the QCT-BOSS results.

Assuming detailed balance, the rotational quadrupole alignment parameter for associative desorption was computed using [5]:

$$A_0^{(2)} = \frac{A}{B} = \frac{\sum\limits_{m_J} R_{v,J,m_J}(E)\{3m_J^2 - J(J+1)\}/\{J(J+1)\}}{\sum\limits_{m_J} R_{v,J,m_J}(E)}, \tag{3.1}$$

with the denominator B being equal to $(2J+1)R_{v,J}$, and the quantum numbers referring to the initial state of D_2. $A_0^{(2)}$ is positive if the molecule prefers to react with its bond axis parallel to the surface (helicopter rotation, $|m_J| = J$), and negative if the molecule prefers to react end-on (cartwheel rotation, $m_J = 0$), and 0 if reaction is independent of orientation. In all theoretical results shown here, errors and error bars represent 68.3% confidence intervals. Calculations were done for the two D_2 rovibrational states investigated experimentally, at E values for which statistically accurate AIMD results could be obtained. The AIMD results were based on 3120 (1840) trajectories for the lowest E investigated for $v = 1, J = 6$ ($v = 0, J = 11$), and on half these amounts for the other E's.

3.3 Results and Discussion

For the two states for which energy resolved experimental results are available, the $A_0^{(2)}$ values computed with AIMD are lower than the AIMD results computed for a fixed surface at 0 K (AIMDf) for all but one case (($v = 1, J = 6$) at $E = 0.6$ eV, see Figure 3.2). An analysis based on statistical hypothesis testing and the sum of the individual differences between the AIMD and AIMDf results divided by the standard errors in these differences shows that, for the two rovibrational states addressed and the collision energies for which reasonably accurate AIMD results could be obtained, the AIMD results fall below the AIMDf results on average (significance level $\alpha = 0.05$, see Appendix 3.A.1). Modeling surface motion with AIMD also leads to a clear and statistically significant improvement in the overall agreement with experiment when comparing to the AIMDf results and the previous quantum dynamical and quasi-classical BOSS results [10, 11] (see Appendix 3.A.1). On average, the AIMDf alignment parameters are significantly lower, and therefore in better agreement with experiment than the previous QCT-BOSS results (see Appendix 3.A.1), which we attribute to improvements in the static surface model achieved here through the AIMDf calculations as already discussed in Section 3.2. Finally, we note that the similarity between the quantum dynamical and QCT-BOSS results in Figure 3.2 validates the use of quasi-classical mechanics in AIMD to compute $A_0^{(2)}$.

In Figure 3.3 the AIMD results for $R_{v,J}(E)$ are in much better agreement with experimentally fitted [15,30] results for the ($v = 0, J = 11$) state at $T_s = 925$ K than the previous QCT-BOSS model results with experimentally fitted [15, 30] results for $T_s = 120$ K [10,11], for the lower E for which the experimental fits can be expected to be most reliable. The improvement may well be due in large part to improvements introduced in AIMD other than allowing surface motion (see also Section 3.2), as the difference between the AIMD and AIMDf results is smaller than between AIMD and QCT-BOSS. The AIMD value of the energy E_0 (0.574 ± 0.009 eV) at which the reaction probability becomes equal to half the maximum experimentally fitted value ($A = 0.27$ [30]) agrees with the experimental value (0.546 eV) to within chemical accuracy (1 kcal/mol $\approx$ 43 meV). AIMD calculations for additional rovibrational states are needed to establish whether the AIMD method can describe the experimental $E_0(v, J)$ values for D_2 with chemical accuracy for the greater part of the (v, J) states for which experimental results

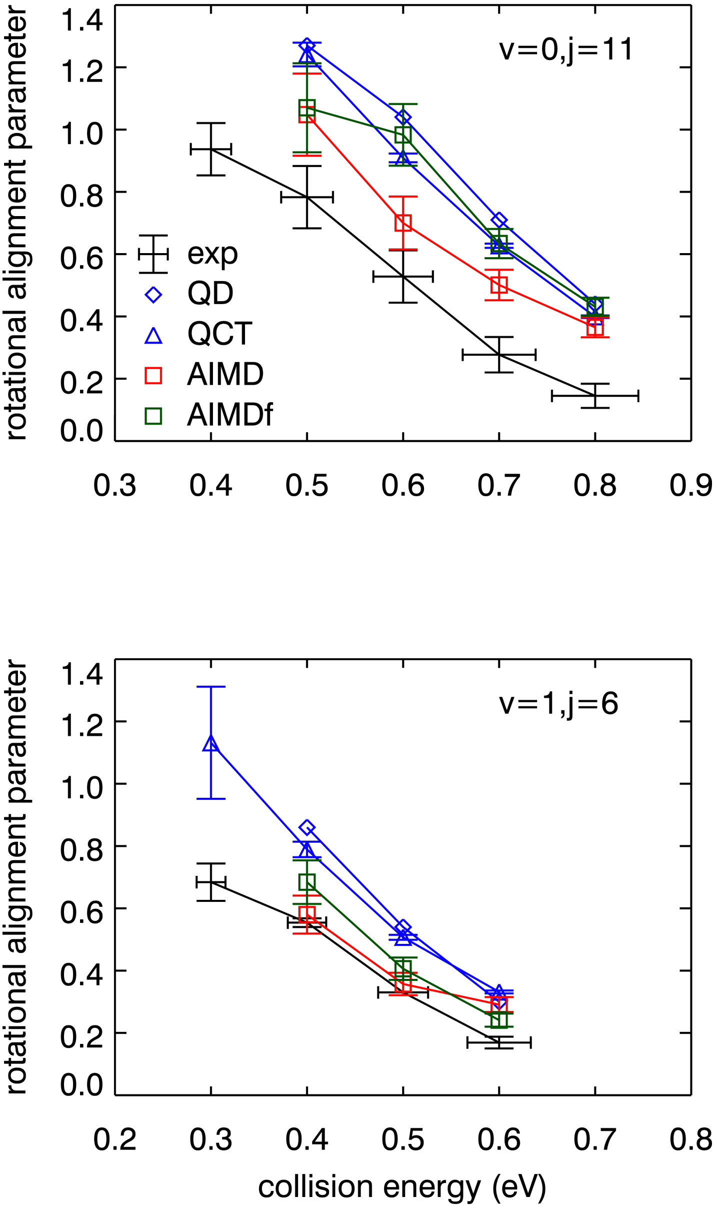

Figure 3.2: Comparison of $A_0^{(2)}$ values measured in associative desorption experiments [3] with theoretical values computed using the AIMD method, the AIMD method with the surface held fixed at 0 K (AIMDf), and with quantum dynamics (QD) and the QCT method using the BOSS model [10, 11].

are available (see also Chapter 4); only marginal improvement was observed for ($v = 1, J = 6$) here (Figure 3.3, the difference between the AIMD and experimental E_0 values is 45 meV). The comparison of the AIMD and AIMDf results is consistent with the finding of low-dimensional calculations using surface oscillator approximations [13, 17] and experiments [15, 31] that raising T_s broadens the reaction probability around a common midpoint.

The fact that $A_0^{(2)}$ may be written as a fraction (Equation 3.1) suggests the existence of two distinguishable mechanisms that may lead to a decrease of this parameter. Figure 3.4 illustrates these two mechanisms, for the ($v = 1, J = 6$) state. At the lowest E the denominator of the fraction increases because $R_{v,J}(E)$ increases with T_s (see also Figure 3.3), leading to a decrease in $A_0^{(2)}$ (Figure 3.2) even though cartwheel (low $|m_J|$) reaction probabilities do not increase more than helicopter (high $|m_J|$) reaction probabilities, leaving the numerator in Equation 3.1 almost unchanged (mechanism I, see Appendix 3.A.2). The importance of this mechanism at low E is consistent with DFT findings that the molecule-surface interaction is decreased in an isotropic fashion for the two lowest high symmetry barrier geometries (bridge-to-hollow and the t2h site halfway between a top and hcp site) if the closest second layer (or hcp) Cu atom moves down (see Figure 9 of Ref. [20]). Such configurations will be increasingly available at high T_s. At these configurations the energy available to reaction (the molecule's energy minus the height of the barrier) is increased, whereas the 'anisotropy energy' (which may be defined as the interaction energy of a tilted molecule minus that of a parallel molecule at the reaction barrier geometry [3]) is unchanged. Under these conditions, the reaction probability may be expected to increase by the same amount for all m_J (as seen in Figure 3.4 for 0.4 eV), which is consistent with the mechanism discussed above. A reasoning based on increasing available energy and unchanged anisotropy energy has also been invoked to explain the dependence of $A_0^{(2)}$ on incidence energy [3].

Figure 3.4 shows that at the intermediate E of 0.5 eV the decrease in $A_0^{(2)}$ (Figure 3.2) is due to increased reaction of states with low $|m_J|$ and decreased reaction of states with high $|m_J|$, leading to a decrease in the numerator of Equation 3.1 whereas the

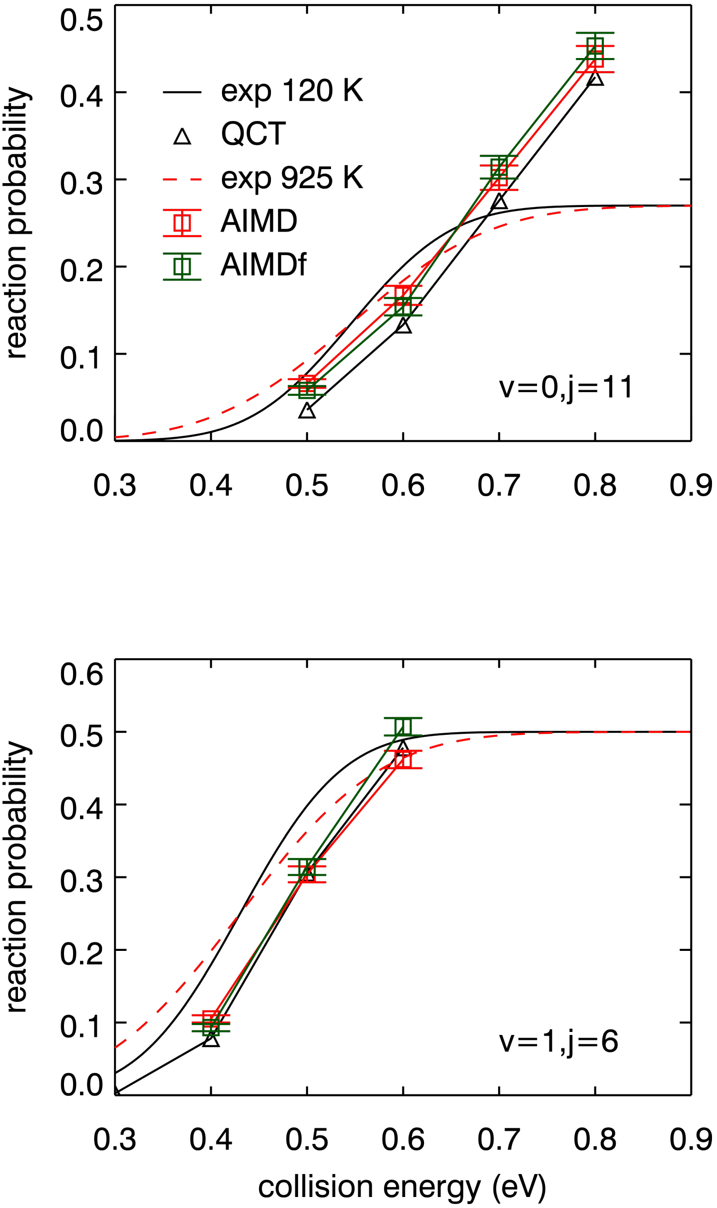

Figure 3.3: Comparison of experimentally fitted [15, 30] values of $R_{v,J}(E)$ for $T_s = 120$ and 925 K with theoretical values computed using the AIMD and AIMDf methods and with the QCT method using the BOSS model [10, 11].

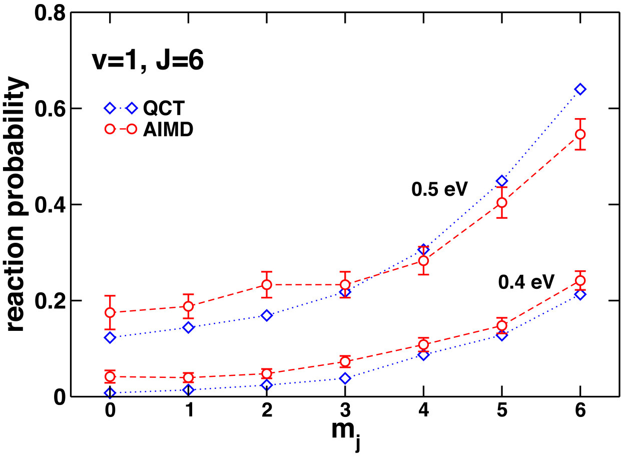

Figure 3.4: Comparison of $R_{v,J,m_J}(E)$ computed with AIMD with QCT results using the BOSS model [10, 11] for ($v = 1, J = 6$) D_2 + Cu(111).

denominator is almost unchanged (it is actually decreased see Appendix 3.A.2), in what we call mechanism II. The above two cases represent ideal cases: in some cases a change in $A_0^{(2)}$ reflects both changes in the preference for helicopter vs. cartwheel reaction and changes in $R_{v,J}(E)$. We have also seen cases where changes in the numerator and the demoninator work in opposite ways but one of the effect dominates, see Appendix 3.A.2. Our interpretation of mechanism II is as follows. On a cold surface, the preference found for reaction with D_2 parallel to the surface arises from the barrier being lowest in this alignment, because it best allows the D-atoms to simultaneously form bonds to the surface. On a hot surface the preference for parallel reaction is diminished because the molecule is more likely to encounter environments in which the surface is locally distorted, such that the simultaneous formation of D-metal bonds may be favored for tilted configurations. One would then expect increased reaction of states with low $|m_J|$ and decreased reaction of states with high $|m_J|$, whereas $R_{v,J}(E)$ might remain unchanged.

The increase in $R_{v,J}(E)$ in mechanism I is not only correlated with motion of the second layer Cu atom closest to the impinging D_2 molecule, but also to motion of the closest first layer Cu atom, because the barrier height is decreased for the lowest

D_2 state	E (eV)	Z_{12}^{av}, reaction	Z_{12}^{av}, scattering
$v = 1, J = 6$	0.4	2.273 ± 0.012	2.194 ± 0.004
$v = 0, J = 11$	0.5	2.292 ± 0.022	2.196 ± 0.005
$v = 0, J = 11$	0.6	2.260 ± 0.019	2.182 ± 0.008

Table 3.1: The average value of Z_{12} (in Å) and its error is shown for reacting D_2 (computed when r first becomes larger than 1.032 Å, the value at the SRP minimum reaction barrier geometry [10]) and for scattering D_2 (computed at the largest outer turning point in r of scattering D_2).

reaction barrier geometry if this Cu atom moves up [20]. Indeed, in reactive events, and for the initial states and energies at which mechanism I operates or an increase in $R_{v,J}(E)$ contributes to a decreased alignment parameter (Appendix 3.A.2), we observe significantly larger values Z_{12} of the vertical distance between these Cu-atoms than for scattering (Table 3.1). At the T_s considered here large Z_{12} values do not only result from large amplitude phonon motion, but also from thermal expansion: experiments show that the first interlayer distance d_{12} goes up by 2.7% going from 0 to 925 K. The large increase of d_{12} reflects both thermal expansion of the bulk (1.54% [27, 28]) and d_{12} being contracted with respect to the bulk at low T_s, but bulk-like at high T_s [32]. Our DFT and AIMD calculations reproduce this trend: The average d_{12} obtained with AIMD for $T_s = 925$ K (2.189 ± 0.034 Å) is larger than the d_{12} value that characterizes a (0 K) relaxed slab (2.10 Å, see Table 3.2) and agrees, within error bars, with the bulk interlayer distance of 2.16 Å expected for the (expanded) lattice constant of 3.74 Å. The lowering of the barrier heights we see (Table 3.2) with increased tensile strain (T_s) may be explained [33] from the d-band model [34]: smaller overlap between substrate atoms reduces the width of the d-band, causing an upshift of the band if it is more than half-filled, which usually leads to higher reactivity.

The error bars on the experimental results in Figure 3.2 are estimates of confidence intervals based on an assessment of systematic errors that affect the energy calibration and limited information on statistical errors: They were based on noise in the time-of-flight spectra and uncertainties in the fits used, but on only one set (two sets) of measurements for $v = 1, J = 6$ ($v = 0, J = 11$) [35]. Conversely, the AIMD error bars only represent statistical errors. In the AIMD, systematic errors can arise from the use

Parameter	925 K	0 K
d_{12} (Å)	2.16	2.10
a_{3D} (Å)	3.74	3.68
E_b (bth)	0.593	0.628
E_b (ttb)	0.865	0.877

Table 3.2: Parameters describing slab geometry and molecule-surface interaction energies (E_b, in eV) obtained with DFT and the SRP48 functional are presented for the bridge-to-hollow (bth) and top-to-bridge (ttb) dissociation routes at SRP reaction barrier geometries [10], for $T_s = 0$ and 925 K.

of too few Cu layers or a too small surface unit cell to adequately model surface motion. Considering the uncertainties in the experimental and theoretical error analyses, we argue that the best statement we can make presently about the agreement with experiment is that going from the BOSS model to the AIMD model, which allows the surface to move, the overall agreement is improved significantly. We believe that further theoretical work aimed at eliminating the systematic errors that may still be present in the AIMD is best performed when experimental results accompanied by a more complete error analysis become available. If the differences between theory based on the detailed balance assumption and associative desorption experiments persist, further research should be performed to address the validity of this assumption. For instance, it is possible that the permeation technique leads to an overestimated contribution of reaction involving D-atoms coming directly from the subsurface, which may be investigated with additional calculations, or using alternative techniques to dose D-atoms to the surface [31].

3.4 Summary and Conclusions

We have employed the AIMD method to study the effect of surface temperature on the rotational quadrupole alignment parameter for D_2 desorbing from Cu(111). We have investigated the two molecular rovibrational states for which experimental data [3] are available at various collision energies, basing our model on the assumption of detailed balance. Our calculations show that the alignment parameter is on average lowered when the high experimental surface temperature (925 K) is modeled, improving in this way the agreement with the experiment. We suggest two mechanisms to explain the decrease of the rotational alignment parameter with increased surface temperature. The first mechanism is related to an increased reactivity for all the molecular alignments: the impinging molecules experience lower dissociation barriers because of the larger vertical distance between the closest first layer atom and second layer atom sampled at high surface temperature. The second mechanism, on the other hand, has to do with a diminished reactivity of the molecular orientations with the bond parallel to the surface and an increased reactivity of the tilted orientations, provoked by local surface deformations, also frequently sampled at high surface temperature. The mismatch still present between theory and experiment in the alignment parameter could be due to systematic errors in the AIMD method or to an incomplete error analysis of the experimental data. For what concerns the initial-state-selected reaction probability, only slight improvement is observed against previous static surface calculations, with AIMD curves being slightly broader than AIMDf curves. This increase of the width is in agreement with previous theoretical [13, 17] and experimental [15, 31] findings about the effect of surface temperature on the shape of the dissociation probability curves, but the size of the increase is too small when compared with experimental findings [15, 31].

3.A Appendix

3.A.1 Statistical Analysis

In this section we aim to show that the rotational quadrupole alignment parameters obtained with AIMD are smaller than the AIMDf values obtained for a 0 K static surface. Such a proof can be put on a firm statistical basis by using the method of statistical hypothesis testing [36]. We will concern ourselves with differences d_i divided by the standard error s_i in these differences, or by the standard deviation σ_i in these differences, for combinations of translational energies and (v, J) D_2 states denoted by i. The difference may be between any two sets of measurements, but in the example considered here first it concerns the AIMD and the AIMDf calculations of the alignment parameter. For this case, d_i is defined by:

$$d_i = A_0^{(2)}(J; \mathrm{AIMDf}, i) - A_0^{(2)}(J; \mathrm{AIMD}, i). \tag{3.A.1}$$

In hypothesis testing, we take the hypothesis we try to prove as the alternative hypothesis, which we may write as:

- H_1: Modeling the effect of surface temperature decreases the rotational quadrupole alignment parameter. The AIMD results should therefore fall below the AIMDf results, and the differences defined in Equation 3.A.1 should be positive.

Next, we formulate the null hypothesis, which can be taken opposite to the hypothesis we are trying to prove, as:

- H_0: Modeling the effect of surface temperature does not affect the rotational quadrupole alignment parameter, or increases it. The AIMDf results should therefore fall below or on the AIMD results, and the differences defined in Equation 3.A.1 should be zero or negative.

In order to be able to accept the H_1 hypothesis posed, in statistical hypothesis testing one then demands than, on the basis of the data obtained, H_0 can be rejected with a pre-defined confidence level α, which imposes a maximum on the probability to reject

#	State	E (eV)	d_i	σ_i	Z-statistic	p-value
1	$(v = 1, J = 6)$	0.4	0.10342	0.09298	1.1123	0.1335
2	$(v = 1, J = 6)$	0.5	0.04986	0.05092	0.9792	0.1635
3	$(v = 1, J = 6)$	0.6	-0.04941	0.03178	-1.5548	N/A
4	$(v = 0, J = 11)$	0.5	0.02161	0.19466	0.1110	0.4562
5	$(v = 0, J = 11)$	0.6	0.28366	0.13105	2.1645	0.0152
6	$(v = 0, J = 11)$	0.7	0.13286	0.06751	1.9680	0.0244
7	$(v = 0, J = 11)$	0.8	0.06643	0.04335	1.5324	0.0630

Table 3.A.1: Z-statistics and p-values for 7 computational experiments, comparing AIMDf with AIMD results.

H_0 if H_0 is true. A typical value used for α is 0.05 and this is the value we will work with. One next calculates the actual probability of rejecting H_0 although H_0 is true, in the light of the data obtained. This probability is called the p-value, which should be lower than α for H_0 to be rejected. Assuming for now that the calculated standard error in the difference, s_i, equals the standard deviation in the difference, σ_i, we base our test on the so-called Z-statistic or Z-score, which for the condition i may be written as [36]:

$$Z_i = \frac{d_i}{\sigma_i}. \tag{3.A.2}$$

Table 3.A.1 lists the Z-statistics for our seven computational experiments, and the p-values for rejecting H_0 on the basis of an individual measurement. The Table shows a drawback of the AIMD method, which is computionally expensive. As a result, the computed alignment parameters are based on reaction probabilities calculated from a limited number of trajectories. The statistical errors in these probabilities are inversely proportional to the square root of the number of trajectories, and these errors are therefore rather large. This results in rather large statistical errors in the alignment parameters and their differences d_i. As a result, in only two of the 7 individual cases the Z-statistics are large enough, and the p-values small enough to allow rejection of the null hypothesis for the specific condition investigated.

However, six of the seven Z-statistics are positive, pointing to the fact that a much stronger statement is possible if the measurements are considered together. We reformulate our hypotheses as follows:

- H_1: On average, for the two rovibrational states for which energy resolved measurements are available and the ranges of collision energies for which statistically accurate alignment parameters could be obtained, modeling surface temperature decreases the rotational quadrupole alignment parameter. On average, the AIMD results should therefore fall below the AIMDf results.
- H_0: On average, for the two rovibrational states for which energy resolved measurements are available and the ranges of collision energies for which statistically accurate alignment parameters could be obtained, modeling surface temperature does not affect the rotational quadrupole alignment parameter, or increases it. On average, the AIMDf results should therefore fall below or on the AIMD results.

We can test these hypotheses using the sum of the individual Z-scores. This weighs each measurement according to the error in it, and we obtain a test-statistic which is guaranteed to have a normal distribution, provided that the individual Z-scores also obey a normal distribution, which we assume to be the case anyway.

The individual Z-statistics obey the normal distribution $N(0,1)$, 0 being the average and 1 the variance. It is easy to see that $\sum_{i=1}^{7} Z_i$ obeys the normal distribution $N(0,7)$. We may then obtain a composite Z-statistic by defining:

$$Z_{comp} = \frac{\sum\limits_{i=1}^{7} Z_i}{\sqrt{7}} \tag{3.A.3}$$

(this composite Z-score is also known as Stouffer's Z-score [37]). From the data in Table 3.A.1 we obtain $Z_{comp} = 2.38$. The H_0 hypothesis may be formulated as $Z_{comp} \leq 0$. The p-value of the outcome $Z_{comp} = 2.38$ is 0.0085. Clearly, the null hypothesis may be rejected with a significance level of 0.05, and we may accept our new H_1 hypothesis which concerns the ensemble of initial conditions we have AIMD results for.

In a similar way, we may test the alternative hypothesis that, on average, for the two rovibrational states for which energy resolved measurements are available and the ranges of collision energies for which statistically accurate alignment parameters could be obtained, the AIMD method modeling the effect of T_s yields results in better agreement with experiment than the AIMDf method. This requires the sum of the absolute values of the differences between the experimental results and the AIMD results to be smaller than the sum of the absolute values of the differences between the experimental results and the AIMDf results. Because in all cases i the experimental $A_0^{(2)}(J)$ values are lower than both the AIMD values of $A_0^{(2)}(J)$ and the AIMDf values of $A_0^{(2)}(J)$, this amounts to proving that on average, modeling surface temperature with AIMD decreases the rotational quadrupole alignment parameter. This was already done above, and we can reject the null hypothesis that, on average, modeling surface temperature with AIMD does not yield increased agreement with experiment with a confidence level α=0.05 and with the same p-value as obtained before (0.0085).

In a similar vein, we are able to prove that, on average, the fixed surface model implicit in the AIMDf calculations improves the agreement with experiment compared to the fixed surface model used in the previous QCT-BOSS calculations [10, 11], due to the improvements discussed above (p-value of 0.003). Finally, the improved agreement with experiment going from the QCT-BOSS fixed surface model to the AIMDf fixed surface model and then to the AIMD model with T_s = 925 K can also be seen simply by comparing the sum of the absolute differences:

$$S = \sum_{i=1}^{7} |d_i| , \tag{3.A.4}$$

with:

$$d_i = A_0^{(2)}(J; \mathrm{exp}, i) - A_0^{(2)}(J; \mathrm{method}, i). \tag{3.A.5}$$

The results are presented in Table 3.A.2. If we take S as a measure of the disagreement with experiment, going from the AIMDf model to the AIMD model the disagreement with experiment is reduced by almost a facor 1.6. Going from the previous QCT-BOSS static surface results to the AIMD results modeling surface motion, the disagreement with experiment is reduced by almost a factor 2.

Model	S
QCT-BOSS	2.02
AIMDf	1.66
AIMD	1.06

Table 3.A.2: The sum of the absolute differences with the experimental alignment parameter values, S, is given for the alignment parameters computed with the AIMD, the AIMDf, and the QCT-BOSS models.

3.A.2 Relative Importance of the Two Mechanisms for Reducing the Alignment Parameter

The fractional decrease of the AIMD alignment parameter due to surface motion may be written as:

$$\frac{A_0^{(2)}(J;\mathrm{AIMDf}) - A_0^{(2)}(J;\mathrm{AIMD})}{A_0^{(2)}(J;\mathrm{AIMDf})} = (1 - A_{fac}) + (1 - B_{fac}) - (1 - A_{fac})(1 - B_{fac}), \tag{3.A.6}$$

with:

$$A_{fac} = A_{\mathrm{AIMD}}/A_{\mathrm{AIMDf}}, \tag{3.A.7a}$$

$$B_{fac} = B_{\mathrm{AIMD}}/B_{\mathrm{AIMDf}}. \tag{3.A.7b}$$

and where A and B are defined in Equation 3.1 in Section 3.2. The last term on the rhs of Equation 3.A.6 is small and, for ease of interpretation in terms of the contribution of mechanisms I and II to the decrease of the alignment parameter, we may ignore it (it hardly affects the contributions discussed below). We therefore write:

$$\frac{A_0^{(2)}(J;\mathrm{AIMDf}) - A_0^{(2)}(J;\mathrm{AIMD})}{A_0^{(2)}(J;\mathrm{AIMDf})} = (1 - A_{fac}) + (1 - B_{fac}). \tag{3.A.8}$$

On the basis of Equation 3.A.8 the fractional decrease may be analyzed in terms of two fractional contributions to the decrease of the alignment parameter, one being due to mechanism I:

$$C_I = \frac{1 - B_{fac}}{(1 - A_{fac}) + (1 - B_{fac})}, \tag{3.A.9}$$

#	State	E (eV)	C_I	C_{II}
1	$(v=1, J=6)$	0.4	0.69	0.31
2	$(v=1, J=6)$	0.5	< 0	> 1
3	$(v=1, J=6)$	0.6	N/A	N/A
4	$(v=0, J=11)$	0.5	> 1	< 0
5	$(v=0, J=11)$	0.6	0.26	0.74
6	$(v=0, J=11)$	0.7	< 0	> 1
7	$(v=0, J=11)$	0.8	< 0	> 1

Table 3.A.3: The fractional contributions of the two mechanisms to the decrease of the alignment parameter with T_s computed with the AIMD method is shown for the seven initial conditions investigated in the calculations.

and one being due to mechanism II:

$$C_{II} = \frac{1 - A_{fac}}{(1 - A_{fac}) + (1 - B_{fac})}. \tag{3.A.10}$$

With the approximation made in Equation 3.A.8, these coefficients add up to 1. Their interpretation is that if $C_I > C_{II}$ mechanism I makes a dominant contribution to the decrease of the alignment parameter, whereas mechanism II makes the dominant contribution if $C_I < C_{II}$.

The fractional contributions are given in Table 3.A.3 for the 7 initial conditions considered here. Mechanism I is most important for the lowest incidence energy for both initial rovibrational states and makes a considerable contribution for $(v = 0, J = 11)$ at $E = 0.6$ eV. It is precisely for these three conditions that, in a statistically significant way, we can correlate reaction with a collective motion of the Cu atoms that are in the upper two surface layers and closest to the reacting D_2, which motion results in an isotropic decrease of the reaction barrier height at the lowest reaction barrier geometry (see Section 3.3 and Table 3.1). For the higher incidence energies, mechanism II dominates.

Bibliography

[1] B. L. Yoder, R. Bisson, and R. D. Beck, Science **329**, 553 (2010).

[2] M. Rutkowski, D. Wetzig, and H. Zacharias, Phys. Rev. Lett. **87**, 246101 (2001).

[3] H. Hou, S. J. Gulding, C. T. Rettner, A. M. Wodtke, and D. J. Auerbach, Science **277**, 80 (1997).

[4] M. Rutkowski and H. Zacharias, Phys. Chem. Chem. Phys. **3**, 3645 (2001).

[5] D. A. McCormack, G. J. Kroes, R. A. Olsen, J. A. Groeneveld, J. N. P. van Stralen, E. J. Baerends, and R. C. Mowrey, Chem. Phys. Lett. **328**, 317 (2000).

[6] I. Chorkendorff and J. W. Niemantsverdriet, *Concepts of Modern Catalysis and Kinetics*, Wiley-VCH, Weinheim, 2003.

[7] R. Peverati and D. G. Truhlar, Phys. Chem. Chem. Phys. **14**, 13171 (2012).

[8] R. Peverati and D. G. Truhlar, Phil. Trans. R. Soc. A **372**, 20120476 (2014).

[9] A. Dianat and A. Groß, Phys. Chem. Chem. Phys. **4**, 4126 (2002).

[10] C. Díaz, E. Pijper, R. A. Olsen, H. F. Busnengo, D. J. Auerbach, and G. J. Kroes, Science **326**, 832 (2009).

[11] C. Díaz, R. A. Olsen, D. J. Auerbach, and G. J. Kroes, Phys. Chem. Chem. Phys. **12**, 6499 (2010).

[12] P. Nieto, E. Pijper, D. Barredo, G. Laurent, R. A. Olsen, E. J. Baerends, G. J. Kroes, and D. Farías, Science **312**, 86 (2006).

[13] M. Dohle and P. Saalfrank, Surf. Sci. **373**, 95 (1997).

[14] Y. Y. Chuang, M. L. Radhakrishnan, P. L. Fast, C. J. Cramer, and D. G. Truhlar, J. Phys. Chem. A **103**, 4893 (1999).

[15] H. A. Michelsen, C. T. Rettner, D. J. Auerbach, and R. N. Zare, J. Chem. Phys. **98**, 8294 (1993).

[16] Z. S. Wang, G. R. Darling, B. Jackson, and S. Holloway, J. Phys. Chem. B **106**, 8422 (2002).

[17] Z. S. Wang, G. R. Darling, and S. Holloway, J. Chem. Phys. **120**, 2923 (2004).

[18] H. F. Busnengo, W. Dong, and A. Salin, Phys. Rev. Lett. **93**, 236103 (2004).

[19] H. F. Busnengo, M. A. Di Césare, W. Dong, and A. Salin, Phys. Rev. B **72**, 125411 (2005).

[20] M. Bonfanti, C. Díaz, M. F. Somers, and G. J. Kroes, Phys. Chem. Chem. Phys. **13**, 4552 (2011).

[21] A. Groß and A. Dianat, Phys. Rev. Lett. **98**, 206107 (2007).

[22] G. Kresse and J. Hafner, Phys. Rev. B **47**, 558 (1993).

[23] G. Kresse and J. Hafner, Phys. Rev. B **49**, 14251 (1994).

[24] G. Kresse and J. Furthmüller, Comput. Mat. Sci. **6**, 15 (1996).

[25] G. Kresse and J. Furthmüller, Phys. Rev. B **54**, 11169 (1996).

[26] G. Kresse and D. Joubert, Phys. Rev. B **59**, 1758 (1999).

[27] F. R. Kroeger and C. A. Swenson, J. Appl. Phys. **48**, 853 (1977).

[28] I. E. Leksina and S. I. Novikova, Sov. Phys-Solid State **5**, 798 (1963).

[29] J. P. Perdew, K. Burke, and M. Ernzerhof, Phys. Rev. Lett. **77**, 3865 (1996).

[30] C. T. Rettner, H. A. Michelsen, and D. J. Auerbach, Faraday Discuss. **96**, 17 (1993).

[31] M. J. Murphy and A. Hodgson, J. Chem. Phys. **108**, 4199 (1998).

[32] K. H. Chae, H. C. Lu, and T. Gustafsson, Phys. Rev. B **54**, 14082 (1996).

[33] S. Sakong and A. Groß, Surf. Sci. **525**, 107 (2003).

[34] B. Hammer and J. K. Nørskov, Surf. Sci. **343**, 211 (1995).

[35] D. J. Auerbach and A. M. Wodtke, Private Communication, 2012.

[36] W. L. Hayes, *Statistics*, Holt, Rinehart and Winston, NY, 3rd edition, 1981.

[37] S. A. Stouffer, E. A. Suchman, L. C. De Vinney, S. A. Star, and R. M. Williams Jr., *The American Soldier: Adjustment During Army Life (Vol. 1)*, Princeton University Press, Princeton, 1949.

Chapter 4

Dissociation and Recombination of D_2 on Cu(111): *Ab initio* Molecular Dynamics Calculations and Improved Analysis of Desorption Experiments

This chapter is based on:
F. Nattino, A. Genova, M. Guijt, A. S. Muzas, C. Díaz, D. J. Auerbach and
G. J. Kroes, J. Chem. Phys. **141**, 124705 (2014).

Abstract

Obtaining quantitative agreement between theory and experiment for dissociative adsorption of hydrogen on and associative desorption of hydrogen from Cu(111) remains challenging. Particularly troubling is the fact that theory gives values for the high energy limit to the dissociative adsorption probability that are as much as two times larger than experiment. In the present work we approach this discrepancy in three ways. First, we carry out a new analysis of the raw experimental data for D_2 associatively desorbing from Cu(111). We also perform new *ab initio* molecular dynamics (AIMD) calculations

that include effects of surface atom motion. Finally, we simulate time-of-flight (TOF) spectra from the theoretical reaction probability curves and we directly compare them to the raw experimental data. The results show that the use of more flexible functional forms for fitting the raw TOF spectra gives fits that are in slightly better agreement with the raw data and in considerably better agreement with theory, even though the theoretical reaction probabilities still achieve higher values at high energies. The mean absolute error (MAE) for the energy E_0 at which the reaction probability equals half the experimental saturation value is now lower than 1 kcal/mol, the limit that defines chemical accuracy, while a MAE of 1.5 kcal/mol was previously obtained. The new AIMD results are only slightly different from the previous static surface results and in slightly better agreement with experiment.

4.1 Introduction

Heterogeneously catalyzed processes, which are composed of sequences of elementary molecule-surface reactions, are widely employed in the industrial production of many important chemicals. Despite the relevance of the field, even the simplest elementary reactions on metal surfaces like the dissociation of the smallest molecule, H_2, on metals remains challenging to model quantitatively [1]. In this framework, the dissociative chemisorption of H_2 on copper surfaces is ideal for testing the accuracy of dynamical models and electronic structure calculations, as evidence exists that it is essentially electronically adiabatic [2–4]. Furthermore, working on this benchmark for activated chemisorption is advantageous due to the large number of experimental [5–21] and theoretical [22–47] studies available for comparison. In surface chemistry, the H_2 + Cu(111) reaction [8,11,12,19,26,39,43] has a status that is similar to that of the H_2 + H exchange reaction [48–54] in gas phase chemistry, major challenges to theorists being to explain the associated chemical physics and to demonstrate the validity of their methods for the system concerned.

A previous theoretical study [39, 40] based on the Born-Oppenheimer and static-surface approximations (BOSS) reached chemical accuracy (errors $\leq$ 1 kcal/mol) in the description of many sets of experimental data for H_2 and D_2 on Cu(111). Electronic structure calculations were performed using density functional theory (DFT) with a semi-empirical density functional, developed according to the specific reaction parameter (SRP) approach originally developed by Truhlar and coworkers for gas-phase reactions [55, 56]. Nevertheless, a quantitative description of some experimental observables, like the rotational quadrupole alignment parameter ($A_2^{(0)}$) [19], the probability of vibrational excitation [14] and the influence of the initial rovibrational state of D_2 on the reactivity [13], was not yet achieved.

Data on the initial state-resolved reaction probability of D_2 on Cu(111) were obtained from post-permeation associative desorption experiments [13, 19], in which D atoms were supplied to the surface through permeation of the bulk. The experiments used a high surface temperature ($T_s = 925$ K) in order to have a sufficient flux of permeating atoms. The quantum state of the desorbing molecules was probed via laser excitation using resonance-enhanced multiphoton ionization (REMPI) [57], and their translational energy distribution was determined from time-of-flight (TOF) measurements of the ions through a field free region.

In previous theoretical work, the failure of the BOSS study in describing $A_2^{(0)}$ was attributed to the static surface approximation employed, considered unable to describe this observable measured at high surface temperature [39, 40]. The effect of phonons on the reactivity of H_2 on Cu(111) was first modeled in a very approximate way [40], using the surface oscillator model [58, 59], but this was insufficient to account for the discrepancies in $A_2^{(0)}$ between theory and experiment. The fact that the measured initial-state-selected effective barrier heights ($E_0(v, J)$) of H_2 could be accurately reproduced using the BOSS model, even though the experiments were performed at high surface temperature, can be explained on the basis of observations according to which $E_0(v, J)$ should be independent of surface temperature effects. It has been shown that varying only the width of the reaction probability curve is sufficient to account for most of the surface temperature effects on reaction [21]. Despite the good agreement obtained for H_2, a larger mean absolute error (MAE) was obtained for D_2 in the description of

$E_0(v, J)$ (1.48 kcal/mol) [39].

More recently, *ab initio* molecular dynamics (AIMD) has been used to introduce the motion of the surface atoms in the calculations and to model the effect of the experimental surface temperature (Ref. [43] and Chapter 3). The results showed that modeling surface temperature effects substantially improves the agreement between theory and experiment for the rotational alignment parameter, and slightly improves the agreement for the reaction probability of the two initial rovibrational states investigated. Wijzenbroek and Somers developed the so-called static corrugation model (SCM), in which the 'static' effects of surface temperature, i.e. of the thermal lattice expansion and of the thermal distribution of the displacements of the surface atoms from their equilibrium positions, were simulated [44]. Their results, which showed that modeling surface temperature with the SCM affects the reaction probability curves through both a small shift in energy and a 'broadening' of the curves, are in better agreement with experimental data than the BOSS results, and in good agreement with AIMD.

As alternative to dynamical models, Harrison and coworkers proposed a dynamically-biased microcanonical model, in which a limited number of adjustable parameters are fitted to an experimental set of data sensible to the dynamical biases part of the model [47]. This semi-empirical model was able to accurately describe a large variety of experimental data, over a large range of collision energies, but it may be argued that this was done to some extent by simply fitting the vibrational and rotational efficacies to experiment. The model also gave a good description of the surface temperature dependence of the state-specific reaction probability curves extracted from TOF data by Murphy and Hodgson [21]. However, such a microcanonical model is still limited in which 'dynamical' experimental observables can be computed (for instance, the rotational alignment parameter, or the vibrational excitation probability cannot be computed with the present model). On the other hand, our dynamical model for H_2 + Cu(111) can be systematically improved by adding more (phonon) degrees of freedom, and describing these more accurately, while the SRP density functional we developed is firmly rooted in a validation against observables either measured at low surface temperature (sticking probability determined via molecular beam experiments, data on rotationally inelastic scattering) or against observables that experiments suggest to exhibit no, or little, dependence on surface temperature ($E_0(v, J)$). Our model is best suited to describing the reactivity at the (111) terraces, which should dominate the reactivity of the surfaces defined by accurately cut crystals for the higher translational energies considered in our study (close to E_0). Such conditions are presently best for validating electronic structure theory for highly activated molecule-surface reactions [60], as the presence of defects, of which there may be an ill-defined variety [61], would strongly affect the thermal reactivity of molecules on metal surfaces [62, 63]. We consider the dynamically biased microcanonical theory currently less useful for such validation purposes, as it produces a zero-point energy corrected reaction threshold value for which comparison of electronic structure theory to experiment through rate theory might lead to ambiguous results for highly activated reactions.

In the current work we tackle some of the significant discrepancies that still exist between dynamical models and experiments. For instance, both the BOSS and the AIMD models mentioned above overestimate the experimental D_2 reaction probabilities at the high collision energies (see Figure 4.1). Also, in contrast to theory the experimental maximum reaction probability showed a strong dependence on v [13, 15], the value for $v = 1$ exceeding the $v = 0$ value by a factor 1.85. Furthermore, the BOSS model has a MAE in the description of $E_0(v, J)$ which is considerably larger for D_2 than for H_2 [39], as mentioned earlier. Moreover, theory is slightly shifted to lower energies (20-40 meV) compared to the highest nozzle temperature sticking probability curve determined via molecular beam experiments [11]. In contrast, the theoretical initial state-selected reaction probabilities are shifted towards higher energies by about 50-100 meV compared to the experimental curves [39, 40], the shift being the largest for $v = 0$ and $v = 1$ D_2. Finally, the state-averaged average desorption energy computed from the experimental reaction probability curves is 71 meV lower than the value measured by Comsa and David [64], considered to be the most accurate measurement of this observable, as discussed by Sementa et al. [65].

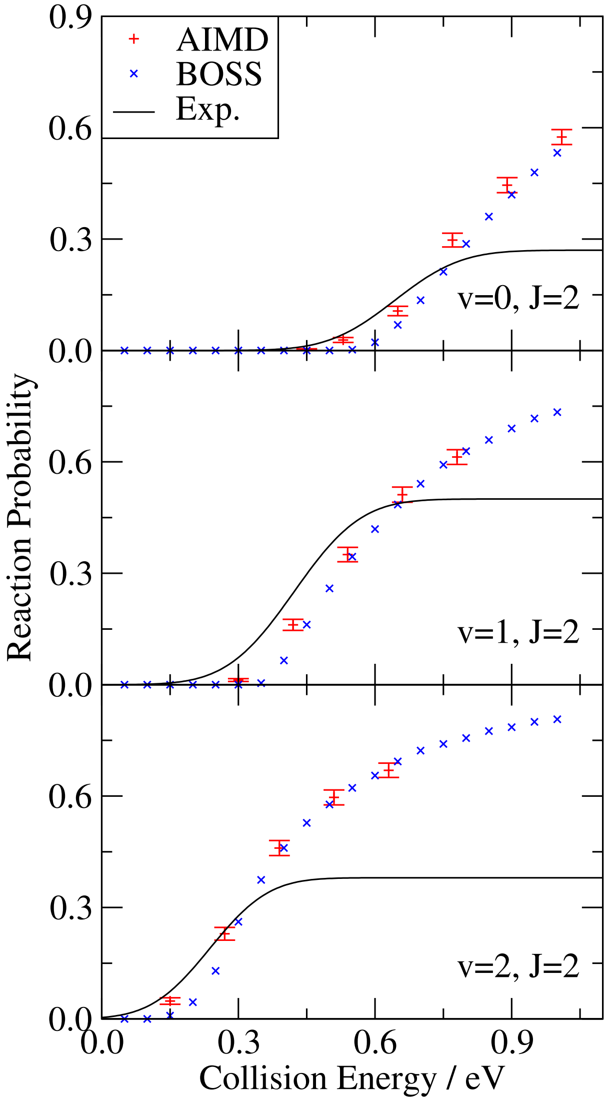

Figure 4.1: Initial-state-selected reaction probability curves for three representative states: ($v = 0, 1, 2; J = 2$). Black curve: experimental data from Ref. [13]. Blue ×: BOSS results from Refs. [39, 40]. Red +: AIMD data.

Here, we present four approaches to resolving these discrepancies and inconsistencies. First, we re-examined the raw TOF data from associative desorption experiments [13] to see if the form of the initial-state-selected reaction probability curve ($S_{v,J}(E)$) used to fit the data might be responsible for the discrepancies in $S_{v,J}$ at high incidence energy. In particular, more flexible sigmoid functions than the traditionally used error function (ERF) have been tested in modeling the reaction probability curves when fitting the TOF spectra. The choice to also test asymmetric sigmoid functions was motivated by the outcome of calculations with the hole model [66, 67], of which results are also presented here. Second, in the fits of the TOF spectra, we have used an expression for the influence of the angle with which the molecule leaves the surface on its TOF that is more accurate than the one used before [13]. Note that the choice of fitting function is also relevant to activated reactions other than H_2 + Cu(111) [13,16], such as N_2+W(110) [68], CH_4+Pt(111) [69], CH_4+Ni(111) [70] and H_2O+Ni(111) [71], which have all been modeled with the ERF form. Third, we have extended the number of initial rovibrational states of D_2 investigated with AIMD, and compare these new AIMD results both to the previous BOSS data and to the newly-fitted experimental reaction probabilities. Finally, we have simulated TOF spectra from the computed reaction probabilities, to achieve a more direct comparison between the theoretical results and experimental raw data, without any manipulation of the latter other than the background subtraction. To our knowledge, this is the first time that TOF data describing associative desorption are simulated directly on the basis of computed dissociative chemisorption probabilities.

We find that the choice of the functional form employed for the reaction probability curve when fitting an experimental TOF spectrum strongly influences the saturation value of the experimental reaction probability curves for $v = 0$. However, the new analysis does not fully solve the discrepancies between theoretical and experimental saturation values, and theoretical reaction probabilities are still larger than the experimental values at high energies. Furthermore, due to corrections to the method of doing angular averaging in the analysis of the TOF spectra, the experimental reaction probability curves are now slightly shifted to higher collision energies, improving the agreement between theory and experiment in the $E_0(v, J)$ value: the MAE of experiment relative to both BOSS and AIMD is now lower than 1 kcal/mol, the limit which conventionally defines ‘chemical accuracy’. Compared to the BOSS model, the AIMD method produces reaction probability curves which are in most cases slightly broader and slightly shifted to lower energies, and therefore in better agreement with the experimental data. Finally the TOF spectra simulated from the AIMD reaction probability curves agree better with experiment than the ones simulated using the BOSS reaction probability curves.

This chapter is structured as follows. In Sections 4.2.1-4.2.3 we describe the theoretical methods employed (BOSS model, AIMD methods and hole model). In Section 4.2.4 the various functional forms which have been used in the fitting of the reaction probability curves are presented. In Sections 4.2.5-4.2.7 we describe how the experimental state-selected reaction probability curves have been extracted from the measured TOF spectra and how the relative and absolute saturation values of these curves have been determined. In Section 4.2.8 we show how the average desorption energy can be computed from the state-selected reaction probability curves. In Section 4.3, all the results are presented and discussed: Section 4.3.1 includes the hole model results; in Section 4.3.2 all the fits of the theoretical reaction probabilities are presented; in Sections 4.3.3 and 4.3.4 the fits of the experimental TOF spectra, and the reaction probabilities extracted from these are presented, respectively; in Section 4.3.5 simulated TOF spectra are presented and compared to measured ones; in Sections 4.3.6 and 4.3.7 the effective barrier heights and average desorption energies obtained theoretically and experimentally are compared. Finally, conclusions are presented in Section 4.4.

4.2 Methods

4.2.1 BOSS Model

Details about the BOSS model are given elsewhere [39,40], therefore only a brief description is given here. An accurate six-dimensional potential energy surface (PES) [39, 40], based on a large number of DFT calculations, describes the interaction between H_2 and the ideal Cu(111) surface. The semi-empirical SRP functional [39] was employed in the electronic structure calculations. The SRP-PES is characterized by a minimum barrier height (E_b) of 0.628 eV, which corresponds to the so-called bridge-to-hollow (bth) configuration [39]. For D_2, zero-point energy (ZPE) corrections lower the barrier by about 30 meV. Further barrier heights with the relative barrier geometries can be found in Table 4.A.1. We report calculations performed using the quasi-classical trajectory (QCT) method, the appropriateness of which is justified by the good agreement between quantum and quasi-classical dynamics results found previously [39,40]. In the QCT method, vibrational ZPE is imparted to the molecule, the initial conditions of which are described via an appropriate sampling of coordinates and velocities.

4.2.2 AIMD Method

The AIMD technique [72,73] relies on the Born-Oppenheimer approximation, as does the just described BOSS model. However, due to the 'on-the-fly' calculation of the forces, AIMD circumvents the need of computing and fitting a PES and allows for the simulation of surface atom motion, which is used to model the experimental surface temperature (T_s = 925 K [13]). The procedure according to which the initial displacements from the equilibrium positions and the velocities are assigned to surface atoms is described in Ref. [43] and Chapter 3. Note that the equilibrium lattice constant has been expanded by 1.54% [74,75] in order to account for thermal expansion. Just like the BOSS calculations, the AIMD calculations use the QCT method. The AIMD technique has already been shown [43] to quantitatively reproduce the sticking probability measured by Michelsen et al. [13] using molecular beam experiments (see Figure 3.1 in Chapter 3).

The AIMD calculations are performed with the VASP package [76–80]. The surface is modeled using a slab consisting of 4 layers, three of which are allowed to move. A 2x2 supercell is employed. The first Brillouin zone is sampled by a 8x8x1 k-point grid which includes the Γ point. Other computational details, which are given elsewhere (Ref. [43] and Chapter 3), are very similar to the ones used in the BOSS calculations. The SRP48 functional used here differs from the original SRP functional [39] in the use of the PBE exchange-correlation functional [81,82] instead of the PW91 one [83,84], and in the use of a slightly different mixing coefficient (see Ref. [43] and Chapter 3 for more details). However, with the mixing coefficient chosen, the SRP48 functional reproduces the SRP minimum barrier height [43]. Calculations suggest that surface temperature should have little effect on the barrier heights that would be extracted from dynamics experiments. If only thermal expansion of the surface is considered, the barrier heights computed for high symmetry sites are significantly lowered (by 27 to 44 meV at $T_s = 925$ K) [85], provoking a shift of the reaction probability curves towards a lower energy [44, 85]. Dynamics calculations suggest that this effect is counteracted by the displacement of surface atoms from their equilibrium position [44] and from the modeling of dynamical recoil effects [43], which tend to shift the reaction probability curve by the same amount of energy, but in the opposite direction. The net effect observed in the calculations is a broadening of the reaction probability curve, though not by the same amount as observed experimentally.

Between 400 and 900 trajectories per initial rovibrational state and collision energy have been computed. Reaction probabilities and confidence intervals are estimated with the Wilson (or score) [86] method, except if a zero binomial proportion is observed (if no reactive events are found), for which case a proper interval has been employed [87]. Reaction probability error bars represent 68.3% confidence intervals.

4.2.3 The Hole Model

The consequence of the multidimensionality of the PES for an activated system like H_2 + Cu(111) is that each molecule experiences a different energy barrier along the path it attempts to follow towards reaction. Formally, the barrier distribution function $N(E)$ is the fractional number of barriers with an energy which falls between E and $E + dE$. According to the classical hole model [66,67] the reaction probability S as a function of the collision energy E_i can be computed from the barrier distribution function:

$$S(E_i) = \int_0^{E_i} N(E')dE'. \tag{4.1}$$

This model assumes the applicability of a sudden model to the parallel translational motion and the rotation of the molecule, and a purely classical over-the-barrier mechanism: no effects such as tunneling or vibrational softening at the transition state are considered. The model also assumes that the only energy available for the reaction is the collision energy. Note that $N(E)$ is determined from a (static) analysis of the PES, therefore $S(E)$ cannot be initial-state specific. We expect this model to be reasonable for $(v = 0, J = 0)$ H_2, which contains only zero-point vibrational energy, and for which each orientation is equally likely. Dai and Light [35] have shown that for this state, and for the translational energies of interest to our study, the reaction probability can be accurately computed by summing fixed-site reaction probabilities with appropriate weights, meaning that the sudden approximation may be assumed to work reasonably well at least for parallel translational motion. The analysis with the hole model, which involves the evaluation of $N(E)$ from the PES and the calculation of $S(E)$ according to Equation 4.1, is likely to demonstrate whether it is likely that an asymmetric fitting function should be employed to fit the sticking probability for at least the $(v = 0, J = 0)$ state. Fitting TOF spectra for other (v, J) states with a fitting function that is flexible enough to both describe asymmetric and symmetric sticking probability curves can then show to what extent the results of the hole model regarding asymmetry of the reaction probability curve generalize to other (v, J) states.

$N(E)$ is often arbitrarily assumed to be a Gaussian function [88]. With this assumption, we can rewrite Equation 4.1 as [88]:

$$S(E) = \frac{A}{\sqrt{\pi}W} \int_0^E \exp\left[-\left(\frac{E' - E_0}{W}\right)^2\right] dE' = \frac{A}{2}\left[1 + \mathrm{erf}\left(\frac{E - E_0}{W}\right)\right]. \qquad (4.2)$$

This result motivated the use of a form (ERF) incorporating the error function to model the reaction probability curve for activated systems [89, 90]. For instance, the reaction probability of the systems H_2+Cu(111) [16], D_2+Cu(111) [13], N_2+W(110) [68], CH_4+Pt(111) [69], CH_4+Ni(111) [70] and H_2O+Ni(111) [71] has been modeled with the ERF form. More generally, any $N(E)$ symmetric about E_0 will give a $S(E)$ that is symmetric with respect to inversion about its inflection point, for which $E = E_0$.

However, application of the hole model to a non-symmetric barrier distribution function would lead to a reaction probability curve that is 'non-symmetric' with respect to the inflection point. Such a curve would not be properly described by the ERF functional form.

The ERF form (Equation 4.2) is symmetric with respect to inversion through its inflection point, increases monotonically and has an upper asymptote at $S = A$. In the literature, people often refer to A, E_0 and W as the saturation parameter, the effective barrier height and the width parameter respectively.

In order to test the degree to which the barrier distribution function $N(E)$ for H_2 + Cu(111) resembles a Gaussian distribution, we have calculated $N(E)$ from the accurate six-dimensional PES [39, 40] by computing the energy distribution of the first-order saddle points (transition states) found in more than 10^7 (r, Z) cuts of the PES, using a small bin width. A modified Newton-Raphson approach as described in Ref. [91] has been used to locate the transition states. The two-dimensional cuts were chosen on a grid in X, Y, $\cos\theta$ and φ: X and Y uniformly cover the surface unit cell, and $\cos\theta$ and φ uniformly range from -1 to 1 and from 0 to 2π, respectively. Note that $N(E)$ is normalized by the total volume of possible configurations.

4.2.4 Reaction Probability Curve Fitting

Previous work in fitting $S(E)$ to experimental dissociative adsorption and associative desorption measurements have used either the ERF or the hyperbolic tangent (TANH) functions. Both are symmetric with respect to inversion about their inflection points [7, 92]. As we will see in Section 4.3.1, the hole model predicts an asymmetric barrier distribution, $N(E)$. We are thus motivated to try sigmoidal fitting functions that are flexible enough to allow for $S(E)$ curves that are not symmetric with respect to inversion about their inflection point. Figure 4.2 displays the asymmetric functions we have tried in comparison to the ERF and TANH functions.

One of these is the generalized logistic function (LGS):

$$S(E) = \frac{A}{\left[1 + \nu \cdot \exp\left(-\frac{E-E_0'}{W'}\right)\right]^{\frac{1}{\nu}}}. \tag{4.3}$$

The $\nu = 1$ special case of the LGS function is the ordinary logistic curve, a function which is symmetric with respect to inversion through its inflection point and can be related to the TANH function:

$$S(E) = \frac{A}{1 + \exp\left(-\frac{E-E_0'}{W'}\right)} = \frac{A}{2} \cdot \left[1 + \tanh\left(\frac{E-E_0'}{2W'}\right)\right]. \tag{4.4}$$

Another special case of the LGS function is obtained for $\nu \to 0^+$; this limit corresponds to the Gompertz function (GMP), a sigmoid curve which approaches the upper asymptote more gradually than the lower one (and is therefore 'non-symmetric' with respect to the inflection point):

$$S(E) = A \cdot \exp\left[-\exp\left(-\frac{E-E_0'}{W'}\right)\right]. \tag{4.5}$$

Note that for the LGS function the value of W' itself is not strictly related to the 'broadening' of the curve; the width of the curve also depends on the value of ν. This is illustrated by Figure 4.2B, which includes curves with different values of ν but the same W' and E_0' value: all the curves have similar widths above the inflection point, but the TANH curve is significantly broader than the GMP curve below the inflection point. The broadening of the different curves can be compared through a parameter defining the broadening of a curve in an absolute sense. We define the parameter W with the same physical meaning as the width parameter of the ERF form, i.e. half of the additional collision energy necessary to raise the reaction probability from $S(E_0 - W)$ to $S(E_0 + W)$:

$$W = \frac{1}{2} \cdot \left[S^{-1}\left(\frac{A}{2}\left[1 + \mathrm{erf}(1)\right]\right) - S^{-1}\left(\frac{A}{2}\left[1 + \mathrm{erf}(-1)\right]\right)\right]. \tag{4.6}$$

Additionally, W_1 and W_2 are defined as the parameters that allow us to distinguish between the broadening of the low energy portion and the high energy portion:

$$W_1 = E_0' - S^{-1}\left(\frac{A}{2}\left[1 + \mathrm{erf}(-1)\right]\right), \tag{4.7a}$$

$$W_2 = S^{-1}\left(\frac{A}{2}\left[1 + \mathrm{erf}(1)\right]\right) - E_0'. \tag{4.7b}$$

A function with a larger number of parameters, which is therefore more flexible, arises from the product of the GMP and the TANH. We refer to this function, which contains five parameters, as the five parameter curve (FPC):

$$S(E) = A \cdot \frac{\exp\left[-\exp\left(-\frac{E-E_0'}{W'}\right)\right]}{1 + \exp\left(-\frac{E-E_0''}{W''}\right)}. \tag{4.8}$$

The values that a specific parameter assumes if the same functional form is fitted to various sets of data can give indications about general trends. However, we use parameters with a physical meaning for comparisons independent on the functional form employed in the fitting. For all the investigated functions, we define the effective barrier height E_0 using the physical meaning that this parameter has for the ERF form (Equation 4.2), i.e. the energy at which the reaction probability first reaches half the saturation value of the reaction probability curve: $E_0 = S^{-1}(A/2)$. Note that according to the current definition of E_0, the effective barrier height for a certain initial state is the energy larger than 50% of the dynamical barriers, i.e. the median of the dynamical barrier distribution. The dynamical barrier distribution can differ significantly from the barrier distribution function $N(E)$ described in Section 4.2.3, since the former also includes dynamical effects that are specific for each rovibrational state while the latter is a ‘static’ property of the PES. In a similar way, E_0, the effective barrier height, has a different meaning from E_b, the static minimum energy barrier: the former is the median of the dynamical barrier distribution, while the latter is the minimum energy required to react on a specific PES within a classical approximation, and represents the onset of the barrier distribution function $N(E)$.

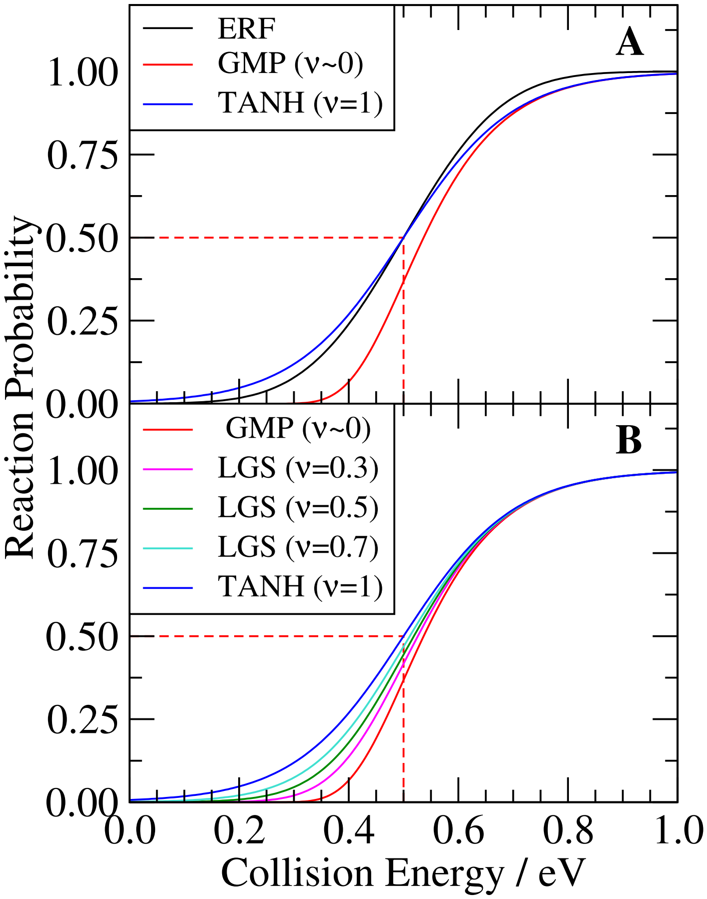

Figure 4.2: Illustrative representation of the various functions used to model the reaction probability curves. (A): the error function (ERF, black, $E_0 = 0.5$ eV, $A = 1$, $W = 0.2$ eV) is compared to the two limiting cases of the logistic function ($E_0' = 0.5$ eV, $A = 1$, $W' = 0.1$ eV), which are the hyperbolic tangent (TANH, blue, obtained for $\nu = 1$) and the Gompertz function (GMP, red, obtained for $\nu \to 0^+$). (B): the same TANH and GMP functions as in panel A are plotted together with logistic functions obtained with $E_0' = 0.5$ eV, $A = 1$, $W' = 0.1$ eV and intermediate values of ν.

4.2.5 Time of Flight (TOF) Spectra Analysis

In the present work, we perform a re-analysis of the raw data from Ref. [13] (a description of the experimental apparatus can be found there). D_2 molecules desorbing from a single crystal surface were detected via laser ionization. The experimental conditions were such that the flight time t' of the ions from the laser to the detector was dominated by the flight time t in a field-free region.

According to the principle of detailed balance, the recorded TOF spectra can be related to the initial-state-selected reaction probabilities. In particular, the TOF intensity at the field-free flight time t is given by a flux-weighted velocity distribution (expressed in the time domain) multiplied by the reaction probability S and divided by the velocity $v = x/t$, to account for the fact that the detection method used (REMPI) yields a signal that is proportional to the density in the probe volume:

$$I\left(t, \theta, \varphi\right) \sin\theta d\theta d\varphi dt = K \cdot \exp\left(-\frac{m(x/t)^2}{2k_b T_s}\right) \left(\frac{x}{t}\right)^4 S\left(E_n\right) \cos^2\theta \sin\theta d\theta d\varphi dt. \qquad (4.9)$$

Here K is a proportionality constant, m is the mass of the D_2 molecule, k_b is the Boltzmann constant, T_s is the surface temperature, θ and φ identify the polar and the azimuthal desorption angles, respectively, and x is the distance flown by the molecules in the field-free region. We assume normal energy scaling, therefore $S = S(E_n)$, E_n being the energy associated with motion of the molecules normal to the surface: $E_n = mv^2 \cos^2\theta/2$. Equation 4.9 is slightly different from the TOF intensity expression originally used (Equation 4.2 of Ref. [13]). Here we take into account that molecules traveling along a linear path that makes an angle θ with the surface normal have flight lengths x that depend on θ, i.e. $x = L/\cos\theta$, where L is the length of the field-free region. In contrast, $x = L$ was originally assumed; in Equation 4.9 the $\cos^2\theta$ factor, in place of the originally used $\cos\theta$, also comes from the variation in x with θ.

The experimental apparatus, schematically represented in Figure 4.3, dictated some geometrical constraints on the desorbed molecules reaching the detector and contributing to the signal. We can assume that the laser was focused along a short line, whose length

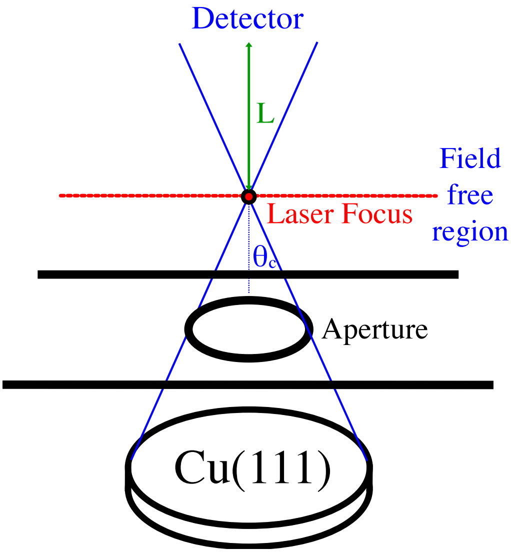

Figure 4.3: Schematic representation of the experimental apparatus.

was determined by the laser optics. In the limit of a point detector, only the molecules in a cone with the crystal as base and the crystal-detector distance as height were ionized. To account for this, we have to integrate Equation 4.9 over a solid angle with the same aperture as the cone just described, estimated to be approximately 40° from the experimental setup. This integration is performed over the azimuthal and the polar coordinates φ and θ, from 0 to 2π and from 0 to θ_c, respectively, θ_c being half the aperture of the cone ($\theta_c = 20°$). We also analyzed some representative TOF spectra assuming that the detector is focused to a line segment parallel to the surface. Under this assumption, the molecules contributing to the signal were the ones for which a straight path from the surface to the line segment and through the aperture located between them was available. However, results obtained assuming a line detector with length up to 9.4 mm are not considerably different from the ones obtained under the assumption of a point detector (fitted E_0' and W' values differ by less than 15 meV). For this reason, we have considered the point detector approximation as valid for the rest of the analysis.

The observed total flight time t' has to be corrected [13] by subtracting from it $t_{corr} = 1.79$ μs, which is the time the ions flew after leaving the field-free region, in order to obtain the field-free flight time t. The low energy ions were deflected more easily than the high energy ones, resulting in a distortion of the spectra which can be reproduced by multiplying Equation 4.9 by the following 'cut-off' function [13]: $f(t') = 1 - \tanh\left[(t' - t_c)/t_w\right]$, with $t_c = 19.5$ μs and $t_w = 6.6$ μs. The final expression obtained for the TOF signal at the observed time t' corresponding to the field-free flight time t is the following:

$$I(t')\,dt' = K' \int_{\varphi=0}^{2\pi} d\varphi \int_{\theta=0}^{\theta_c} I(t,\theta,\varphi)\sin\theta d\theta \left[1 - \tanh\left(\frac{t'-t_c}{t_w}\right)\right] dt'. \tag{4.10}$$

Here $t' = t + t_{corr}$. The calibration procedure, which was originally performed without angular averaging, has been repeated using the new expression of the TOF intensity (which includes the integration over the solid angle). This calibration returned a length L of the field-free region of 23.7 mm, as compared to the earlier estimated value of 24 mm.

Equation 4.10 has been fitted to experimental TOF spectra in order to extract the D_2 reaction probabilities $S(E_n)$ (note that the dependence on $S(E_n)$ is in the term $I(t,\theta,\varphi)$, see also Equation 4.9). Note that a thermal (300 K) background has been subtracted from some of the measured spectra [13]. The Levenberg-Marquardt algorithm [93,94], as implemented in the MINPACK library [95,96], has been employed in order to minimize the sum of the squared residuals. Spectra have been fitted over the range of times for which the signal is $\geq 5\%$ of the maximum signal. The goodness of the fits has been evaluated on the basis of the value of χ^2, the sum of the squared residuals. Error bars in the fitted parameters represent 68.3% confidence intervals and have been estimated from replicate measurements.

For further analysis, we have also extracted reaction probabilities directly from the TOF spectra, using the following expression:

$$S(E_n) = \frac{K \cdot I(t')\,dt'}{\int_{\theta=0}^{\theta_c} \exp\left(-\frac{m(x/t)^2}{2k_bT_s}\right)\left(\frac{x}{t}\right)^4 \cos^2\theta \sin\theta d\theta dt'}. \tag{4.11}$$

In practice, the TOF intensity is divided by a 'θ-averaged' velocity distribution. Equation 4.11 is therefore valid only if normal energy scaling is assumed, under which condition $S(E_n)$ is not a function of the θ angle and can be extracted from the integral in Equation 4.10. The comparison between fitted reaction probability curves and curves extracted from the TOF spectra using Equation 4.11 is a test of the ability of modeling $S(E_n)$ using the functional form employed in the fits.

Note that only the shape of $S(E_n)$ can be extracted from the fits of the absolute TOF spectra intensities, as no information about the saturation values (relative or absolute) of the reaction probability curves is contained in the absolute TOF signal by itself. To determine relative saturation values, it is necessary to compare the desorption intensities to intensities recorded from a Knudsen source. Absolute saturation values can only be obtained by comparing the fitted curves to adsorption data.

4.2.6 Determination of the Relative Saturation Values

In order to determine the relative saturation values of the various reaction probability curves we have to compare the vibrational populations computed from the initial-state-selected reaction probabilities, assuming unit saturation values, with the measured vibrational populations [13]. The latter can be determined by comparing the measured state-selected signals (integrated TOF intensities) to the intensities recorded from a Knudsen source. The former are computed by summing the rotational state populations corresponding to the same vibrational level; the rotational state population can be related to the initial-state-selected reaction probability $S_{v,J}$ in the following way [13]:

$$P(v,J) \propto F_{v,J}\left(T_s\right)\int_{E=0}^{\infty} dE \int_{\theta=0}^{\theta_c} \sqrt{E}\exp\left(-\frac{E}{k_b T_s}\right) S_{v,J}\left(E_n\right)\cos\theta\sin\theta d\theta, \qquad (4.12)$$

where $F_{v,J} = N\cdot(2J+1)\cdot d^J_{o-p}\cdot\exp\left(-\frac{E(v,J)}{k_b T_s}\right)$ is the Boltzmann factor corresponding to the (v,J) state, in which $E(v,J)$ is the internal energy of the state, N is a normalization constant and d^J_{o-p} is a factor which accounts for the ortho-para population ratio of D_2.

4.2.7 Determination of absolute saturation values

The sticking probabilities, which were measured directly by adsorption of molecules incident on the surface from a seeded supersonic molecular beam source, can be related to the initial-state-selected reaction probabilities determined by the application of detailed balance to desorption data through the following equation [11, 13]:

$$S_0\left(v_s,\alpha,T_n,\Theta\right)=\sum_{v,J}F_{v,J}\left(T_n\right)\int_{E=0}^{\infty}S_{v,J}\left(E_n\right)f\left(v_s,\alpha,E\right)dE+S_{atoms}. \tag{4.13}$$

Here T_n is the nozzle temperature, S_{atoms} is the contribution to the sticking probability from D atoms in the beam (estimated from the stagnation pressure and nozzle temperature, assuming unity sticking probability for the atoms [11]) and $f(v_s,\alpha,E)$ is the velocity distribution of the molecules in the beam, characterized by the experimentalists and expressed as a function of the stream velocity (v_s) and a width parameter (α) [7].

In order to determine the absolute saturation values of the reaction probability curves obtained from the desorption experiments, Equation 4.13 has been least-squares fitted to adsorption data [11]. The relative saturation values among states have been kept fixed. Because the sticking probability values range over different orders of magnitude, we have performed the fit in two stages. First, the function $R_{\log}=\log(S_0^{exp})-\log(S_0^{fit})$ has been employed as residual function. In order to account for the different surface temperature between adsorption and desorption experiments, the absolute values of the width parameters W' characterizing the initial-state-selected reaction curves were allowed to vary, but the relative values of W' were constrained to the ratios determined from the desorption data. In the second stage of the fit, in order to make the fit more sensitive to the saturation values, another residual function has been minimized, keeping the W' parameters (and therefore the 'shape') of the reaction probability curves fixed to the values determined in the first stage: $R=S_0^{exp}-S_0^{fit}$.

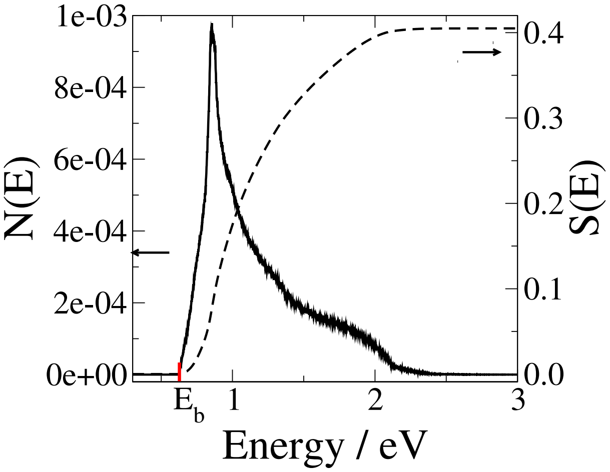

Figure 4.4: Barrier distribution function $N(E)$ computed from the PES of Ref. [39, 40] (solid line) and sticking probability $S(E)$ evaluated according to the hole model (dashed line). Note that the minimum energy barrier ($E_b = 0.628$ eV) has been marked in red on the energy axis.

4.2.8 Average Desorption Energy

The average desorption energy has been computed from the initial-state-selected reaction probabilities using the following expression [7]:

$$\langle E_{trans} \rangle = \frac{\sum\limits_{v,J} F_{v,J}\left(T_s\right) \int_{E=0}^{\infty} E^2 \exp\left(-\frac{E}{T_s}\right) S_{v,J}\left(E_n\right) dE}{\sum\limits_{v,J} F_{v,J}\left(T_s\right) \int_{E=0}^{\infty} E \exp\left(-\frac{E}{T_s}\right) S_{v,J}\left(E_n\right) dE}. \quad (4.14)$$

4.3 Results and Discussion

4.3.1 Hole Model Results

The barrier distribution function $N(E)$ computed from the SRP-DFT PES is plotted in Figure 4.4. Note that the onset of $N(E)$ is, as expected, at $E_b = 0.628$ eV, the minimum energy barrier in the PES. The distribution presents a broad high-energy tail and is therefore non-symmetric. Consequently, the sticking probability $S(E)$ estimated according to the hole model (Figure 4.4) is also non-symmetric and would not be expected to be fitted accurately by the ERF expression.

4.3.2 Fits to BOSS and AIMD Reaction Probabilities

BOSS initial-state-selected reaction probabilities, computed from the same PES for which the barrier distribution has been evaluated, have been fitted using the ERF, the LGS and the FPC expression. Results of the fitting for some representative initial states are shown in Figure 4.A.1. Table 4.A.2 contains the parameters obtained from these fits. The best fits (as based on χ^2 values) are obtained using the flexible FPC expression, since it contains the largest number of parameters (see Table 4.A.2). The LGS generally produces good quality fits. We observe a ν parameter which is close to zero for all the examined states, which means that the non-symmetric (GMP) form of the LGS expression better fits the BOSS data than the symmetric (TANH) limit of the LGS form. Note that both the FPC expression and the LGS expressions perform better than the ERF expression in fitting the data. The fact that non-symmetric functions effectively produce better fits of the BOSS reaction probabilities, in addition to the shape of the barrier distribution function calculated from the PES, suggests that non-symmetric functions might in general yield a better description of experimental reaction probabilities as well.

AIMD initial-state-selected reaction probabilities have also been fitted using both the ERF and the LGS expressions. Fitted curves are plotted in Figure 4.A.2, and the corresponding parameters are included in Table 4.A.3. Due to the higher computational cost of AIMD, we were able to investigate fewer collision energies (5) than what has been done with the BOSS model (20). As a consequence, the scatter is larger and we observe larger variability in the shape of the fitting functions across states. For the $(v = 0, J = 4)$ initial state, we investigated one additional collision energy compared to the other initial states. The ERF and LGS fits of the 5 lower collision energy points for this initial state were almost superimposed (see dashed lines in Figure 4.A.2, $(v = 0, J = 4)$). In order to check whether this result was a statistical fluke, we included a sixth high collision energy to the set of data. The inclusion of this collision energy confirmed that this was indeed the case, since the LGS and ERF fits are now considerably different. Considering all the investigated initial states, the LGS form produces better fits than the ERF form for the AIMD data, as is the case for the BOSS results. Due to the lower number of AIMD reaction probability points compared to the BOSS results, we consider the AIMD results reliable only in the range of collision energies for which we have data. Having said that, the LGS fits of the AIMD reaction probabilities look somewhat broader than the LGS fits of the BOSS data (see Figure 4.5). The AIMD reaction probabilities are generally larger than the BOSS ones close to the threshold. The noise in the AIMD fits can be reduced by removing one fitted parameter; for instance, we can constrain the saturation values of the AIMD fits to the corresponding values from the BOSS fits. In most cases the AIMD curves remain slightly broader than the BOSS ones (except for $v = 0, J = 4$) and are slightly shifted to lower energies (see Figure 4.A.3), which is consistent with observed effects of surface temperature [21, 44]. However, the broadening observed when going from the BOSS (ideal, frozen lattice) to the AIMD ($T_s = 925$ K) reaction probability curves, is much smaller than the broadening observed experimentally [21].

4.3.3 Fits of measured TOF spectra

The measured TOF spectra have been fitted modeling the reaction probability curves with the ERF and the LGS expressions. Better fits of the experimental spectra are obtained if the LGS is employed, even though reasonable fits are obtained using both functions (see Figure 4.6, and Table 4.A.4 for the corresponding fitting parameters). Especially for the $v = 0$ rotational states, lower χ^2 values are obtained with the LGS fits. We also tested the use of the FPC form in the fits, but this function turned out to pair lack of stability to its higher flexibility in some cases and to give results not considerably different from the LGS ones in other cases. The relative quality of the fits performed with the symmetric ERF expression increases with increasing vibrational quantum number v, but the LGS fits are better in all cases, even for ($v = 2, J = 2$) where $\nu = 1.0$, meaning that the symmetric TANH expression is used (Equation 4.4).

The values of the E_0 parameter obtained from the ERF fits of the TOF spectra using Equation 4.10 are slightly larger than the values obtained previously. This is clearly visible in Figure 4.7, where the E_0 values from the new ERF fits are compared

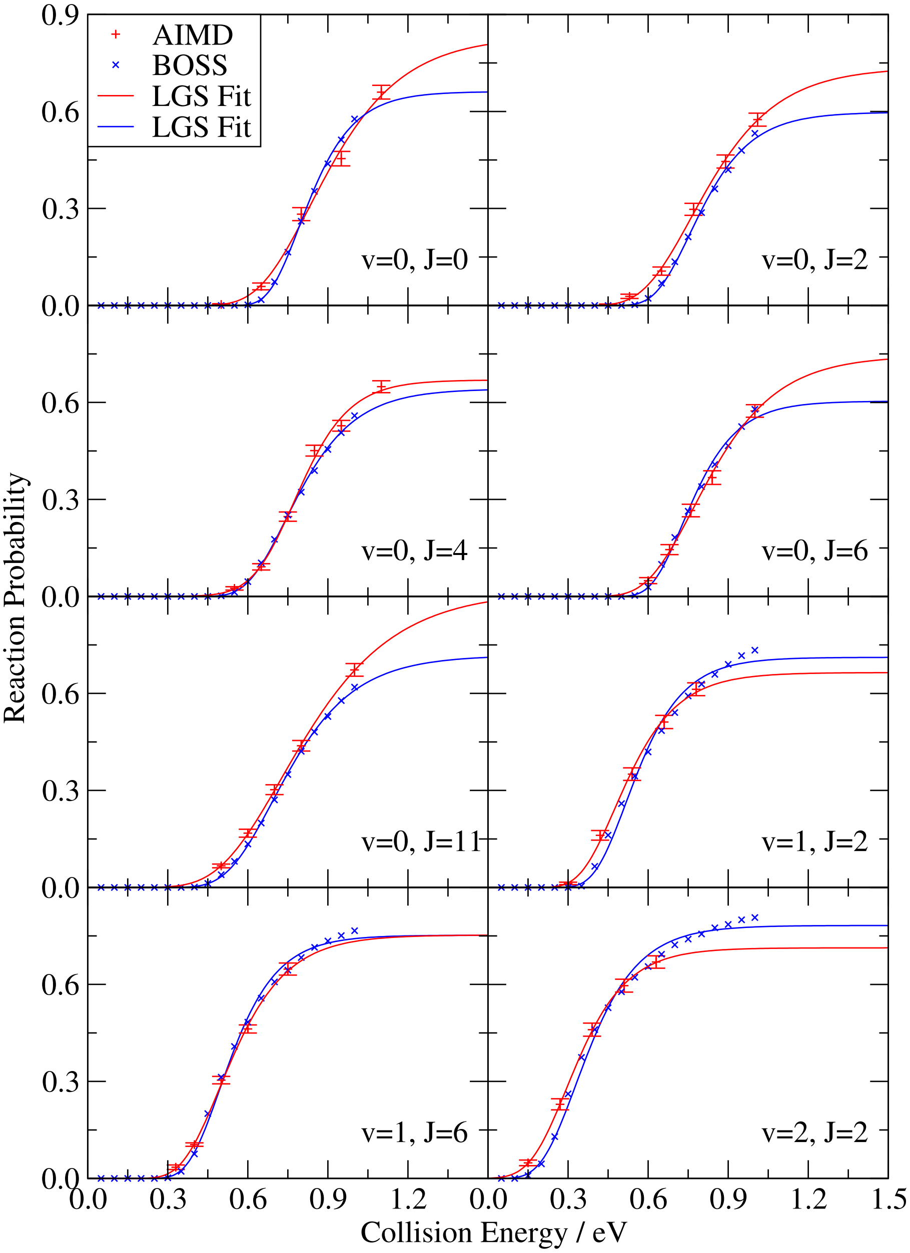

Figure 4.5: BOSS and AIMD reaction probabilities (blue × and red +, respectively) are plotted as a function of the collision energy for some representative initial states; the solid lines represent LGS fits of the probabilities.

to the earlier values [13]. This is due to the fact that our new TOF expression takes into account the longer flight paths of molecules traveling at non-zero angle from the surface normal. The fitted W parameters, on the other hand, do not change significantly if the new expression of the TOF signal is employed (see Figure 4.A.4). If the LGS is employed in the fits, the same trend in E'_0 is observed as for the ERF form in E_0: E'_0 first increases with J (up to $J = 4 - 5$) and then decreases (see Figure 4.A.5 A).

The shape of the fitted reaction probability curve depends on the vibrational state. The LGS form that fits the experimental data best is close to a GMP function (ν parameter close to 0) for low v but ν increases with v until the LGS form takes on the hyperbolic tangent form (a symmetric function, the LGS form with $\nu = 1$) for $v = 2$ (Figure 4.A.5 C). This suggests that dynamical effects lead molecules in high vibrational states to sample a distribution of effective barrier heights which is more symmetric than the distribution which appears to govern the reaction of D_2 in the lowest vibrational state.

In order to compare the widths of the $v = 0, 1$ and 2 LGS curves, we also calculated the W,W_1 and W_2 parameters for the fitted curves (see Section 4.2.4, Equations 4.6, 4.7a and 4.7b respectively). The width parameter W computed for the $v = 0$ reaction probability curves is significantly larger than the values computed for $v = 1$ and $v = 2$, meaning that the $v = 0$ probability curves are broader than the $v = 1, 2$ curves (see Figure 4.A.6). In particular, the broadening of the high energy portion of the reaction probability curves differs substantially across states, while we observe that the LGS fits are very similar, independently from v, in the broadening of the low energy portion: in fact, W_1 does not vary much with v. The observation that the W_2 values are closer to the W_1 values for $v = 2$ than for $v = 0$ is consistent with the fit function being more symmetric for $v = 2$.

4.3.4 Experimental Reaction Probability Curves

Representative ERF and LGS reaction probability curves fitted to TOF spectra using Equation 4.10 are compared to the curves directly extracted from the TOF spectra us-

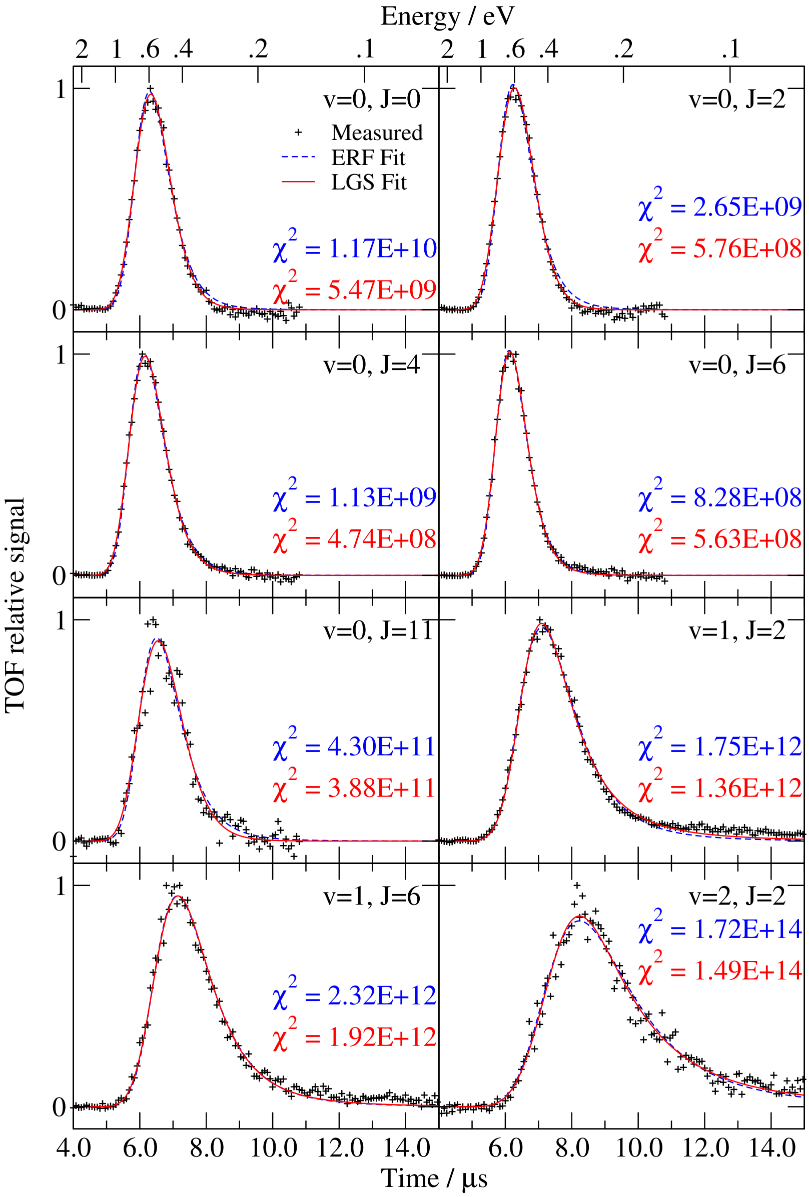

Figure 4.6: TOF intensities (black symbols) are plotted as a function of the detection time for some representative sets of data; dashed blue (solid red) lines correspond to TOF fits in which the ERF (LGS) form has been used to model the reaction probability curve. The sum of the squared residuals χ^2 is also reported for each fitted curve (in blue and red for ERF form and LGS form fit, respectively).

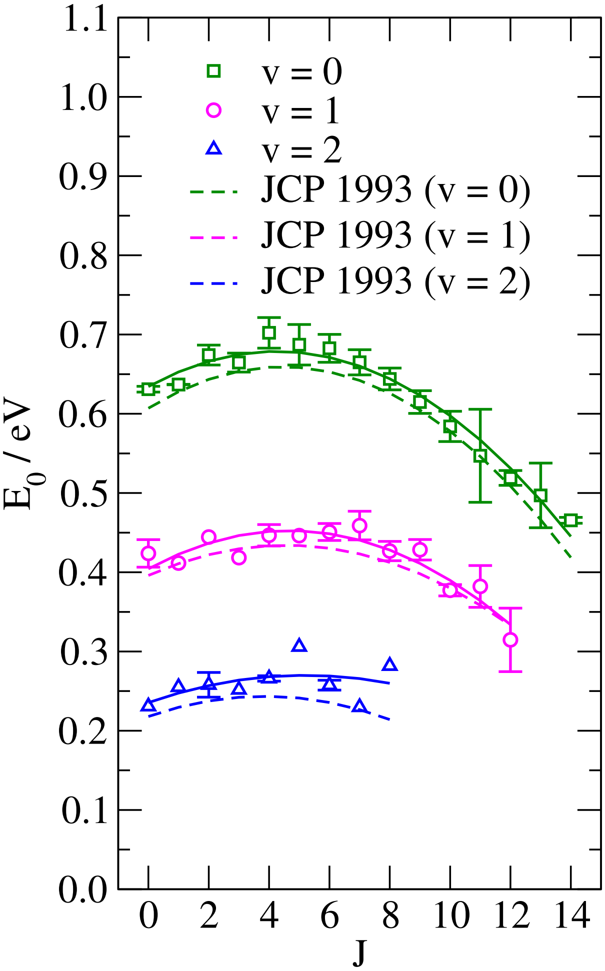

Figure 4.7: E_0 parameters obtained from ERF fits of all the available desorption TOF spectra are plotted as a function of the initial rotational state J. Green, violet and blue symbols correspond to $v = 0, 1$ and 2 initial vibrational states, respectively. Solid curves in the plot represent quadratic fits of the $v = 0, 1, 2$ data, while dashed lines are quadratic fits of the data using the method of Ref. [13]. Line colors are as for the symbols.

ing Equation 4.11 in Figure 4.8. Fitted ERF and LGS curves for the same state are in general very similar at low energies. However, the $v = 0$ LGS curves are characterized by saturation values significantly larger than the ERF ones. This is not the case for $v = 1$ and $v = 2$, where LGS and ERF fitted curves are quite similar over the whole energy range. Compared to the reaction probabilities directly extracted from the TOF spectra, the ERF fits generally underestimate the saturation values for $(v = 0, J)$ states, especially for the cases where the A values obtained with the LGS and ERF forms differ widely. Overall, the LGS seems to better describe the directly extracted reaction probabilities at high collision energies, even though it overestimates the reaction probability somewhat at high collision energies in a few cases ($v = 0, J = 2$ and $J = 6$ in the figure). The above observations are consistent with the finding that LGS fits of the experimental TOF spectra are clearly more accurate than ERF fits for $v = 0$, whereas the accuracy is more similar for $v = 1$ and $v = 2$ (see Figure 4.6). Given the fact that the main differences between ERF form and LGS form fits are observed at high energies, the transmission of the apparatus and the background subtraction procedure are unlikely to have influence on the fits. In fact, the transmission is close to one for most of the energies and small deviations are only expected at long times (low energies). Similarly, the subtraction of a thermal background might affect the reaction probabilities, but only at low energies, where the ERF and LGS forms are very similar [13].

The reaction probability curves obtained from the fits of the desorption data have been used to compute rotational populations via Equation 4.12, assuming a unit saturation value for all the curves. Next, vibrational populations have been computed by summing over the rotational populations corresponding to the same vibrational level. The ratio between the measured vibrational populations ($P(v = 1)/P(v = 0) = 0.25 \pm 0.07$ and $P(v = 2)/P(v = 0) = 0.015 \pm 0.004$) [13] and the ones computed in the just described way allows us to determine the relative saturation values of the initial-state-selected probability curves: $A(v = 0) : A(v = 1) : A(v = 2) = 0.96 : 1 : 0.81$. The relative saturation values are much closer to each other than the values previously obtained using ERF fits ($A(v = 0) : A(v = 1) : A(v = 2) = 0.54 : 1 : 0.77$) [13]. As in the

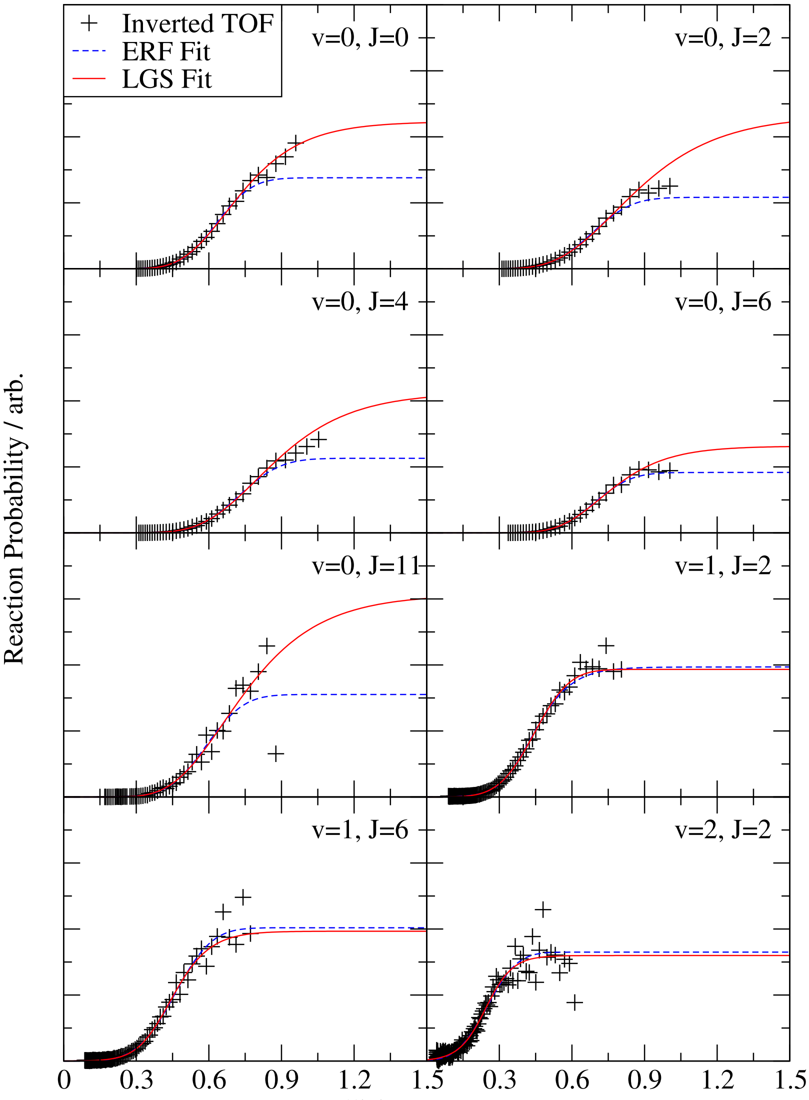

Figure 4.8: Reaction probability curves obtained from the fit of some representative TOF spectra are plotted as a function of the collision energy. Dashed blue (solid red) lines correspond to ERF (LGS) fits. Reaction probabilities directly extracted from the spectra are plotted as black symbols.

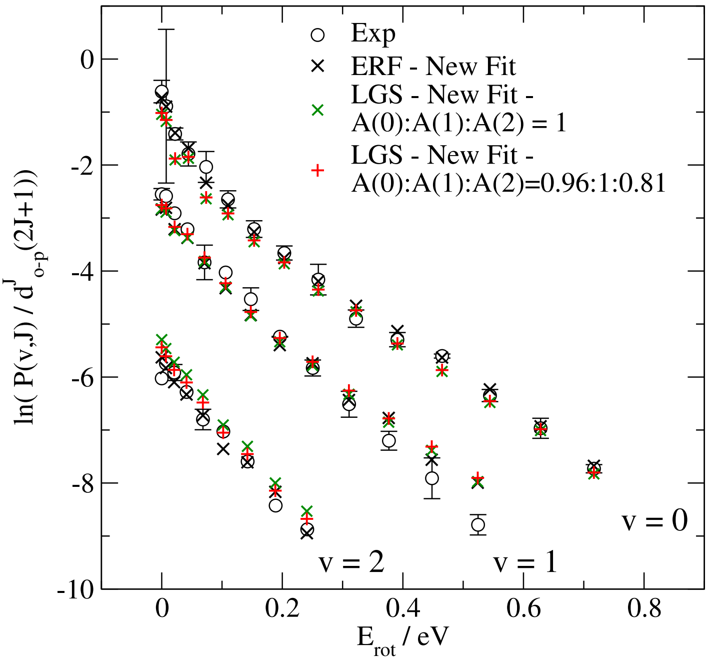

Figure 4.9: The measured rotational distribution (empty circles) is compared to the distribution computed from newly fitted reaction probability curves assuming the relative saturation values being 0.96:1:0.81 for $v = 0, 1$ and 2 (red +) and assuming the same saturation value across vibrational states (green ×). The rotational distribution computed from the newly fitted ERF-form reaction probability curves is plotted with black ×.

original analysis, we consider A to be independent of the rotational state: the measured rotational populations, plotted in Figure 4.9, are qualitatively reproduced under this assumption ($\chi^2 = 3.391$, close to the χ^2 value obtained using the original ERF fits: $\chi^2 = 3.193$). It is worth noting that even if the same saturation value is assumed for the three vibrational states ($A(v = 0) : A(v = 1) : A(v = 2) = 1 : 1 : 1$) we obtain population ratios that still agree with the measured populations within their error bars ($P(v = 1)/P(v = 0) = 0.239$ and $P(v = 2)/P(v = 0) = 0.0178$), and the rotational distribution remains reasonably well described ($\chi^2 = 4.197$, see Figure 4.9). Furthermore, the fact that similar saturation values are obtained for the different vibrational states is consistent with theory: the saturation values of the probability curves fitted to the BOSS and AIMD data do not differ considerably across states, if the same functional form is used (see Figures 4.A.1 and 4.A.2 and Tables 4.A.2 and 4.A.3).

Absolute saturation values of the reaction probability curves have been obtained by fitting the sticking probabilities obtained from adsorption experiments using the expression in Equation 4.13 while optimizing the A parameters and adjusting the W' parameters characterizing the initial state-selected reaction probability curves (see Section 4.2.7). The sticking probabilities measured with molecular beam experiments and the results of the fit are plotted in Figure 4.10. Overall, the sticking probability is reasonably well described using the LGS fitted curves. In particular, the sticking probability curve measured with seeded beams at the highest nozzle temperature (2100 K) is much better described in the high energy range than was achieved previously with the ERF fits, suggesting that our new A value for $v = 0$ is much more accurate than the old one (this is clearest if the measured sticking probabilities are plotted together with the fitted curves on a linear scale, see Figure 4.A.7). Absolute values of 0.47, 0.49 and 0.40 are obtained as saturation values for the $v = 0, 1$ and 2 probability curves, respectively, the earlier values being 0.27, 0.50, and 0.38 [15], respectively. The width parameters of the reaction probability curves obtained for the surface temperature at which the adsorption experiments were performed (120 K), are about 70% of the 925 K values. A similar decrease in the width parameter was observed in the original fits [13].

In Figure 4.11 the LGS reaction probability curves extracted from experiments are compared on an absolute scale to the theoretical results (BOSS model and AIMD). Overall, the theoretical curves are closer to experimental data in the onset of the reaction probability curves, compared to the previously fitted experimental curves (see also Figure 4.1). Furthermore, the experimental saturation values of the $v = 0$ probability curves (0.47) is significantly larger than the earlier value (0.27 [15]), resulting in better agreement with the theoretical results.

Unfortunately, the discrepancies between theory and experiment are not yet fully resolved: at high collision energies, theory still gives larger values for the reaction probability than does our reanalysis of the experimental raw data. Moreover, the effect that surface temperature has on the broadening of the reaction probability curves is much smaller for theory than for experiments: the AIMD ($T_s = 925$ K) curves are only slightly

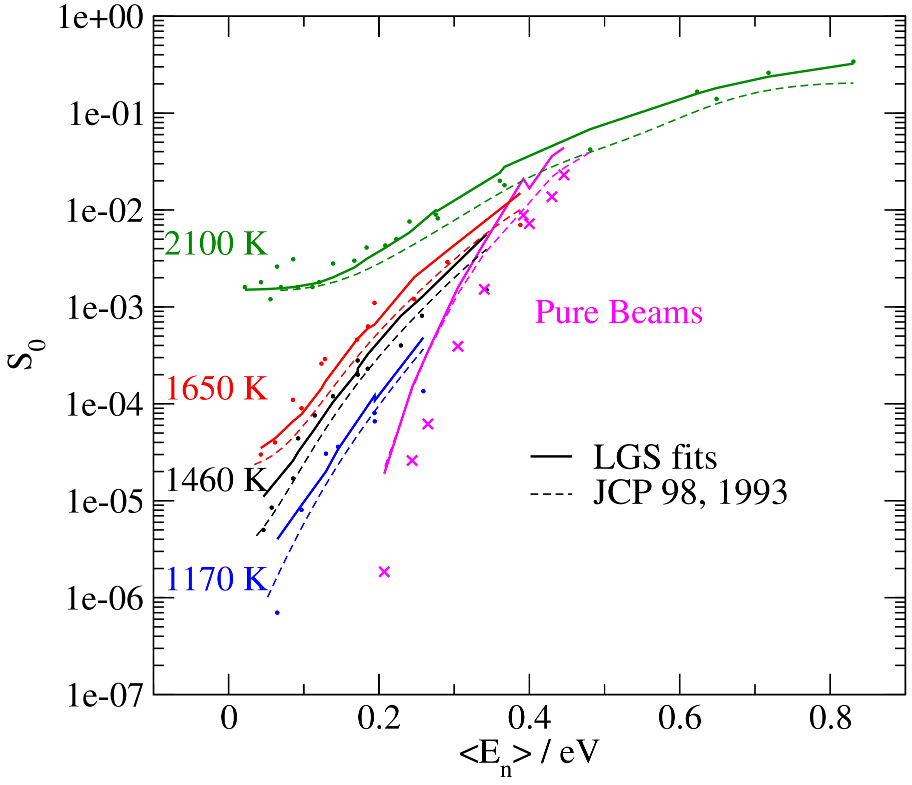

Figure 4.10: The sticking probability measured in molecular beam experiments is shown as a function of the average collision energy using a logarithmic scale. Seeded beam results corresponding to specific nozzle temperatures are plotted as circles, pure beam results using crosses. The results of our fits are plotted as solid lines. Dashed lines are from the previous fit (Ref. [13]).

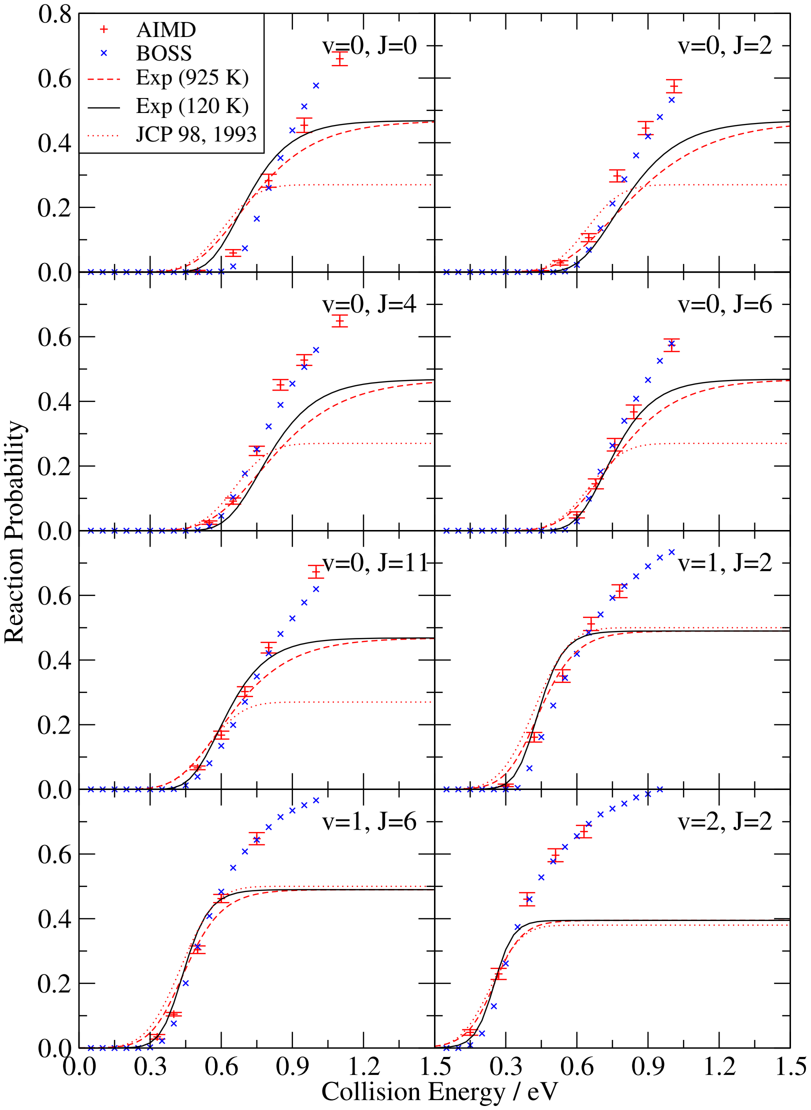

Figure 4.11: Experimental reaction probability curves for a surface temperature of 925 K (dashed red curve) and 120 K (solid black curve) are compared to theoretical data: BOSS (blue ×) and AIMD (red +). The reaction probability curves from Ref. [13] are plotted as red dotted curves for comparison.

broader than the BOSS ones (frozen ideal surface), in contrast with the large difference in width between the 120 K and 925 K experimental curves. The broadening we observe in theory is also much smaller than observed by Murphy and Hodgson, who studied the dependence of the reactivity on surface temperature [21]. The authors of this study also observed a surface temperature dependent low energy tail in the reaction probability curves which can not be described as a broadening effect. However, the AIMD method is not expected to be accurate at these collision energies, where S_0 is as low as 10^{-4}, given that a very large number of trajectories would be needed in order to provide statistically significant results (small error bars).

4.3.5 Simulated TOF Spectra

In Figure 4.12 A-C, TOF spectra simulated from the interpolated theoretical reaction probabilities are compared to experimental spectra for three representative states ($v = 0, 1, 2, J = 2$). The comparison between theory and experiment in the time domain highlights differences in the 'shape' of the reaction probability curves, without carrying any information on the saturation values. The theoretical spectra are generally too narrow compared to the experimental ones, and they peak at too short times. The AIMD spectra are broader than the BOSS ones, and therefore in closer agreement with experiments. Spectra much more similar to the experimental TOF are obtained from the theoretical models if the reaction probability curves are allowed to rigidly shift in energy (Figure 4.12 D-F, where the amount by which each reaction probability curve had to be shifted in order to best fit the corresponding experimental spectrum is presented is also reported). Note that the experimental TOF spectra are characterized by a sparser sampling of the high energies (short times) compared to the low energies (long times), as data have been measured at constant time intervals. Therefore, the fit of the theoretical data to the experimental spectra in the time domain is particularly sensitive to the low energy part of the reaction probability curves. In line with the better initial agreement with the experimental data, the shift required by AIMD to reproduce experimental data is smaller than for the BOSS model.

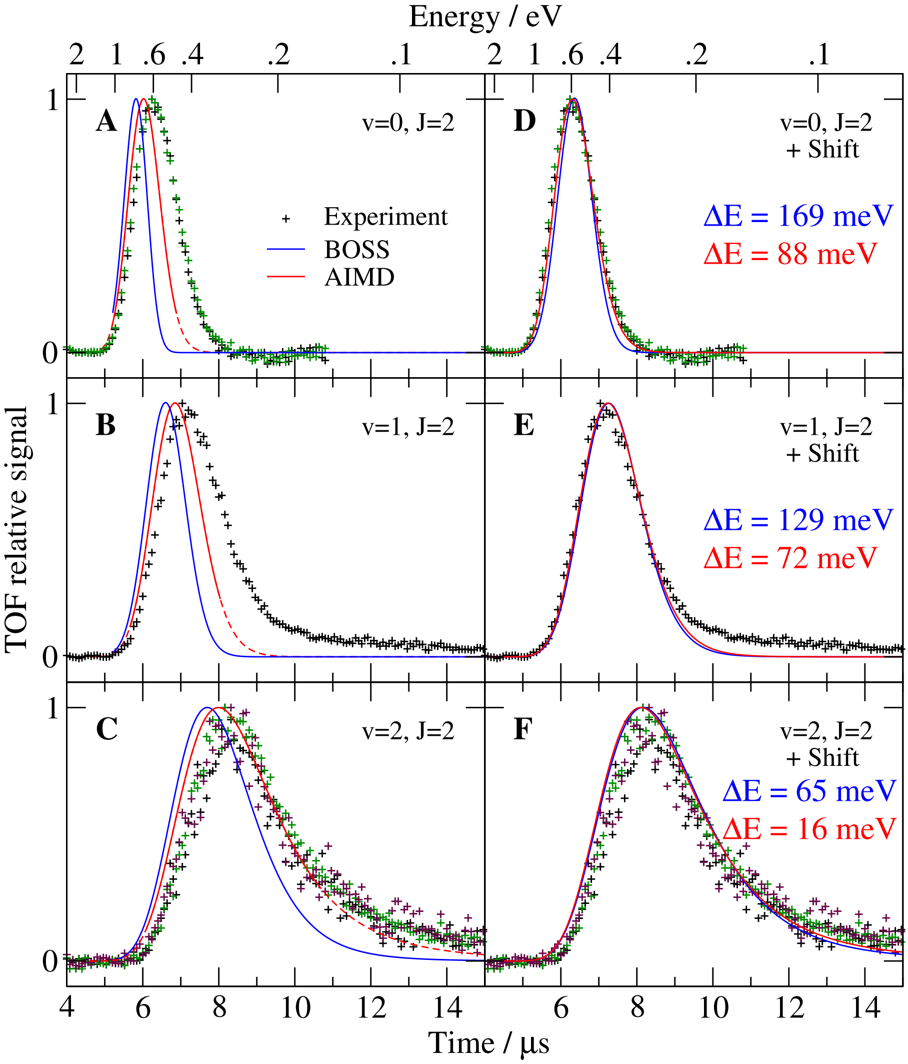

Figure 4.12: (A-C): TOF spectra calculated from theoretical reaction probabilities are plotted together with experimental data (symbols, different colors are used for different sets of measurements). Blue lines describe BOSS results, red lines AIMD results (solid lines indicate the time ranges which correspond to energies for which reaction probability points are available). (D-F): Simulated TOF spectra in which the reaction probability curves were free to shift along the energy axis in order to best fit the experimental data. The energy shifts ΔE (meV) applied to the theoretical reaction probability curves are reported (blue for BOSS and red for AIMD).

Model	Experiment	MAE (kcal/mol) (only $v = 0, 1$)	MAE (kcal/mol) ($v = 0, 1, 2$)
BOSS	Ref. [13]	1.482*	-
BOSS	New Fits	0.765	0.745
AIMD	New Fits	-	0.594

Table 4.1: Mean absolute error (MAE) computed for BOSS and AIMD values of E_0 with respect to the newly fitted experimental E_0. The value marked with (*) is from Ref. [39], where the BOSS results were compared to the previously fitted experimental data.

4.3.6 Experimental and Theoretical Effective Barrier Heights (E_0)

Another way of comparing theory with experiment is by plotting the E_0 value, defined as the collision energy at which the reaction probability equals half the saturation value of the corresponding experimental reaction probability curve. E_0 values extracted from experiments (note that E_0 differs from E_0' for the states characterized by a non-symmetric reaction probability curve), and from BOSS and AIMD calculations are plotted as a function of J in Figure 4.13. Table 4.1 contains the computed mean absolute error (MAE) for BOSS and AIMD, taking as a reference the quadratic fits of the experimental E_0. While single BOSS and AIMD E_0 values deviate from the experimental values by more than 1 kcal/mol, for both theoretical models the MAE is lower than 1 kcal/mol, the limit which defines chemical accuracy. The same level of accuracy is reached if the experimental points are chosen as the reference instead of their quadratic fits. The MAE obtained with the AIMD calculations is somewhat lower than obtained with the BOSS model. Chemical accuracy of the E_0 values could not yet be obtained for D_2 + Cu(111) using the earlier analysis [39, 40] of the experimental results.

4.3.7 Average Desorption Energies

Finally, in Table 4.2 we report desorption translational energies computed according to Equation 4.14 using the newly fitted experimental reaction probability curves. We also computed the average desorption energy for the BOSS model. Since reaction probability curves for a large set of rovibrational states are required in order to estimate this quantity, it has not been possible to evaluate it for the AIMD calculations. Experimental

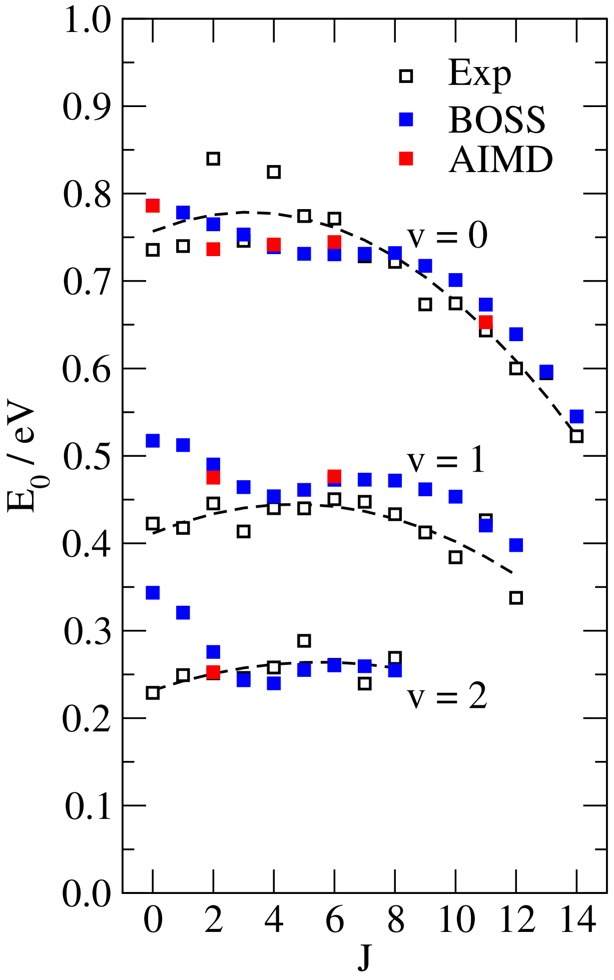

Figure 4.13: Experimental (empty squares) and theoretical (blue and red for BOSS and AIMD, respectively) E_0 values are plotted as a function on J. E_0 values have been estimated from FPC fits of the BOSS data and from LGS fits of the AIMD data. The dashed lines are quadratic fits of the experimental E_0 values, for $v = 0, 1$ and 2 as indicated in the figure.

	$\langle E_{trans} \rangle$
Exp. - Original ERF Fit [13] (T_s = 925 K)	0.559
Exp. - Original ERF Fit [13] (T_s = 925 K, but W from T_s = 120 K)	0.618
Exp. - New LGS Fit (T_s = 925 K)	0.572
Exp. - Comsa&David [64] (T_s = 1000 K)	0.63
Theory - BOSS	0.71

Table 4.2: Experimental and theoretical (BOSS) desorption energies (eV) averaged over D_2 rovibrational states.

desorption energies are now in somewhat better agreement with the value reported by Comsa and David [64]. The value computed from the BOSS reaction probabilities is larger than both experimental values. Experiments, however, were performed at high surface temperature, while a static ideal surface (0 K) characterizes the BOSS calculations. As discussed by Sementa et al. [65], the average desorption energy estimated from reaction probability curves measured at high surface temperature is lower than what would be estimated using low surface temperature reaction probability curves, due to the larger width of the curves at high surface temperature. Specifically, the effect of using the experimental reaction probability curves determined for T_s = 120 K [13] when calculating the average desorption energy at T_s = 925 K, is an increase in the average desorption energy of about 60 meV (see Table 4.2). If we assume that a similar correction might apply to the average desorption energy computed from BOSS data in order to account for surface temperature effects, the agreement of theory (0.71 − 0.06 = 0.65 eV) with the experimental value from Comsa and David [64] (0.63 eV) would be significantly improved.

4.4 Summary and Conclusions

In the present study, the raw associative desorption data from which the experimental initial-state-selected reaction probabilities for D_2 on Cu(111) were extracted [13] have been re-analyzed. In addition, we present new AIMD calculations for this system, in which the reaction probability has been calculated for various initial states simulating the high experimental surface temperature. We also present time-of-flight spectra simulated from theory, which allow a more direct comparison with the raw experimental data.

Results show that the saturation value of the experimental reaction probability curves is strongly influenced by the functional form employed in the fits. This conclusion might apply to other systems, given that in many studies the reaction probability has been modeled with the ERF form (see Section 4.2.3). The use of the LGS expression, which can assume either a symmetric or non-symmetric shape around the inflection point, suggests similar saturation values for $v = 0, 1$ and 2, in contrast to what was observed earlier with the ERF form. Furthermore, a general trend according to which the degree of symmetry of the reaction probability curves increases with vibrational state is observed. This suggests that the barrier distribution dynamically sampled by the reacting molecules does not have the same shape for the three vibrational states, and that the width of the reaction probability curve is significantly smaller for vibrationally excited molecules ($v = 1, 2$) than for molecules in the ground state. The newly fitted reaction probability curves are closer to the theoretical ones in the onset of the curves and in the saturation values.

The use of a time-of-flight intensity expression that takes into account the longer flight of molecules leaving the surface in an off-normal direction results in a systematic shift of about 40 meV of the fitted reaction probability curves towards higher collision energies. This shift is relevant for the assessment of the accuracy of theoretical models, given that the 'target' chemical accuracy is defined as the ability of modeling an experimental observable within a shift of 1 kcal/mol (≈43 meV). The agreement between theory and experiment, evaluated in terms of energy difference between the theoretical and experimental E_0 values, is now significantly improved: the mean absolute error for the BOSS and AIMD models is now 0.745 kcal/mol (about 50% lower than in Ref. [39]) and 0.594 kcal/mol, respectively, which means that both models now achieve a chemically accurate description of E_0.

The AIMD model slightly improves the agreement between theory and experiment: reaction probability curves are slightly broader and slightly shifted to lower energies, compared to previous BOSS calculations. These findings are consistent with surface temperature effects. However, theory predicts less broadening of the reaction probability curve with increasing surface temperature than experiment, where the 925 K reaction probability curves are considerably broader than the 120 K ones. Furthermore, even though a larger saturation value is suggested by our reanalysis of the $v = 0$ and $v = 2$ experimental reaction probability curves, theory still gives larger values than experiment for the reaction probability at high collision energies, for all vibrational states, meaning that discrepancies persist between theoretical models and experiments.

4.A Appendix

This appendix contains the barrier heights and geometries in the SRP-PES for high symmetry impact sites (Table 4.A.1); BOSS and AIMD reaction probability curve fitting results (Table 4.A.2 and 4.A.3 and Figures 4.A.1 and 4.A.2); experimental TOF spectra fitting parameters (Table 4.A.4); AIMD reaction probability curve fitting results in which the saturation values of the AIMD fits have been constrained to the corresponding values from the BOSS fits (Figure 4.A.3); W parameters computed for ERF experimental reaction probability curves (Figure 4.A.4); E_0', W' and ν parameters computed for LGS experimental reaction probability curves (Figure 4.A.5); W, W_1 and W_2 parameters computed for LGS experimental reaction probability curves (Figure 4.A.6); adsorption experiment fits plotted on a linear scale (Figure 4.A.7).

Configuration	r (Å)	Z (Å)	E_b (eV)
bth	1.032	1.164	0.628
ttb	1.397	1.386	0.891
fcc, $\varphi = 0°$	1.588	1.270	1.013
t2f, $\varphi = 0°$	1.270	1.270	0.770

Table 4.A.1: Barrier heights and barrier geometries for some configurations in the SRP-DFT PES [39, 40]. The configurations are bridge-to-hollow (bth), top-to-bridge (ttb), above the fcc site (fcc), and above the site midway between a top and fcc site (t2f).

State	Function	A	E_0'	W'	ν	E_0''	W''	χ^2
$v = 0, J = 0$	ERF	0.549	0.808	0.122	-	-	-	546.459
	LGS	0.662	0.792	0.113	3.69 10^{-7}	-	-	69.560
	FPC	1.000	0.723	0.077	-	0.914	0.228	5.963
$v = 0, J = 2$	ERF	0.503	0.776	0.143	-	-	-	1093.929
	LGS	0.598	0.756	0.128	4.85 10^{-7}	-	-	226.596
	FPC	0.699	0.635	0.066	-	0.832	0.144	7.208
$v = 0, J = 4$	ERF	0.534	0.762	0.160	-	-	-	1014.269
	LGS	0.642	0.741	0.144	1.64 10^{-7}	-	-	144.116
	FPC	1.000	0.653	0.099	-	0.911	0.292	3.331
$v = 0, J = 6$	ERF	0.520	0.750	0.124	-	-	-	2858.227
	LGS	0.604	0.728	0.114	7.96 10^{-7}	-	-	585.047
	FPC	0.896	0.639	0.064	-	0.875	0.206	7.756
$v = 0, J = 11$	ERF	0.594	0.714	0.187	-	-	-	1611.941
	LGS	0.718	0.691	0.171	3.10 10^{-7}	-	-	265.116
	FPC	0.691	0.481	0.066	-	0.746	0.123	34.501
$v = 1, J = 2$	ERF	0.672	0.562	0.154	-	-	-	6179.267
	LGS	0.712	0.517	0.119	1.15 10^{-7}	-	-	2099.695
	FPC	0.777	0.518	0.177	-	0.395	0.018	62.617
$v = 1, J = 6$	ERF	0.711	0.537	0.149	-	-	-	5510.366
	LGS	0.752	0.495	0.118	1.13 10^{-7}	-	-	977.690
	FPC	0.808	0.476	0.180	-	0.406	0.035	70.940
$v = 2, J = 2$	ERF	0.754	0.381	0.178	-	-	-	6301.884
	LGS	0.782	0.328	0.130	7.24 10^{-7}	-	-	1626.766
	FPC	0.869	0.261	0.080	-	0.248	0.287	78.902

Table 4.A.2: Fit parameters corresponding to the BOSS reaction probability curves plotted in Figure 4.A.1. E_0', E_0'', W' and W'' parameters are in eV.

State	# Data	Function	A	E_0	W'	ν	χ^2
$v = 0, J = 0$	5	ERF	0.673	0.853	0.209	-	10.673
		LGS	0.833	0.832	0.193	$2.04\ 10^{-7}$	4.055
$v = 0, J = 2$	5	ERF	0.587	0.775	0.192	-	6.275
		LGS	0.737	0.761	0.180	$1.70\ 10^{-7}$	3.327
$v = 0, J = 4$	6	ERF	0.638	0.790	0.192	-	7.331
		LGS	0.669	0.773	0.110	0.434	5.037
$v = 0, J = 6$	5	ERF	0.617	0.793	0.204	-	2.427
		LGS	0.745	0.770	0.174	$3.79\ 10^{-7}$	0.886
$v = 0, J = 11$	5	ERF	0.734	0.746	0.265	-	1.405
		LGS	0.917	0.726	0.235	$1.25\ 10^{-5}$	0.111
$v = 1, J = 2$	5	ERF	0.596	0.511	0.159	-	11.912
		LGS	0.665	0.475	0.130	$5.67\ 10^{-7}$	2.435
$v = 1, J = 6$	5	ERF	0.655	0.522	0.175	-	7.356
		LGS	0.753	0.493	0.140	0.002	2.707
$v = 2, J = 2$	5	ERF	0.662	0.326	0.177	-	2.202
		LGS	0.713	0.293	0.124	0.116	0.088

Table 4.A.3: Fit parameters corresponding to the AIMD reaction probability curves plotted in Figure 4.A.2. E_0' and W' parameters are in eV.

State	Dataset	Function	E_0'	W'	ν	χ^2
$v = 0, J = 0$	DS0609A	ERF	0.660	0.171	-	$1.166\ 10^{10}$
		LGS	0.713	0.186	0.050	$5.471\ 10^{9}$
$v = 0, J = 2$	DS0609E	ERF	0.696	0.182	-	$2.647\ 10^{9}$
		LGS	0.785	0.229	$3.67\ 10^{-7}$	$5.759\ 10^{8}$
$v = 0, J = 4$	DS0608D	ERF	0.760	0.199	-	$1.130\ 10^{9}$
		LGS	0.853	0.230	0.055	$4.744\ 10^{8}$
$v = 0, J = 6$	DS0606E	ERF	0.724	0.176	-	$8.276\ 10^{8}$
		LGS	0.757	0.162	0.136	$5.626\ 10^{8}$
$v = 0, J = 11$	DS0607A	ERF	0.617	0.180	-	$4.297\ 10^{11}$
		LGS	0.705	0.228	$1.35\ 10^{-5}$	$3.875\ 10^{11}$
$v = 1, J = 2$	DS0620E	ERF	0.468	0.169	-	$1.750\ 10^{12}$
		LGS	0.454	0.096	0.461	$1.358\ 10^{12}$
$v = 1, J = 6$	DS0620C	ERF	0.483	0.178	-	$2.317\ 10^{12}$
		LGS	0.462	0.094	0.518	$1.917\ 10^{12}$
$v = 2, J = 2$	DS0624D	ERF	0.266	0.145	-	$1.724\ 10^{14}$
		LGS	0.258	0.057	1.000	$1.493\ 10^{14}$

Table 4.A.4: Fit parameters corresponding to the curves plotted in Figure 4.6 obtained in a specific experiment, as indicated by the name of the corresponding data set. E_0' and W' parameters are in eV.

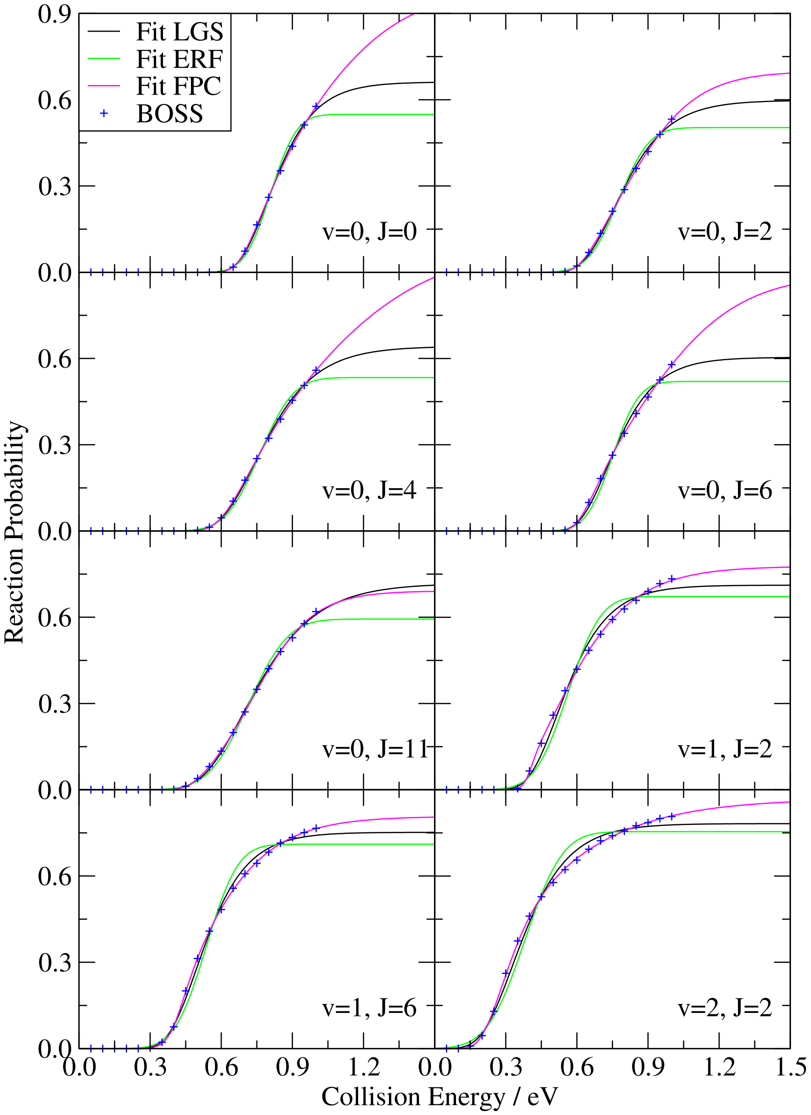

Figure 4.A.1: BOSS reaction probabilities (blue symbols) are plotted as a function of the collision energy for some representative initial states. ERF, LGS and FPC fits of the BOSS data are plotted as green, black and violet solid lines, respectively.

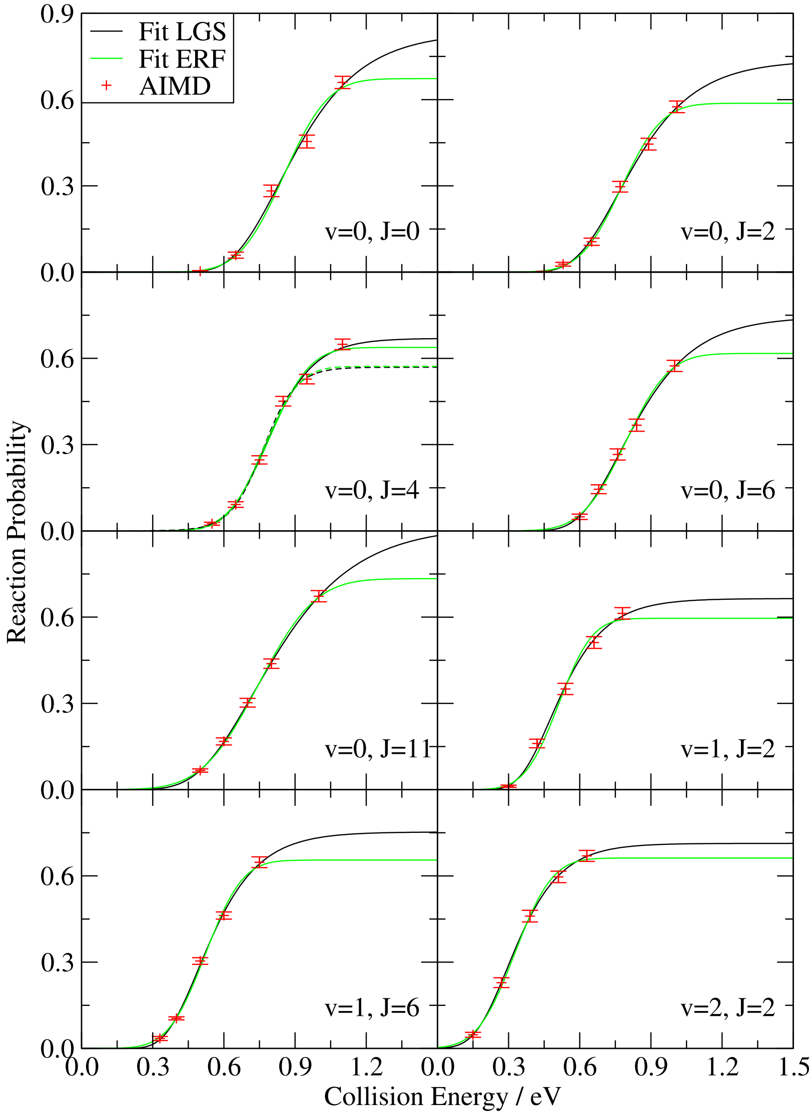

Figure 4.A.2: AIMD reaction probabilities (red symbols) are plotted as a function of the collision energy for some representative states. ERF and LGS fits of the AIMD data are plotted as green and black lines, respectively. For $(v = 0, J = 4)$, also the ERF and LGS fits of the 5 lowest collision energy points are plotted as dashed lines (see text, Section 4.3.2).

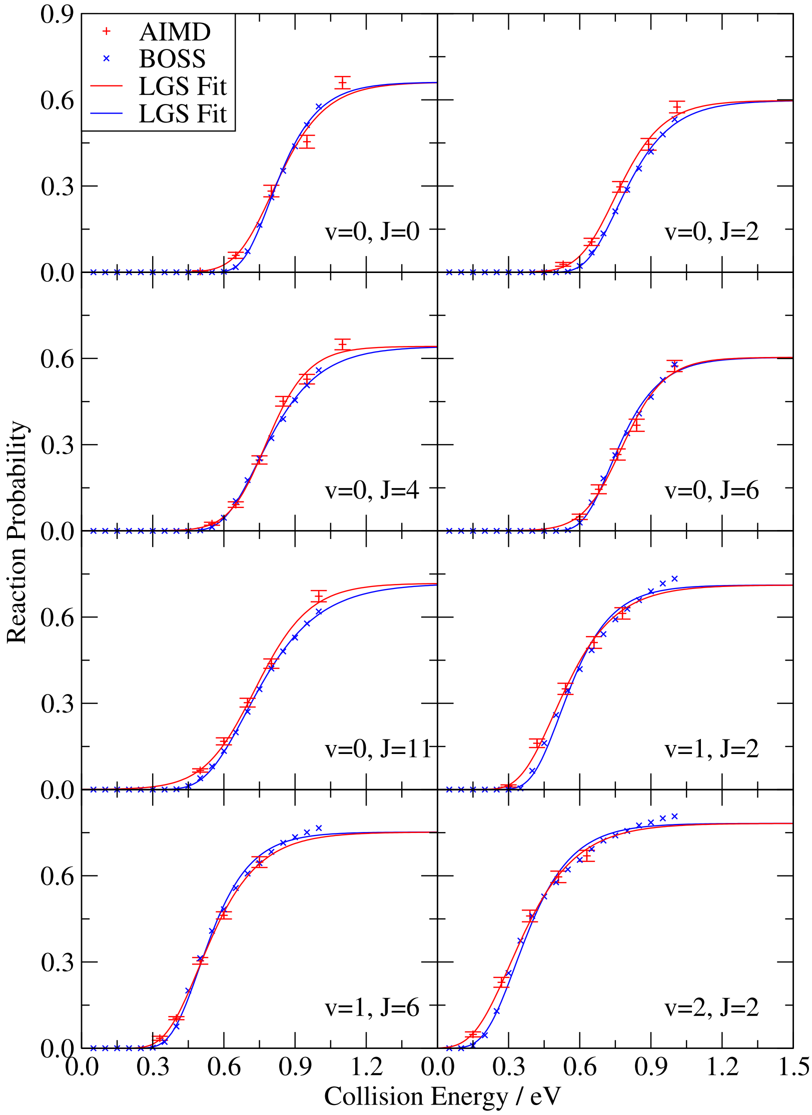

Figure 4.A.3: BOSS and AIMD reaction probabilities (blue × and red +, respectively) are plotted as a function of the collision energy for some representative initial states; the solid lines are LGS fits of the probabilities. The fits of the AIMD data have been constrained to have the same saturation values as the BOSS fits.

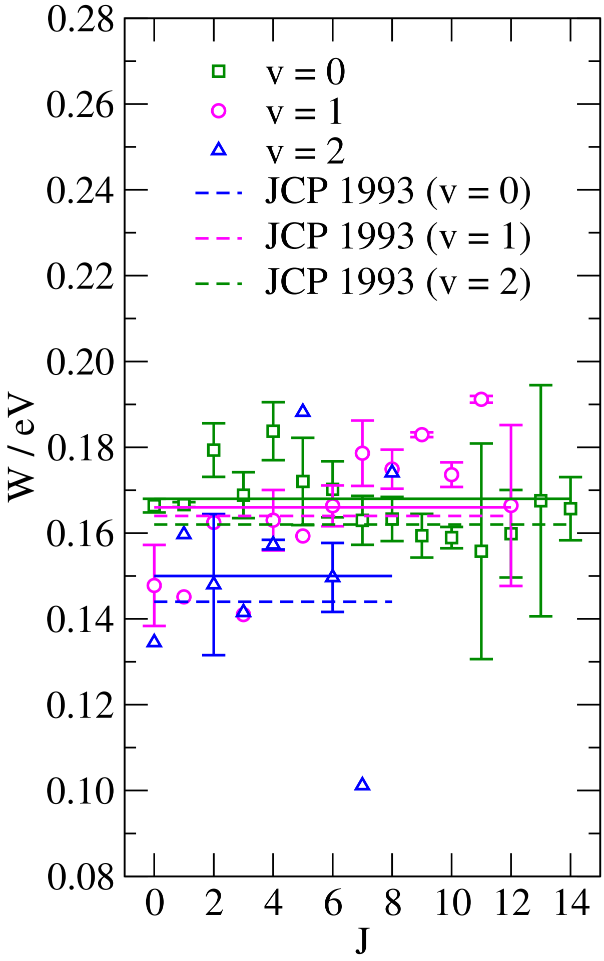

Figure 4.A.4: *W* parameters obtained from ERF fits of all the available desorption TOF spectra are plotted as a function of the initial rotational state J. Green, violet and blue symbols correspond to $v = 0, 1$ and 2 initial vibrational states, respectively. Solid curves represent average of the $v = 0, 1, 2$ data, while dashed lines are average of the data from Ref. [13]. Line colors are as for the symbols.

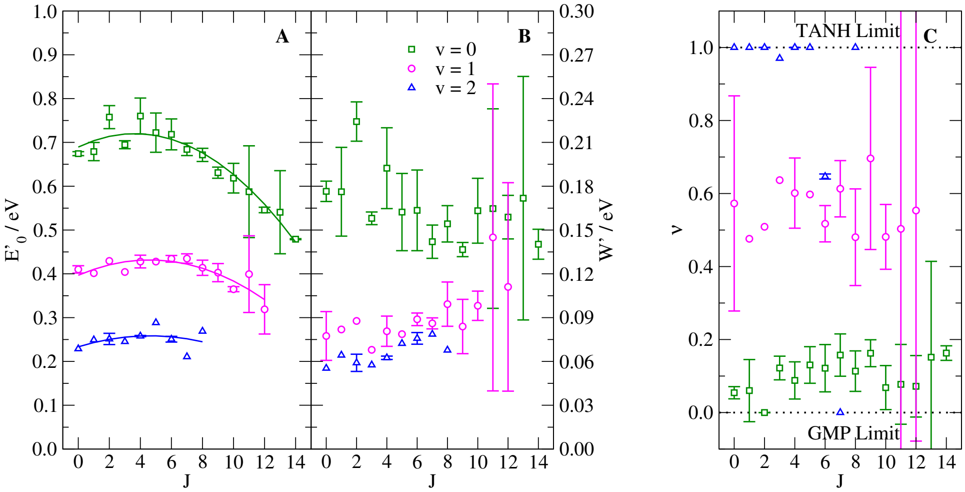

Figure 4.A.5: Parameters obtained from LGS fits of all the available desorption TOF spectra are plotted as a function of the initial rotational state J. Green squares, violet circles and blue triangles correspond to $v = 0, 1$ and 2 initial vibrational states, respectively. Solid curves in the E_0' plot represent quadratic fits of the $v = 0, 1, 2$ data (colors as for the symbols).

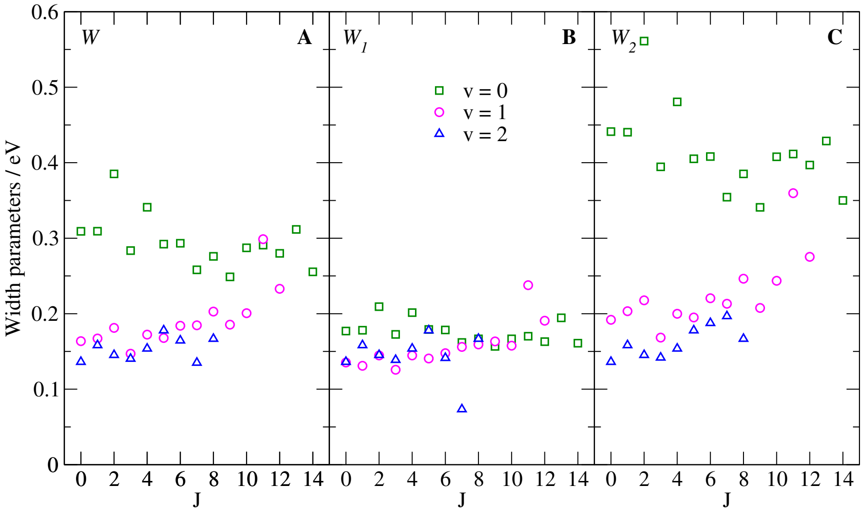

Figure 4.A.6: W, W_1 and W_2 parameters computed for the experimental LGS reaction probability curves are plotted as a function of the initial rotational state J. Green squares, violet circles and blue triangles correspond to $v = 0, 1$ and 2 initial vibrational states, respectively.

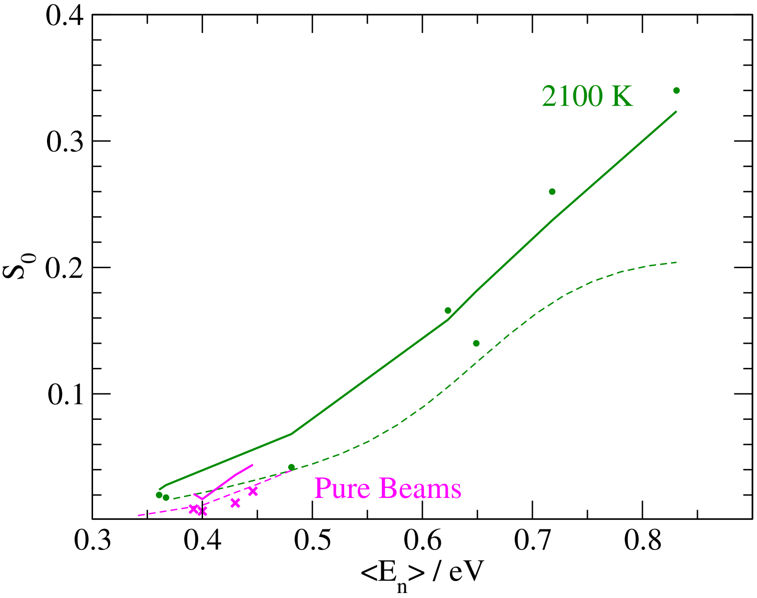

Figure 4.A.7: The sticking probability measured in molecular beam experiments is shown as a function of the average collision energy using a linear scale (only probabilities larger than 1%). Seeded beam results corresponding to specific nozzle temperatures are plotted as circles, pure beam results using crosses. The results of our fits are plotted as solid lines. Dashed lines are from the previous fit (Ref. [13]).

Bibliography

[1] G. J. Kroes, Phys. Chem. Chem. Phys. **14**, 14966 (2012).

[2] P. Nieto, E. Pijper, D. Barredo, G. Laurent, R. A. Olsen, E. J. Baerends, G. J. Kroes, and D. Farías, Science **312**, 86 (2006).

[3] A. C. Luntz and M. Persson, J. Chem. Phys. **123**, 074704 (2005).

[4] J. I. Juaristi, M. Alducin, R. Díez Muiño, H. F. Busnengo, and A. Salin, Phys. Rev. Lett. **100**, 116102 (2008).

[5] G. Anger, A. Winkler, and K. D. Rendulic, Surf. Sci. **220**, 1 (1989).

[6] H. F. Berger, M. Leisch, A. Winkler, and K. D. Rendulic, Chem. Phys. Lett. **175**, 425 (1990).

[7] H. A. Michelsen and D. J. Auerbach, J. Chem. Phys. **94**, 7502 (1991).

[8] A. Hodgson, J. Moryl, P. Traversaro, and H. Zhao, Nature **356**, 501 (1992).

[9] H. A. Michelsen, C. T. Rettner, and D. J. Auerbach, Phys. Rev. Lett. **69**, 2678 (1992).

[10] H. A. Michelsen, C. T. Rettner, and D. J. Auerbach, Surf. Sci. **272**, 65 (1992).

[11] C. T. Rettner, D. J. Auerbach, and H. A. Michelsen, Phys. Rev. Lett. **68**, 1164 (1992).

[12] C. T. Rettner, D. J. Auerbach, and H. A. Michelsen, Phys. Rev. Lett. **68**, 2547 (1992).

[13] H. A. Michelsen, C. T. Rettner, D. J. Auerbach, and R. N. Zare, J. Chem. Phys. **98**, 8294 (1993).

[14] C. T. Rettner, H. A. Michelsen, and D. J. Auerbach, Chem. Phys. **175**, 157 (1993).

[15] C. T. Rettner, H. A. Michelsen, and D. J. Auerbach, Faraday Discuss. **96**, 17 (1993).

[16] C. T. Rettner, H. A. Michelsen, and D. J. Auerbach, J. Chem. Phys. **102**, 4625 (1995).

[17] D. Wetzig, M. Rutkowski, R. David, and H. Zacharias, Europhys. Lett. **36**, 31 (1996).

[18] S. J. Gulding, A. M. Wodtke, H. Hou, C. T. Rettner, H. A. Michelsen, and D. J. Auerbach, J. Chem. Phys. **105**, 9702 (1996).

[19] H. Hou, S. J. Gulding, C. T. Rettner, A. M. Wodtke, and D. J. Auerbach, Science **277**, 80 (1997).

[20] A. Hodgson, P. Samson, A. Wight, and C. Cottrell, Phys. Rev. Lett. **78**, 963 (1997).

[21] M. J. Murphy and A. Hodgson, J. Chem. Phys. **108**, 4199 (1998).

[22] U. Nielsen, D. Halstead, S. Holloway, and J. K. Nørskov, J. Chem. Phys. **93**, 2879 (1990).

[23] G. R. Darling and S. Holloway, J. Chem. Phys. **97**, 734 (1992).

[24] J. Sheng and J. Z. H. Zhang, J. Chem. Phys. **99**, 1373 (1993).

[25] A. Gross, B. Hammer, M. Scheffler, and W. Brenig, Phys. Rev. Lett. **73**, 3121 (1994).

[26] B. Hammer, M. Scheffler, K. W. Jacobsen, and J. K. Nørskov, Phys. Rev. Lett. **73**, 1400 (1994).

[27] A. Forni, G. Wiesenekker, E. J. Baerends, and G. F. Tantardini, Int. J. Quantum Chem. **52**, 1067 (1994).

[28] G. R. Darling and S. Holloway, J. Chem. Phys. **101**, 3268 (1994).

[29] G. R. Darling and S. Holloway, Surf. Sci. **321**, L189 (1994).

[30] G. R. Darling and S. Holloway, Surf. Sci. **307-309**, 153 (1994).

[31] J. Q. Dai, J. Sheng, and J. Z. H. Zhang, J. Chem. Phys. **101**, 1555 (1994).

[32] J. Q. Dai and J. Z. H. Zhang, Surf. Sci. **319**, 193 (1994).

[33] J. Q. Dai and J. Z. H. Zhang, J. Chem. Phys. **102**, 6280 (1995).

[34] A. Forni, G. Wiesenekker, E. J. Baerends, and G. F. Tantardini, J. Phys.: Condens. Matter **7**, 7195 (1995).

[35] J. Q. Dai and J. C. Light, J. Chem. Phys. **107**, 1676 (1997).

[36] J. Q. Dai and J. C. Light, J. Chem. Phys. **108**, 7816 (1998).

[37] M. F. Somers, S. M. Kingma, E. Pijper, G. J. Kroes, and D. Lemoine, Chem. Phys. Lett. **360**, 390 (2002).

[38] S. Nave, D. Lemoine, M. F. Somers, S. M. Kingma, and G. J. Kroes, J. Chem. Phys. **122**, 214709 (2005).

[39] C. Díaz, E. Pijper, R. A. Olsen, H. F. Busnengo, D. J. Auerbach, and G. J. Kroes, Science **326**, 832 (2009).

[40] C. Díaz, R. A. Olsen, D. J. Auerbach, and G. J. Kroes, Phys. Chem. Chem. Phys. **12**, 6499 (2010).

[41] G. J. Kroes, C. Díaz, E. Pijper, R. A. Olsen, and D. J. Auerbach, Proc. Natl. Acad. Sci. U. S. A. **107**, 20881 (2010).

[42] M. Bonfanti, C. Díaz, M. F. Somers, and G. J. Kroes, Phys. Chem. Chem. Phys. **13**, 4552 (2011).

[43] F. Nattino, C. Díaz, B. Jackson, and G. J. Kroes, Phys. Rev. Lett. **108**, 236104 (2012).

[44] M. Wijzenbroek and M. F. Somers, J. Chem. Phys. **137**, 054703 (2012).

[45] A. S. Muzas, J. I. Juaristi, M. Alducin, R. Díez Muiño, G. J. Kroes, and C. Díaz, J. Chem. Phys. **137**, 064707 (2012).

[46] M. Bonfanti, M. F. Somers, C. Díaz, H. F. Busnengo, and G. J. Kroes, Z. Phys. Chem. **227**, 1397 (2013).

[47] S. B. Donald and I. Harrison, J. Phys. Chem. C **118**, 320 (2014).

[48] D. L. Diedrich and J. B. Anderson, Science **258**, 786 (1992).

[49] D. Neuhauser, R. S. Judson, D. J. Kouri, D. E. Adelman, N. E. Shafer, D. A. V. Kliner, and R. N. Zare, Science **257**, 519 (1992).

[50] S. C. Althorpe, F. Fernandez-Alonso, B. D. Bean, J. D. Ayers, A. E. Pomerantz, R. N. Zare, and E. Wrede, Nature **416**, 67 (2002).

[51] S. A. Harich, D. Dai, C. C. Wang, X. Yang, S. D. Chao, and R. T. Skodje, Nature **419**, 281 (2002).

[52] J. C. Juanes-Marcos, S. C. Althorpe, and E. Wrede, Science **309**, 1227 (2005).

[53] S. J. Greaves, E. Wrede, N. T. Goldberg, J. Zhang, D. J. Miller, and R. N. Zare, Nature **454**, 88 (2008).

[54] D. G. Fleming, D. J. Arseneau, O. Sukhorukov, J. H. Brewer, S. L. Mielke, G. C. Schatz, B. C. Garrett, K. A. Peterson, and D. G. Truhlar, Science **331**, 448 (2011).

[55] A. Chakraborty, Y. Zhao, H. Lin, and D. G. Truhlar, J. Chem. Phys. **124**, 044315 (2006).

[56] Y. Y. Chuang, M. L. Radhakrishnan, P. L. Fast, C. J. Cramer, and D. G. Truhlar, J. Phys. Chem. A **103**, 4893 (1999).

[57] E. E. Marinero, C. T. Rettner, and R. N. Zare, Phys. Rev. Lett. **48**, 1323 (1982).

[58] M. Hand and J. Harris, J. Chem. Phys. **92**, 7610 (1990).

[59] H. F. Busnengo, W. Dong, P. Sautet, and A. Salin, Phys. Rev. Lett. **87**, 127601 (2001).

[60] S. J. Klippenstein, V. S. Pande, and D. G. Truhlar, J. Am. Chem. Soc. **136**, 528 (2014).

[61] Ž. Šljivančanin and B. Hammer, Phys. Rev. B **65**, 085414 (2002).

[62] T. Zambelli, J. Wintterlin, J. Trost, and G. Ertl, Science **273**, 1688 (1996).

[63] S. Dahl, A. Logadottir, R. C. Egeberg, J. H. Larsen, I. Chorkendorff, E. Tornqvist, and J. K. Nørskov, Phys. Rev. Lett. **83**, 1814 (1999).

[64] G. Comsa and R. David, Surf. Sci. **117**, 77 (1982).

[65] L. Sementa, M. Wijzenbroek, B. J. van Kolck, M. F. Somers, A. Al-Halabi, H. F. Busnengo, R. A. Olsen, G. J. Kroes, M. Rutkowski, C. Thewes, N. F. Kleimeier, and H. Zacharias, J. Chem. Phys. **138**, 044708 (2013).

[66] K. Gundersen, K. W. Jacobsen, J. K. Nørskov, and B. Hammer, Surf. Sci. **304**, 131 (1994).

[67] M. Karikorpi, S. Holloway, N. Henriksen, and J. K. Nørskov, Surf. Sci. **179**, L41 (1987).

[68] H. E. Pfnür, C. T. Rettner, J. Lee, R. J. Madix, and D. J. Auerbach, J. Chem. Phys. **85**, 7452 (1986).

[69] R. Bisson, M. Sacchi, T. Dang, B. Yoder, P. Maroni, and R. Beck, J. Phys. Chem. A **111**, 12679 (2007).

[70] P. M. Holmblad, J. Wambach, and I. Chorkendorff, J. Chem. Phys. **102**, 8255 (1995).

[71] P. M. Hundt, B. Jiang, M. E. van Reijzen, H. Guo, and R. D. Beck, Science **344**, 504 (2014).

[72] A. Groß and A. Dianat, Phys. Rev. Lett. **98**, 206107 (2007).

[73] A. De Vita, I. Štich, M. J. Gillan, M. C. Payne, and L. J. Clarke, Phys. Rev. Lett. **71**, 1276 (1993).

[74] I. E. Leksina and S. I. Novikova, Sov. Phys-Solid State **5**, 798 (1963).

[75] F. R. Kroeger and C. A. Swenson, J. Appl. Phys. **48**, 853 (1977).

[76] G. Kresse and J. Hafner, Phys. Rev. B **47**, 558 (1993).

[77] G. Kresse and J. Hafner, Phys. Rev. B **49**, 14251 (1994).

[78] G. Kresse and J. Furthmüller, Comput. Mat. Sci. **6**, 15 (1996).

[79] G. Kresse and J. Furthmüller, Phys. Rev. B **54**, 11169 (1996).

[80] G. Kresse and D. Joubert, Phys. Rev. B **59**, 1758 (1999).

[81] J. P. Perdew, K. Burke, and M. Ernzerhof, Phys. Rev. Lett. **77**, 3865 (1996).

[82] J. P. Perdew, K. Burke, and M. Ernzerhof, Phys. Rev. Lett. **78**, 1396 (1997).

[83] J. P. Perdew, J. A. Chevary, S. H. Vosko, K. A. Jackson, M. R. Pederson, D. J. Singh, and C. Fiolhais, Phys. Rev. B **48**, 4978 (1993).

[84] J. P. Perdew, J. A. Chevary, S. H. Vosko, K. A. Jackson, M. R. Pederson, D. J. Singh, and C. Fiolhais, Phys. Rev. B **46**, 6671 (1992).

[85] A. Mondal, M. Wijzenbroek, M. Bonfanti, C. Díaz, and G. J. Kroes, J. Phys. Chem. A **117**, 8770 (2013).

[86] E. B. Wilson, J. Am. Statist. Assoc. **22**, 209 (1927).

[87] T. A. Louis, Am. Stat. **35**, 154 (1981).

[88] A. C. Luntz, J. Chem. Phys. **102**, 8264 (1995).

[89] L. B. F. Juurlink, D. R. Killelea, and A. L. Utz, Prog. Surf. Sci. **84**, 69 (2009).

[90] A. C. Luntz, J. Chem. Phys. **113**, 6901 (2000).

[91] R. A. Olsen, G. J. Kroes, G. Henkelman, A. Arnaldsson, and H. Jónsson, J. Chem. Phys. **121**, 9776 (2004).

[92] J. Harris, Surf. Sci. **221**, 335 (1989).

[93] K. Levenberg, Q. Appl. Math. **2**, 164 (1944).

[94] D. Marquardt, J. Soc. Ind. Appl. Math. **11**, 431 (1963).

[95] J. J. Moré, D. C. Sorensen, K. E. Hillstrom, and B. S. Garbow, The MINPACK Project, in *Sources and Development of Mathematical Software*, edited by W. J. Cowell, pages 88–111, Prentice-Hall, Englewood Cliffs, 1984.

[96] J. J. Moré, B. S. Garbow, and K. E. Hillstrom, User Guide for MINPACK-1, Report ANL-80-74, Argonne, 1980.

Chapter 5

Ab Initio Molecular Dynamics Calculations versus Quantum-State Resolved Experiments on CHD_3 + Pt(111): New Insights into a Prototypical Gas-Surface Reaction

This chapter is based on:

F. Nattino, H. Ueta, H. Chadwick, M. E. van Reijzen, R. D. Beck, B. Jackson, M. C. van Hemert, and G. J. Kroes, J. Phys. Chem. Lett. **5**, 1294 (2014).

Abstract

The dissociative chemisorption of methane on metal surfaces is of fundamental and practical interest, being a rate-limiting step in the steam reforming process. The reaction is best modeled with quantum dynamics calculations, but these are currently not guaranteed to produce accurate results because they rely on potential energy surfaces based on untested density functionals, and on untested dynamical approximations. To

help overcome these limitations, here we present for the first time statistically accurate reaction probabilities obtained with *ab initio* molecular dynamics (AIMD) for a polyatomic gas phase molecule reacting with a metal surface. Using a general purpose density functional, the AIMD reaction probabilities are in semi-quantitative agreement with new quantum-state resolved experiments on CHD_3 + Pt(111). The comparison suggests the use of the sudden approximation for treating the rotations even though CHD_3 has large rotational constants, and yields an estimated reaction barrier of 0.9 eV for CH_4 + Pt(111).

5.1 Introduction

The steam reforming process, in which methane and water react over a Ni catalyst, is the main commercial source of molecular hydrogen. The dissociation (or dissociative chemisorption) of CH_4 on the catalyst into CH_3(ad) + H(ad) is a rate-determining step of the full process [1]. Moreover, dissociation of methane on metal surfaces is of fundamental interest [2–13]. Already from early molecular beam experiments it is known that vibration is very effective in promoting reactivity [3,4,14]. More recently, it has been shown that the reaction is mode specific, i.e., the degree to which energizing the molecule promotes reaction depends on whether the energy is put in translation or vibration, and even on which vibration it is put in (vibrational mode-specificity) [5–8]. These observations, which have been explained qualitatively on the basis of different models [9, 15], rule out the application of fully statistical models. For some vibrational modes, the vibrational efficacy, which measures how effective putting energy into vibration is at promoting reaction relative to increasing the incidence energy (E_i), is even larger than one [7, 10]. In addition, the dissociation of partially deuterated molecules shows bond-selectivity; for instance, in CHD_3, the CH bond can be selectively broken upon excitation to an appropriate initial vibrational state [11, 12]. Finally, dissociative chemisorption of methane on metal surfaces represents a current frontier in the theoretical description of the dynamics of reactions of gas phase molecules on metal surfaces [15–24], with much current efforts now being aimed at achieving an accurate description of this reaction through high-dimensional quantum dynamics calculations [16,23,24].

A wealth of experiments exist for the methane + Pt(111) system [3,8,12,17,25–29]. There has been considerable debate [2,25] concerning the importance of tunneling in this and similar systems. Recent calculations [17,23,30] suggest only a minor role for tunneling under the conditions addressed by us. Research on Ni [31] and on Pt [17] surfaces suggests that the dissociation of methane should proceed through a direct mechanism under both thermal and hyperthermal conditions on these surfaces. This suggests the possibility to accurately model experiments relevant to both kinetics and dynamics with a unified approach. Harrison and coworkers have indeed shown [17] that a dynamically biased semi-empirical statistical model yields an accurate description of a large range of experiments. However, this model cannot describe that, as also observed for CH_4 + Pt(111) [8,26,27], the extent to which putting energy into vibration promotes reaction depends on which vibrational state is excited. The model also does not yield the minimum reaction barrier height (E_b), which would be useful for testing new electronic structure methods that are potentially more accurate than the present state-of-the-art method for computing potential energy surfaces (PESs) for molecule-metal surface reactions (density functional theory (DFT) at the generalized gradient approximation (GGA) level) [32]. The DFT-GGA method is known to yield E_b with an accuracy no better than 3.8 kcal/mol for gas phase reactions [33,34], with GGA functionals both underestimating and overestimating E_b for gas-metal surface reactions [35], while adsorption energies on metal surfaces exhibit similar lack of accuracy [36]. An accurate value of E_b is also relevant to accurately modeling the steam reforming reaction over a Pt(111) surface, as kinetics calculations of rates of heterogeneously catalyzed processes require reaction barrier heights as input parameters [1].

Within the appropriate level of dynamical theory and if an accurate PES is available, dynamics calculations can in principle solve all of the above problems and yield a consistently accurate description of all experiments described above. Dynamics calculations and their comparison to supersonic molecular beam experiments directly test whether the PES contains an accurate description of E_b and of the couplings of the molecule's and surface atoms' vibrations to the reaction coordinate. The quasi-classical trajectory (QCT) method (trajectory method with zero-point energy (ZPE) imparted to all molecular vibrational modes) is cheap to use, but with this method artificial energy flow between vibrations of similar frequency can occur even in the isolated molecule [22]. This could hamper the accurate calculation of vibrational efficacies, and explains that vibrational efficacies computed with the QCT method for CH_4 + Ni(111) are too low when compared with experiments and results of quantum dynamics (QD) calculations [15,22]. It would therefore be best to use QD to describe methane dissociation on metal surfaces. Ideally, such calculations would treat all molecular degrees of freedom (DOFs) and the relevant surface DOFs without approximations. This is currently not possible, and the high-dimensional (i.e., modeling motion in many DOFs) QD calculations published so far rely on untested dynamical approximations [16,22–24] and PESs based on untested density functionals [16,22–24].

To help overcome these two shortcomings, we have performed *ab initio* molecular dynamics (AIMD) calculations and molecular beam experiments on the dissociation of CHD_3 on Pt(111) at normal incidence, comparing sticking (dissociation) probabilities of hyperthermal and CH-stretch excited CHD_3. The use of AIMD bypasses the need to fit a high-dimensional PES as forces are calculated on the fly with DFT, and allows motion to be described in all molecular DOFs as well as of the surface atoms, which should also be relevant: The minimum energy barrier to dissociative adsorption is considerably lowered if the surface atom below the dissociating molecule moves out of the surface plane [37], and the reaction shows a high surface temperature dependence [3,38–41]. Our goal is to test the validity of the dynamical approximations and the density functionals used in earlier high-dimensional QD [16,22–24] and QCT [15,18,22] calculations on dissociation of methane on metal surfaces. Our calculations can help pave the way towards chemically accurate quantum dynamical calculations on reactions of methane on metal surfaces, as accomplished earlier for H_2 + Cu(111) [42].

5.2 Methods

AIMD calculations are performed with the VASP code [43–47]. The Pt surface is modeled with a 5 layer slab within a 3x3 supercell. A Γ-centered grid with 4x4x1 k-points samples the first Brillouin zone. Fermi smearing with a width of 0.1 eV has been used to facilitate convergence. The basis set includes plane waves up to a kinetic energy of 350 eV and core electrons have been represented with the projected augmented wave (PAW) method [47, 48] (see also Appendix 5.A.2). With the described computational setup, an equilibrium lattice constant of 3.975 Å has been obtained for bulk Pt, in reasonable agreement with the experimental value of 3.916 Å [49, 50].

In order to take the experimental surface temperature into account, a similar procedure as described in Ref. [51] and Chapter 3 has been followed: velocities and displacements from the equilibrium position have been assigned to surface atoms through an appropriate sampling and the optimized lattice constant has been expanded by 0.049% [49, 50] in order to simulate the platinum thermal expansion from 0 to 120 K, and by 0.386% for 0 to 500 K. These configurations are used in AIMD NVE simulations (constant number of atoms N, cell volume V and total energy E) to generate surface configurations for Monte-Carlo sampling, after which the molecule-surface collisions are simulated using NVE dynamics. Sticking probabilities are based on 1000 trajectories if the computed S_0 value is included in the range $1\% < S_0 < 10\%$, while 2000 and 500 trajectories have been computed for the $S_0<1\%$ and the $S_0 > 10\%$ cases, respectively. The dissociation probability values and their error bars (95% confidence interval unless otherwise stated) are evaluated using the Wilson (or score) method [52], which has been shown to provide a reasonable estimate of confidence intervals even for extremely low probabilities (close to 0%) [53], and which yields probabilities and standard deviations converging to the values obtained with the binomial distribution for large numbers of trajectories and probabilities.

The AIMD calculations we present use the QCT method. The usual QCT pitfalls (problems due to the absence of ZPE conservation and to neglect of tunneling effects) are avoided by performing the calculations for average total molecular energies $\langle E_{tot} \rangle$

E_b	E_b^c (CH_4)	E_b^c (CHD_2-D)	E_b^c (CD_3-H)
0.805	0.700	0.729	0.683

Table 5.1: Values of E_b and of E_b^c are given in eV for dissociation of CH_4 and CHD_3. The barrier geometry that we consider is computed from the minimum energy transition state configuration from Ref. [55].

well above E_b^c (the ZPE corrected value of E_b, see Table 5.1), and by avoiding reduced dimensionality calculations [22] (see also Appendix 5.A.3). The primary reason that we consider CHD_3 is that this allows us to also accurately study the effect of initial vibrational energy on the reactivity with the QCT method for the case that the ν_1 CH-stretch is pre-excited with one quantum. In CHD_3 the ν_1 CH-stretch is mostly localized on one bond and has a frequency that is off-resonance with other vibrations, so that artificial intra-molecular vibrational energy redistribution is minimized [54] (see Appendix 5.A.3). Compared to earlier QD and QCT calculations with a claim to high accuracy, advantages of the present AIMD calculations are that dynamical approximations [15, 16, 22–24], artificial energy flow between CH_4 vibrations of similar frequency [15, 18, 22], and errors in PES fitting [15, 16, 18, 22–24] are avoided, while the comparison of calculated laser-off reaction probabilities with experiment probes the quality of the density functional used more directly than other calculations [18].

Previously Sacchi et al. used AIMD to investigate the reaction of methane on Ni. However, they modeled the dynamics for the reverse associative desorption reaction, starting from the transition state towards the reactants (CH_4 + clean surface), invoking detailed balance in order to extract qualitative information regarding the relative efficacies of vibrational modes for promoting the forward dissociation reaction [19–21]. The present work is the first study using AIMD as a quantitative tool to compute probabilities for methane dissociation on a metal surface.

The GGA-level PBE density functional [56,57] has been used in the calculations. This makes our calculations relevant to earlier high-dimensional QD and QCT calculations on dissociation of methane on Ni and Pt surfaces: In these calculations, either the PW91 functional [58] was used [15, 16, 18] or the PBE functional, which was designed to reproduce PW91 energies [56], was used [18, 23, 24]. Boltzmann distributions of vibrational states are used to describe the experimental gas temperature of the simulated laser-off beams. On the other hand, only molecules in the ($\nu_1 = 1$) initial state are considered when simulating laser-on beams, as appropriate. The initial conditions of each molecule are chosen such that normal vibrational coordinates and momenta sample classical microcanonical distributions. The initial molecular angular momentum is set to zero, and the initial E_i of the molecule samples velocity distributions as recorded experimentally using time-of-flight techniques. Details on the experimental techniques can be found in the Appendix 5.A.1. The experiments were done by the group of Rainer Beck at the EPFL (Lausanne, Switzerland)

5.3 Results and Discussion

We find semi-quantitative agreement between the theoretical and experimental dissociation probabilities (Figure 5.1). The calculations overestimate the experimental laser-off reactivity. The results therefore strongly suggest that the PBE functional used underestimates the E_b value (Table 5.1) for methane + Pt(111) by approximately 0.1 eV, this value being the energy with which the theoretical curve needs to be shifted in order to obtain agreement with experiment near the reaction threshold, while the E_b value obtained with the RPBE functional (1.06 eV [59]) is probably too high by 0.15 eV. These results are consistent with the finding that the PBE density functional typically overestimates and the RPBE functional usually underestimates the reactivity in activated dissociation of H_2 on metal surfaces [42, 60]. The value that our calculations suggest for E_b^c for CH_4 dissociating on Pt(111) (0.80 eV, i.e., our PBE value (Table 5.1) plus 0.1 eV), is consistent with an experimental estimate of this quantity (0.60 ± 0.20) eV. This estimate can be calculated [17] on the basis of calorimetry [28] and associative desorption experiments [29]. The agreement further improves if one considers that the barrier sampled in the desorption experiments (0.6 eV) is about 0.15 eV lower than the one sampled in adsorption (0.8 eV) due to lattice relaxation [55], i.e. the puckering of the Pt atom on which the methyl is adsorbed before desorption of methane.

Both experiment and theory show a large increase in the sticking probability when

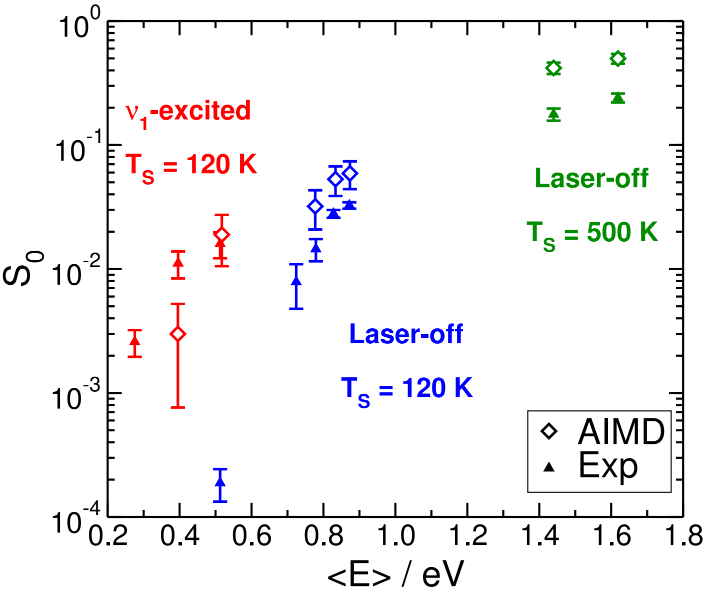

Figure 5.1: Sticking probability as a function of $\langle E_i \rangle$. Triangles are experimental and diamonds are AIMD results. Red symbols represent ν_1-excited beams, and blue symbols laser-off beams, both on a 120 K surface. Green symbols are for laser-off beams on a 500 K surface.

the CH-stretch mode is excited. Jiang et al. justified the observed enhancement in the CHD_3 + Ni(111) reactivity after pre-excitation of the ν_1 mode by considering the large projection that this mode has on the reaction coordinate at the transition state [15]. This argument, which is not specific to gas-surface reactions [61] and considered valid under the assumption that vibrational energy remains localized on the CH stretch, is expected to be valid for our system as well. Note that the theory underestimates the experimental vibrational efficacy, since the energy shift between the laser-off and the ν_1-excited reaction probability curves is lower for the AIMD results than for the experiments. One reason for this [62] could be that the barrier obtained with the PBE functional occurs at a too small value of the length of the breaking bond, as also found for H_2 + Cu(111) [42].

We analyzed the contribution of thermally excited vibrational states to the theoretical laser-off reactivity (Table 5.2). At the lowest E_i, the vibrationally excited molecules are 2.5 times more reactive than the ground state ones; this factor decreases with increasing

$\langle E_i \rangle$ (eV)	T_s (K)	T_n (K)	$P(v=0)$	$S_0^{v=0}$	$S_0^{v\neq 0}$	$S_0^{v\neq 0}/S_0^{v=0}$
0.78	120	836	42.4%	(1.8 ± 0.6) %	(4.4 ± 0.9) %	2.4
0.83	120	902	37.6%	(3.3 ± 0.9) %	(6.6 ± 1.0) %	2.0
0.87	120	971	29.4%	(3.9 ± 1.1) %	(6.9 ± 1.0) %	1.8
1.38	500	768	47.2 %	(34.3 ± 3.1) %	(48.5 ± 3.1) %	1.4
1.53	500	901	38.8 %	(49.5 ± 3.6) %	(50.0 ± 2.9) %	1

Table 5.2: Population and computed reactivity of ground state and vibrationally excited molecules in the laser-off simulations. $\langle E_i \rangle$ is the average translational energy, T_s is the surface temperature, T_n is the gas temperature in the expansion nozzle, $P(v=0)$ is the $v=0$ population and $S_0^{v=0}$ ($S_0^{v\neq 0}$) is the dissociation probability of the ground state (vibrationally excited) molecules in the thermally excited beams. Error bars represent 68.3 % confidence intervals.

	State	E_{tot}	%CD cleavage	% CH cleavage	% Error bars
AIMD	Laser-off	0.92	81.3	18.7	6.9
	Laser-off	1.00	77.4	22.6	5.7
	Laser-off	1.07	76.3	23.7	5.5
	$\nu_1 = 1$	0.77	0.0	100.0	24.9
	$\nu_1 = 1$	0.89	0.0	100.0	6.5
Experiment	Laser-off	0.55	71.4	28.6	-
	$\nu_1 = 1$	0.65	< 1	> 99	-

Table 5.3: Experimental and calculated branching ratios for different states and E_{tot} (eV). Error bars represent 68.3 % confidence intervals.

E_i. At the highest simulated E_i (1.53 eV), the reactivity of ground-state molecules is roughly equal to that of the vibrationally excited molecules. The larger effect of vibration at low E_i arises because at low E_i vibrational energy is needed to overcome the barrier for dissociation, whereas at higher E_i molecules already possess enough translational energy to dissociate.

The ratio between CH and CD bond cleavage is, within the error bars of the calculations, equal to the statistical value of 1:3 for laser-off beams, but only CH cleavage is observed when the CH-stretch is pre-excited (Table 5.3). This is in qualitative agreement with experiments, which were however done for lower E_{tot}, for which reaction probabilities could not be computed with AIMD. The reaction of vibrationally pre-excited CHD_3 is bond-selective because at the low E_i investigated vibrationless methane cannot react, so that the reaction should come from the vibrationally pre-excited normal mode, which in the present case is localized on the CH-stretch.

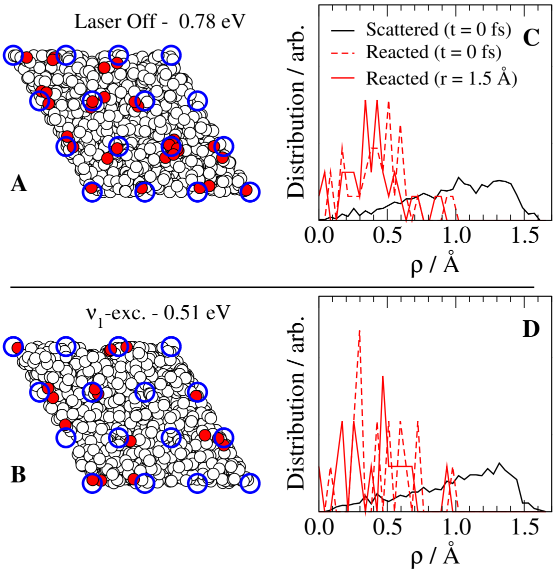

Figure 5.2: (A and B): Initial lateral displacement of the molecules in the supercell for two collision energies; red and white circles represent reacted and scattered molecules, respectively; blue open circles are the top sites in the supercell. (C and D): Impact parameter distributions for the collisions of the reacting molecules with the closest first layer atoms, evaluated at the beginning of the trajectories (dashed red line) and when the dissociating bond length reaches the lowest-energy transition-state value (solid red line). For comparison, the initial distributions of the scattered trajectories are plotted in black.

Insight into the microscopic details of the reaction and the validity of common dynamical approximations can be extracted from the collected dynamical data. For instance, we observe that dissociating molecules impact close to the top site (equilibrium position of a first layer atom, Figure 5.2), consistent with minimum energy paths for adsorption. The impact parameter distributions for collisions of normally incident CHD_3 with top layer surface atoms confirm this, and show that there is little steering towards reactive sites: the distributions do not shift much to lower impact parameters upon the approach of the reacting molecules to the transition state (Figure 5.2, panels C and D). This gives support to the use of sudden approximations [16, 23, 24], which assume that observables of interest can be computed by averaging results of calculations performed for fixed values of the coordinate(s) that remain almost unchanged, to describe the lateral motion of the molecule.

Angular distributions show that the initially non-rotating reacting molecules have their reactive bond initially pointing obliquely down to the surface, forming an angle with the surface normal in the range of $90° < \theta < 180°$ (Figure 5.3). During the subsequent approach to the barrier, there is little rotational steering (distributions only become a little bit narrower), and the distributions at the transition state are centered around values that are close to the orientation at the minimum energy barrier in the static calculations ($= 132.60°$) [37]. Molecules with small moments of inertia (high rotational constants) would be expected to easily reorient towards the minimum energy barrier orientation when approaching the transition state. Perhaps based on this argument, some of the earlier QD calculations [23, 24] employed the rotationally adiabatic approximation, which means that perfect steering of the reacting molecules was assumed along the reaction path. Our calculations show that this approximation is not valid for $CHD_3(\nu_1 = 1)$ because the initial distribution of the reacting molecules does not resemble a $\sin\theta$ distribution at all (the validity of this approximation for laser-off reaction has been discussed elsewhere [63]). In contrast, our result that the θ distributions at $t = 0$ and at the transition state are narrow and similar supports the use of the sudden approximation for the polar angle θ. In the light of the fairly large rotational constants of CHD_3 ($B = 3.3$ cm^{-1} and $C = 2.6$ cm^{-1} [64]) and our current findings, the sudden approximation is probably applicable to any direct gas-surface reaction of a polyatomic molecule under conditions similar as studied here. No correlation has been found between the reactivity and the azimuthal orientation of the dissociating bond (described by the ϕ angle), in agreement with observations of a flat PES with respect to ϕ in the static calculations [37].

In a similar analysis as used in earlier work that only allowed one-dimensional motion of a single surface atom [41], we looked at the time evolution of the vertical displacement of the surface atom closest to the incident molecule (Figure 5.4). Recoil is observed if the average is performed over scattered trajectories at all E_i, but for reactive trajectories recoil is only seen at high E_i. The profile for reactive trajectories at low E_i is different: reaction occurs only if the closest surface atom is above the surface plane and moves

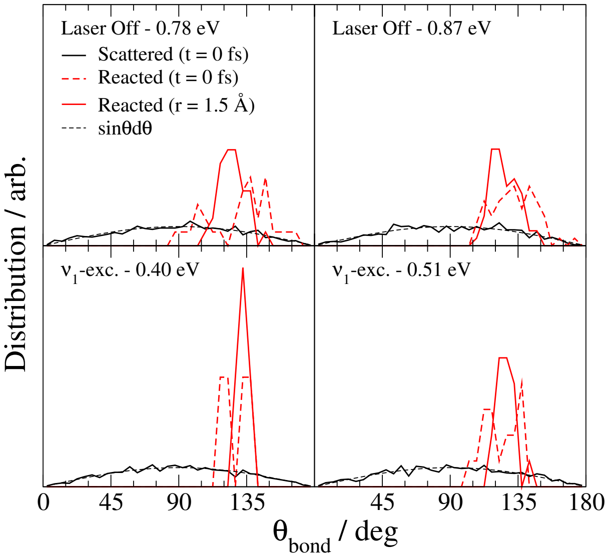

Figure 5.3: θ distributions evaluated at the beginning of the trajectories (dashed red line) and when the dissociating bond length reaches the lowest-energy transition-state value (solid red line) for reacting trajectories for four collision energies. For comparison, the distributions computed for the CH bonds of scattered trajectories are plotted in black. The dashed black lines correspond to sinθ, which is the distribution sampled when generating the initial orientations of the molecules.

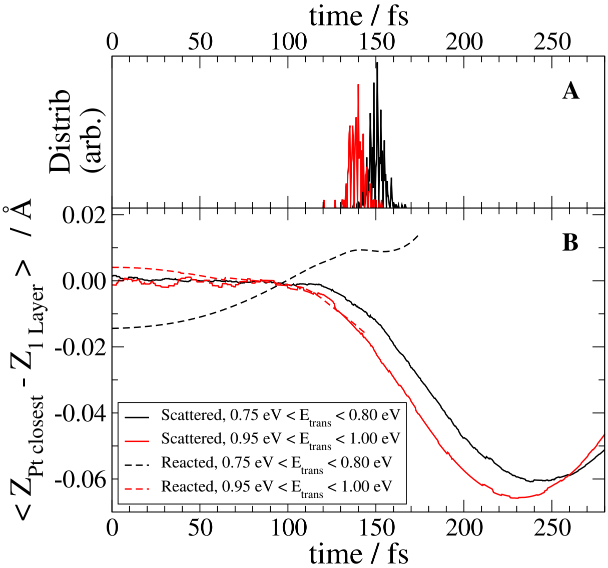

Figure 5.4: (A): Arrival distributions at the inner turning point in Z for scattered molecules for 0.75 eV $< E_i <$ 0.80 eV (black) and for 0.95 eV $< E_i <$ 1.00 eV (red). (B): Vertical displacement of the closest first layer atom as a function of time, averaged over scattered (solid lines) and reacted (dashed lines) laser-off trajectories in the two ranges of E_i (black and red, as in panel A).

towards the projectile, thereby lowering the barrier and increasing the relative velocity. At higher E_i reaction occurs regardless of the surface atom behaviour, and only recoil is seen [41]. Our AIMD results confirm the validity of the same result obtained earlier with models using a much more simplified treatment of surface motion [24, 38, 39, 41].

5.4 Summary and Conclusions

The AIMD method has been used for the first time to obtain quantitative results for the direct reaction of a polyatomic gas phase molecule colliding with a metal surface, in the form of statistically accurate reaction probabilities. The comparison of the AIMD results with new quantum-state resolved experiments on the reaction of CHD_3 with Pt(111), which is a prototypical example of such reactions, suggests that the AIMD method using the general purpose PBE functional is capable of a semi-quantitative description of this category of reactions. Somewhat surprisingly, even though methane has fairly large rotational constants, our calculations suggest that a sudden approximation to the rotations should yield an accurate description of this reaction. This suggests a general applicability of the rotational sudden approximation to direct reactions of polyatomic molecules with surfaces for hyperthermal energies. The suitability of the sudden approximation for describing the lateral motion of the methane molecule, and the active role played by the surface atom motion in the dissociation dynamics at low collision energies, which have been previously put forward for similar systems (Refs. [16,23,24] and Refs. [24,38,39,41], respectively), have been confirmed by the current study. The AIMD calculations also reproduce the observed bond-selectivity in the dissociation of CH-stretch pre-excited CHD_3, and they suggest that the PBE functional underestimates the reaction barrier height by ≈ 0.1 eV for CH_4 + Pt(111). The latter finding, and similar observations for H_2 + Cu(111) and Ru(0001), suggest that the PBE and PW91 functionals, which were used in earlier high-dimensional QD and QCT calculations on methane dissociation on Ni and Pt surfaces, underestimate the barriers for these systems by a similar amount.

5.A Appendix

5.A.1 Experimental Methods

Quantum state resolved dissociation probabilities of CHD_3 on Pt(111) were measured in a molecular beam/surface science apparatus described previously [27, 65]. Reflection absorption infrared spectroscopy (RAIRS) was used to detect the nascent dissociation products CD_3(ads) and CHD_2(ads) of CHD_3 on the cold Pt(111) surface ($T_s = 120$ K) in order to measure both the absolute dissociation probability (S_0) and the branching ratio of the C-H and C-D cleavage channels with and without state specific laser preparation of the incident CHD_3. For the laser-off measurements above 0.7 eV incident energy, where the dissociation coefficient exceeds 1%, the King&Wells beam reflectivity technique [66] was used to measure absolute sticking coefficients of CHD_3 on Pt(111). With this method, the branching ratio could not be measured.

Molecular beam parameters are supplied in Table 5.A.1. The stream velocity (v_s) and the width parameter (α) of the beams have been obtained by fitting a flux-weighted velocity distribution (Equation 4 of Ref. [67]) to recorded TOF spectra.

5.A.2 Convergence Tests

Table 5.A.2 shows the convergence of our computational setup in the evaluation of the energy barrier (E_b) for CH_4 + Pt(111). E_b is calculated as $E_{b,abs} - E_\infty$, where E_∞ is the energy of the system with the CH_4 molecule in its equilibrium geometry at large distance from the ideal metal slab and $E_{b,abs}$ is the absolute barrier energy, computed for the minimum energy transition state configuration (the D1 configuration in figure 3 of Ref. [55]). The calculations with a 2x2 surface unit cell show that converged results may be obtained with 5 layers. The calculations with 5 layers show that converged results may be obtained with a 3x3 surface unit cell. We estimate that, with our computational setup, the PBE value of E_b is converged to within 1 kcal/mol (43 meV).

Translational Energy (eV)	Total Energy (eV)	State	Set Nozzle Temperature (K)	Gas Temperature (K)	v_s (m/s)	α (m/s)
0.514	0.552	Laser-off	500	534	2263	156
0.727	0.837	Laser-off	700	764	2679	227
0.781	**0.919**	**Laser-off**	**750**	**836**	**2774**	**248**
0.830	**0.997**	**Laser-off**	**800**	**902**	**2857**	**265**
0.875	**1.074**	**Laser-off**	**850**	**971**	**2926**	**291**
1.376	**1.487**	**Laser-off**	**700**	**768**	**3739**	**417**
1.535	**1.7016**	**Laser-off**	**800**	**901**	**3948**	**482**
0.276	0.648	$\nu_1 = 1$	-	300	1662	98
0.397	**0.769**	$\nu_1 = 1$	**400**	**412**	**1992**	**122**
0.514	**0.886**	$\nu_1 = 1$	**500**	**534**	**2263**	**156**

Table 5.A.1: Molecular beam parameters. v_s and α represent the stream velocity and the width parameter of the beams, respectively. The beams which have been simulated using AIMD have been highlighted.

Surface Unit Cell Size	Number of Atomic Layers	k-point grid	Cut-off energy (eV)	E_b (eV)
2x2	4	8x8x1	350	0.926
2x2	4	8x8x1	400	0.931
2x2	4	8x8x1	600	0.933
2x2	4	16x16x1	350	0.928
2x2	5	8x8x1	350	0.872
2x2	10	8x8x1	350	0.885
3x3	4	6x6x1	350	0.887
3x3	**5**	**4x4x1**	**350**	**0.805**
3x3	5	4x4x1	500	0.811
3x3	5	8x8x1	350	0.813
4x4	4	4x4x1	350	0.861
4x4	5	4x4x1	500	0.801

Table 5.A.2: Convergence tests of the electronic structure calculations for CH_4 + Pt(111). The barrier energy E_b has been computed varying the surface unit cell size, the number of atomic layers in the slab, the k-point grid size (Γ-point is always included) and the cut-off energy for the plane waves expansion. The energy barrier of our computational setup has been highlighted.

5.A.3 Avoiding the Pitfalls of the Quasi-Classical Trajectory (QCT) Method

5.A.3.1 Zero Point Energy (ZPE) Conservation Problems

Calculations for D_2 + Cu(111) show that, if motion in all molecular DOFs is modeled for average total energies of the molecule $\langle E_{tot} \rangle$ above the ZPE-corrected minimum barrier height (E_b^c), QCT calculations essentially reproduce the quantum dynamics (QD) results [68]. We therefore expect that ZPE conservation problems, which may hamper the accurate calculation of reaction probabilities near the reaction threshold if some of the coordinates are kept frozen or treated with other dynamical approximations [22,69], will not much affect the accuracy of our calculations, which are all done for $\langle E_{tot} \rangle$ well above E_b^c (Table 5.1).

To make sure that ZPE conservation problems have no significant effect on our calculations, we looked at whether evidence of ZPE violation could be found in our actual AIMD calculations. No strong proof of ZPE violation has been found in the dynamics as a possible reason of the too high reaction probability even at low average incidence energy $\langle E_i \rangle$: the available energy to the reaction (the sampled E_{tot}) is larger than the ZPE-corrected minimum energy barrier from static calculations, in almost all (i.e., 143) of the 144 reacted trajectories computed in total for the three lowest $\langle E_i \rangle$ laser-off simulations, and in all of the laser-on reacted trajectories. Furthermore, the reaction probability is overestimated even at the highest $\langle E_i \rangle$, where the experimental reaction probabilities are larger than 15% and ZPE violation is not expected to play a role.

5.A.3.2 Artificial Intramolecular Vibrational Energy Redistribution (IVR)

In order to avoid the potential problem of artificial energy flow among vibrations alluded to above, we focus on two types of experiment. The first (‘laser-off’) experiment addresses the reactivity of CHD_3 in a hyperthermal supersonic beam, in which the vibrational ground state has the highest population. In the second type of experiment the ν_1 (CH-stretch) mode is pre-excited with one quantum but due to the localization of the

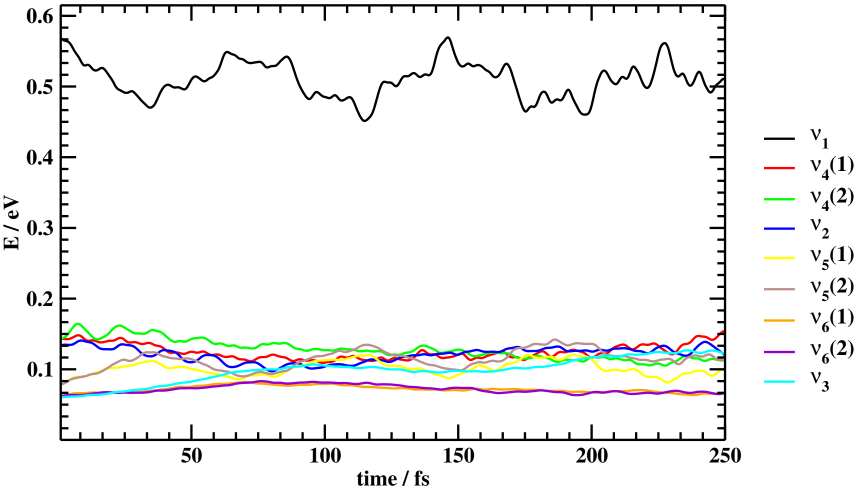

Figure 5.A.1: The normal mode energies are plotted as a function of time for freely vibrating CH-stretch (ν_1, in black) excited CHD_3. The energies plotted here are the result of an average over 100 trajectories.

vibrational mode on the CH bond, this mode is off-resonance with other vibrations, so that artificial intra-molecular vibrational energy redistribution (IVR) is minimized [54]. We carefully verified that AIMD is able to simulate freely vibrating CH-stretch (ν_1) excited CHD_3 without significant energy ‘leakage’ from the ν_1 mode to others. Figure 5.A.1 shows the normal mode energies as a function of time, averaged over 100 trajectories for which the initial conditions (normal mode vibrational coordinates and velocities) sample classical microcanonical distributions. The normal mode energies have been evaluated by projecting the vibrational coordinates of CHD_3 onto its equilibrium normal mode coordinates. As evident from Figure 5.A.1, the vibrational energy imparted to the ν_1 mode remains localized in this vibrational mode on the time-scale of the collisions in our simulations (100-200 fs).

5.A.3.3 Role of Tunneling

Early on, it was argued that an exponential dependence of the dissociation probability on E_i observed in supersonic molecular beam experiments between $E_i = 0.70$ to 0.98 eV should be due to tunneling, on the basis of a one-dimensional model [25]. However, this model implied a very high ZPE-corrected barrier height of 1.25 eV, whereas experiments

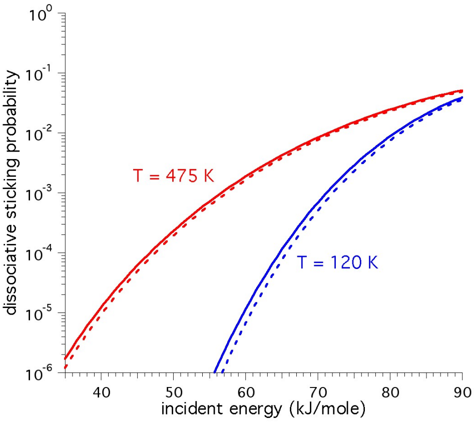

Figure 5.A.2: Dissociative sticking probability as a function of incident energy for vibrationally ground state CH_4 incident on Ni(100) at the temperatures indicated. The curves are from the reaction path model described in Ref. [23], for the case where the vibrationally non-adiabatic couplings are set equal to zero. The dashed lines exclude contributions to the sticking from tunneling. The results reported for $T_s = 475$ K are from Ref. [23].

suggest a value of only 0.6 ± 0.2 eV [17].

Even though we use it here for a different surface (Ni(100)), the reaction path Hamiltonian model described in Ref. [23] allows an estimate to be made of the tunneling contribution for the lowest surface temperature (T_s) considered in our calculations on CHD_3+Pt(111). The reaction probability has been computed by averaging the results of one-dimensional (1D) quantum dynamics calculations over surface sites and a surface atom coordinate, after setting all the vibrationally non-adiabatic couplings to zero (see figure 9 of Ref. [23] and the corresponding more detailed discussion in Ref. [23]). The tunneling contribution can be excluded by setting all the 1D reaction probabilities ≤ 0.5 equal to zero. The reaction probability curves including and excluding tunneling contributions are plotted in Figure 5.A.2. The two curves are displaced from one another along the energy axis by less than 1 kJ/mol (0.01 eV) when $S_0 = 10^{-3}$ for $T_s = 120$ K.

Since we only simulate conditions for which the experimental reaction probabilities are > 0.01, we do not expect that the neglect of tunneling effects in our calculations has a large effect on our most important conclusions. In particular, the neglect of tunneling should hardly affect our conclusion regarding the barrier height for CHD_3 + Pt(111), the conclusion being that the PBE functional underestimates this quantity by 0.1 eV. This does not mean that tunneling does not influence the reaction: at the incidence energy where the quantum mechanical reaction probability is 0.01 (80.5 kJ/mol $\approx$ 0.83 eV), the tunneling contribution to the reaction is approximately 10% (i.e., the tunneling contribution to the reaction probability is approximately 0.001). The reason that the tunneling contribution is so low for this low incidence energy (for Ni(100) the zero-point energy corrected barrier height for the static surface is 0.78 eV [55]) is that even at T_s = 120 K excited surface vibrational states are populated, and this allows reaction through a classical over the barrier mechanism because the outward motion of the surface atom above which methane reacts lowers the reaction barrier [55].

The comparison of calculations on reaction of a supersonic beam of CH_4 with Pt(111) at E_i = 0.62 eV and T_s = 200 K [70], which used a statistical model and either included [17] or excluded [30] the effect of tunneling, likewise suggests only a minor role for tunneling under the conditions addressed by us.

Finally, we also expect no problems due to neglect of tunneling with computing branching ratios for CHD_3 dissociation into CD_3 + H and CHD_2 + D, as a recent QCT study was able to show that the strong kinetic isotope effect observed previously when comparing CH_4 to CD_4 dissociation on Pt(111) [3] could be explained on the basis of the molecules' different ZPEs [18].

Bibliography

[1] G. Jones, J. G. Jakobsen, S. S. Shim, J. Kleis, M. P. Andersson, J. Rossmeisl, F. Abild-Pedersen, T. Bligaard, S. Helveg, B. Hinnemann, J. R. Rostrup-Nielsen, I. Chorkendorff, J. Sehested, and J. K. Nørskov, J. Catal. **259**, 147 (2008).

[2] L. B. F. Juurlink, D. R. Killelea, and A. L. Utz, Prog. Surf. Sci. **84**, 69 (2009).

[3] A. C. Luntz and D. S. Bethune, J. Chem. Phys. **90**, 1274 (1989).

[4] C. T. Rettner, H. E. Pfnür, and D. J. Auerbach, J. Chem. Phys. **84**, 4163 (1986).

[5] R. D. Beck, P. Maroni, D. C. Papageorgopoulos, T. T. Dang, M. P. Schmid, and T. R. Rizzo, Science **302**, 98 (2003).

[6] L. B. F. Juurlink, P. R. McCabe, R. R. Smith, C. L. DiCologero, and A. L. Utz, Phys. Rev. Lett. **83**, 868 (1999).

[7] P. Maroni, D. C. Papageorgopoulos, M. Sacchi, T. T. Dang, R. D. Beck, and T. R. Rizzo, Phys. Rev. Lett. **94**, 246104 (2005).

[8] J. Higgins, A. Conjusteau, G. Scoles, and S. L. Bernasek, J. Chem. Phys. **114**, 5277 (2001).

[9] L. Halonen, S. L. Bernasek, and D. J. Nesbitt, J. Chem. Phys. **115**, 5611 (2001).

[10] R. R. Smith, D. R. Killelea, D. F. DelSesto, and A. L. Utz, Science **304**, 992 (2004).

[11] D. R. Killelea, V. L. Campbell, N. S. Shuman, and A. L. Utz, Science **319**, 790 (2008).

[12] L. Chen, H. Ueta, R. Bisson, and R. D. Beck, Faraday Discuss. **157**, 285 (2012).

[13] B. L. Yoder, R. Bisson, and R. D. Beck, Science **329**, 553 (2010).

[14] M. B. Lee, Q. Y. Yang, and S. T. Ceyer, J. Chem. Phys. **87**, 2724 (1987).

[15] B. Jiang and H. Guo, J. Phys. Chem. C **117**, 16127 (2013).

[16] B. Jiang, R. Liu, J. Li, D. Xie, M. Yang, and H. Guo, Chem. Sci. **4**, 3249 (2013).

[17] S. B. Donald, J. K. Navin, and I. Harrison, J. Chem. Phys. **139**, 214707 (2013).

[18] X. J. Shen, A. Lozano, W. Dong, H. F. Busnengo, and X. H. Yan, Phys. Rev. Lett. **112**, 046101 (2014).

[19] M. Sacchi, D. J. Wales, and S. J. Jenkins, J. Phys. Chem. C **115**, 21832 (2011).

[20] M. Sacchi, D. J. Wales, and S. J. Jenkins, Phys. Chem. Chem. Phys. **14**, 15879 (2012).

[21] M. Sacchi, D. J. Wales, and S. J. Jenkins, Comput. Theor. Chem. **990**, 144 (2012).

[22] M. Mastromatteo and B. Jackson, J. Chem. Phys. **139**, 194701 (2013).

[23] B. Jackson and S. Nave, J. Chem. Phys. **135**, 114701 (2011).

[24] B. Jackson and S. Nave, J. Chem. Phys. **138**, 174705 (2013).

[25] G. Schoofs, C. Arumainayagam, M. Master, and R. Madix, Surf. Sci. **215**, 1 (1989).

[26] R. Bisson, M. Sacchi, T. Dang, B. Yoder, P. Maroni, and R. Beck, J. Phys. Chem. A **111**, 12679 (2007).

[27] L. Chen, H. Ueta, R. Bisson, and R. D. Beck, Rev. Sci. Instrum. **84**, 053902 (2013).

[28] E. M. Karp, T. L. Silbaugh, and C. T. Campbell, J. Am. Chem. Soc. **135**, 5208 (2013).

[29] F. Zaera, Surf. Sci. **262**, 335 (1992).

[30] S. B. Donald and I. Harrison, Phys. Chem. Chem. Phys. **14**, 1784 (2012).

[31] B. Ølgaard Nielsen, A. C. Luntz, P. M. Holmblad, and I. Chorkendorff, Catal. Lett. **32**, 15 (1995).

[32] G. J. Kroes, Phys. Chem. Chem. Phys. **14**, 14966 (2012).

[33] J. Zheng, Y. Zhao, and D. G. Truhlar, J. Chem. Theory Comput. **5**, 808 (2009).

[34] R. Peverati and D. G. Truhlar, Phil. Trans. R. Soc. A **372**, 20120476 (2014).

[35] M. Wijzenbroek and G. J. Kroes, J. Chem. Phys. **140**, 084702 (2014).

[36] J. Greeley, J. Nørskov, and M. Mavrikakis, Annu. Rev. Phys. Chem. **53**, 319 (2002).

[37] S. Nave and B. Jackson, J. Chem. Phys. **130**, 054701 (2009).

[38] S. Nave and B. Jackson, J. Chem. Phys. **127**, 224702 (2007).

[39] S. Nave and B. Jackson, Phys. Rev. Lett. **98**, 173003 (2007).

[40] A. K. Tiwari, S. Nave, and B. Jackson, Phys. Rev. Lett. **103**, 253201 (2009).

[41] A. K. Tiwari, S. Nave, and B. Jackson, J. Chem. Phys. **132**, 134702 (2010).

[42] C. Díaz, E. Pijper, R. A. Olsen, H. F. Busnengo, D. J. Auerbach, and G. J. Kroes, Science **326**, 832 (2009).

[43] G. Kresse and J. Hafner, Phys. Rev. B **47**, 558 (1993).

[44] G. Kresse and J. Hafner, Phys. Rev. B **49**, 14251 (1994).

[45] G. Kresse and J. Furthmüller, Comput. Mat. Sci. **6**, 15 (1996).

[46] G. Kresse and J. Furthmüller, Phys. Rev. B **54**, 11169 (1996).

[47] G. Kresse and D. Joubert, Phys. Rev. B **59**, 1758 (1999).

[48] P. E. Blöchl, Phys. Rev. B **50**, 17953 (1994).

[49] J. W. Arblaster, Platinum Met. Rev. **41**, 12 (1997).

[50] J. W. Arblaster, Platinum Met. Rev. **50**, 118 (2006).

[51] F. Nattino, C. Díaz, B. Jackson, and G. J. Kroes, Phys. Rev. Lett. **108**, 236104 (2012).

[52] E. B. Wilson, J. Am. Statist. Assoc. **22**, 209 (1927).

[53] A. Agresti and B. A. Coull, Am. Stat. **52**, 119 (1998).

[54] Z. Xie, J. M. Bowman, and X. Zhang, J. Chem. Phys. **125**, 133120 (2006).

[55] S. Nave, A. K. Tiwari, and B. Jackson, J. Chem. Phys. **132**, 054705 (2010).

[56] J. P. Perdew, K. Burke, and M. Ernzerhof, Phys. Rev. Lett. **77**, 3865 (1996).

[57] J. P. Perdew, K. Burke, and M. Ernzerhof, Phys. Rev. Lett. **78**, 1396 (1997).

[58] J. P. Perdew, J. A. Chevary, S. H. Vosko, K. A. Jackson, M. R. Pederson, D. J. Singh, and C. Fiolhais, Phys. Rev. B **46**, 6671 (1992).

[59] F. Viñes, Y. Lykhach, T. Staudt, M. P. A. Lorenz, C. Papp, H. P. Steinrück, J. Libuda, K. M. Neyman, and A. Görling, Chem. - Eur. J. **16**, 6530 (2010).

[60] P. Nieto, D. Farías, R. Miranda, M. Luppi, E. J. Baerends, M. F. Somers, M. J. T. C. van der Niet, R. A. Olsen, and G. J. Kroes, Phys. Chem. Chem. Phys. **13**, 8583 (2011).

[61] F. F. Crim, Proc. Natl. Acad. Sci. U. S. A. **105**, 12654 (2008).

[62] D. Halstead and S. Holloway, J. Chem. Phys. **93**, 2859 (1990).

[63] B. Jackson, F. Nattino, and G. J. Kroes, J. Chem. Phys. **141**, 054102 (2014).

[64] C. Roche, J. P. Champion, and A. Valentin, J. Mol. Spectrosc. **160**, 517 (1993).

[65] H. Ueta, L. Chen, R. D. Beck, I. Colon-Diaz, and B. Jackson, Phys. Chem. Chem. Phys. **15**, 20526 (2013).

[66] D. A. King and M. G. Wells, Proc. R. Soc. Lond. A-Math. Phys. Sci. **339**, 245 (1974).

[67] H. A. Michelsen and D. J. Auerbach, J. Chem. Phys. **94**, 7502 (1991).

[68] C. Díaz, R. A. Olsen, D. J. Auerbach, and G. J. Kroes, Phys. Chem. Chem. Phys. **12**, 6499 (2010).

[69] G. R. Darling, Z. S. Wang, and S. Holloway, Phys. Chem. Chem. Phys. **2**, 911 (2000).

[70] J. Harris, J. Simon, A. C. Luntz, C. B. Mullins, and C. T. Rettner, Phys. Rev. Lett. **67**, 652 (1991).

Chapter 6

Methane Dissociation on Pt(111): Searching for a Specific Reaction Parameter Density Functional

Abstract

The theoretical description of methane dissociating on metal surfaces is a current frontier in the field of gas-surface dynamics. Dynamical models that aim at achieving an highly accurate description of this reaction rely on potential energy surfaces based on density functional theory calculations at the generalized gradient approximation. We focus here on the effect that the exchange-correlation functional has on the reactivity of methane on a metal surface, using CHD_3 + Pt(111) as a test case. We present new *ab initio* molecular dynamics calculations performed with various density functionals, looking also at functionals that account for van der Waals (vdW) interactions. Results show that the use of a weighted average of the PBE and the RPBE exchange functionals together with a vdW-corrected correlation functional leads to good agreement with quantum state-resolved experimental data for the sticking probability.

6.1 Introduction

The level of accuracy that can be achieved in modeling gas-surface reaction dynamics strongly depends on the accuracy of the interaction potential employed. Assuming the Born-Oppenheimer approximation to be valid, the state-of-the-art electronic structure method that allows the computation of potential energy surfaces (PESs) for molecules interacting with metal surfaces is density functional theory (DFT) at the generalized gradient approximation (GGA) level [1]. However, many implementations of the GGA exist due to the unknown exchange-correlation functional (E_{XC}). Even though functionals at the GGA level are not expected to be accurate in predicting, for instance, the reaction barrier height for a given system (for gas phase reactions the lowest mean absolute error is 3.8 kcal/mol, as obtained with the MOHLYP2 functional [2, 3]), semi-empirical versions of E_{XC} allow one to produce accurate PESs through the fitting of one parameter to a single set of experimental data [4, 5].

Methane dissociation on metal surfaces is a reaction for which an accurate theoretical description has not yet been achieved. Many of the studies that focused on this system have been motivated by fundamental questions [6–27], but the reaction is also of industrial interest, as it is believed to represent a rate limiting step in the methane steam reforming process [28]. Mode specificity [11] with unusually large vibrational efficacies [12, 13], bond selectivity for the partially deuterated isotopologues [14, 21] and rotational alignment dependence [16,29], are just a few examples of the interesting properties of the sticking probabilities that have been observed for this system.

We have previously shown (Ref. [30] and Chapter 5) that by using the PBE density functional [31,32] in combination with the *ab initio* molecular dynamics (AIMD) method, semi-quantitative agreement can be obtained with quantum state-resolved experimental sticking probabilities. The combination of the AIMD method and the system considered, CHD_3 + Pt(111), is suitable for testing the accuracy of the underlying PES. In fact, the quasi-classical trajectory technique can be used to accurately study the vibrational efficacy of the CH-stretch mode, as this vibrational mode is off-resonance with other modes due to the mass mismatch between the H and the heavier D atoms. Therefore, less 'artificial' intramolecular vibrational energy redistribution caused by the use of classical mechanics is expected for this isotopologue of methane in the case of pre-excitation of the CH-stretch mode [33]. Furthermore, by using the AIMD method no dynamical approximation with respect to the time evolution of any of the molecular degrees of freedom has to be made *a priori* [30,34] (see also Chapter 5). Moreover, the motion of the surface atoms, which has been shown to play a role in the dissociation dynamics of methane on metal surfaces [30,35], can be explicitly included in the dynamics.

The agreement with experimental data obtained using the PBE functional was limited (Ref. [30] and Chapter 5): The reactivity computed when simulating molecular beams in which the vibrational ground state is the most populated state ('laser-off' experiments) is overestimated. Furthermore, the vibrational efficacy obtained for the CH-stretch mode of CHD_3 is underestimated. In order to tackle these limitations, we present here a study of the influence of E_{XC} on the dissociation of methane on Pt(111). Our goal is to develop a semi-empirical density functional for this system, following the specific reaction parameter (SRP) approach. This approach, inspired by the work of Truhlar and coworkers [36,37], has been successfully applied to the reactive scattering of H_2 from low-index copper surfaces [4,5,38]. A SRP functional for this system, to be considered as such, must produce good agreement with the laser-off experimental reaction probabilities on the whole energy range for which data are available. Furthermore, it must predict the correct vibrational efficacy for the CH-stretch mode. We have considered various functionals, including functionals that mimic van der Waals (vdW) interactions [39], motivated by recent studies that demonstrated the improved description of two molecule-surface reactions achieved with vdW-corrected density functionals [40,41]. Note that the long ranged dispersion interactions are generally not described by traditional GGA functionals. First, we have investigated the presence of the vdW physisorption well that appears if a vdW-corrected correlation functional is employed. Secondly, static calculations have been performed to identify the minimum barrier height for each of the functionals considered. Finally, we present new AIMD calculations for CHD_3 dissociation on Pt(111), comparing the computed sticking probabilities to the previous

PBE-AIMD calculations and to the results of quantum state-resolved experiments [30].

The results indicate that the use of a density functional that employs the correlation functional of Dion et al. [39], which is able to mimic vdW-type interactions, and a weighted average of the PBE and the RPBE [42] exchange functionals, leads to improved agreement with experimental data. Surprisingly, this density functional returns a minimum barrier height that is equal to the PBE barrier height, suggesting that also other aspects of the PES affect the reactivity. The larger and improved vibrational efficacy obtained for the CH-stretch mode can be explained by invoking Polanyi's rule [43], according to which the more extended the dissociating CH bond is at the transition state, the higher should be the vibrational efficacy.

The structure of this chapter is as follows. In Section 6.2 the methodology is described. In Section 6.3, all the results are presented and discussed: Static calculations that focus on the vdW well (Section 6.3.1) and on the dissociation barrier (Section 6.3.2), and AIMD calculations (Section 6.3.3). Finally, the conclusions are presented in Section 6.4.

6.2 Methods

The sticking probability S_0 of methane on Pt(111) has been determined using the AIMD technique [44, 45]. Details about the calculations have been given previously (Ref. [30] and Chapter 5) and are only briefly summarized here. A (3x3)-surface-unit-cell slab with 5 atomic layers is employed to model the surface, and 13 Å of vacuum space have been used to separate periodic replicas of the surface. The bulk lattice constant as well as the interlayer distances have been self-consistently relaxed for each of the tested density functionals. The electronic structure calculations are characterized by an energy cutoff for the plane wave expansion equal to 350 eV. A Γ-centered 4x4x1 k-point grid has been employed to sample the first Brillouin zone, with the projector augmented wave (PAW) method [46, 47] to represent core electrons and a Fermi smearing with width parameter $\sigma = 0.1$ eV. All the calculations have been performed with the Vienna *ab initio* simulation package (VASP) [46,48–52]. In order to mimic surface temperature effects, the optimized

E_{XC}	a
PBE	3.975
RPBE	3.991
vdW-DF	4.032
optPBE-vdW	3.990
PBE-vdW	4.014
RPBE-vdW	4.039
RPBE:PBE/0.24:0.76	3.975
RPBE:PBE/0.1:0.9-vdW	4.017
Experimental	3.916

Table 6.1: Optimized lattice constants (in Å) for bulk Pt calculated using the various tested exchange-correlation functionals. The experimental value is from Refs. [53, 54].

lattice constants have been expanded according to experimental information [53, 54]. Note that for all the tested functionals, the optimized lattice constants (reported in Table 6.1) are in reasonable agreement with the experimental value of 3.916 Å [53, 54]. Displacements and velocities are initially assigned to the surface atoms to simulate their thermal motion, with exception of the atoms of the bottommost layers, which are kept fixed at their ideal positions. The procedure employed to sample the surface initial conditions is essentially the same as described in Ref. [30] and Chapter 5. To summarize, clean surface dynamical runs in which the number of particles in the simulation box, the volume and the total energy are kept constant (NVE runs), are employed to equilibrate ten surfaces at a specific surface temperature ($T_s = 120$ K and $T_s = 500$ K).

Between 500 and 2000 NVE trajectories have been computed to estimate S_0 for each molecular beam simulated. The initial conditions of the trajectories are chosen such that the velocity of the center of mass of the molecule samples the velocity distribution of the beam [55] determined by the experimentalists using time-of-flights (TOF) techniques (all beam parameters have been reported in Ref. [30] and Chapter 5). The angular momentum of the molecule is initially set to zero. Standard Monte Carlo techniques are employed to represent the initial vibrational state of the molecule, as already described in Ref. [30] and Chapter 5. We exploit the quasi-classical trajectory (QCT) method, which means that vibrational zero-point energy (ZPE) is initially imparted to the impinging molecules. With respect to our previous work, we have slightly modified the operational definition of a reactive event. A trajectory is considered reacted if a CH or CD bond becomes larger than 2 Å and remains in this configuration for at least 100 fs, or, alternatively, if a CH or CD bond becomes larger than 3 Å. This operational definition accounts, at least in part, for the possibility of barrier recrossing. No considerable difference has been found if this definition of reactive event is applied to the previous PBE-AIMD calculations. A trajectory is considered scattered if the center of mass of the molecule reaches the distance of 6 Å from the surface, with the velocity pointing away from the surface. Error bars on the sticking probability values have been estimated using the Wilson method [56] and represent 95% confidence interval unless otherwise stated.

For what concerns the vibrational population of the supersonic molecular beams simulated, two types of beams have been considered. In the first type of beam, the vibrational ground state is the most populated state, but vibrationally exited molecules are also present due to collisions with a heated nozzle ('laser-off' beams). In order to simulate these beams, we have assumed the vibrational population to be Boltzmann-like with a vibrational temperature equal to the gas temperature. In the second class of beam, the CHD_3 molecules are selectively prepared with one quantum of vibration in the CH-stretch (ν_1) mode using a laser. Only molecules in the $\nu_1 = 1$ vibrational state have been used to simulate this second type of beam.

Two types of functional have been employed to represent the exchange-correlation functional in the electronic structure calculations. The first type of functional employed is characterized by PBE correlation [31, 32]. Apart from the PBE functional itself, we have considered the RPBE functional [42] and the use of a density functional that employs PBE correlation and an exchange functional of the following form:

$$E_X = x \cdot E_X^{RPBE} + (1 - x) \cdot E_X^{PBE}, \tag{6.1}$$

where E_X^{PBE} and E_X^{RPBE} are the PBE and the RPBE exchange functionals, respectively. The RPBE functional is known to be more repulsive than the PBE functional. By using a functional as in Equation 6.1 we can tune the barrier height of a system by changing the value of the x coefficient [4, 5].

Wijzenbroek et al. [40] have recently shown that vdW-corrected density functionals improve the description of a molecule-surface reaction (H_2 + Ru(0001)). Moreover, vdW-corrected density functionals have been shown to better describe properties such as adsorption energy and reaction barriers for N_2 interacting with W(110), compared to traditional density functionals like PBE and RPBE. Motivated by these findings, the second class of functionals that we have tested is characterized by the non-local correlation functional proposed by Dion et al. [39] to mimic dispersion interactions (van der Waals forces), which are generally not correctly described with regular GGA functionals. Note that an efficient implementation of this non-local correlation functional has recently become available [52, 57]. This correlation functional (from now on vdW correlation) has been originally paired with revPBE [58] exchange, forming the so-called vdW-DF exchange-correlation functional [39], but it could in principle be used in combination with any exchange functional. In the current work, in addition to the vdW-DF functional, we have tested vdW correlation paired with PBE exchange (PBE-vdW), with RPBE exchange (RPBE-vdW), with optPBE exchange (optPBE-vdW) [59] and with an exchange functional of the form described by Equation 6.1. Note that the optPBE exchange functional is also defined as a weighted average of the PBE and the RPBE exchange expressions, with an addition modification of the κ and μ parameters which appear in both the PBE and the RPBE exchange functionals [59].

Barrier heights have been determined with climbing image nudged elastic band (CINEB) calculations, as implemented in the VASP transition state tools developed by Henkelman and Jónsson [60, 61]. Nave and Jackson explored different reaction paths for methane dissociating on Pt(111) [62, 63]. They identified the reaction pathway that leads to the adsorption of both the methyl group and the hydrogen atom on top sites as the path with the lowest energy transition state (TS). We have considered the same path for the CINEB calculations, optimizing four images between a methane molecule placed with its center of mass 4 Å far from the surface (the reactant state) and the dissociated configuration (the product state). The path has been optimized until all the forces became smaller than 15 meV/Å. Note that for all the tested functionals the slab employed has been constructed using the optimized bulk lattice constant. Note also that the surface atoms have been kept fixed at their equilibrium positions during the CINEB calculations.

6.3 Results and Discussion

6.3.1 The Van der Waals Well

As mentioned earlier, regular GGA density functionals are known to fail at describing dispersion interactions. As a consequence, functionals like PBE or RPBE do not correctly model the physisorption of molecules on metal surfaces. Figure 6.1 A shows the interaction energy calculated as a function of the distance between the center of mass of CH_4 and an ideal Pt(111) slab (Z coordinate). The geometry of the molecule has been kept frozen at the optimized gas-phase configuration. The molecule is placed above the hcp hollow site with one hydrogen atom pointing away from the surface ($\theta = 0°$) and the other H atoms oriented toward the top sites. Note that the zero is defined as the energy of a methane molecule in its gas-phase relaxed geometry placed midway between two periodic replicas of the slab ($Z = 6.5$ Å). Using the PBE functional, only a shallow potential well that is about 20 meV deep is observed at $Z \approx 4$ Å. Using the vdW correlation functional that accounts for dispersion interactions, a considerably deeper adsorption well is obtained. As expected from the more repulsive nature of the RPBE exchange with respect to the PBE exchange, the vdW well calculated with the PBE-vdW functional is deeper and the minimum is slightly closer to the surface than for the RPBE-vdW functional. The energy profile for large Z, however, is very similar for the two vdW-corrected functionals: at $Z = 4.5$ Å the interaction energy calculated with the two functionals differs by only 10 meV, and this difference becomes even smaller at larger values of Z. This is consistent with the fact that the correlation functional only (the same for PBE-vdW and RPBE-vdW) is responsible for the interaction at the largest distances [39].

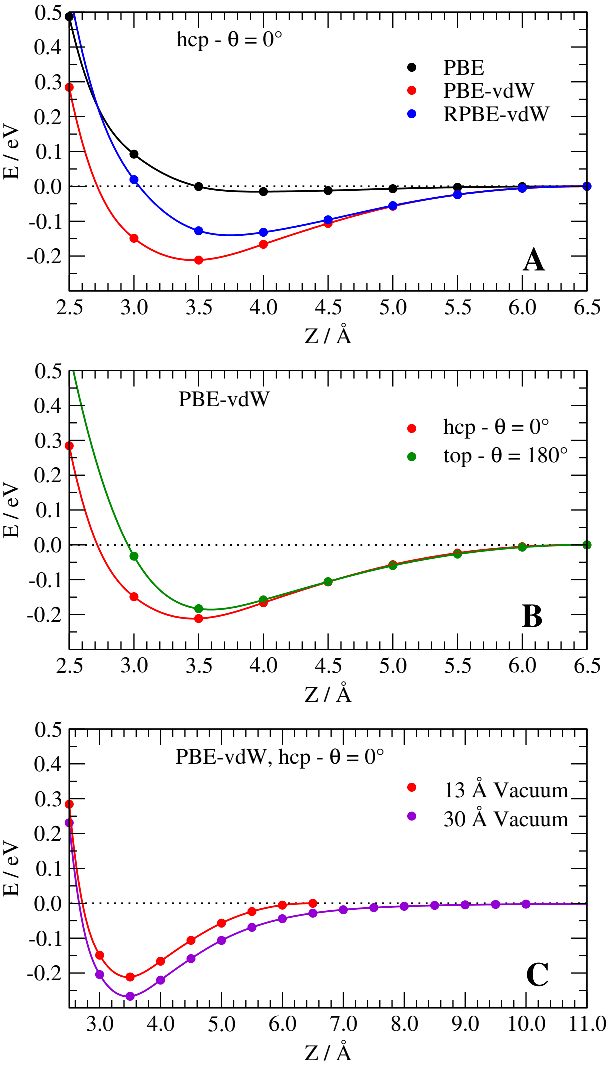

Figure 6.1: Interaction energy as a function of the distance of CH_4 from an ideal Pt(111) surface. We compare the energy profiles for three density functionals (A), for two molecular orientations and surface impact sites (B) and for two computational setups differing only in the amount of vacuum space between two periodic replicas of the slab (C).

In Figure 6.1 C we have plotted two 1D cuts of the PES calculated for the same molecular configuration chosen for Figure 6.1 A, using the PBE-vdW functional but employing different amounts of vacuum space between the slab and its periodic replica. The curve calculated with the setup characterized by the smaller vacuum space (13 Å) is shifted upwards by about 45 meV with respect to the other curve. For each computational setup the zero of the interaction energy is defined as the energy of a methane molecule in its gas-phase configuration placed midway between two periodic replicas of the slab. Note that for the system with 30 Å of vacuum space, at $Z = 6.0$ Å the interaction energy is about 45 meV. Therefore, the shift between the two curves is due to a residual attractive interaction for the gas-phase configuration of the setup with the smaller vacuum space. Unfortunately, the use of a larger vacuum space leads to an increase in the computational cost of the electronic structure calculations caused by the increased plane wave basis set size. Moreover, performing dynamics with the molecule initially placed at larger distances from the surface requires more time propagation steps for the molecule to reach the surface (and for the molecule to reach again the gas-phase after the impact with the surface, in the case of a scattering event). We have estimated that adding 3 Å of vacuum space to our computational setup would overall increase the computational cost of a scattered trajectory by about 50 %. On the other hand, using 13 Å of vacuum space affects the energetics by only a systematic 45 meV upward shift of the gas-phase level, while it allows to keep the computational cost relatively low. We only have to keep in mind that the presented values of adsorption energies and energy barriers calculated using the vdW correlation functional apply to the computational setup that we have employed, while with the use of a larger vacuum space the adsorption energies are expected to be about 45 meV larger and the barriers 45 meV lower.

In Figure 6.1 B we plot similar energy profiles as shown in Figure 6.1 A but for two different adsorption sites and molecular orientations. The functional employed is PBE-vdW. The two curves are only slightly different, and the biggest differences are observed at closer distances from the surface, suggesting that the multidimensional PES calculated using the vdW correlation functional is rather independent of X and Y, and of the

E_{XC}	E_{Ads}
PBE-vdW	0.214
RPBE-vdW	0.141
RPBE:PBE/0.1:0.9-vdW	0.205

Table 6.2: Adsorption energies (in eV) corresponding to the bottom of the van der Waals well calculated with various density functionals.

Euler angles of orientation in the proximity of the vdW (physisorption) well. We have optimized the molecular geometry testing various surface impact sites and molecular orientations and we have found that the configuration that corresponds to the minimum of the curves in Figure 6.1 A is the lowest in energy ($E_{ads} = 0.214$) while the adsorption energy differs by less than 43 meV if other molecular adsorption configurations (including other local minima) are considered. Note that for all the adsorption configurations considered the geometry of the molecule does not considerably differ from the gas-phase configuration. In Table 6.2 we report the molecular adsorption energy E_{ads} calculated with three different exchange correlation functionals: PBE-vdW, RPBE-vdW and a functional that employs the vdW correlation and the exchange of the form of Equation 6.1 with $x = 0.1$ (the choice of this value for the x coefficient will become clearer later on). Consistently with the curves reported in Figure 6.1 A, the adsorption energy calculated with the PBE-vdW functional is about 60 meV larger than the RPBE-vdW value, while the RPBE:PBE/0.1:0.9-vdW functional returns an intermediate value. As mentioned earlier in this section, these values of E_{ads} are expected to be about 45 meV larger for a computational setup with a larger amount of vacuum space.

Experimentally, methane is known to molecularly adsorb on Pt(111) with an adsorption energy in the range 0.17 eV - 0.23 eV [64–68]. The values of E_{Ads} reported in Table 6.2 are in fairly good agreement with this experimental range. Considering the extra 45 meV that would have to be added when considering a larger vacuum space, the PBE-vdW and the RPBE:PBE/0.1:0.9-vdW functionals would slightly overestimate the adsorption energy, while the adsorption energy calculated with the RPBE-vdW functional would fall inside the experimental range.

We note in passing that accurately modeling the vdW well for methane interacting with metal surfaces would be relevant for describing two recent sets of experimental data [69,70]. In a first study, the Beck's group focused on the effect that vibrational excitation has on the physisorption probability of CH_4 and on the dissociation probability of CH_4 physisorbed on Pt(111) [69]. In a second study, Utz and coworkers, suggested a precursor-mediated dissociation channel for CH_4 impinging at very low collision energies on Ir(111) [70]. To our knowledge all dynamical studies that have appeared so far relied on density functionals that fail at modeling dispersion interactions, and therefore cannot be used to model these two sets of experimental data.

6.3.2 The Dissociation Barrier

Using CINEB calculations, we have identified the TS along a reaction path that connects a molecule in its equilibrium geometry placed at $Z = 4$ Å to a dissociated configuration corresponding to a methyl fragment and a hydrogen atom adsorbed on two neighboring top sites with one CH bond of the methyl group pointing toward the adsorbed H. This path, illustrated in Figure 6.2, has been suggested by Nave et al. to correspond to the minimum energy path for dissociation for CH_4 on Pt(111) [63]. In Figure 6.2 we plot the energy computed along the dissociation path for the various tested functionals. Note that the density functionals that account for vdW interactions predict negative energies on the reactant side of the barrier, as expected from the presence of a vdW well (see Section 6.3.1). Product energies also can vary significantly, and the dissociation path considered is predicted to be endothermic or slightly exothermic depending on the functional employed.

Some details about the TSs obtained are summarized in Table 6.3, where we report the TS energy (with and without zero-point energy corrections) and some descriptors of the TS geometry: the distance of the C atom to the surface Z_C, the distance of the dissociating H atom to the surface Z_H, the angle included between the dissociating CH bond and the surface normal θ_{diss}, and the length of the dissociating CH bond, r_b. Note again that the TS energies calculated using the vdW correlation functional are expected to be about 45 meV larger for computational setups including a larger amount of vacuum

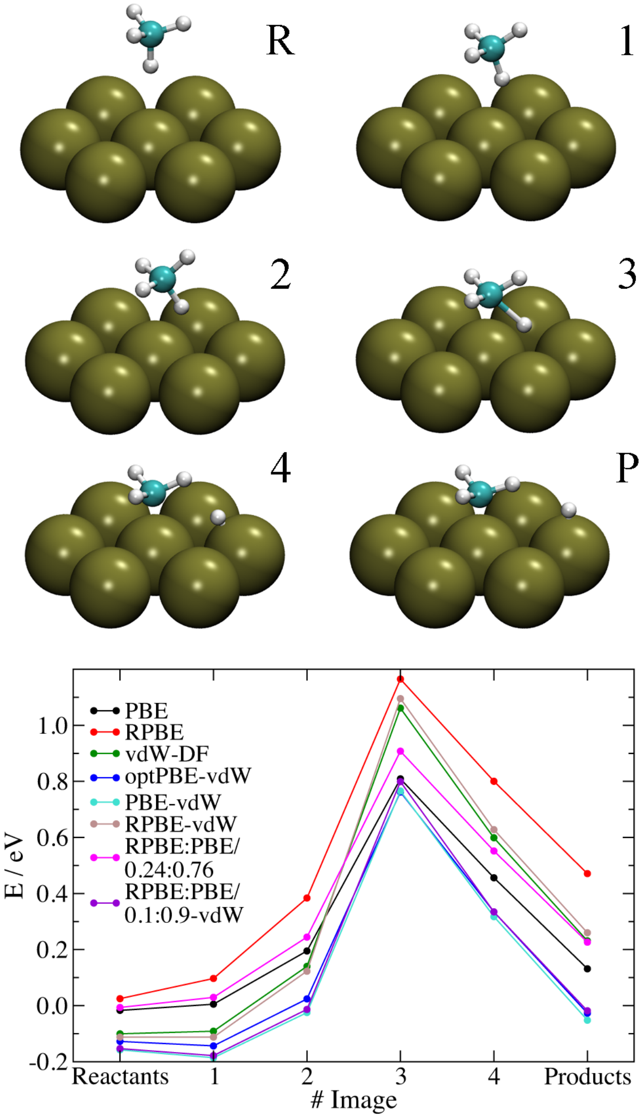

Figure 6.2: Above: Illustration of the molecular configurations that correspond to the images resulting from CINEB calculations. Below: The energy of each image is plotted as a function of the image number (R and P are for reactants and products, respectively). The colors distinguish the various density functionals (lines are for guiding the eye).

E_{XC}	E_b (E_b^c)	Z_C	Z_H	θ_{diss}	r_b
PBE	0.809 (0.687)	2.251	1.213	133.8	1.500
RPBE	1.165 (1.042)	2.274	1.218	133.5	1.534
vdW-DF	1.061 (0.942)	2.307	1.220	134.0	1.566
optPBE-vdW	0.762 (0.638)	2.278	1.224	133.5	1.531
PBE-vdW	0.766 (0.643)	2.286	1.217	133.9	1.541
RPBE-vdW	1.096 (0.976)	2.313	1.219	134.1	1.572
RPBE:PBE/0.24:0.76	0.908 (0.785)	2.257	1.222	133.2	1.512
RPBE:PBE/0.1:0.9-vdW	0.799 (0.679)	2.288	1.225	133.3	1.550

Table 6.3: Transition state properties calculated with various density functionals for CH_4 reacting on Pt(111). E_b^c and E_b are the minimum barrier heights with and without zero-point energy corrections (in eV), Z_C and Z_H are the distance to the surface of the C atom and of the dissociating H atom (in Å), respectively, θ_{diss} is the angle included between the dissociating CH bond and the surface normal (in degrees) and r_b is the length of the dissociating CH bond at the transition state (in Å).

space between periodic replicas of the slab (see Section 6.3.1).

We observe that the geometries of the TSs identified do not differ considerably in the values of θ_{diss} and Z_H, while Z_C and r_b are the most affected by the choice of the density functional employed. We also observe that ZPE corrections affect the barrier heights with a shift downwards of about 0.12 eV, independent of the density functional employed. In the case of a different isotopologue of methane, like CHD_3, slightly different ZPE corrections may apply, which would also depend on whether a CH bond or a CD bond is dissociating. However, we expect these corrections to be the same for all the functionals, and therefore they would not affect the comparison between the functionals.

The TS geometry that we have found using the PBE functional is very similar in the values of Z_C, Z_H, θ_{diss} and r_b to the barrier geometry found by Nave et al. [63]. Small differences could be expected from the different computational setups (surface unit cell size, number of atomic layers, cutoff energy, k-point grid). The TS energy that we have found, however, is about 0.12 eV lower than the value of Ref. [63]. This difference can be explained accounting for the different surface unit cell size and the different number of atomic layers, as already shown in our previous work [30, 34] (see also Chapter 5).

The overestimation of the laser-off reactivity using the PBE functional made us conclude that the PBE functional underestimates the dissociation barrier by about 0.1 eV (Ref. [30] and Chapter 5). A popular density functional that is known to produce higher reaction barriers is the RPBE functional. Viñes et al. [71] reported a TS energy of 1.06 eV for the RPBE functional and a computational setup similar to the one that we have used. Here, we have also obtained a larger E_b value for the RPBE functional (about 1.17 eV, see Table 6.3). The discrepancy could be explained if the barrier reported in Ref. [71] would include surface relaxation effects, which is not explicitly mentioned. In fact, the upward motion of the surface atom below the dissociating molecule has been shown to be able to lower the barrier by up to 0.15 eV for this system [63].

The barrier that we have computed using the RPBE functional is about 0.36 eV larger than the PBE barrier, as expected from the more repulsive nature of the former with respect to the latter. Considering the 0.1 eV energy shift between the experimental reaction probability curve and the PBE simulations, we expect the RPBE functional to highly overestimate the barrier height for this system. We note in passing that the RPBE barrier is slightly 'later' than the PBE barrier, with r_b being about 35 mÅ more elongated. Calculations employing the PBE correlation together with an exchange functional of the form of Equation 6.1 with a mixing coefficient $x = 0.24$, have produced a barrier of 0.91 eV (see Table 6.3), approximately 0.1 eV larger than the E_b value obtained with the PBE functional.

Table 6.3 also includes the results of CINEB calculations performed with various density functionals that employ vdW correlation. The originally proposed vdW-DF density functional, which exploits revPBE [58] exchange, returns a TS energy which is similar to the one obtained using the RPBE-vdW functional (35 meV difference). Similarly, the optPBE-vdW and the PBE-vdW functionals produce almost identical barrier heights (4 meV difference). We note that the TS energy calculated using the PBE-vdW (RPBE-vdW) functional is lower than the corresponding PBE (RPBE) value. Surprisingly, dynamics performed using the PBE-vdW functional returned a laser-off reactivity slightly lower than the PBE one, but still overestimating the experimental values. By mixing PBE exchange with more repulsive RPBE exchange (mixing coefficient $x = 0.1$) we obtain a barrier which is about 35 meV larger than the PBE-vdW value. Note that the TS states obtained using the PBE-vdW and the RPBE-vdW functionals are characterized by somewhat larger r_b values compared to the PBE and the RPBE functionals, respectively.

6.3.3 The Sticking Probability

We have previously shown (Ref. [30] and Chapter 5) that the sticking probability S_0 calculated for CHD_3 on Pt(111) using AIMD in combination with the PBE functional gave semi-quantitative agreement with experimental data (see also Figure 6.3 A). The discrepancies between theory and experiment can be summarized in three points: (i) the PBE-AIMD calculations overestimate the experimental laser-off reaction probability; (ii) the PBE-AIMD reaction probability increases too steeply with increasing collision energy; (iii) the energy shift between the PBE-AIMD CH-stretch excited and laser-off reaction probability curves (i.e. the vibrational efficacy of the CH-stretch mode) is too small compared to experiment.

In order to address point (i), we have performed AIMD calculations using the RPBE:PBE/0.24:0.76 density functional. The energy shift between the PBE laser-off sticking probability points and the experimental data at the lowest collision energies simulated is about 0.1 eV, just like 0.1 eV is the energy difference between the RPBE:PBE/0.24:0.76 and the PBE minimum barrier heights (see Section 6.3.2). Results are plotted in Figure 6.3 A and Figure 6.4 A, together with the PBE-AIMD results and the experimental data. As expected from the larger energy barrier, the reaction probability computed with the RPBE:PBE/0.24:0.76 functional is lower than the PBE one for all the collision energies. Very good agreement with experimental data is obtained for the laser-off beams at the lowest collision energies. The laser-off reactivity at the highest collision energies simulated is only slightly lowered compared to PBE results. The small relative change in S_0 is presumably due to the fact that the translational energy is so much in excess of the minimum energy barrier that the dynamics is not much affected by a 0.1 eV difference in the barrier height. The use of the RPBE:PBE/0.24:0.76 functional, however, dramatically affects the reactivity of the CH-stretch excited beams, and the computed reaction probability falls considerably below the experimental values

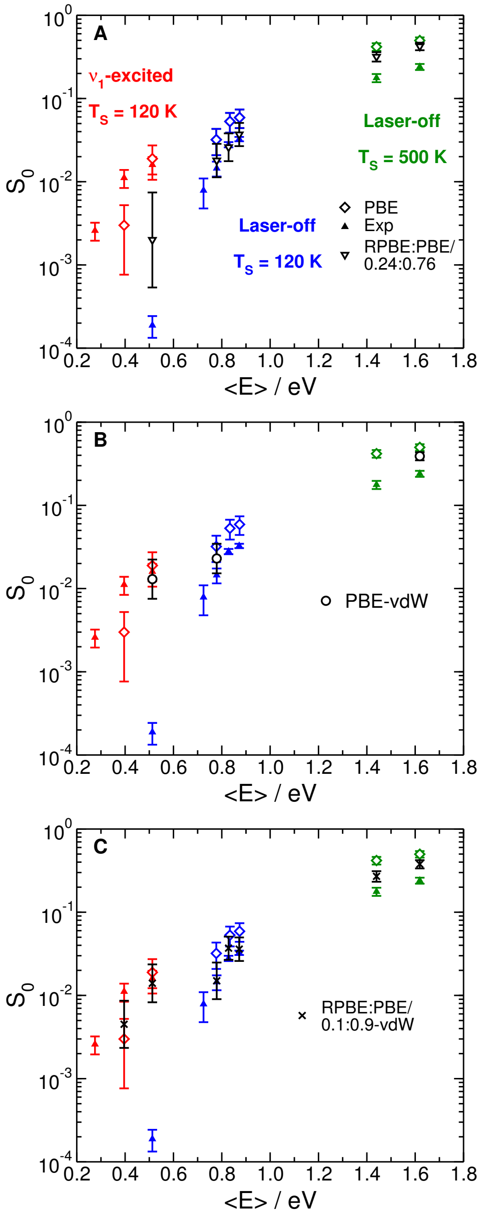

Figure 6.3: Dissociation probability as a function of the average collision energy for CHD_3 on Pt(111). Experimental data are compared to AIMD calculations performed with various exchange-correlation functionals.

when using this functional.

In Figure 6.5 A we plot the projection of the center of mass on the surface unit cell for all the molecules that go on to react, as computed with the PBE functional for the largest collision energy considered ($\langle E_i \rangle = 1.54$ eV). Reaction clearly occurs all over the surface unit cell, and is not limited to the top site (i.e. the minimum energy barrier impact site [62, 63]), in contrast to what was observed at lower collision energies (Ref. [30] and Chapter 5). Consistently, the impact parameter distribution, i.e., the distribution of the lateral displacements between the center of mass of the reacting molecules and the closest first layer Pt atom, is very broad (Figure 6.5 C). A possible explanation for the too steep increase in the PBE-AIMD reaction probability curve (point (ii)), which is not solved by the RPBE:PBE/0.24:0.76 density functional, could be that the PES corrugation is not correctly described by the PBE (and RPBE:PBE/0.24:0.76) functional: if the energy difference between the minimum barrier height and the barrier heights at other surface sites would be larger, the reaction probability would increase less rapidly with incidence energy.

Density functionals that account for dispersion interactions have been recently shown to produce broader reaction probability curves for H_2 on Ru(0001) [40]. In order to verify whether this finding also applies to our system of interest, we have calculated S_0 for CHD_3 on Pt(111) using the PBE-vdW functional. Due to the computational cost of the method, we have computed only three sticking probability points using this functional. The three points chosen are representative of the laser-off reactivity on the large range of collision energies studied and of the two vibrational state populations considered. Surprisingly, even though the minimum energy barrier calculated for the PBE-vdW functional is about 40 meV lower than the PBE energy barrier (see Table 6.3), the reaction probability calculated with the PBE-vdW functional is lower than for PBE in all cases (see Figure 6.3 B and Figure 6.4 B). In particular, the PBE-vdW laser-off reactivity agrees with the experimental data at the lowest collision energy simulated to within the experimental and calculated error bars, and S_0 is decreased with respect to the PBE value by about 10% at the highest collision energy. The reactivity

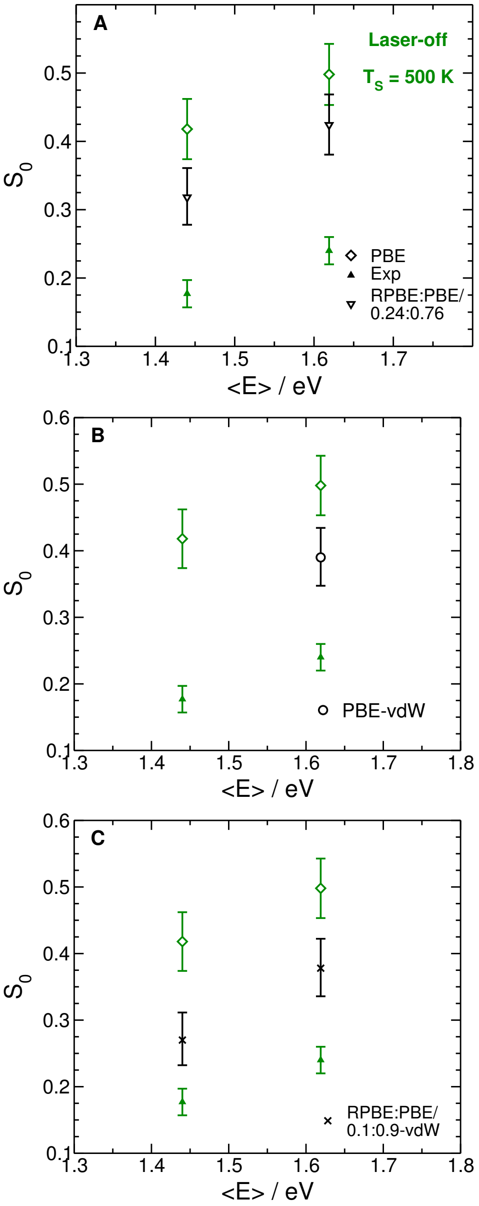

Figure 6.4: Same as Figure 6.3, but the focus is on the highest energy points and the sticking probability is plotted on a linear scale.

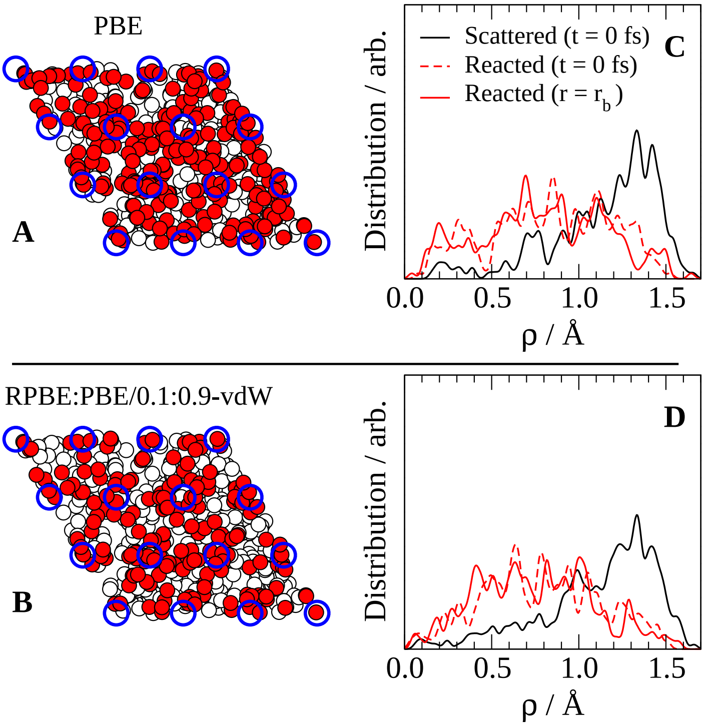

Figure 6.5: A and B: Bird-eye view of the initial center of mass positions of all the simulated molecules. Reacting and scattered molecules are plotted as red and white dots, respectively. The blue circles represent the first layer Pt atoms in their equilibrium positions. C and D: Lateral displacement distributions calculated between the center of mass of the molecule and the closest first layer Pt atom (impact parameter ρ). The initial distribution and the distribution calculated at the transition state for the reacting molecules are plotted as a dashed and a solid red lines, respectively. The initial distribution calculated for scattered molecules is plotted as a solid black line. All data refer to CHD_3 on Pt(111) at $T_s = 500$ K and $\langle E_i \rangle = 1.54$ eV.

obtained simulating a CH-stretch excited molecular beam is only slightly affected, and the agreement with experimental data is still good.

If we use an exchange of the form of Equation 6.1, with a mixing coefficient $x = 0.1$ in combination with the vdW correlation (RPBE:PBE/0.1:0.9-vdW functional), we obtain a slightly lower laser-off reactivity compared to the PBE-vdW functional (see Figure 6.3 C), which is consistent with a slightly higher dissociation barrier for the former (see Table 6.3). The agreement with the experimental data is thereby further improved. At the highest collision energies considered, theory still overestimates the experimental data (see Figure 6.4 C), but the discrepancy is reduced with respect to PBE calculations.

However, it is not completely clear why the PBE-vdW and the RPBE:PBE/0.1:0.9-vdW functionals return lower reactivity than the PBE functional. At the highest collision energy, in fact, the RPBE:PBE/0.1:0.9-vdW functional returns as broad an impact parameter distribution as the PBE functional (Figure 6.5 D). Therefore, the reason seems not to lie in an increased PES corrugation in the degrees of freedom corresponding to the lateral motion of the molecule (X and Y). Similarly, θ and ϕ distributions computed with the PBE and the RPBE:PBE/0.1:0.9-vdW functionals for the reactive molecules seem to be equally broad (not shown). The reason for the lower reactivity of the RPBE:PBE/0.1:0.9-vdW functional could lie in a somewhat more difficult access to the TS due to, for instance, the more elongated CH bond at the TS (see Table 6.3). Most notably, by using the RPBE:PBE/0.1:0.9-vdW functional, we obtain a good description of the reactivity for the CH-stretch excited beams. Considering the improved agreement for both laser-off and CH-stretch excited conditions, we conclude that the proposed functional better describes the vibrational efficacy of the CH-stretch mode than the PBE functional (point (iii)). An explanation for this is that the TS is slightly 'later', since the dissociating CH bond is 50 mÅ more elongated than with the PBE functional. According to Polanyi's rule [43] vibrational excitation should then be more effective in enhancing reactivity.

Considering the discrepancy still present between the simulated and the experimental reactivity of the laser-off beams at the highest collision energies, we consider the aim of obtaining a SRP density functional for methane reacting on Pt(111) not yet achieved with the RPBE:PBE/0.1:0.9-vdW functional. Our work suggests that a good functional for this system should exhibit a larger energetic corrugation than the PBE and the RPBE:PBE/0.1:0.9-vdW functionals. Other functionals that account for vdW interactions, like the vdW-DF2 [72], could be tested for this purpose.

As a final note, we mention again that the level of agreement obtained with experimental data using AIMD in combination with the RPBE:PBE/0.1:0.9-vdW functional, is expected to depend on the computational setup employed in the sense that this functional would return a barrier about 45 meV lower when using a larger amount of vacuum space (see Section 6.3.1). However, we expect that by adjusting the mixing coefficient towards a larger percentage of RPBE exchange, the same level of agreement with experimental data could be obtained. This might even improve the description of the CH-stretch excited molecular beam reactivity further, as the barrier will become slightly later (larger r_b at the TS), consequently increasing the efficacy of the CH-stretch vibrational mode in promoting the reactivity.

6.4 Summary and Conclusions

We have tested the influence of the exchange-correlation functional E_{XC} on the reactivity of methane on a platinum surface, using the dissociation of the CHD_3 isotopologue on Pt(111) as a test case. Dynamical calculations have been performed using the AIMD technique, which is ideal for the purpose of testing the influence of E_{XC} on the sticking probability. In fact, the AIMD method allows the calculation of statistically accurate dissociation probabilities without the need of introducing *a priori* dynamical approximations concerning the evolution of specific molecular degrees of freedom or concerning the role played by surface atom motion. The computed sticking probabilities have been compared to recent quantum state-resolved experimental data and to previous calculations performed using the PBE density functional (Ref. [30] and Chapter 5). Calculations reveal that a density functional that returns a minimum barrier height 0.1 eV larger than the PBE functional (RPBE:PBE/0.24:0.76) improves the agreement with laser-off experimental data at the lowest collision energies simulated, but only slight improvement is observed at the high collision energies, and the agreement is drastically worsened for CH-stretch excited beams. The overall best agreement is observed for a density functional consisting of the correlation functional of Dion et al. [39], developed to mimic vdW interactions, and a linear combination of the RPBE and PBE exchange functionals (the RPBE:PBE/0.1:0.9-vdW functional). This functional still returns a too high reaction probability when simulating the high collision energy laser-off molecular beams, but for the lower collision energies the agreement with the experimental data is good. Surprisingly, the barrier height that this functional returns is the same as for the

PBE functional, so that the lower reactivity of the laser-off RPBE:PBE/0.1:0.9-vdW functional should be due to other aspects of the PES. The improved (larger) vibrational efficacy of the CH-stretch mode obtained with the RPBE:PBE/0.1:0.9-vdW functional is most likely due to the more elongated dissociating CH bond at the TS obtained with this functional.

Bibliography

[1] G. J. Kroes, Phys. Chem. Chem. Phys. **14**, 14966 (2012).

[2] R. Peverati and D. G. Truhlar, Phil. Trans. R. Soc. A **372**, 20120476 (2014).

[3] J. Zheng, Y. Zhao, and D. G. Truhlar, J. Chem. Theory Comput. **5**, 808 (2009).

[4] C. Díaz, E. Pijper, R. A. Olsen, H. F. Busnengo, D. J. Auerbach, and G. J. Kroes, Science **326**, 832 (2009).

[5] C. Díaz, R. A. Olsen, D. J. Auerbach, and G. J. Kroes, Phys. Chem. Chem. Phys. **12**, 6499 (2010).

[6] C. T. Rettner, H. E. Pfnür, and D. J. Auerbach, J. Chem. Phys. **84**, 4163 (1986).

[7] A. C. Luntz and D. S. Bethune, J. Chem. Phys. **90**, 1274 (1989).

[8] L. B. F. Juurlink, P. R. McCabe, R. R. Smith, C. L. DiCologero, and A. L. Utz, Phys. Rev. Lett. **83**, 868 (1999).

[9] J. Higgins, A. Conjusteau, G. Scoles, and S. L. Bernasek, J. Chem. Phys. **114**, 5277 (2001).

[10] L. Halonen, S. L. Bernasek, and D. J. Nesbitt, J. Chem. Phys. **115**, 5611 (2001).

[11] R. D. Beck, P. Maroni, D. C. Papageorgopoulos, T. T. Dang, M. P. Schmid, and T. R. Rizzo, Science **302**, 98 (2003).

[12] R. R. Smith, D. R. Killelea, D. F. DelSesto, and A. L. Utz, Science **304**, 992 (2004).

[13] P. Maroni, D. C. Papageorgopoulos, M. Sacchi, T. T. Dang, R. D. Beck, and T. R. Rizzo, Phys. Rev. Lett. **94**, 246104 (2005).

[14] D. R. Killelea, V. L. Campbell, N. S. Shuman, and A. L. Utz, Science **319**, 790 (2008).

[15] L. B. F. Juurlink, D. R. Killelea, and A. L. Utz, Prog. Surf. Sci. **84**, 69 (2009).

[16] B. L. Yoder, R. Bisson, and R. D. Beck, Science **329**, 553 (2010).

[17] M. Sacchi, D. J. Wales, and S. J. Jenkins, J. Phys. Chem. C **115**, 21832 (2011).

[18] B. Jackson and S. Nave, J. Chem. Phys. **135**, 114701 (2011).

[19] M. Sacchi, D. J. Wales, and S. J. Jenkins, Phys. Chem. Chem. Phys. **14**, 15879 (2012).

[20] M. Sacchi, D. J. Wales, and S. J. Jenkins, Comput. Theor. Chem. **990**, 144 (2012).

[21] L. Chen, H. Ueta, R. Bisson, and R. D. Beck, Faraday Discuss. **157**, 285 (2012).

[22] B. Jiang and H. Guo, J. Phys. Chem. C **117**, 16127 (2013).

[23] B. Jiang, R. Liu, J. Li, D. Xie, M. Yang, and H. Guo, Chem. Sci. **4**, 3249 (2013).

[24] S. B. Donald, J. K. Navin, and I. Harrison, J. Chem. Phys. **139**, 214707 (2013).

[25] M. Mastromatteo and B. Jackson, J. Chem. Phys. **139**, 194701 (2013).

[26] B. Jackson and S. Nave, J. Chem. Phys. **138**, 174705 (2013).

[27] X. J. Shen, A. Lozano, W. Dong, H. F. Busnengo, and X. H. Yan, Phys. Rev. Lett. **112**, 046101 (2014).

[28] G. Jones, J. G. Jakobsen, S. S. Shim, J. Kleis, M. P. Andersson, J. Rossmeisl, F. Abild-Pedersen, T. Bligaard, S. Helveg, B. Hinnemann, J. R. Rostrup-Nielsen, I. Chorkendorff, J. Sehested, and J. K. Nørskov, J. Catal. **259**, 147 (2008).

[29] B. L. Yoder, R. Bisson, P. M. Hundt, and R. D. Beck, J. Chem. Phys. **135**, 224703 (2011).

[30] F. Nattino, H. Ueta, H. Chadwick, M. E. van Reijzen, R. D. Beck, B. Jackson, M. C. van Hemert, and G. J. Kroes, J. Phys. Chem. Lett. **5**, 1294 (2014).

[31] J. P. Perdew, K. Burke, and M. Ernzerhof, Phys. Rev. Lett. **77**, 3865 (1996).

[32] J. P. Perdew, K. Burke, and M. Ernzerhof, Phys. Rev. Lett. **78**, 1396 (1997).

[33] Z. Xie, J. M. Bowman, and X. Zhang, J. Chem. Phys. **125**, 133120 (2006).

[34] B. Jackson, F. Nattino, and G. J. Kroes, J. Chem. Phys. **141**, 054102 (2014).

[35] A. K. Tiwari, S. Nave, and B. Jackson, J. Chem. Phys. **132**, 134702 (2010).

[36] Y. Y. Chuang, M. L. Radhakrishnan, P. L. Fast, C. J. Cramer, and D. G. Truhlar, J. Phys. Chem. A **103**, 4893 (1999).

[37] A. Chakraborty, Y. Zhao, H. Lin, and D. G. Truhlar, J. Chem. Phys. **124**, 044315 (2006).

[38] L. Sementa, M. Wijzenbroek, B. J. van Kolck, M. F. Somers, A. Al-Halabi, H. F. Busnengo, R. A. Olsen, G. J. Kroes, M. Rutkowski, C. Thewes, N. F. Kleimeier, and H. Zacharias, J. Chem. Phys. **138**, 044708 (2013).

[39] M. Dion, H. Rydberg, E. Schröder, D. C. Langreth, and B. I. Lundqvist, Phys. Rev. Lett. **92**, 246401 (2004).

[40] M. Wijzenbroek and G. J. Kroes, J. Chem. Phys. **140**, 084702 (2014).

[41] L. Martin-Gondre, J. I. Juaristi, M. Blanco-Rey, R. Díez Muiño, and M. Alducin, J. Chem. Phys. **142**, 074704 (2015).

[42] B. Hammer, L. B. Hansen, and J. K. Nørskov, Phys. Rev. B **59**, 7413 (1999).

[43] J. C. Polanyi, Acc. Chem. Rev. **5**, 161 (1972).

[44] A. Groß and A. Dianat, Phys. Rev. Lett. **98**, 206107 (2007).

[45] F. Nattino, C. Díaz, B. Jackson, and G. J. Kroes, Phys. Rev. Lett. **108**, 236104 (2012).

[46] G. Kresse and D. Joubert, Phys. Rev. B **59**, 1758 (1999).

[47] P. E. Blöchl, Phys. Rev. B **50**, 17953 (1994).

[48] G. Kresse and J. Hafner, Phys. Rev. B **47**, 558 (1993).

[49] G. Kresse and J. Hafner, Phys. Rev. B **49**, 14251 (1994).

[50] G. Kresse and J. Furthmüller, Comput. Mat. Sci. **6**, 15 (1996).

[51] G. Kresse and J. Furthmüller, Phys. Rev. B **54**, 11169 (1996).

[52] J. Klimeš, D. R. Bowler, and A. Michaelides, Phys. Rev. B **83**, 195131 (2011).

[53] J. W. Arblaster, Platinum Met. Rev. **41**, 12 (1997).

[54] J. W. Arblaster, Platinum Met. Rev. **50**, 118 (2006).

[55] H. A. Michelsen and D. J. Auerbach, J. Chem. Phys. **94**, 7502 (1991).

[56] E. B. Wilson, J. Am. Statist. Assoc. **22**, 209 (1927).

[57] G. Román-Pérez and J. M. Soler, Phys. Rev. Lett. **103**, 096102 (2009).

[58] Y. Zhang and W. Yang, Phys. Rev. Lett. **80**, 890 (1998).

[59] J. Klimeš, D. R. Bowler, and A. Michaelides, J. Phys.: Cond. Matt. **22**, 022201 (2010).

[60] G. Henkelman, B. P. Uberuaga, and H. Jónsson, J. Chem. Phys. **113**, 9901 (2000).

[61] G. Henkelman and H. Jónsson, J. Chem. Phys. **113**, 9978 (2000).

[62] S. Nave and B. Jackson, J. Chem. Phys. **130**, 054701 (2009).

[63] S. Nave, A. K. Tiwari, and B. Jackson, J. Chem. Phys. **132**, 054705 (2010).

[64] V. A. Ukraintsev and I. Harrison, Surf. Sci. **286**, L571 (1993).

[65] D. L. Meixner and S. M. George, Surf. Sci. **297**, 27 (1993).

[66] Y. Matsumoto, Y. A. Gruzdkov, K. Watanabe, and K. Sawabe, J. Chem. Phys. **105**, 4775 (1996).

[67] K. Watanabe and Y. Matsumoto, Surf. Sci. **390**, 250 (1997).

[68] A. F. Carlsson and R. J. Madix, Surf. Sci. **458**, 91 (2000).

[69] L. Chen, H. Ueta, H. Chadwick, and R. D. Beck, J. Phys. Chem. C **119**, 14499 (2015).

[70] E. Dombrowski, E. Peterson, D. Del Sesto, and A. L. Utz, Catal. Today **244**, 10 (2015).

[71] F. Viñes, Y. Lykhach, T. Staudt, M. P. A. Lorenz, C. Papp, H. P. Steinrück, J. Libuda, K. M. Neyman, and A. Görling, Chem. - Eur. J. **16**, 6530 (2010).

[72] K. Lee, E. D. Murray, L. Kong, B. I. Lundqvist, and D. C. Langreth, Phys. Rev. B **82**, 081101 (2010).

Chapter 7

N_2 Dissociation on W(110): an ***Ab Initio*** Molecular Dynamics Study on the Effect of Phonons

This chapter is based on:
F. Nattino, F. Costanzo and G. J. Kroes, J. Chem. Phys. **142**, 104702 (2015).

Abstract

Accurately modeling the chemisorption dynamics of N_2 on metal surfaces is of both practical and fundamental interest. The factors that may have hampered this achievement so far are the lack of an accurate density functional and the use of approximate methods to deal with surface phonons and non-adiabatic effects. In the current work, the dissociation of molecular nitrogen on W(110) has been studied using *ab initio* molecular dynamics (AIMD) calculations, simulating both surface temperature effects, such as lattice distortion, and surface motion effects, like recoil. The forces were calculated using density functional theory, and two density functionals were tested, namely the PBE and the RPBE functionals. The computed dissociation probability considerably differs from earlier static surface results, with AIMD predicting a much larger contribution of the

indirect reaction channel, in which molecules dissociate after being temporally trapped in the proximity of the surface. Calculations suggest that the surface motion effects play a role here, since the energy transfer to the lattice does not allow molecules that have been trapped into potential wells close to the surface to find their way back to the gas phase. In comparison to experimental data, AIMD results overestimate the dissociation probability at the lowest energies investigated, where trapping dominates, suggesting a failure of both tested exchange-correlation functionals in describing the potential energy surface in the area sampled by trapped molecules.

7.1 Introduction

Heterogeneous catalysis is employed in various industrial processes, of which ammonia synthesis is probably the most famous example. This industrial procedure, also known as the Haber-Bosch process, is based on the reaction of nitrogen and hydrogen over an iron catalyst. The dissociative chemisorption of N_2 on the catalyst is believed to be the rate-limiting step of the full process [1] and for this reason the reactive and non-reactive scattering of molecular nitrogen from metal surfaces has been the subject of many studies, with the aim of promoting a fundamental understanding on the key-elements that play a role in this reaction.

Tungsten surfaces, among others, have received much attention [2–21], with particular focus on the large crystallographic anisotropy that this metal exhibits with respect to nitrogen adsorption. For instance, the thermal reactivity of W(100) is about two orders of magnitude larger than the W(110) reactivity [2]. Molecular beam experiments found typical non-activated behaviour for the dissociation of N_2/W(100), with a non-zero sticking probability S_0 at vanishing incidence energies, and S_0 first decreasing, then increasing with increasing collision energy [9]. On the other hand, a monotonically increasing sticking probability function was observed for N_2/W(110), suggesting that only activated paths might lead to dissociation on this surface [5]. Alducin et al. [12–14] were able to show that this apparently activated behaviour could be reproduced by calculations performed on a potential energy surface (PES) that includes non-activated paths for dissociation. However, the ‘shape’ of the PES is such that these non-activated paths are difficult to access at low collision energies.

The PES first used by Alducin et al. [12,13] for N_2/W(110), which includes all the six molecular degrees of freedom, was calculated with DFT at the generalized gradient approximation (GGA) level, using the PW91 exchange-correlation functional [22,23]. The agreement with experiments, however, was not quantitative: The sticking probability curve at normal incidence angle exhibits a ‘bump’ between 0 and 500 meV, which was not observed in the experiments. The bump is caused by the dissociation of molecules that are temporally trapped in the proximity of the surface, due to the energy transfer from the molecules’ normal translational component to other molecular degrees of freedom (dynamic trapping). A different PES, which was computed with a different GGA density functional, the RPBE functional [24], produced better agreement for normal incidence, but dramatically failed at describing the reactivity at 60° incidence angle [15], with the majority of the molecules being scattered at large distance from the surface (about 3 Å). The authors concluded that the PW91-PES is less accurate close to the surface, in the area where the dissociation takes place, while the RPBE-PES is too repulsive at larger distances from the surface. A similar conclusion concerning the RPBE-PES was obtained from a comparison of non-reactive scattering simulations to experiments, which also suggested that the PW91-PES is too corrugated [19].

Modeling non-adiabatic effects for N_2/W(110), such as electron-hole pair excitation, was first tackled by Juaristi et al. [16]. The energy transfer from molecular to electronic degrees of freedom was modeled as energy dissipation, included in the dynamics through friction coefficients. Such coefficients were calculated using the local density friction approximation (LDFA), and the electronically non-adiabatic results deviated only slightly from the fully adiabatic calculations [16,18]. However, discussion is still open about the appropriateness of the LDFA for computing friction coefficient [25–28].

Martin-Gondre et al. [20] simulated the rotationally inelastic scattering of N_2 from W(110) simultaneously modeling energy dissipation to phonons, using the approximate generalized Langevin oscillator (GLO) model, and taking into account non-adiabatic effects, using the LDFA. They found that the inclusion of phonon dissipative forces is more relevant than electronic ones, and suggested that the static surface electronically adiabatic calculations already include relevant aspects of the scattering dynamics. More recently, Petuya et al. looked at the non-reactive scattering of N_2 from W(100) [21]. They modeled energy dissipation to phonons using the GLO method, and compared these results to static-surface data and to experiments, finding reasonable agreement between experimental data and both models.

In a very recent study [29], the dissociation of N_2 on W(110) has been investigated using density functionals in which the correlation has been corrected to account for dispersion interactions [30, 31]. The authors have shown that some of these density functionals better describe properties such as adsorption energy and barriers for dissociation and desorption from the adsorption configuration that they have determined. Furthermore, the long range attractive interaction can correct for the excessive repulsion generated by some functionals (e.g. RPBE) at large distances from the surface, and also lower the barrier for dissociation most sampled by the molecules dissociating at 60° incidence angle. However, despite all the improvements achieved in the static properties of the PES, none of the tested vdW-corrected functionals has been found able to provide an overall good agreement with experimental data both at normal incidence and at a 60° incidence angle within the static surface approximation.

Summarizing, modeling both the reactive and the non-reactive scattering of N_2 from tungsten surfaces remains a challenge, and it is not clear whether the main cause of errors is the lack of an accurate exchange-correlation functional, or the use of approximate models to deal with surface temperature and surface motion effects and electronic non-adiabaticity in the dynamics. For this type of system, calculations explicitly including surface atom motion are desirable. In the first place, they could serve as a benchmark for models that aim at approximately describing the effect of surface phonons. Furthermore, if DFT-AIMD calculations employing a specific density functional could demonstrate good agreement with experiments on both reactive and non-reactive scattering, this would suggest that electron-hole pair excitation affects the dynamics only marginally [28]. On the other hand, a failure to correctly describe the experimental data would either confirm the relevance of non-adiabatic effects in the dynamics or the lack of accuracy obtained with the exchange-correlation functional used. In this work, we present calculations that represent a first step in the direction of these objectives, since they include, apart from the six molecular degrees of freedom, the relevant surface phonons, and we also carry out a test on the influence of the density functional on the observables computed by performing the calculations with two density functionals.

Ab initio molecular dynamics (AIMD) has been employed to investigate gas-surface reactions since the early 90's [32–34]. However, the computational cost of AIMD limited these first studies to a few explorative trajectories. With the growth of computational power and the development of efficient algorithms, the use of AIMD to perform statistically relevant calculations of sticking probabilities for gas-surface reactions has recently become possible [35–37]. Advantages of this method lie in the 'on-the-fly' computation of the forces, since this strategy bypasses the need of pre-calculating and fitting a PES, with the possibility to model the effect of surface phonons through the inclusion of the motion of the surface atoms. Here, we apply the AIMD method to investigate the dissociation of N_2 on W(110), simulating the experimental surface temperature (800 K). In particular, we look at the effects that the explicit inclusion of surface temperature and surface motion have on the dissociation probability. Given the differences observed between dynamics on PESs computed with different exchange correlation functionals, both the PBE and RPBE functionals are tested with the AIMD method.

The AIMD results for N_2/W(110) are found to considerably differ from previous static surface results, especially at the lowest collision energies examined. The differences are due to a larger trapping-mediated (indirect) dissociation channel contribution observed in AIMD. An analysis of the trajectories reveals that a large portion of the molecules performing multiple rebounds on the surface are temporally trapped in areas of the energy landscape close to three configurations that correspond to potential wells of N_2 on an ideal surface, which may be associated with molecular adsorption states. These findings, together with the observation of a significant energy transfer from the molecules to the lattice, suggest that the larger indirect dissociation channel contribution is due to molecules that are trapped in the potential wells and dissipate energy to phonons, such that they are not able to find their way back towards the gas phase and dissociation or molecular adsorption are the only possible outcomes. Both PBE- and RPBE-AIMD results are in qualitative agreement with experimental data at high collision energies, but they both fail to describe the experimental trend according to which the sticking probability monotonically increases with the initial collision energy (E_i). This failure, which is probably related to the overestimation of the indirect dissociation mechanism or molecular chemisorption, which dominate at low energies, might be caused by a wrong description given by both the PBE and the RPBE functionals of the area of the PES sampled by trapped molecules, in particular the area associated with molecular adsorption states.

This chapter is organized as follows: Section 7.2 describes the methodology; in section 7.3 we present and discuss our results, divided in four subsections: In 7.3.1 we discuss the molecular adsorption states that we observe on an ideal lattice; in 7.3.2 we present the results of our molecular beam simulations; in 7.3.3 we analyze the energy exchange between the molecule and the lattice; and in 7.3.4 we investigate the role that molecular adsorption plays in the chemisorption dynamics. Finally, the main conclusions are summarized in section 7.4.

7.2 Methods

The sticking probability of N_2 on W(110) has been determined using the AIMD technique [32, 35], following an implementation similar to the one described in Refs. [36, 37] and Chapters 3 and 5. Each sticking probability point has been determined from the computation of a set of 400 NVE trajectories (constant number of atoms, volume and total energy), representing single molecule-surface collisions. Trajectories belonging to the same set are characterized by the same initial normal translational energy for N_2. Our implementation exploits the quasi-classical trajectory method, in which vibrational zero-point energy is imparted to the N_2 molecules. The molecule's impact-site on the surface, its vibrational phase and its orientation are randomly sampled using standard Monte-Carlo techniques, while the molecular angular momentum is set to zero. Only normal incidence scattering has been simulated. As in Ref. [12], the W(110) surface has been modeled by a periodic slab, using a 2x2 surface unit cell and 5 atomic layers. In order to model the experimental surface temperature ($T_S = 800$ K), the lattice constant has been taken as 1.0037 times the equilibrium DFT lattice constant, to account for the tungsten thermal expansion [38]. The equilibrium lattice constant values of 3.172 Å and 3.184 Å have been obtained from the optimization of the tungsten bulk primitive cell volume using the PBE functional and the RPBE functional, respectively. These values are in good agreement with the low-temperature experimental value of 3.163 Å [39] and with the previous calculations from Alducin et al. [12] and Bocan et al. [15].

In addition to accounting for the thermal expansion of the lattice, we model the experimental surface temperature by assigning velocities and displacements from the equilibrium positions to the surface atoms of the first four layers in a way similar to that used earlier in Ref. [36] and Chapter 3. Starting from initial displacements and velocities generated according to an independent harmonic oscillator model applied to the surface atoms of the uppermost four layers, we perform 1.5 ps long NVE equilibration runs for ten differently-initialized clean surfaces, using 1 fs as time-step. We have then performed a second 1 ps long NVE run for the ten equilibrated surfaces. The average surface temperatures computed for this second run are 723 (σ =113 K) and 728 (σ = 117 K) for PBE and RPBE, respectively, in reasonable agreement with the initially imposed temperature (i.e. 800 K, the experimental surface temperature). The surface initial conditions in the N_2/W(110) dynamics randomly sample the configurations (and the velocities) experienced during these second clean-surface runs.

We have also determined the root mean square displacements (RMSDs) for the tungsten atoms, averaging over all the moving atoms in the slab or considering only the first layer atoms (Table 7.1). The computed values are in reasonable agreement with the values extracted from clean surface equilibration runs performed with a larger (3x3) surface unit cell (PBE only, see also Table 7.1), the average surface temperature of

	All Atoms		Only First Layer	
Surface Unit Cell	2x2	3x3	2x2	3x3
PBE	0.154	0.147	0.185	0.177
RPBE	0.163	-	0.196	-

Table 7.1: Root mean square displacements (RMSD, in Å) of the surface atom positions calculated for the equilibration runs from which the surface initial conditions are extracted, for PBE and RPBE, and for a similar run with a larger surface unit cell (3x3, only PBE).

which is 779 K ($\sigma = 48$ K). From the model of Sears et al. [40], which has been fitted to neutron inelastic scattering measurements, we have computed a RMSD value for bulk tungsten equal to 0.129 Å at 800 K. Both Buchholz et al. [41] and Smith et al. [42] have observed a larger vibrational amplitude for the first layer atoms of a W(110) surface along the surface normal, the amplitude being a factor 1.4 to 2.6 larger than for bulk atoms. Smith et al. [42] also reported that no enhancement has been observed for the vibrational amplitude of the first layer atoms in the direction parallel to the surface. The measurements of Smith et al. were performed at a surface temperature of 300 K, while the data of Buchholz et al. were obtained from the analysis of data measured in a range of surface temperatures, not reported in Ref. [41]. If we assume the enhancement of the vibrational amplitude of the first layer surface atoms along the surface normal relative to the bulk vibrational amplitude to be independent on surface temperature, we can estimate the three dimensional first layer atom RMSD at 800 K to be in the range 0.148 Å to 0.220 Å which is in good agreement with the values that we have computed (Table 7.1).

All calculations have been performed with the DFT-AIMD code VASP [43–47]. Electronic structure calculations are characterized by a plane wave basis set with kinetic energy up to 400 eV, a 8x8x1 equally spaced Γ-centered first Brillouin zone sampling grid, a Fermi smearing with 0.1 eV width and the projected augmented wave (PAW) method [47,48] to represent the core electrons. Note that the PAW pseudopotential employed for tungsten has a Xe core, leaving six active electrons to be modeled explicitly (the valence electrons). A large vacuum space (13 Å) has been employed to separate the slab from its periodic images along the surface normal. We have verified that the residual interaction energy for a molecule placed midway between two slabs with the bond length equal to its equilibrium value (our zero of energy) is lower than 10 meV. The influence of the exchange-correlation functional on the dynamics has been investigated by performing calculations with two GGA density functionals, i.e. PBE [49, 50] and RPBE [24]. Note that our computational setup is essentially the same as in Refs. [12, 15], with only small differences in the k-point grids and energy cut-offs for the plane wave expansion, the use of PAW pseudopotentials instead of ultrasoft pseudopotentials and the use of the PBE functional instead of the PW91 [22, 23] functional. Note, however, that the PBE functional has been designed to reproduce PW91 energies [49].

The AIMD trajectories have been integrated using the Verlet algorithm as implemented in VASP, employing a time-step of 1 fs and a maximum propagation time of 2.7 ps. The maximum propagation time, however, has been extended to 4.2 ps for the lowest initial collision energies investigated (0.9 eV and 1.3 eV), where the trapping-mediated dissociation mechanism dominates. In fact, molecules which are trapped can remain in this condition for several ps before dissociating, and therefore require longer time propagation. Given the larger computational cost of AIMD trajectories compared to the static-surface calculations, we cannot integrate AIMD calculations for longer times. The N_2 molecules, which are initially placed at 6 Å from the surface, are considered dissociated when the distance between the two N atoms becomes larger than 2 Å (the equilibrium N_2 bond length is 1.117 Å). In order to account at least in part for the possibility of scattering after barrier recrossing, we additionally require the distance between two atoms to become larger than the distance between one N atom and the closest periodic image of the other N atom. On the other hand, we consider a N_2 molecule to be scattered when Z, the distance between the surface and the center of mass (COM) of the molecule, becomes larger than 6 Å with the COM velocity pointing away from the surface. We label as ‘unclear’ the outcome of the trajectories in which the nitrogen molecule is neither scattered nor dissociated at the end of the propagation time (less than 7%, for each set of data).

Error bars presented in this article represent 68.3 % confidence intervals, and have been estimated using the standard Wald interval [51]: for an estimated proportion p, e.g. a sticking probability value, for which $p = m/N$, where m is the number of reacted trajectories and N is the number of trajectories computed to estimate the proportion, $\sigma_p = \sqrt{p(1-p)/N}$.

Adsorption energies, which are defined as $E_a = -(\epsilon_{ads} - \epsilon_{asym})$, where ϵ_{ads} and ϵ_{asym} are the absolute energies of the adsorption system and of the configuration with N_2 at its equilibrium bond distance and at large distance from the surface, have been estimated for PBE and RPBE using an ideal slab optimized for the functional employed. The adsorption configurations have been obtained from geometry optimization procedures in which the lattice atoms have been kept fixed at the equilibrium slab geometry. Note that frequency analyses have confirmed that the results of geometry optimizations are true local minima, since no imaginary frequencies have been found. The adsorption energy values obtained with our computational setup have been compared to values from calculations with six additional active electrons included in the PAW pseudopotential description for tungsten, and to values from all-electron calculations. For the calculations with additional active electrons, the bulk tungsten lattice constant, the clean-slab interlayer distances and the adsorbate configurations have been re-optimized, but no considerable differences have been observed with respect to the geometries obtained for the PAW pseudopotential modeling only the valence electrons as active electrons. We have also increased the energy cutoff for the plane wave expansion to 600 eV, since the PAW pseudopotential with more active electrons employs a smaller cutoff radius for the pseudization sphere around the nucleus. The all-electron calculations have been performed with the FHI-AIMS package [52], using the 'tight' setting for the basis set size, for the same system geometry as optimized for the PAW with more active electrons.

In order to estimate the energy barriers that separate the molecular adsorption states from the dissociated state, we have performed nudged elastic band (NEB) calculations, using the VASP transition-state tools from Henkelman and Jónsson [53, 54]. Four images have been placed between the reactant configuration (the molecular adsorption geometry) and the product configuration (the dissociated configuration), and optimized

		X	Y	θ	ϕ	r	Z	E_a	Ref. [15]	Exp.
PBE	Top	0	0	0	-	1.137	2.672	0.621	0.665 *	0.260, 0.450
	Hollow	2.243	0	90	0	1.363	1.378	1.444	-	
	BH	3.657	1.264	74.48	-121.89	1.307	1.537	0.984	-	
RPBE	Top	0	0	0	-	1.141	2.694	0.385	0.389	
	Hollow	2.251	0	90	0	1.370	1.391	0.972	-	
	BH	3.669	1.262	74.61	-122.27	1.316	1.544	0.543	-	

Table 7.2: Adsorption energies (eV) and geometries (r, Z, X and Y are in Å, θ and ϕ in degrees) for three minima corresponding to N_2 adsorption. Our adsorption energies are compared to the values of Ref. [15], and to experimental values from Refs. [3, 8]. Note that the value marked with (*) was obtained with the PW91 functional (not PBE).

through the fast inertial relaxation engine (FIRE) algorithm [55]. Through the use of climbing-image NEB (CI-NEB) calculations, the highest energy images are driven to the saddle points [53]. Calculations have been considered converged when all the forces are smaller than 20 meV/Å if not otherwise stated. Frequency analyses have confirmed that the highest energy images obtained are true first-order saddle points (only one imaginary frequency found).

7.3 Results and Discussion

7.3.1 Molecular Adsorption States

We identified three energetic minima that might be considered molecular adsorbed states for an ideal lattice. These minima are illustrated in Figure 7.1, and the corresponding adsorption energies and geometries are presented in Table 7.2 for both PBE and RPBE. Note that the adsorption energies calculated with PBE are always larger than the corresponding RPBE values, as expected from the more repulsive character of the latter [24].

As also described in Refs. [12,15], we find an adsorption well for N_2 placed above the top site at about 2.7 Å from the surface with the bond oriented perpendicular to the surface plane (top-vertical configuration). The adsorption energies that we determine for this configuration with PBE (0.621 eV) and RPBE (0.385 eV) reasonably reproduce the DFT values from Refs. [12,15] (0.665 eV and 0.389 eV, respectively), and differences should be expected due to the slightly different computational setups and, in one case,

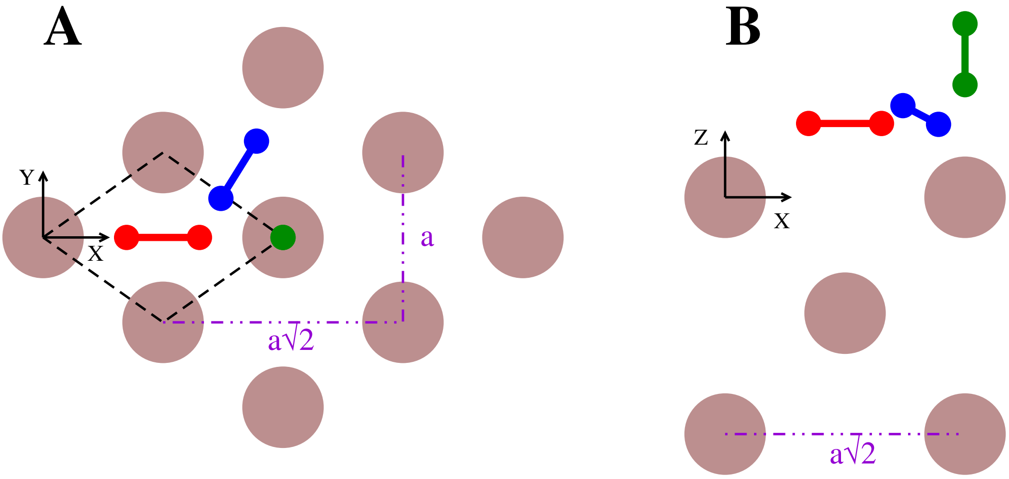

Figure 7.1: Graphical illustration of the molecular adsorption states: green for top-vertical, red for hollow-parallel and blue for bridge-hollow-tilted, using nomenclature as in the text. A and B represent bird's-eye and side views, respectively. Brown circles represent the surface atoms. The dashed black line delimits the surface unit cell.

the functional (PBE vs. PW91, see Section 7.2). In addition, we find two adsorption wells closer to the surface ($Z < 1.6$ Å). The first minimum is characterized by N_2 oriented parallel to the surface with its COM above the hollow site (hollow-parallel configuration). The adsorption energy is about 1.4 eV for PBE (1.0 eV for RPBE). Note that a similar adsorption geometry has been found on both Fe(110) [56] and Fe/W(110) [57], but the adsorption energy is larger on W(110). Note also the rather extended bond length of the adsorbed molecules with respect to the gas-phase value (about 20% longer). An additional molecular adsorption geometry has been found in the proximity of the bridge site, slightly shifted towards the hollow site, with one of the two N atoms approximately above the bridge site. The N_2 bond, slightly tilted from the parallel orientation ($\theta \approx 75°$), is almost perpendicular to the line connecting two adjacent top sites (bridge/hollow-tilted configuration). The adsorption energy at this site is intermediate between the hollow-parallel and the top-vertical geometries, about 1.0 eV and 0.5 eV for PBE and RPBE, respectively.

Figures 7.2 and 7.3 show two-dimensional (r, Z) potential energy plots for PBE and RPBE, respectively, in which the remaining molecular degrees of freedom are kept equal

Functional	Molecular Adsorption Geometry	E_b^{Ads}	E_b^{Diss}
PBE	Top-vertical	0.005	-0.432
	Hollow-parallel	0.406	-0.977
	Bridge/hollow-tilted	0.387	-0.486
RPBE	Top-vertical	0.071	-0.114
	Hollow-parallel	0.629	-0.550
	Bridge/hollow-tilted	0.610	-0.043

Table 7.3: The energy barriers experienced by the molecule when accessing the molecular adsorption wells (E_b^{Ads}) are compared to the barriers along the minimum energy paths that connect each of the molecular adsorption configurations to the dissociated configuration (E_b^{Diss}), in eV. Note that the E_b^{Ads} values refer to the barriers in the 2D plots in Figure 7.2 and in Figure 7.3, while the E_b^{Diss} values have been computed through CI-NEB calculations, and are therefore first order saddle points in the six-dimensional space of the N_2 configurations. The zero of energy is defined as the energy of the molecule in its equilibrium geometry placed midway between two slabs.

to the values corresponding to the three molecular adsorption geometries described. As for the calculation of the molecular adsorption energies, the surface atoms have been kept in their equilibrium configuration. Alducin et al. [12, 13] and Bocan et al. [15] noted that the access to the top-vertical adsorption geometry is barrier-less if the PW91 functional is employed, while the RPBE functional predicts a barrier of about 80 meV. Similarly, along the same path, at about 3.7 Å from the surface, we have found a barrier of about 70 meV when using the RPBE functional (Table 7.3 and Figure 7.3A). Using the PBE functional, we find a very small barrier (about 5 meV) at $Z = 4$ Å (see Figure 7.4, blue symbols, and Table 7.3) where the PW91-PES from Refs. [12, 13] returns an interaction energy of about -5 meV (Figure 3 of Ref. [12]). We verified that in our computational setup a small barrier (which is, however, less than 1 meV high) is still present even after adding 10 Å of vacuum along the surface normal and after shifting the asymptotic configuration further from the surface (see Figure 7.4, red symbols), which suggests that the observed barrier is not an ‘artifact’ of residual attractive interactions for the asymptotic configuration (our zero of energy). The size of this barrier, however, is negligible when compared to the collision energies that we have investigated (0.9 eV or larger), therefore we do not expect differences in the dynamics due to the absence of a non-activated path, which characterizes the PW91-PES from Refs. [12, 13].

For what concerns the other two molecular adsorption geometries, a barrier is en-

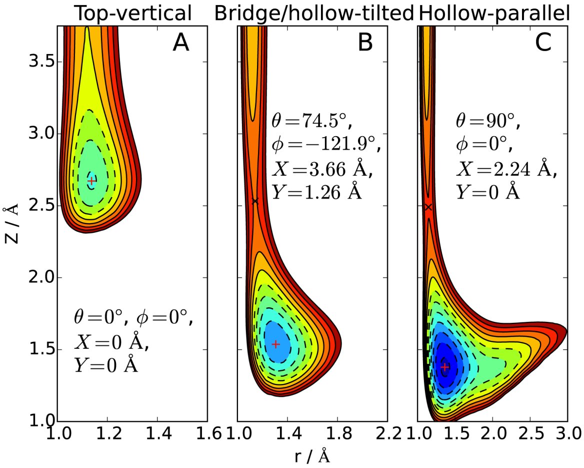

Figure 7.2: The PBE interaction energy is plotted as a function of r and Z for the three configurations corresponding to the molecular adsorption geometries. The position of the adsorption geometries is indicated in the plots by a red +, and a black × indicates the position of the saddle point in the entrance channel. Interaction energies have been evaluated on a dense grid in r and Z and spline interpolated for illustration purposes. Contour lines separate 0.2 eV energy intervals up to a maximum of 0.8 eV. Dashed lines identify negative energy values.

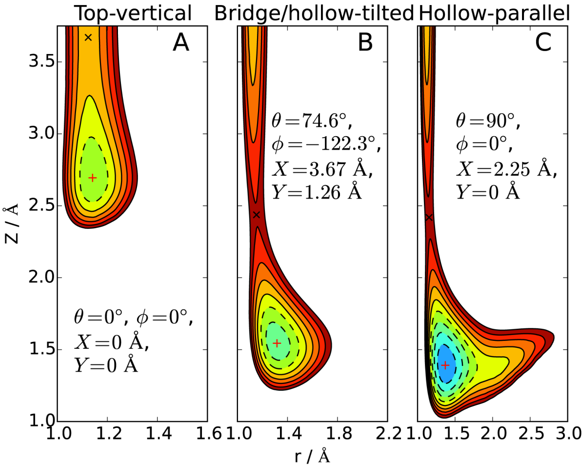

Figure 7.3: Same as Figure 7.2, but for RPBE.

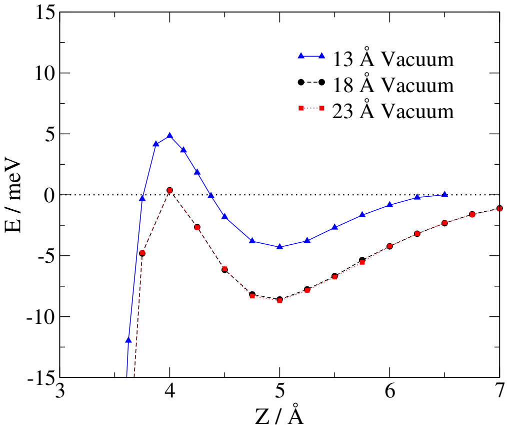

Figure 7.4: The PBE interaction energy is plotted as a function of Z, using the same equilibrium 5-layer slab to model the W(110) surface, but using different vacuum spaces along the surface normal. The N_2 bond length has been kept equal to the equilibrium value of 1.117 Å. The zero of energy is defined as the energy of the molecule in its equilibrium geometry placed midway between two slabs.

countered in the access to the adsorption wells from the gas-phase, independently of which functional is employed (Figure 7.2B-7.2C, Figure 7.3B-7.3C and Table 7.3). To enter both the bridge/hollow-tilted and the hollow-parallel adsorption wells, the saddle points that the molecule has to overcome in the 2D-cuts in Figure 7.2 and 7.3 are located between 2.4 and 2.6 Å from the surface. The height of the barrier is about 0.6 eV for RPBE, and only about 0.4 eV for PBE. Note that all the mentioned barriers are lower than the minimum collision energy simulated (0.9 eV).

The configurations of the hollow-parallel and of the bridge/hollow-tilted adsorption geometries were not part of the set of configurations that have been interpolated in the PES employed in Refs. [12] and [15]. However, elbow plots computed for these PESs for the configurations corresponding to the hollow-parallel and bridge/hollow-tilted molecular adsorption states reveal features similar to the plots in Figure 7.2 and 7.3 [58]. For the hollow-parallel configuration, the bottoms of the adsorption wells are located at $r \sim 1.4 - 1.5$ Å and $Z \sim 1.4$ Å, with interaction energy values of 1.916 eV and 1.313 eV for PW91 and RPBE, respectively (cf. Table 7.2). For the bridge/hollow-tilted configuration, the minima in the 2D-cuts are located at $r \sim 1.3$ Å and $Z \sim 1.6$ Å, with the interaction energy being 0.670 eV and 0.205 eV for PW91 and RPBE, respectively

PBE	W PAW 6 v.e.	W PAW 12 v.e.	AE
Top-vertical	0.621	0.604	0.640
Hollow-parallel	1.444	1.368	1.360
Bridge/hollow-tilted	0.984	0.919	0.943

Table 7.4: Adsorption energies (eV) for the three identified molecular adsorption geometries, for PBE. The results obtained using the PAW pseudopotential that includes 6 valence electron for W are compared to the results obtained using the PAW pseudopotential that includes 12 valence electron (i.e. including the six 5p electrons). Adsorption energies are also compared to results of all electron (AE) calculations.

(cf. Table 7.2). Therefore, the positions of the minima agree reasonably well with the positions of the minima that we have found. The well depths, however, can differ up to almost 0.5 eV (for the hollow-parallel configurations with PW91), with the hollow-parallel (bridge/hollow-tilted) adsorption energies in the PESs being larger (smaller) than the values that we have determined. Note, however, that these analyses have been based on the two dimensional (r, Z)-cuts of the PESs only [58]; we do not know whether these represent 'true' minima in the full dimensional PESs.

Adsorption energies calculated using more active electrons in conjunction with the PAW pseudopotential for tungsten are reported in Tables 7.4 and 7.5 for PBE and RPBE, respectively. The adsorption energy values differ from our computational setup values by no more than 80 meV. Note that we have measured an increase in the computational cost when going from six to twelve active electrons of about a factor 2 for single point energy calculations. Table 7.4 and Table 7.5 also report all-electron adsorption energy values, which compare reasonably well with the adsorption energies computed using our computational setup: differences range from 7 meV for the RPBE top-vertical adsorption geometry to less than 130 meV for the RPBE hollow-parallel geometry. In the light of these results, we are confident that the pseudopotentials employed in our computational setup are able to capture with reasonable accuracy the effect of the presence of the deep adsorption wells predicted by the PBE and RPBE functionals for this system, at a relatively low computational cost.

Experimentally, N_2 is known to molecularly adsorb on W(110) in the so-called γ adsorption state, with estimates of the adsorption energy of 0.260 eV [3] and 0.450

RPBE	W PAW 6 v.e.	W PAW 12 v.e.	AE
Top-vertical	0.385	0.366	0.378
Hollow-parallel	0.972	0.895	0.850
Bridge/hollow-tilted	0.542	0.479	0.466

Table 7.5: Same as Table 7.4, but for RPBE.

eV [8]. Note that another molecular adsorption state, α-N_2, with larger adsorption energy (about 0.8 eV), has been observed on tungsten surfaces [59], but not on the (110) crystal face [2]. The experimental molecular adsorption energies for γ-N_2 are much smaller than the theoretical predictions. Only the top-vertical adsorption energy computed with the RPBE functional is comparable to the experimental estimates for γ-N_2, as already noted by Bocan et al. [15]. However, both Lin et al. [7] and Zhang et al. [8] suggested the presence of a molecular adsorption state different from the γ-N_2 state for N_2 + W(110). In particular, Zhang et al. [8] found some evidence for a δ-N_2 state, populated through electron bombardment of γ-N_2. According to the authors, this molecular adsorption state does not desorb through further electron impact, but can be dissociated to atomic N. The authors also suggested a “lying down” adsorption geometry for this state, and a N-N bond length “abnormally long” [8]. Analogies with the hollow-parallel adsorption geometry that we have identified using both the PBE and the RPBE functionals are evident. However, no significant differences have been found between thermal programmed desorption (TPD) spectra recorded for δ-N_2 and for γ-N_2, and the authors interpreted this finding as a similar desorption activation energy for the two molecular adsorption states, or a possible conversion of δ-N_2 to γ-N_2 before desorption. Our calculations, on the other hand, suggest a rather large difference in adsorption energies between top-vertical and hollow-parallel adsorption states.

We have performed CI-NEB calculations in order to find the minimum energy paths (MEPs) connecting the molecularly adsorbed states to the dissociated configuration (see Appendix 7.A.1). While the most stable adsorption site for one N atom on the W(110) surface is found to be the four fold hollow site, as already noted by Alducin et al. [12], we find that the configuration with two N atoms adsorbed in two adjacent hollow sites is stabilized, within the 2x2 surface unit cell employed, by a 0.5 Å shift of both atoms in the same direction towards the neighboring long top-hollow sites. This configuration has been used as the product state for the CI-NEB calculations. In Table 7.3, we report the barriers computed with respect to the configuration with N_2 at its equilibrium bond distance at large distance from the surface. For all the MEPs analyzed, we observe that the molecule can dissociate without any barrier with respect to the gas-phase, since the dissociation barriers of Table 7.3 are negative in all cases when going from the molecular to the dissociative chemisorption well. For the PBE functional, the energy required to move from the bridge/hollow-tilted and the hollow-parallel adsorption configurations towards dissociation are about 0.50 eV and 0.47 eV, respectively, with respect to the bottom of the molecular adsorption wells. For the RPBE functional, the barrier along the path that connects the bridge/hollow-tilted geometry to dissociation is also 0.50 eV, while a slightly lower barrier (0.42 eV) is found for dissociating molecules adsorbed in the hollow-parallel configuration.

For the MEP connecting the top-vertical adsorption geometry to the dissociated state we found that the potential is quite flat in the proximity of the barrier. Therefore, a small amount of noise in the forces can drive the images away from the MEP and we were not able to converge all the forces below 40 meV/Å. For the PBE path, CI-NEB calculations only converged when allowing the highest-energy image to be optimized while the other images were frozen in the configurations optimized with regular NEB calculations (without CI). The barriers observed along this path are about 0.20 eV and 0.27 eV for PBE and RPBE, respectively, with respect to the bottom of the molecular adsorption well.

7.3.2 Sticking Probability

The N_2 sticking (dissociation) probability computed with AIMD is plotted in Figure 7.5 as a function of the initial collision energy. In the same figure, two sets of experimental data have been reported [5, 9], as a measure of the uncertainty of the experimental values. The agreement between both PBE- and RPBE-AIMD results and experimental data is semi-quantitative at the high collision energies. However, AIMD overestimates the experimental sticking probability at low collision energies. Note that the AIMD method predicts a reaction probability that does not depend on E_i, failing to reproduce the experimental trend according to which the dissociation probability monotonically increases with increasing collision energy.

For both the PBE and the RPBE functionals, the AIMD probabilities are considerably larger than the probabilities obtained in the previous static-surface study, in particular at the lowest collision energies, where probabilities differ by more than a factor two. These discrepancies cannot be due to the small differences in the computational setups, listed in section 7.2. Note that the previous static surface study implemented the classical-trajectory (CT) method, while our AIMD calculations make use of a QCT approach. However, differences between the QCT and CT reaction probabilities have been found to be small (less than 5%) for this system, in the range of collision energies examined [12]. Furthermore, we have performed AIMD calculations simulating an ideal frozen surface (AIMD-IF), using the PBE functional, at a collision energy of 1.3 eV (Figure 7.5) and the computed dissociation probability reproduces (within error bars) the value from the previous PW91 static surface study [12]. Therefore, the inclusion of surface temperature effects (i.e., lattice distortion) or surface motion effects (for instance, recoil) or a combination of the two in the calculations has to be responsible for the mismatch between the present AIMD results and the previous static surface study.

In order to shed light on the main factor that is responsible for the sticking probability increase with respect to static surface data, we have performed AIMD calculations simulating a distorted lattice as in the moving surface calculations, but keeping the surface atoms frozen at their initial positions, thereby blocking energy transfer to the surface (AIMD on a distorted frozen lattice, AIMD-DF). We have computed one sticking probability point for the collision energy and density functional at which the largest discrepancy from static surface calculations was observed ($E_i = 0.9$ eV, PBE). The computed dissociation probability does not considerably differ from the previous PW91 static surface data, suggesting a much larger influence of surface motion effects (energy transfer to the lattice) than of 'static' lattice distortion effects.

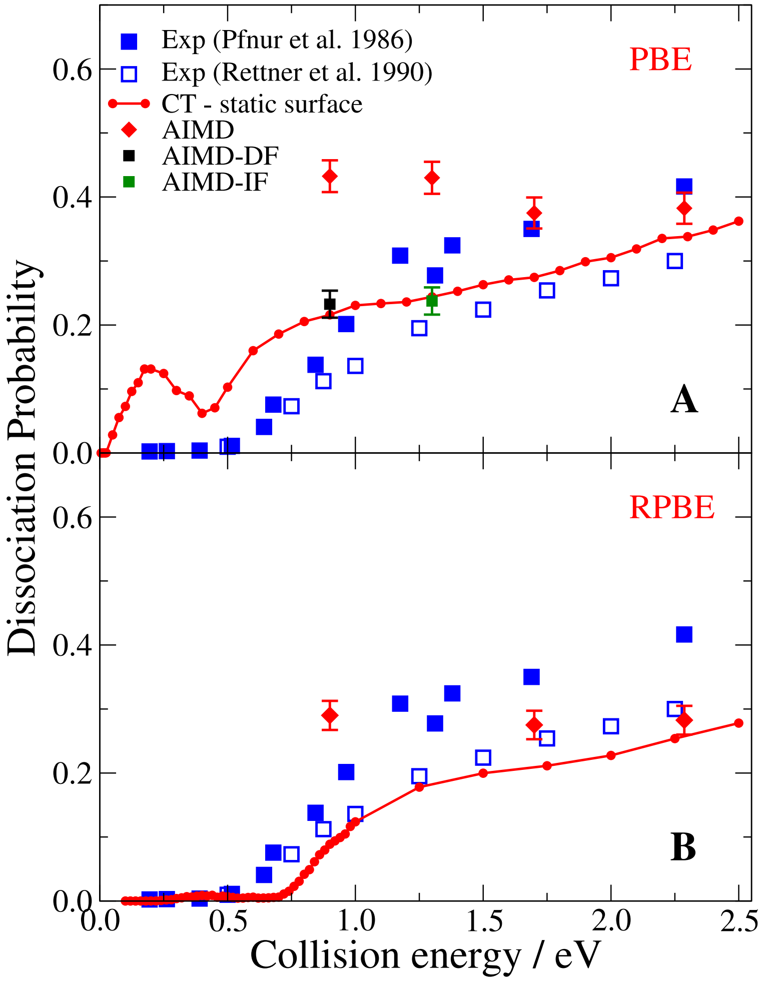

Figure 7.5: Dissociation probability as a function of the initial collision energy. AIMD moving-surface results (AIMD, diamonds) are compared to experimental data (blue squares, solid from Ref. [5] and empty from Ref. [9]) and to previous static-surface CT calculations [15]. The dissociation probability values computed using AIMD, simulating an ideal frozen surface (AIMD-IF, green) and simulating a distorted frozen surface (AIMD-DF, black) are also reported. In A, all AIMD calculations employed the PBE functional and the CT calculations the PW91 functional, while in B the RPBE functional has been employed by both AIMD and CT calculations.

The analysis of our moving surface calculations shows that the dissociation of N_2 can occur either at the first impact on the surface or after many rebounds, as already observed by Alducin et al. [12]. In that study the dissociation was separated into a direct and a trapping-mediated (indirect) contribution, defined on the basis of the number of rebounds that the molecules experience before dissociation (less than four and more than three, respectively). The direct mechanism was found to become more and more relevant with increasing E_i, while the indirect mechanism, dominant at low energies, was found to have a small contribution at high energies. Adopting the same definition [12] for the direct and the indirect dissociation channels, we observe the same trend in our AIMD study, for both the PBE and the RPBE functional (see Figure 7.6A and 7.6B, respectively). The direct mechanism accounts for about one third of the reactivity at 0.9 eV and two thirds at 2.287 eV. Note that the direct dissociation probabilities computed with PBE-AIMD are similar to the direct dissociation probabilities from the previous PW91 static surface study, while the indirect dissociation probabilities are considerably larger for AIMD. Note also that AIMD-DF direct and indirect dissociation probabilities (Figure 7.6A) reproduce reasonably well the corresponding static surface values, suggesting that surface motion effects (energy transfer) constitute the main factor responsible for the larger trapping-mediated dissociation probability observed in AIMD.

Upper-bounds to the AIMD dissociation probabilities, calculated assuming that all the molecules of which the outcome is still unclear at the end of the propagation time (neither dissociated nor scattered) would in the end dissociate, slightly increase the indirect dissociation channel, but are not dramatically different from the actual dissociation probabilities. Therefore, the trends that we discuss should not be affected by additional dissociation upon longer time propagation.

As shown in Figure 7.6C and 7.6D, the decrease of the indirect dissociation probability is due to a decreased trapping probability, whereas, interestingly, the dissociation probability of the trapped molecules does not depend on the initial collision energy E_i. This is consistent with a model in which the higher the collision energy is, the larger is the number of available direct paths for dissociation (more direct reaction) and the lower

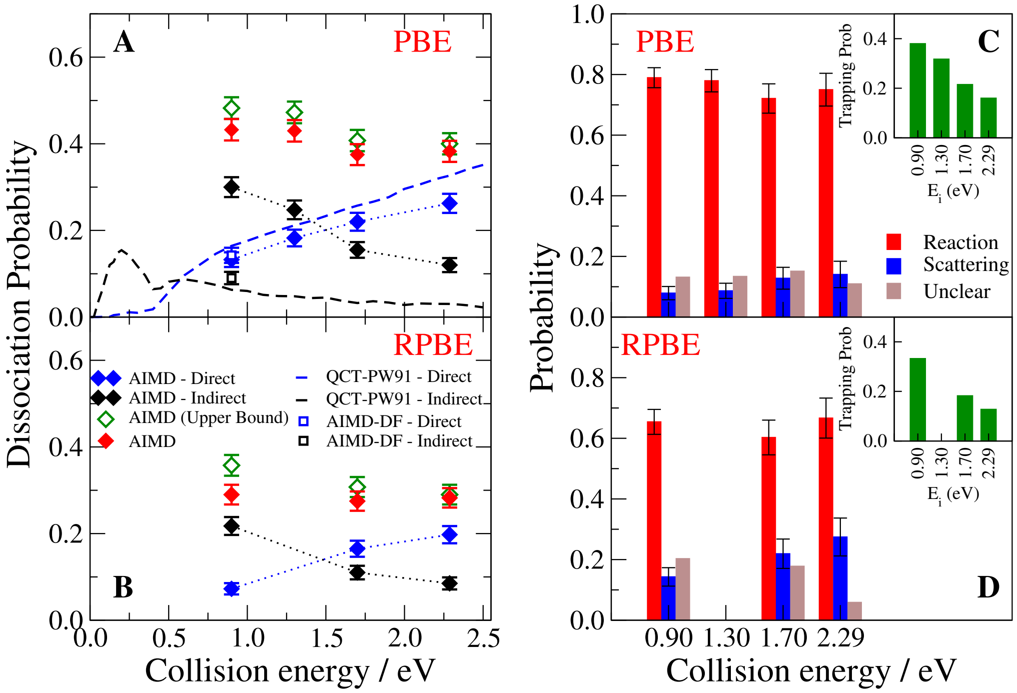

Figure 7.6: A-B: The direct (blue diamonds) and trapping-mediated (black diamonds) contributions to the dissociation probability (full red diamonds) obtained with AIMD are plotted as a function of E_i. The upper bound for the dissociation probabilities is also provided (empty green diamonds), assuming that all the unclear trajectories will dissociate. Direct and indirect dissociation probabilities for AIMD calculations simulating a distorted frozen surface (AIMD-DF) are plotted as empty blue and black squares, respectively. The direct and trapping-mediated contributions to the dissociation probability determined in the previous static-surface QCT study [12] are also plotted as dashed lines for comparison. In A, the AIMD employed the PBE functional and the QCT calculations the PW91 functional, while in B the RPBE functional has been employed in the AIMD. C-D: Reaction and scattering probabilities for trapped molecules are plotted as red and blue bars, respectively. The fraction of trapped molecules that are neither dissociated nor scattered at the end of the propagation time is plotted in brown. In the insets, the trapping probability as a function of E_i. C is for PBE, D is for RPBE.

is the probability that a molecule would be stabilized in an adsorption state (resulting in less indirect reaction). As a result of the increasing direct reaction probability and the decreasing indirect reaction probability with increasing E_i, the total reaction probability remains more or less constant. We note in passing that the reaction probability of the trapped molecules is larger for PBE than for RPBE.

7.3.3 Energy Transfer to the Lattice

In order to better understand trapping, we have looked at the energy exchanged between the molecules and the surface. For the scattered trajectories, a significant amount of energy is transferred from the molecules to the lattice, as visible from the energy transfer distributions in Figure 7.7A and 7.7B for PBE and RPBE, respectively. Quite broad distributions are observed, with negative energy tails representing energy transferred from the surface to the molecules, without significant differences between PBE and RPBE data. Note that the higher the initial collision energy, the broader and the more shifted to high energies the distributions are. Note also that the larger energy transfer directed from the molecules to the surface is consistent with the fact that surface atoms only possess thermal energy, while much more (collision) energy is initially available in the molecules.

Average energy transfer values are reported in Table 7.6 and Table 7.7 for PBE and RPBE, respectively. The average energy transfer with a single collision, $\langle \Delta E \rangle_1$, is about 20% of E_i. The observed values of $\langle \Delta E \rangle_1$ are considerably lower than the estimates obtained on the basis of the Baule model [60, 61], which are reported in Table 7.8. According to this model, which assumes the molecule-surface impact to be equivalent to the collision of two hard-spheres, the energy transferred to the lattice is:

$$\Delta E = \frac{4\mu}{(1+\mu)^2} E_i, \tag{7.1}$$

where μ is the ratio between the molecular (projectile) mass and the mass of one surface atom M_W. For a system for which the molecular adsorption energy V is non-negligible,

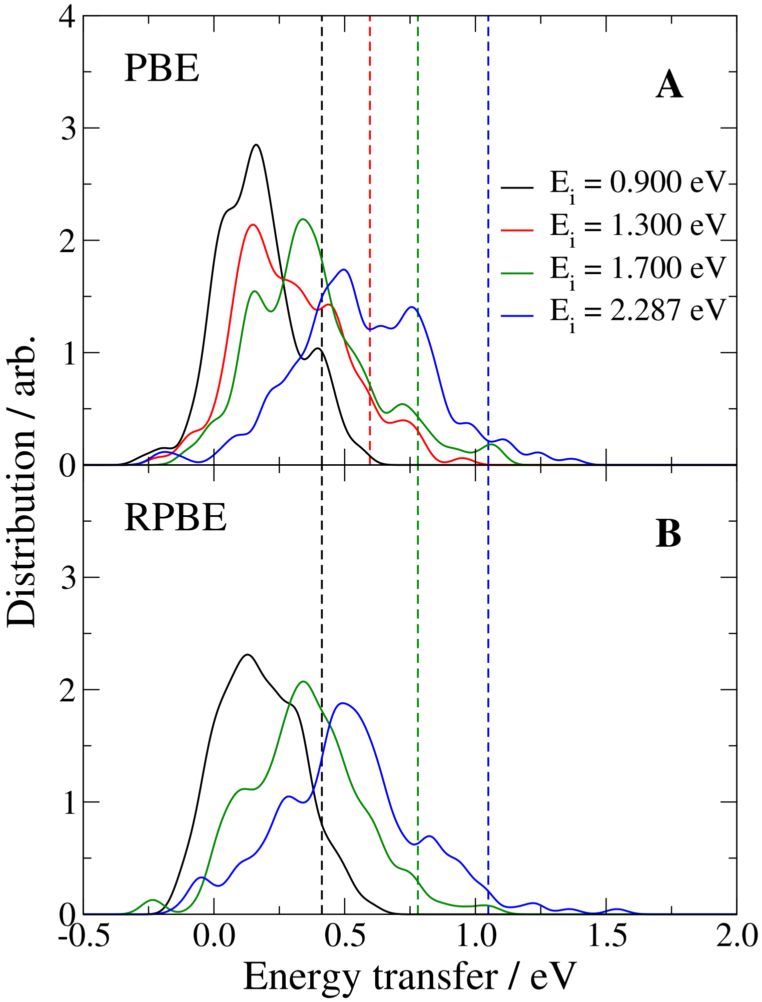

Figure 7.7: Energy transfer distributions computed for molecules scattered without performing any rebound on the surface are plotted as solid lines. Smooth distributions have been obtained by summing Gaussian functions centered at the computed energy distribution values with a σ parameter equal to 40 meV. The energy transfer values according to the Baule model are plotted as vertical dashed lines. Different colors correspond to the various initial collision energies: black for 0.9 eV, red for 1.3 eV, green for 1.7 eV and blue for 2.287 eV. A is for PBE and B is for RPBE.

PBE	$\langle \Delta E \rangle$			
E_i(eV)	0 Rebounds	>0 Rebounds	All	α
0.900	0.166± 0.012 (151)	0.344 ± 0.025 (56)	0.214 ± 0.013 (207)	0.269 ± 0.016
1.300	0.299± 0.016 (164)	0.517 ± 0.039 (47)	0.348 ± 0.017 (211)	0.291 ± 0.014
1.700	0.376 ± 0.017 (180)	0.820 ± 0.050 (57)	0.483 ± 0.022 (237)	0.303 ± 0.014
2.287	0.565 ± 0.020 (183)	0.938 ± 0.054 (57)	0.654 ± 0.022 (240)	0.300 ± 0.010

Table 7.6: Average energy transfer to the lattice ($\langle \Delta E \rangle$, eV) evaluated for the molecules scattered with no rebounds on the surface, for the molecules scattered after one or more rebounds, and for all the molecules. The calculated accommodation coefficient α is also reported. Standard errors of the mean are presented together with the number of scattered trajectories for each set of data (in brackets). The data refer to PBE calculations.

like N_2/W(110), E_i is usually replaced by $E_i + V$ in Eq. 7.1, in order to account for the extra kinetic energy that a molecule acquires when flying over the potential well (modified Baule model). The energy transfer values predicted by the modified Baule model, assuming V to be equal to the largest adsorption energy computed (i.e. for the hollow-parallel configuration, see Tables 7.4 and 7.5), are also reported in Table 7.8. The ΔE values predicted by the modified Baule model are even larger than the values predicted by the standard Baule model, and therefore in even worse agreement with the values found in AIMD. Due to the large adsorption energies ($E_a = 1.4$ eV with PBE), the modified Baule model even predicts an energy transfer larger than the initial collision energy for PBE at $E_i = 0.9$ eV. Given the simplicity of the (modified) Baule model, it is not surprising that discrepancies with AIMD results are observed. An effective surface atom mass can be obtained by fitting Eq. 7.1 to the computed ΔE values using the surface atom mass atom as a free parameter. This fit returns an effective surface atom mass equal to 2.4 M_W for the case in which the presence of a potential well is neglected, while a value of 4.7 (4.1) M_W is obtained if we consider V to be equal to the largest adsorption energy observed with the PBE (RPBE) functional. Effective surface atom mass values significantly different from M_W indicate a behaviour of the lattice quite far from the independent hard-sphere model, as expected for close packed surfaces.

The average energy transfer values computed for the trajectories that experience more than one rebound on the surface are considerably larger than the corresponding

RPBE	$\langle\Delta E\rangle$			
E_i(eV)	0 Rebounds	>0 Rebounds	All	α
0.900	0.178 ± 0.011 (186)	0.296 ± 0.024 (69)	0.210 ± 0.011 (257)	0.264 ± 0.014
1.700	0.351 ± 0.015 (217)	0.806 ± 0.046 (60)	0.450 ± 0.019 (277)	0.282 ± 0.012
2.287	0.512 ± 0.019 (216)	0.975 ± 0.047 (68)	0.623 ± 0.022 (284)	0.285 ± 0.010

Table 7.7: Same as Table 7.6, but for RPBE.

E_i(eV)	Baule	Modified Baule ($V = E_a^{PBE}$)	Modified Baule ($V = E_a^{RPBE}$)
0.900	0.413	1.075	0.859
1.300	0.596	1.259	1.042
1.700	0.780	1.443	1.226
2.287	1.049	1.712	1.495

Table 7.8: Energy transfer (eV) estimated using the Baule model, or modified Baule model, using as adsorption energy the largest PBE and RPBE adsorption energies, respectively.

$\langle\Delta E\rangle_1$ values, as expected for multiple collisions. The energy transfer averaged over all scattered trajectories amounts to about 25% of the initial collision energy, in good agreement with the findings of Pétuya et al. [21], who looked at the non-reactive scattering of N_2 from a different tungsten surface (W(100)) and included dissipation to phonons using the GLO method.

An experimental observable related to the energy transfer to the lattice is the accommodation coefficient α, defined as the average energy that a molecule exchanges with the surface divided by the difference between the average collision energy of the molecules and the translational energy that they would have if they would be in thermal equilibrium with the surface [62]:

$$\alpha = \frac{\langle\Delta E\rangle}{E_i - \frac{3}{2}k_b T_s}. \tag{7.2}$$

Thermal accommodation coefficients for nitrogen on tungsten have been determined by Chen and Saxena [63,64] using a heat-transfer column apparatus. They have determined the heat transfer from a heated gas-covered tungsten wire to the surrounding nitrogen gas, and calculated an accommodation coefficient in the range 0.18-0.32 for a surface temperature of 850 K. From our calculations, we extract a value of α in the range 0.26-

0.30 (Table 7.6 and Table 7.7), in reasonable agreement with the experimental data. However, we want to stress the fact that experimental conditions are quite far from the ones that we are simulating: the tungsten wire is not a well-cut single crystal and the gas pressures at which they have worked are relatively high (100-400 mbar). Furthermore, the authors report the possible presence of nitrogen atoms and oxygen impurities on the surfaces.

Hanisco et al. investigated the rotationally inelastic scattering of N_2 from W(110) ($T_s = 1200$ K) [10]. They determined the total (rotational + translational) final energy E_f for various final rotational states, for normal incidence and normal detection, for two different initial collision energies E_i. For $E_i = 0.75$ eV they also reported the average fraction of energy retained by the molecules $\langle E_f/E_i \rangle = 0.68$. Given the computational cost of AIMD, the number of simulated trajectories is limited, and we cannot compute theoretical final-state-resolved data with satisfying statistical accuracy. The value of $\langle E_f/E_i \rangle$ that we compute for the lowest collision energy simulated ($E_i = 0.90$ eV), assuming an acceptance angle $\Theta = 20°$ from the surface normal, is 0.82 ± 0.02 (0.80 ± 0.02) with PBE (RPBE). Note that considering only the trajectories in which the final vibrational energy does not differ from the (initial) vibrational zero point energy by more that 15% does not change the computed values of $\langle E_f/E_i \rangle$ by more than 3%. The comparison with the experimental value of $\langle E_f/E_i \rangle$ suggests that AIMD is somewhat underestimating the energy transfer to surface phonons.

Significant energy transfer to the lattice also occurs in the reactive trajectories. Figure 7.8 shows the time evolution of the mean kinetic energy of the trapped molecules that react at $t \geqslant 800$ fs. The mean kinetic energy of the molecules decreases rapidly as a function of time, and at $t = 800$ fs, the molecules have lost a large part of their initial kinetic energy, due to multiple collisions with the surface atoms. Since we are forced to employ a slab of limited thickness in the calculations and since the total energy of each AIMD trajectory is constant, energy transfer to the lattice could cause a non-physical heating of the surface. Such a surface temperature increase, however, would not be a concern if the energy flow from the impact site of the molecule to the boundaries of the surface unit cell and back to the molecule would be slower than the dissociation event. Figure 7.9 shows the mean kinetic energy of each atomic layer of the slab as a function of time, for the PBE-AIMD trajectories that react at $t \geqslant 800$ fs for $E_i = 0.9$ eV. The same behaviour is observed for RPBE-AIMD and for the other initial collision energies (not shown), but statistics are poorer as the trapping-mediated dissociation channel decreases in importance with increasing E_i. As expected, the first layer atoms on average undergo a sudden increase of kinetic energy upon collision of the molecule with the surface, at about 175 fs. The layers below experience smoother changes in kinetic energy, and these changes occur at larger times. The fourth layer is almost unperturbed even after several hundreds of fs after the impact of the molecule. These observations suggest that our finite-size slab is thick enough not to observe significant nonphysical energy reflection from the bottom of the slab on the examined time-scale. Note that by 1 ps, almost 70% of the dissociation observed for $E_i = 0.9$ eV, for which the trapping mediated reaction has the largest contribution, has already occurred. Therefore, applying a thermostat to the atoms at the boundary of the cell in order to avoid non-physical phonon reflection is not expected to considerably affect the dynamics of the majority of the dissociating molecules. Moreover, for the minority of the molecules dissociating at larger times, which might be affected by a surface being non-physically 'too hot', the use of a thermostat would facilitate the energy flow from the molecule to the surface. This would make it even more difficult for them to 'escape' from the adsorption wells, increasing even more the sticking probability. Therefore, applying a thermostat to the bottommost moving layer might be necessary to accurately describe the behaviour of the molecules dissociating at large times, but we do not expect this to change the most important conclusions of our study.

Another observation from Figure 7.8 is that at 800 fs the average kinetic energy of the molecules that go on to react is almost independent of the initial collision energy. If the molecules would be in thermal equilibrium with an infinite surface, their expected mean kinetic energy would be $3k_bT_S$ (about 0.2 eV for $T_S = 800$ K, also plotted as a horizontal dash in Figure 7.8). The observed average kinetic energy is about 0.6 eV,

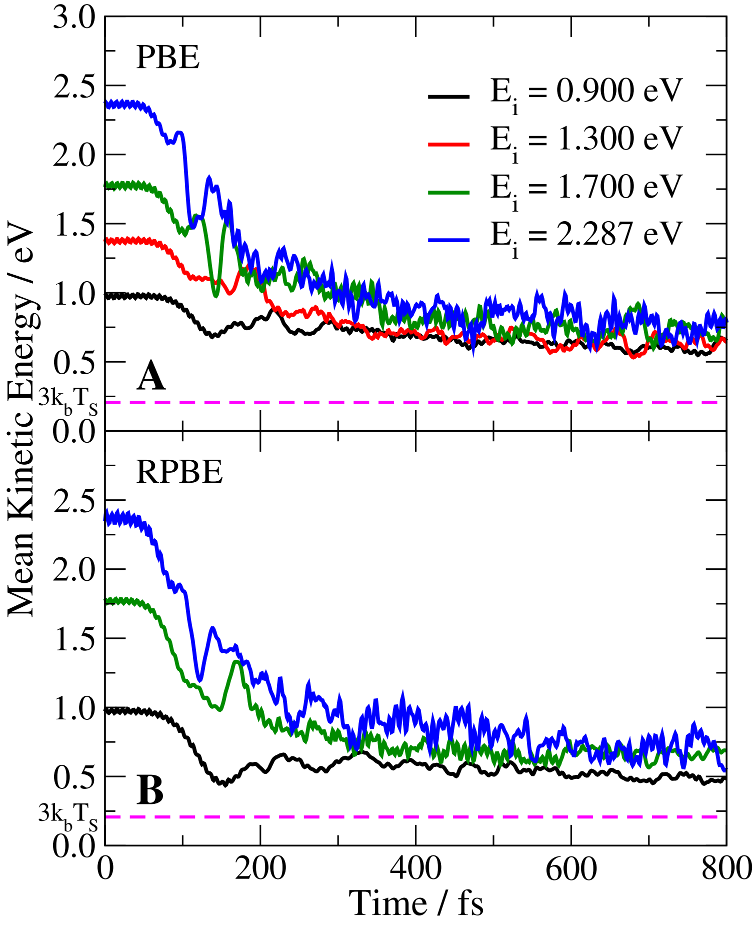

Figure 7.8: The mean kinetic energy of the molecules dissociating at propagation times larger than 800 fs is plotted as a function of time. A is for PBE and B is for RPBE. Colors are as for Figure 7.7. The dashed horizontal line indicates the energy corresponding to $3k_bT_s$.

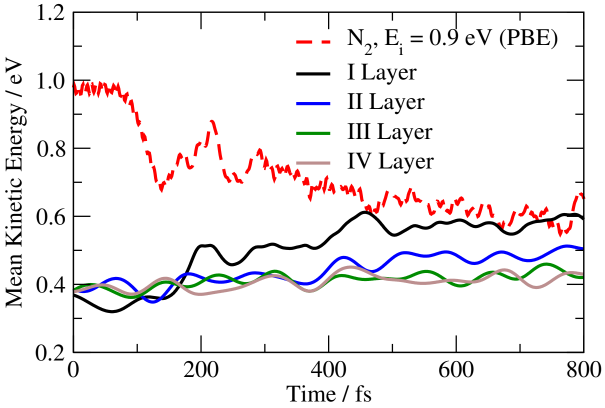

Figure 7.9: The mean kinetic energies evaluated for the PBE trajectories with $E_i = 0.9$ eV dissociating at propagation times larger than 800 fs is plotted as a function of time. The dashed red line corresponds to the mean kinetic energy of the molecule, while black, blue, green and brown solid lines correspond to the mean kinetic energy of the first, second, third and fourth atomic layers, respectively.

which is considerably higher than this thermal limit. However, this can be explained considering that energy transferred from the molecule to the slab generates a ‘hot’ first layer, which has not yet had enough time to equilibrate with the rest of the slab, as shown in Figure 7.9.

The fast energy transfer from the molecule to the surface explains the insensitivity of the dissociation probability of the trapped molecules to the initial collision energy. Trapped molecules quickly dissipate energy to phonons so that similar amounts of energy remain available for the reaction, regardless of the initial E_i. Fast energy transfer to the lattice, together with the role played by the molecular adsorption states, can also explain why a larger indirect dissociation probability is obtained with AIMD than in previous static surface studies, as shown in Section 7.3.4.

7.3.4 The Role of Molecular Adsorption in the Dynamics

We analyzed the configurational space explored by the N_2 molecules that undergo molecular trapping. In particular, we looked for the configurations that might be attributed to the molecular adsorption states identified on an ideal surface. Note that all the molecular adsorption wells can be directly accessed from the gas-phase at all the considered collision energies, since the minimum energy barriers for accessing these wells are lower than the collision energies examined for both the PBE and RPBE functionals (see Table 7.3, Figure 7.2 and Figure 7.3).

Instantaneous surface deformations due to the thermal displacements of the surface atoms might slightly modify the geometry (and the energy) of the molecular adsorption states. Also for this reason, operational definitions that include ranges of molecular coordinates have been used to determine whether the molecule assumes the configuration of a specific adsorption state. We defined the top-vertical adsorption state as exhibiting configurations with the molecule's COM above a first layer surface atom, within a lateral displacement of 0.5 Å and Z and θ within 0.2 Å and 20° from the ideal lattice adsorption state values (see Table 7.2), respectively. Note that the large tolerance that we allow for the lateral displacement is justified by the relatively low corrugation of the PES in X and Y close to this minimum: A displacement of N_2 of 0.5 Å away from the top-site would increase the interaction energy by less than 0.18 eV, for both functionals. The same tolerance in Z and θ was employed for identifying the other two molecular adsorption states. For the hollow-parallel adsorption state the molecule's COM was required to be within a lateral displacement of 0.25 Å from the second layer atom and ϕ to assume a value within 20° from the ideal lattice adsorption state value (see Table 7.2), taking the N_2 inversion symmetry into account. Finally, for the bridge/hollow-tilted configuration, the azimuthal angle ϕ has been required to be perpendicular to the line connecting two adjacent top sites (within 20°), with one of the two N atoms above the bridge site (within a 0.25 Å lateral displacement). Note that the use of tolerance intervals 50 % larger than the employed ones did not considerably affect the analysis.

We find that trapped molecules that go on to react or whose outcome is still unclear at the end of the propagation often visit one or more of the two deepest molecular adsorption states: The hollow-parallel configuration is visited in more than 50 % of the cases, and the bridge/hollow-tilted configuration is visited in more than 60 % of the cases, for both PBE and RPBE. This is not the case for the molecules that will in the end be scattered. In particular, the molecules that reach the hollow-parallel configuration (the deepest adsorption well) are almost never scattered: This event is observed only in one out of 211 trajectories for the PBE calculations, at the highest E_i, and very few times (in 4 out of 122 trajectories, one for $E_i = 1.7$ eV and three for $E_i = 2.287$ eV) for the RPBE calculations. Furthermore, most of the trapped molecules that will eventually react (70% or more, depending on the initial collision energy) visit at least one of the molecular adsorption states before dissociation.

These findings suggest the following picture of the computed dynamics: molecules reaching one of the molecular adsorption states are often (temporally) trapped. From these adsorption states, molecules dissipate energy to the phonons so that retracing the path back towards the gas phase is more difficult or even impossible; dissociation and molecular adsorption are then the only possible outcomes for these molecules. The energy dissipation to phonons therefore enhances the trapping-mediated dissociation channel, and this explains the larger contribution of the indirect mechanism to dissociation observed in AIMD than seen in static-surface calculations [12, 13, 15] and in AIMD-DF calculations. In this picture, the fact that AIMD overestimates the experimental dissociation probabilities at low E_i is consistent with the overestimation of the molecular adsorption energies by both PBE and RPBE, as discussed in Section 7.3.1. With shallower adsorption wells the trapping probability will be reduced and, as a consequence, so will the trapping mediated dissociation channel contribution.

7.4 Summary and Conclusions

In this study we employed the AIMD method to determine the sticking probability for N_2 on W(110). Our method includes improvements with respect to a previous static surface study since we explicitly model surface temperature and surface motion effects. The AIMD results, obtained with two different GGA density functionals (PBE and RPBE), are considerably different from the previous static-surface results, especially for the trapping-mediated dissociation channel, which dominates at low energies. The presence of deep adsorption minima in the multidimensional PES sampled by AIMD, together with a significant energy transfer to the surface, are suggested to be responsible for the large indirect dissociation probability: molecules that are molecularly adsorbed often dissipate kinetic energy to phonons such that they no longer find their way back to the gas phase, with dissociation or molecular adsorption as only possible outcomes. Agreement with experiments is reasonable at high energies, but the AIMD method fails to reproduce the experimental trend according to which the dissociation probability increases with collision energy, predicting a probability that is insensitive to E_i. At low energies, AIMD overestimates the experimental dissociation probability. We attribute the mismatch between the AIMD results and experiments to a failure of both the PBE and RPBE functionals to reproduce the experimental molecular adsorption energies, and the fact that the RPBE functional returns lower molecular adsorption energies might explain the better agreement obtained with this functional with experiments for the dissociation probability at low collision energy.

7.A Appendix

7.A.1 NEB Calculations

In the following Figures we present the results of the CI-NEB calculations. Four images (labeled as 1-4) have been optimized between each of the molecular adsorption configurations (reactants, R) and the lowest-energy dissociated adsorption state (products, P). The zero of energy is defined as the energy of the molecule in its equilibrium geometry placed midway between two slabs.

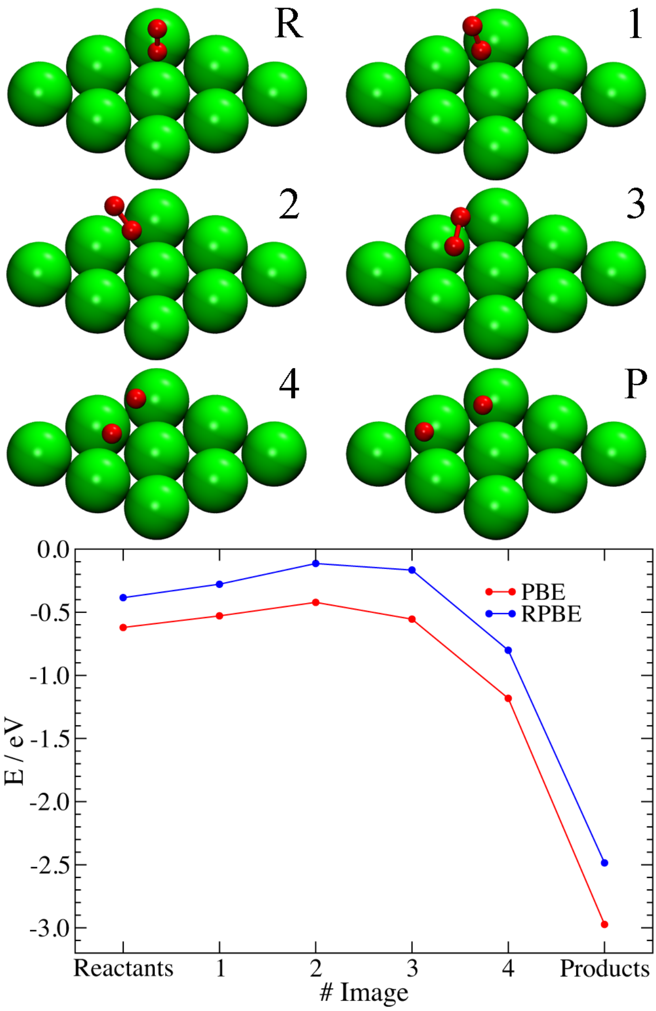

Figure 7.A.1: Results of CI-NEB calculations in which the reactants correspond to the top-vertical molecular adsorption geometry. In the lower panel, the energy of each configuration is plotted as a function of the image number. Red is for PBE and blue for RPBE. Straight lines connect points corresponding to consecutive images. The molecular configurations, as well as first layer surface atoms, are schematically represented above.

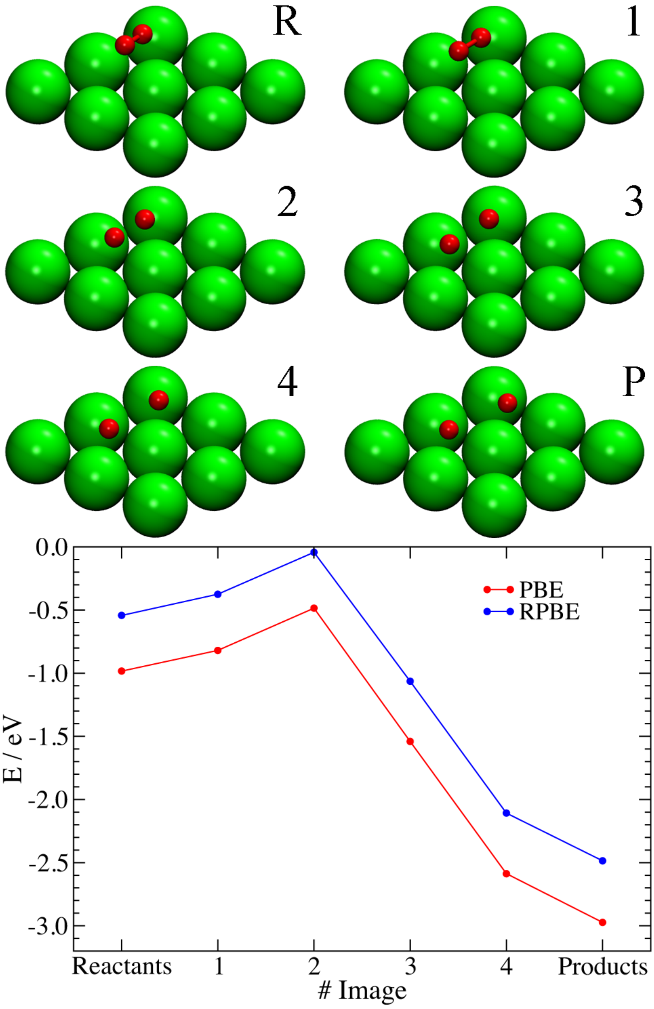

Figure 7.A.2: Same as Figure 7.A.1, but the reactants correspond here to the bridge/hollow-tilted molecular adsorption configuration.

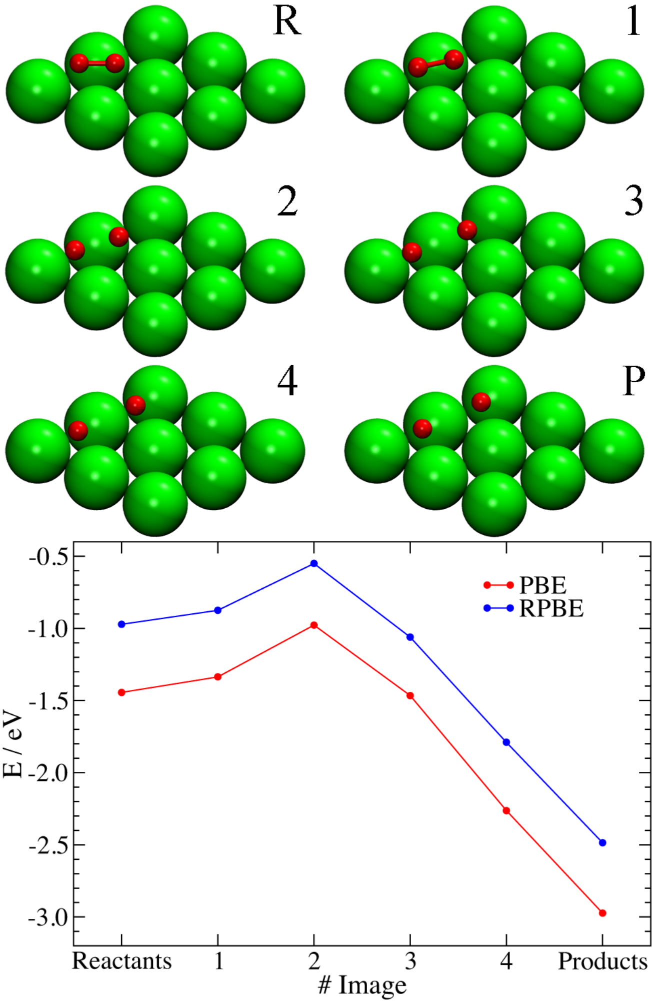

Figure 7.A.3: Same as Figure 7.A.1, but the reactants correspond here to the hollow-parallel molecular adsorption configuration.

Bibliography

[1] G. Ertl, Catal. Rev. Sci. Eng. **21**, 201 (1980).

[2] S. P. Singh-Boparai, M. Bowker, and D. A. King, Surf. Sci. **53**, 55 (1975).

[3] J. T. Yates, R. Klein, and T. E. Madey, Surf. Sci. **58**, 469 (1976).

[4] R. C. Cosser, S. R. Bare, S. M. Francis, and D. A. King, Vacuum **31**, 503 (1981).

[5] H. E. Pfnür, C. T. Rettner, J. Lee, R. J. Madix, and D. J. Auerbach, J. Chem. Phys. **85**, 7452 (1986).

[6] A. Kara and A. E. DePristo, J. Chem. Phys. **88**, 2033 (1988).

[7] J. C. Lin, N. Shamir, Y. B. Zhao, and R. Gomer, Surf. Sci. **231**, 333 (1990).

[8] Q. J. Zhang, J. C. Lin, N. Shamir, and R. Gomer, Surf. Sci. **231**, 344 (1990).

[9] C. T. Rettner, E. K. Schweizer, and H. Stein, J. Chem. Phys. **93**, 1442 (1990).

[10] T. F. Hanisco and A. C. Kummel, J. Vac. Sci. Technol. A **11**, 1907 (1993).

[11] G. Volpilhac and A. Salin, Surf. Sci. **556**, 129 (2004).

[12] M. Alducin, R. Díez Muiño, H. F. Busnengo, and A. Salin, J. Chem. Phys. **125**, 144705 (2006).

[13] M. Alducin, R. Díez Muiño, H. F. Busnengo, and A. Salin, Phys. Rev. Lett. **97**, 056102 (2006).

[14] M. Alducin, R. Díez Muiño, H. F. Busnengo, and A. Salin, Surf. Sci. **601**, 3726 (2007).

[15] G. A. Bocan, R. Díez Muiño, M. Alducin, H. F. Busnengo, and A. Salin, J. Chem. Phys. **128**, 154704 (2008).

[16] J. I. Juaristi, M. Alducin, R. Díez Muiño, H. F. Busnengo, and A. Salin, Phys. Rev. Lett. **100**, 116102 (2008).

[17] S. Riikonen, A. S. Foster, A. V. Krasheninnikov, and R. M. Nieminen, Phys. Rev. B **80**, 155429 (2009).

[18] I. Goikoetxea, J. I. Juaristi, M. Alducin, and R. Díez Muiño, J. Phys.: Condens. Matter **21**, 264007 (2009).

[19] K. R. Geethalakshmi, J. I. Juaristi, R. Díez Muiño, and M. Alducin, Phys. Chem. Chem. Phys. **13**, 4357 (2011).

[20] L. Martin-Gondre, M. Alducin, G. A. Bocan, R. Díez Muiño, and J. I. Juaristi, Phys. Rev. Lett. **108**, 096101 (2012).

[21] R. Pétuya, P. A. Plötz, C. Crespos, and P. Larregaray, J. Phys. Chem. C **118**, 21904 (2014).

[22] J. P. Perdew, J. A. Chevary, S. H. Vosko, K. A. Jackson, M. R. Pederson, D. J. Singh, and C. Fiolhais, Phys. Rev. B **46**, 6671 (1992).

[23] J. P. Perdew, J. A. Chevary, S. H. Vosko, K. A. Jackson, M. R. Pederson, D. J. Singh, and C. Fiolhais, Phys. Rev. B **48**, 4978 (1993).

[24] B. Hammer, L. B. Hansen, and J. K. Nørskov, Phys. Rev. B **59**, 7413 (1999).

[25] G. J. Kroes, Science **321**, 794 (2008).

[26] A. C. Luntz, I. Makkonen, M. Persson, S. Holloway, D. M. Bird, and M. S. Mizielinski, Phys. Rev. Lett. **102**, 109601 (2009).

[27] J. I. Juaristi, M. Alducin, R. Díez Muiño, H. F. Busnengo, and A. Salin, Phys. Rev. Lett. **102**, 109602 (2009).

[28] G. J. Kroes, Phys. Chem. Chem. Phys. **14**, 14966 (2012).

[29] L. Martin-Gondre, J. I. Juaristi, M. Blanco-Rey, R. Díez Muiño, and M. Alducin, J. Chem. Phys. **142**, 074704 (2015).

[30] M. Dion, H. Rydberg, E. Schröder, D. C. Langreth, and B. I. Lundqvist, Phys. Rev. Lett. **92**, 246401 (2004).

[31] K. Lee, E. D. Murray, L. Kong, B. I. Lundqvist, and D. C. Langreth, Phys. Rev. B **82**, 081101 (2010).

[32] A. De Vita, I. Štich, M. J. Gillan, M. C. Payne, and L. J. Clarke, Phys. Rev. Lett. **71**, 1276 (1993).

[33] I. Štich, M. C. Payne, A. De Vita, M. J. Gillan, and L. J. Clarke, Chem. Phys. Lett. **212**, 617 (1993).

[34] I. Štich, A. De Vita, M. C. Payne, M. J. Gillan, and L. J. Clarke, Phys. Rev. B **49**, 8076 (1994).

[35] A. Groß and A. Dianat, Phys. Rev. Lett. **98**, 206107 (2007).

[36] F. Nattino, C. Díaz, B. Jackson, and G. J. Kroes, Phys. Rev. Lett. **108**, 236104 (2012).

[37] F. Nattino, H. Ueta, H. Chadwick, M. E. van Reijzen, R. D. Beck, B. Jackson, M. C. van Hemert, and G. J. Kroes, J. Phys. Chem. Lett. **5**, 1294 (2014).

[38] L. S. Dubrovinsky and S. K. Saxena, Phys. Chem. Miner. **24**, 547 (1997).

[39] J. S. Shah and M. E. Straumanis, J. Appl. Phys. **42**, 3288 (1971).

[40] V. F. Sears and S. A. Shelley, Acta Crystallogr., Sect. A **47**, 441 (1991).

[41] J. C. Buchholz, G. C. Wang, and M. G. Lagally, Surf. Sci. **49**, 508 (1975).

[42] R. J. Smith, C. Hennessy, M. W. Kim, C. N. Whang, M. Worthington, and M. D. Xu, Phys. Rev. Lett. **58**, 702 (1987).

[43] G. Kresse and J. Hafner, Phys. Rev. B **47**, 558 (1993).

[44] G. Kresse and J. Hafner, Phys. Rev. B **49**, 14251 (1994).

[45] G. Kresse and J. Furthmüller, Comput. Mat. Sci. **6**, 15 (1996).

[46] G. Kresse and J. Furthmüller, Phys. Rev. B **54**, 11169 (1996).

[47] G. Kresse and D. Joubert, Phys. Rev. B **59**, 1758 (1999).

[48] P. E. Blöchl, Phys. Rev. B **50**, 17953 (1994).

[49] J. P. Perdew, K. Burke, and M. Ernzerhof, Phys. Rev. Lett. **77**, 3865 (1996).

[50] J. P. Perdew, K. Burke, and M. Ernzerhof, Phys. Rev. Lett. **78**, 1396 (1997).

[51] W. L. Hayes, *Statistics*, Holt, Rinehart and Winston, NY, 3rd edition, 1981.

[52] V. Blum, R. Gehrke, F. Hanke, P. Havu, V. Havu, X. Ren, K. Reuter, and M. Scheffler, Comput. Phys. Commun. **180**, 2175 (2009).

[53] G. Henkelman, B. P. Uberuaga, and H. Jónsson, J. Chem. Phys. **113**, 9901 (2000).

[54] G. Henkelman and H. Jónsson, J. Chem. Phys. **113**, 9978 (2000).

[55] E. Bitzek, P. Koskinen, F. Gähler, M. Moseler, and P. Gumbsch, Phys. Rev. Lett. **97**, 170201 (2006).

[56] I. Goikoetxea, M. Alducin, R. Díez Muiño, and J. I. Juaristi, Phys. Chem. Chem. Phys. **14**, 7471 (2012).

[57] I. Goikoetxea, J. I. Juaristi, R. Díez Muiño, and M. Alducin, Phys. Rev. Lett. **113**, 066103 (2014).

[58] M. Alducin, Private Communication, 2015.

[59] T. A. Delchar and G. Ehrlich, J. Chem. Phys. **42**, 2686 (1965).

[60] B. Baule, Ann. Physik. **44**, 145 (1914).

[61] A. Gross, *Theoretical Surface Science*, Springer, Berlin, 2003.

[62] F. O. Goodman, J. Phys. Chem. **84**, 1431 (1980).

[63] S. H. P. Chen and S. C. Saxena, Int. J. Heat Mass Transfer **17**, 185 (1974).

[64] S. C. Saxena and S. H. P. Chen, J. Phys. B: At. Mol. Phys. **10**, 2011 (1977).

Samenvatting

Ab initio moleculaire dynamica berekeningen aan reacties van moleculen op metaaloppervlakken

Het wetenschappelijke belang van reacties op metaaloppervlakken komt mede voort uit de enorme relevantie van heterogene katalyse. Deeltjes van overgangsmetalen zijn vaak het actieve deel van een katalysator: zij kunnen reactanten vanuit de gasfase binden, bindingen splitsen, een goede omgeving voor atomaire diffusie leveren en reactieproducten laten desorberen. Een katalytische cyclus bestaat uit verschillende elementaire reactiestappen. De studie van deze elementaire reactiestappen is echter zeer complex. Dit komt door het feit dat de actieve fase van een katalysator gewoonlijk slecht gekarakteriseerd is en inhomogeen verdeeld is over een inerte drager. Bovendien wordt bij katalyse vaak een hoge temperatuur en druk gebruikt. De complexiteit van katalytisch relevante molecuul-metaaloppervlak reacties kan gereduceerd worden door een nauwkeurig gesneden enkelkristal oppervlak onder gecontroleerde fysische omstandigheden te gebruiken om de echte katalysator te modelleren. Omdat de adsorptie van een molecuul op een metaaloppervlak vaak de eerste stap van een katalytische cyclus is, zijn een groot aantal studies gericht op de reactieve en niet-reactieve verstrooiing van moleculen op oppervlakken om de adsorptiefenomenen beter te kunnen begrijpen.

In de oppervlaktewetenschap hebben computersimulaties een hoge potentie om met de interpretatie van experimenten te helpen: ze kunnen een 'film' van een chemisch proces op atomaire schaal verstrekken en ze zijn over het algemeen goedkoper, sneller en veiliger dan gewone laboratoriumexperimenten. Veel actuele methoden die de dynamica van molecuul-oppervlak reacties modelleren bestaan uit drie stappen: eerst wordt de molecuul-oppervlak interactieënergie voor verschillende moleculaire configuraties in de grondtoestand berekend met behulp van een geschikte elektronenstructuur methode (meestal dichtheidsfunctionaaltheorie, DFT, binnen de 'generalized gradient approximation', GGA); vervolgens worden de berekende energiepunten gefit of geïnterpoleerd om een continue uitdrukking van de energie als functie van de moleculaire configuratie te verkrijgen (het potentiaaloppervlak, PES); ten slotte worden dynamica berekeningen op de vooraf berekende PES uitgevoerd. De tweede stap legt een aantal beperkingen op voor de algemene toepasbaarheid van de beschreven werkwijze op het gebied van molecuul-oppervlak reacties. Het uitvoeren van een nauwkeurige fit of interpolatie van voorberekende energiepunten is een zeer complexe taak voor een groot aantal nucleaire vrijheidsgraden (> 6). Daarom maken de berekeningen die deze methode gebruiken vaak gebruik van de statische-oppervlak-benadering (of wordt de oppervlaktetemperatuur met benaderende methodes gemodelleerd). Om dezelfde reden zijn dynamische benaderingen of model potentiaaloppervlakken nodig om de reactie van polyatomische moleculen op oppervlakken te beschrijven.

Het doel van het werk dat in dit proefschrift beschreven wordt is de *ab initio* moleculaire dynamica (AIMD) methode toe te passen op de studie van reacties op metaaloppervlakken. Deze methode is niet nieuw en de toepassing ervan op het gebied van de oppervlaktewetenschap ook niet, maar pas recent werd het mogelijk om experimentele observabelen (zoals reactiewaarschijnlijkheden) met redelijke statistische nauwkeurigheid met deze methode te berekenen. Het gebruik van AIMD omzeilt de noodzaak om een PES van tevoren uit te rekenen en te fitten, omdat de krachten die op de atoomkernen werken 'on-the-fly' op elke tijdstap van de dynamica worden uitgerekend.

Drie systemen werden bestudeerd in dit proefschrift. Hoofdstuk 3 en Hoofdstuk 4 gaan over de dissociatie van waterstof op een koperoppervlak. Dit systeem is belangrijk vanwege het grote aantal experimentele en theoretische studies die gericht zijn op deze molecuul-oppervlak reactie, zodat het als een voorbeeldsysteem voor geactiveerde dissociatieve chemisorptie wordt beschouwd, niet vanwege industriële toepassingen van dit systeem. Eerdere berekeningen die gebruik gemaakt hebben van de statische-oppervlakbenadering waren in staat om verschillende observabelen met een hoge nauwkeurigheid te reproduceren, die ofwel bij een lage oppervlaktetemperatuur waren gemeten, of slechts zwak afhankelijk van de oppervlaktetemperatuur zijn. Deze berekeningen konden echter sommige observabelen die bij hoge temperatuur zijn gemeten niet reproduceren, zoals de 'rotational quadrupole alignment' parameter $A_0^{(2)}$. Deze parameter representeert de afhankelijkheid van de reactiviteit van de oriëntatie van het molecuul ten opzichte van het oppervlak. In Hoofdstuk 3 laten we zien dat oppervlaktetemperatuureffecten gemodelleerd met AIMD over het algemeen de 'rotational quadrupole alignment' parameter voor de reactie van D_2 op Cu(111) verlagen. De overeenkomst tussen theorie en experimenten wordt aanzienlijk verbeterd als dit effect gemodelleerd wordt. We laten ook zien dat de initiële-toestand-geselecteerde reactiewaarschijnlijkheid enigszins verbeterd is voor de twee initiële toestanden waarvoor de 'rotational quadrupole alignment' is gemeten, ten opzichte van statische-oppervlak-berekeningen. Vervolgonderzoek is echter noodzakelijk om de oorzaak te begrijpen van de verschillen die nog bestaan tussen theorie en experiment in de beschrijving van $A_0^{(2)}$.

De initiële-toestand-geselecteerde reactiewaarschijnlijkheid van D_2 op Cu(111) is het belangrijkste onderwerp van Hoofdstuk 4. Reeds bestaande verschillen tussen statische-oppervlakberekeningen en experimentele gegevens zijn onderzocht door het uitvoeren van nieuwe AIMD berekeningen die oppervlaktetemperatuureffecten modelleren en door het uitvoeren van een verbeterde analyse van de ruwe experimentele data. We hebben ook 'time-of-flight' spectra op basis van de theoretische reactiewaarschijnlijkheden gesimuleerd om de theorie met experimenten te vergelijken zonder de ruwe meetgegevens te manipuleren. De resultaten laten zien dat de nieuwe analyse van de experimentele data de overeenkomst tussen theorie en experimenten verbetert: door de experimentele data met flexibelere functies te beschrijven, krijgen we reactiewaarschijnlijkheidscurves waarvan de verzadigingswaarde niet (of niet sterk) van de initiële vibrationele toestand afhankelijk is, zoals in de simulaties, terwijl het omgekeerde was gevonden in de oorspronkelijke analyse van de experimentele data. Bovendien is de gemiddelde absolute fout in de energie waarop de initiële-toestand-geselecteerde reactiewaarschijnlijkheid gelijk is aan de helft van de experimentele verzadigingswaarde (de zogenaamde 'effectieve barrière hoogte') nu lager dan 1 kcal/mol (limiet die de chemische nauwkeurigheid bepaalt) voor zowel statische-oppervlak als AIMD berekeningen. Zoals ook in Hoofdstuk 3 gevonden is, is er een lichte verbetering in de initiële-toestand-geselecteerde reactiewaarschijnlijkheidscurves op de statische-oppervlak-berekeningen als oppervlaktetemperatuureffecten met AIMD worden gemodelleerd. Er bestaan echter nog steeds verschillen in de absolute verzadigingswaarden van de reactiewaarschijnlijkheidscurves.

Hoofdstuk 5 en Hoofdstuk 6 gaan over de dissociatie van methaan op een platinaoppervlak. De dissociatie van methaan op metalen is zowel van praktisch als fundamenteel belang. De splitsing van een CH-binding van het molecuul en de opeenvolgende adsorptie van het methylfragment en van het waterstofatoom op een nikkel katalysator is de eerste en een snelheidsbepalende stap in het 'steam reforming' proces, dat de belangrijkste commerciële bron van moleculair waterstof is. Moleculaire bundelexperimenten tonen aan dat de reactiviteit van het molecuul niet statistisch afhangt van de manier waarop energie oorspronkelijk wordt aangebracht in de verschillende vrijheidsgraden van het molecuul.

In Hoofdstuk 5 worden AIMD berekeningen, gebaseerd op de PBE dichtheidsfunctionaal, aan de reactiviteit van de CHD_3 methaan isotopoloog op Pt(111) gepresenteerd. Experimenten die een laser gebruiken om de CH-strekvibratie van de reagerende moleculen vooraf te exciteren toonden aan dat de reactiviteit na deze vibrationele excitatie aanzienlijk stijgt. Bovendien leveren CHD_3 moleculen die normaal dissociëren om $H_{(a)}$ + $CD_{3(a)}$ en $D_{(a)}$ + $CHD_{2(a)}$ met de statistische relatieve verhouding 1:3 te geven, alleen $H_{(a)}$ + $CD_{3,(a)}$ op na voorafgaande excitatie van de CH-strekvibratie. Onze berekeningen reproduceren kwalitatief de experimentele verhoudingen en zij beschrijven semi-kwantitatief de experimentele reactiewaarschijnlijkheden als functie van de gemiddelde botsingsenergie van de moleculen. We hebben ook de geldigheid van de dynamische benaderingen die eerder werden gebruikt om de dissociatie van methaan te modelleren getest. Wij hebben gevonden dat de ‘sudden’ (plotselinge) benadering, die ervan uitgaat dat een vrijheidsgraad ‘bevroren’ kan worden als hij in de dynamica niet sterk verandert, voor de berekening van de reactiewaarschijnlijkheid kan worden gebruikt om de laterale beweging van het molecuul en de rotatie te beschrijven. Ten slotte hebben we de rol van de beweging van het oppervlakteatoom in de dynamica onderzocht. We hebben gevonden dat het oppervlakteatoom onder het molecuul dat aan het dissociëren is gemiddeld buiten het oppervlak is voor reactieve trajecten bij lage botsingsenergieën. Deze bevinding is consistent met eerdere studies die hebben aangetoond dat de beweging van het oppervlakteatoom richting het invallende molecuul de barrière voor dissociatie verlaagt. Deze observaties kunnen de sterke oppervlaktetemperatuur afhankelijkheid die is waargenomen voor methaan dissociatie op metaaloppervlakken verklaren.

In Hoofdstuk 6 wordt het effect van de dichtheidsfunctionaal op de methaan dissociatie op Pt(111) behandeld. Ons doel is om een semi-empirische dichtheidsfunctionaal te vinden die de reactiviteit van moleculaire bundels waarin slechts een fractie van de moleculen vibrationeel geëxciteerd is (‘laser-off’ moleculaire bundels) en van moleculaire bundels waarin de CH-strekvibratie met een laser wordt geëxciteerd nauwkeurig te beschrijven. Verschillende dichtheidsfunctionalen zijn beschouwd, inclusief functionalen die de Van der Waals interactie modelleren. Recentelijk is aangetoond dat dergelijke functionalen redelijk goed werken om de reactie van H_2 en N_2 op metaaloppervlakken te beschrijven. De dichtheidsfunctionaal die in het algemeen het beste overeenkomt met de experimentele data bestaat uit een correlatiefunctionaal ontwikkeld om de Van der Waals interactie te modelleren en een lineaire combinatie van de RPBE en de PBE uitwisselingsfunctionalen. In het bijzonder geeft deze functionaal goede overeenkomst met de ‘laser-off’ experimenten bij lage botsingsenergieën en met experimenten waarin de CH-strek vibrationeel geëxciteerd is. Daarmee is deze functionaal een verbetering ten opzichte van de PBE beschrijving.

We hebben de dissociatie van methaan op Pt(111) gemodelleerd, maar het metaal dat meer relevant is voor het katalytische ‘steam reforming’ proces is nikkel. Daarom kan de reactie van methaan op nikkeloppervlakken het doel van toekomstige studies zijn. Het zou interessant zijn om de functionalen die de Van der Waals interactie op dit systeem modelleren te onderzoeken, zoals al op een Pt oppervlak is gedaan. Op de lange termijn kunnen hoogdimensionale quantumdynamica berekeningen worden gebruikt om de rol van tunneling in de dissociatieve reactie van methaan te onderzoeken, maar dit kan het beste pas gedaan worden nadat een dichtheidsfunctionaal die nauwkeurige potentiaaloppervlakken produceert met AIMD wordt gevonden.

Ten slotte is de dissociatie van stikstof op een wolfraamoppervlak (W(110)) het onderwerp van Hoofdstuk 7. Dit systeem is van belang als modelsysteem voor heterogene katalyse, omdat de dissociatieve adsorptie van N_2 op ijzer de snelheidsbepalende stap van de ammoniaksynthese is. Wolfraam en ijzer hebben een aantal overeenkomsten voor wat betreft de adsorptie van stikstof. Zo tonen beide metalen een grote kristallografische anisotropie, wat betekent dat de dissociatieve adsorptie van N_2 sterk afhangt van welk kristallografisch vlak wordt blootgesteld aan de moleculen. De reactieve en niet-reactieve verstrooiing van N_2 aan wolfraamoppervlakken werd eerder nog niet nauwkeurig gemodelleerd. Wij hebben het effect van de beweging van oppervlakteatomen op de reactiviteit van N_2 op W(110) met AIMD onderzocht. Twee dichtheidsfunctionalen (PBE en RPBE) werden voor wat betreft elektronenstructuurberekeningen getest. We hebben ontdekt dat het modelleren van de roosterbeweging in de dynamica de reactiviteit sterk verhoogt, en we suggereren dat dit voortkomt uit de beschikbaarheid van zeer diepe moleculaire adsorptieputten in de PES en omvangrijke energieuitwisseling aan het oppervlak. De energieoverdracht naar het oppervlak maakt het makkelijker voor moleculen om aan het oppervlak ingevangen ('trapped') te worden, waardoor de moleculen een hogere kans hebben om te reageren dan in de statische-oppervlaksimulaties. Vooralsnog geeft geen geteste uitwisseling-correlatie functionaal echter een goede overeenkomst met de experimentele data.

Met betrekking tot de dissociatie van N_2 op metaaloppervlakken, verdienen de volgende punten nader onderzoek. Allereerst is de rol die de beweging van oppervlakteatomen speelt bij hoge invalshoeken niet bekend. Bovendien zou het interessant zijn om te zien of een Van der Waals-gecorrigeerde dichtheidsfunctionaal goed presteert als de energieuitwisseling met het oppervlak en de oppervlaktetemperatuureffecten voor dit systeem goed worden gemodelleerd. Naast de dissociatiewaarschijnlijkheid is de rotationeel inelastische verstrooiing van N_2 aan W(110) nog een observabele waarbij het effect van oppervlakbeweging kan worden onderzocht en waarvoor experimentele gegevens beschikbaar zijn. Bovendien is de reactieve en de niet-reactieve verstrooiing van N_2 aan een andere wolfraamoppervlak, W(100), nog niet bestudeerd met AIMD om de experimentele oppervlaktetemperatuur te simuleren. Als AIMD berekeningen, die gebaseerd zijn op de Born-Oppenheimer benadering, in staat zouden zijn zowel de reactieve als de niet-reactieve verstrooiing van stikstof aan wolfraamoppervlakken nauwkeurig te modelleren, zou het belang om elektron-gat-paar excitatie te modelleren om de dissociatieve chemisorptie nauwkeurig te beschrijven, wat een onderwerp van een recent debat is, uitgesloten kunnen worden voor dit systeem.

Riassunto

Calcoli di dinamica molecolare *ab initio* per simulare reazioni di molecole su superfici metalliche

Grande interesse scientifico è dedicato alle reazioni chimiche che avvengono su superfici metalliche. Questo interesse è in gran parte dovuto all'importanza della catalisi eterogenea. Infatti, particelle di metalli di transizione sono spesso la parte attiva dei catalizzatori, grazie alle loro particolari proprietà che permettono di legare i reagenti dalla fase gassosa, di rompere i loro legami, di fornire un buon ambiente per la formazione e la diffusione di nuove molecole e di rilasciare infine i prodotti. Purtroppo, studiare le reazioni elementari che costituiscono un ciclo catalitico non è un compito semplice. Le difficoltà derivano dal fatto che la fase attiva in un catalizzatore è generalmente scarsamente caratterizzata e disomogeneamente distribuita su un supporto inerte con elevata area superficiale. Inoltre, le condizioni catalitiche spesso comportano alte temperature e pressioni. La complessità legata allo studio di reazioni gas-superficie di interesse catalitico può essere notevolmente ridotta se la superficie di un monocristallo accuratamente tagliata secondo una direzione cristallografica ben definita e mantenuta sotto condizioni fisiche ben controllate viene impiegata come modello per il 'vero' catalizzatore. Considerando che l'adsorbimento di una molecola su una superficie metallica spesso rappresenta il primo passaggio in un ciclo catalitico, un gran numero di studi si sono concentrati sullo *scattering* reattivo (e non reattivo) di molecole su superfici con l'obiettivo di migliorare la comprensione di base del fenomeno dell'adsorbimento.

Nel campo della scienza delle superfici, le simulazioni al computer possono essere di grande aiuto nell'interpretazione di dati sperimentali. Esse infatti possono fornire un 'filmato' su scala atomica di una reazione chimica e sono generalmente più economiche, sicure e veloci dei normali esperimenti in laboratorio. Molti dei metodi che vengono utilizzati per studiare la dinamica di reazione di molecole su superfici, si sviluppano in tre passaggi: in primo luogo, l'energia di interazione tra molecola e superficie nello stato elettronico fondamentale viene calcolata per diverse configurazioni molecolari attraverso un adeguato metodo di struttura elettronica (solitamente sfruttando l'approssimazione di gradiente generalizzato, GGA, della teoria del funzionale della densità, DFT); successivamente, una procedura di *fitting* o di interpolazione viene eseguita sui valori energetici calcolati in modo da ottenere un'espressione continua dell'energia in funzione della configurazione molecolare (la cosiddetta superficie di energia potenziale, PES); infine, la dinamica viene eseguita sulla PES precalcolata. Il secondo passaggio impone una serie di limitazioni che impediscono di applicare questa procedura a sistemi a piacimento. Infatti, eseguire un *fitting* o un'interpolazione accurata dei valori di energia precalcolati rappresenta un operazione molto complessa quando il numero di gradi di libertà nucleari del sistema diventa elevato (maggiore di sei). Pertanto, gli studi che utilizzano questo approccio spesso comportano l'approssimazione di superficie rigida (o modellano la temperatura della superficie con metodi approssimativi). Per lo stesso motivo, l'utilizzo di approssimazioni dinamiche o potenziali modello è necessario per descrivere la reazione di molecole poliatomiche su superfici.

Lo scopo di questa tesi è stato quello di applicare la tecnica della dinamica molecolare *ab initio* (AIMD) nello studio di reazioni su superfici metalliche. Questa tecnica non è nuova, come non è nuova la sua applicazione nel campo della scienza delle superfici, ma solo di recente è divenuto possibile calcolare osservabili sperimentali (come valori di probabilità di dissociazione) con una ragionevole precisione statistica. L'uso di AIMD scavalca la necessità di precalcolare e di eseguire un *fitting* o un'interpolazione della PES, poiché le forze che agiscono sui nuclei vengono calcolate *on-the-fly*, cioè ad ogni passo della dinamica.

Tre sistemi sono stati oggetto di studio in questa tesi. Il Capitolo 3 e il Capitolo 4 trattano la dissociazione di idrogeno su una superficie di rame. Questo sistema non è importante per particolari applicazioni industriali. La sua rilevanza deriva invece dal gran numero di studi sperimentali e teorici incentrati su questa reazione molecola-superficie, tanto che questo sistema viene considerato un sistema 'riferimento' per il chemisorbimento dissociativo attivato. Utilizzando l'approssimazione di superficie rigida, uno studio teorico precedente è stato in grado di riprodurre con grande accuratezza diversi osservabili determinati tramite esperimenti eseguiti su una superficie a bassa temperatura e osservabili debolmente dipendenti dalla temperatura della superficie. Questo studio, tuttavia, non è stato in grado di riprodurre osservabili misurati su una superficie ad alta temperatura, come il parametro di allineamento rotazionale ($A_0^{(2)}$). Questo parametro esprime la dipendenza della reattività dall'allineamento della molecola rispetto alla superficie. Nel Capitolo 3 mostriamo che gli effetti della temperatura della superficie modellati con AIMD abbassano il valore del parametro di allineamento rotazionale per la reazione di D_2 su Cu(111), migliorando sensibilmente l'accordo tra teoria ed esperimento. Mostriamo inoltre che le curve di probabilità di reazione specifiche per uno stato quantistico iniziale ottenute con AIMD sono leggermente più vicine alle corrispondenti curve sperimentali rispetto alle curve ottenute tramite calcoli con l'approssimazione di superficie rigida per i due stati iniziali per i quali abbiamo calcolato il parametro di allineamento rotazionale. Ulteriore lavoro, tuttavia, è necessario per capire il motivo del disaccordo ancora presente tra teoria ed esperimento nella descrizione di $A_0^{(2)}$.

La probabilità di reazione specifica per uno stato quantistico iniziale di D_2 su Cu(111) è il tema principale del Capitolo 4. In luce delle discrepanze tra i calcoli su una superficie rigida e i dati sperimentali, abbiamo calcolato nuove curve di probabilità di reazione con AIMD modellando gli effetti della temperatura della superficie. Abbiamo inoltre eseguito una migliore analisi dei dati grezzi sperimentali e simulato spettri di tempo di volo a partire dalle probabilità di reazione teoriche, in modo da confrontare teoria ed esperimento senza eseguire alcuna manipolazione dei dati grezzi sperimentali. I risultati ottenuti mostrano che la nuova analisi dei dati sperimentali migliora l'accordo tra teoria ed esperimenti: utilizzando funzioni più ‘flessibili’ nell’eseguire il *fitting* dei dati sperimentali, otteniamo curve di probabilità di reazione il cui valore di saturazione non dipende dallo stato vibrazionale iniziale, come anche trovato nelle simulazioni, mentre l’opposto era stato suggerito dall’originale analisi dei dati. Inoltre, l’errore medio assoluto calcolato sull’energia a cui la probabilità di reazione specifica per uno stato iniziale diventa uguale alla metà del valore di saturazione sperimentale (la cosiddetta barriera efficace) è ora inferiore a 1 kcal/mol (limite che definisce la cosiddetta accuratezza chimica) sia per i calcoli su superficie rigida sia per i calcoli AIMD. Come anche trovato nel Capitolo 3, otteniamo un leggero miglioramento nelle curve di probabilità di reazione specifiche per uno stato iniziale quando modelliamo gli effetti della temperatura della superficie con AIMD rispetto ai calcoli su superficie rigida. Tuttavia, persistono discrepanze nei valori di saturazione assoluti delle curve di probabilità di dissociazione.

Il Capitolo 5 e il Capitolo 6 trattano la dissociazione del metano su una superficie di platino. La dissociazione del metano su superfici metalliche, oltre ad essere interessante dal punto di vista della ricerca di base, è importante per le sue applicazioni pratiche. Infatti, la scissione del legame CH della molecola e il seguente adsorbimento del gruppo metile e dell’atomo di idrogeno su un catalizzatore di nichel rappresenta uno stadio cineticamente limitante nel processo di *reforming* con vapore, che costituisce la principale fonte commerciale di idrogeno molecolare. Studi sperimentali che hanno utilizzato la tecnica del fascio molecolare hanno mostrato come la reattività del metano dipenda in maniera non-statistica dal modo in cui l’energia viene inizialmente disposta nei diversi gradi di libertà della molecola.

Nel Capitolo 5 presentiamo calcoli AIMD basati sul funzionale di scambio e correlazione PBE sulla reattività dell’isotopologo del metano CHD_3 su Pt(111). Usando un laser per eccitare vibrazionalmente lo *stretching* del legame CH nelle molecole reagenti, degli esperimenti hanno dimostrato che l’eccitazione di questo modo normale aumenta significativamente la reattività delle molecole. Inoltre, le molecole di CHD_3 che normalmente dissociano a dare $H_{(a)} + CD_{3(a)}$ e $D_{(a)} + CHD_{2(a)}$ secondo il rapporto statistico 1:3, producono solamente $H_{(a)} + CD_{3,(a)}$ quando lo *stretching* del legame CH viene eccitato. I nostri calcoli riproducono qualitativamente questo risultato e descrivono semiquantitativamente la probabilità di *sticking* sperimentale in funzione dell'energia media di collisione delle molecole. Abbiamo anche testato la validità delle approssimazioni dinamiche utilizzate in studi precedenti per modellare la reazione di dissociazione del metano. Abbiamo trovato che l'approssimazione *sudden*, che presuppone che un certo grado di libertà possa essere 'congelato' quando non cambi sensibilmente nel corso della dinamica, può essere utilizzata nel calcolo della probabilità di reazione per descrivere il movimento laterale della molecola e la sua rotazione. Infine, abbiamo studiato il ruolo svolto dal movimento degli atomi della superficie nella dinamica, e abbiamo trovato che quando una molecola dissocia, l'atomo della superficie sottostante la molecola si trova in media fuori dal piano della superficie nelle traiettorie reattive a basse energie di collisione. Questo risultato è in accordo con studi precedenti secondo cui il movimento dell'atomo della superficie più vicino alla molecola abbassa significativamente la barriera per la dissociazione di quest'ultima se diretto verso la molecola stessa. Queste osservazioni possono spiegare la forte dipendenza dalla temperatura della superficie osservata per la dissociazione del metano su superfici metalliche.

Nel Capitolo 6 abbiamo studiato l'effetto che la scelta del funzionale di scambio e correlazione ha sulla dissociazione del metano su Pt(111). L'obiettivo a lungo termine è quello di trovare un funzionale semiempirico che sia in grado di descrivere accuratamente la reattività di fasci molecolari in cui solo una parte delle molecole è vibrazionalmente eccitata (fasci molecolari 'senza laser'), e la reattività di fasci molecolari in cui lo *stretching* del legame CH è eccitato tramite un laser. Abbiamo considerato vari funzionali di scambio e correlazione, compresi funzionali che cercano di riprodurre l'interazione di tipo van der Waals. È stato recentemente dimostrato che questa classe di funzionali produce buoni risultati nel descrivere la reattività di H_2 e N_2 su superfici metalliche. Il funzionale che restituisce il miglior accordo con i dati sperimentali è un funzionale costituito da un funzionale di correlazione sviluppato per modellare l'interazione di tipo van der Waals, e una combinazione lineare dei funzionali di scambio RPBE e PBE. Nello specifico, questo funzionale produce un buon accordo con gli esperimenti 'senza laser' alle più basse energie di collisione simulate e con gli esperimenti in cui lo *stretching* del legame CH è stato eccitato, migliorando così l'accordo tra teoria ed esperimento rispetto a quanto ottenuto con il funzionale PBE.

In questa tesi abbiamo studiato la dissociazione del metano su Pt(111), ma il metallo che è più rilevante per il processo catalitico di *reforming* con vapore è il nichel. Pertanto, la reazione del metano su superfici di nichel potrebbe essere l'oggetto di studi futuri. Sarebbe interessante studiare l'effetto che l'utilizzo di funzionali che descrivono l'interazione di tipo van der Waals porti nel descrivere questo sistema, come già studiato per la reazione su una superficie di platino. Sul lungo periodo, calcoli di dinamica quantistica multidimensionale potrebbero essere utilizzati per studiare il ruolo del *tunneling* nella reazione di dissociazione del metano, ma solo dopo aver identificato con AIMD un funzionale di scambio e correlazione in grado di produrre accurate superfici di energia potenziale.

Infine, la dissociazione dell'azoto su una superficie di tungsteno (W(110)), è l'argomento del Capitolo 7. Questo sistema è rilevante come sistema modello per la catalisi eterogenea, essendo l'adsorbimento dissociativo di N_2 su una superficie di ferro lo stadio cineticamente limitante del processo di sintesi dell'ammoniaca. Il tungsteno e il ferro presentano alcune somiglianze rispetto all'adsorbimento dell'azoto. Per esempio, entrambi i metalli sono caratterizzati da un'elevata anisotropia cristallografica, che significa che le proprietà di adsorbimento di N_2 dipendono fortemente dalla faccia del metallo esposto alle molecole. Modellare accuratamente lo *scattering* reattivo e non reattivo di N_2 su superfici di tungsteno è un obiettivo che non è ancora stato raggiunto. In questa tesi, abbiamo utilizzato la tecnica AIMD per studiare l'effetto del movimento degli atomi della superficie sulla reattività di N_2 su W(110), testando due funzionali di scambio e correlazione (PBE e RPBE) nei calcoli di struttura elettronica. Modellare il movimento degli atomi della superficie nella dinamica aumenta sensibilmente la reattività di N_2, e suggeriamo che questo abbia a che fare (i) con la disponibilità di profondi minimi di adsorbimento molecolari nella PES e (ii) con il significativo scambio di energia con la superficie. Il trasferimento di energia alla superficie, infatti, facilita l'occorrenza del fenomeno di *trapping*, secondo cui alcune molecole rimangono ‘intrappolate’ in prossimità della superficie, aumentando la probabilità di reazione rispetto alle simulazioni con una superficie rigida. Nessuno dei funzionali di scambio e correlazione testati, tuttavia, produce risultati in accordo con i dati sperimentali.

Per quanto riguarda la dissociazione di N_2 su superfici metalliche, i seguenti punti meritano di essere approfonditi. Innanzitutto, il ruolo che il movimento degli atomi della superficie potrebbe avere nella dissociazione ad alti angoli di incidenza non è noto. Inoltre, sarebbe interessante testare l’uso di funzionali di scambio e correlazione che modellano interazioni di tipo van der Waals e al tempo stesso modellare gli effetti della temperatura della superficie per questo sistema. Oltre alla probabilità di dissociazione, un altro osservabile per cui si potrebbe indagare l’effetto del movimento degli atomi della superficie, è lo *scattering* rotazionalmente inelastico di N_2 su W(110), per cui sono disponibili dati sperimentali. Inoltre, la reazione e lo *scattering* non reattivo di N_2 su altre superfici di tungsteno, come W(100), non è ancora stato studiato con AIMD, simulando la temperatura sperimentale della superficie. Se calcoli AIMD, che si basano sull’approssimazione di Born-Oppenheimer, fossero in grado di descrivere accuratamente sia lo *scattering* reattivo che lo *scattering* non reattivo dell’azoto su superfici di tungsteno, si potrebbe escludere che l’eccitazione di coppie elettrone-buca giochi un ruolo importante nel chemisorbimento dissociativo in questo sistema, argomento di un recente dibattito.

Curriculum Vitae

Francesco Nattino was born on December, 26 1987 in Lecco (Italy). In 2006, he graduated from the high school Liceo Classico A. Manzoni (Lecco). He studied chemistry at the University of Milan from October 2006 to October 2011, obtaining both a bachelor and a master degree *cum laude*. In his bachelor project, he first approached the field of computational chemistry, with a molecular dynamics study of a metabotropic glutamate receptor under the supervision of Dr. Alessandro Contini and Dr. Laura Belvisi. In his master studies, he specialized in physical chemistry and joined the Chemical Dynamics Theory Group of Prof. Dr. Rocco Martinazzo and Prof. Dr. Gian Franco Tantardini. During his master project, which has been partially carried out at the Leiden Institute of Chemistry (LIC) with an Erasmus scholarship, he started working with the *ab initio* molecular dynamics (AIMD) method, investigating the dissociation of molecular hydrogen on a copper surface. In November 2011, he joined the theoretical chemistry group of the LIC as a PhD student, with Prof. Dr. Geert-Jan Kroes as his supervisor. His research project involved the use of AIMD for modeling the reaction of molecules on metal surfaces, as described in this thesis.

List of Publications

- F. Nattino, C. Díaz, B. Jackson, and G. J. Kroes, *Effect of Surface Motion on the Rotational Quadrupole Alignment Parameter of D_2 Reacting on Cu(111)*, Phys. Rev. Lett. **108**, 236104 (2012).
- F. Nattino, H. Ueta, H. Chadwick, M. E. van Reijzen, R. D. Beck, B. Jackson, M. C. van Hemert, and G. J. Kroes, *Ab Initio Molecular Dynamics Calculations versus Quantum-State-Resolved Experiments on CHD_3 + Pt(111): New Insights into a Prototypical Gas-Surface Reaction*, J. Phys. Chem. Lett. **5**, 1294 (2014).
- B. Jackson, F. Nattino, and G. J. Kroes, *Dissociative Chemisorption of Methane on Metal Surfaces: Tests of Dynamical Assumptions Using Quantum Models and Ab Initio Molecular Dynamics*, J. Chem. Phys. **141**, 054102 (2014).
- F. Nattino, A. Genova, M. Guijt, A. S. Muzas, C. Díaz, D. J. Auerbach, and G. J. Kroes, *Dissociation and Recombination of D_2 on Cu(111): Ab Initio Molecular Dynamics Calculations and Improved Analysis of Desorption Experiments*, J. Chem. Phys. **141**, 124705 (2014).
- F. Nattino, F. Costanzo, and G. J. Kroes, *N_2 Dissociation on W(110): An Ab Initio Molecular Dynamics Study on the Effect of Phonons*, J. Chem. Phys. **142**, 104702 (2015).
- F. Nattino, D. Migliorini, and G. J. Kroes, *Methane Dissociation on Pt(111): Searching for a Specific Reaction Parameter Density Functional*, In preparation.